Plutonium multi recycling : self-irradiation effects on the structural properties of future (U,Pu)O2-x nuclear fuels

Orhun Kahraman

THÈSE

Pour obtenir le grade de

DOCTEUR DE L'UNIVERSITÉ GRENOBLE ALPES

École doctorale : I-MEP2 - Ingénierie - Matériaux, Mécanique, Environnement, Energétique, Procédés, Production
Spécialité : MEP - Mécanique des fluides Energétique, Procédés
Unité de recherche : CEA Marcoule

Utilisation d'un Pu à vecteur isotopique dégradé : conséquences sur les propriétés structurales des futurs combustibles (U,Pu)O2-x

Plutonium multi recycling: self-irradiation effects on the structural properties of future (U,Pu)O2-x nuclear fuels

Présentée par :

Orhun KAHRAMAN

Direction de thèse :

Michel MERMOUX DIRECTEUR DE RECHERCHE, Université Grenoble Alpes	Directeur de thèse
Philippe MARTIN INGENIEUR-CHERCHEUR, CEA Marcoule	Co-encadrant de thèse
Florent LEBRETON INGENIEUR-CHERCHEUR, CEA Marcoule	Co-encadrant de thèse

Rapporteurs :

Thierry WISS
SENIOR SCIENTIST, Joint Research Center
Jesse GROENEN
PROFESSEUR DES UNIVERSITES, Université Toulouse III - Paul Sabatier

Thèse soutenue publiquement le **6 décembre 2023**, devant le jury composé de :

Fiqiri HODAJ PROFESSEUR DES UNIVERSITES, Grenoble INP	Président
Nathalie MONCOFFRE DIRECTRICE DE RECHERCHE, CNRS délégation Rhône Auvergne	Examinatrice
Gaëlle GUTIERREZ INGENIEURE, CEA centre de Paris-Saclay	Examinatrice
Michel MERMOUX DIRECTEUR DE RECHERCHE, CNRS délégation Alpes	Directeur de thèse
Thierry WISS SENIOR SCIENTIST, Joint Research Center	Rapporteur
Jesse GROENEN PROFESSEUR DES UNIVERSITES, Université Toulouse III - Paul Sabatier	Rapporteur

Invités :

Florent LEBRETON
INGENIEUR-CHERCHEUR, CEA Marcoule
Philippe MARTIN
INGENIEUR-CHERCHEUR, CEA Marcoule

« Dédiée à Asya »

O. Kahraman 2023

Acknowledgements

At this point I would like to extend my heartfelt gratitude to people who had contribution to my PhD degree. There is no doubt that their support and guidance have been invaluable throughout these important years of my life.

I start with appreciation to the esteemed members of the jury, namely Fiqiri Hodaj, Thierry Wiss, Jesse Groenen, Nathalie Moncoffre, and Gaëlle Gutierrez, for graciously agreeing to assess as well as the thorough evaluation and discussion during the defense of this PhD work.

My deepest appreciation for my supervisors Michel Mermoux, Florent Lebreton and Philippe Martin.

Even though there were tough times during my thesis when I wished to be closer to Michel, he supported me like he was right there with me. I'm sincerely thankful to him for his availability throughout the years. I could have his support anytime and even hearing his voice was enough for me to gain back my motivation. The expertise he shared with the Raman spectroscopy and his scientific approach was invaluable. I was feeling blessed for each moment that I was discussing with him.

I can simply say that Florent is one of the best things that happened in my life. His presence and the joy that he shared in the lab was priceless. I learnt the experimentation and applications in nuclear materials from him and he was not hesitating to come and help anytime I needed. He was extremely practical and intelligent in applications and in calculations. I'm grateful to him for all the information that he shared throughout the years.

I sincerely thank Philippe for opening me the world of synchrotron radiation. I'm grateful to him for the information and experience that he shared in the nuclear materials as well as his scientific approach. I appreciate his patience and unwavering support throughout my PhD journey.

I would like to thank to my previous supervisors that had intensive contributions to this success through supporting my development over my years in the academy. I would like to thank to Deniz Üner, Ertuğrul Erkoç, François Kremer, Roland Dubourg, Paul van Uffelen, Sylvie Delpech, Gérard Cote, Frederico Garrido, Mathieu Lebois, Mehdi Amouei, Türker Gürkan, Güngör Gündüz, Ahmet Yaylı and Cüneyt Hızlı.

I would like to thank to my colleagues in Atalante, with special thanks to Rafael. I was always grateful to have such senpai next to me sharing the office. The discussions that we had together were always helpful. I also appreciate his helps notably for sharing his expertise for the synchrotron radiation and its application in the nuclear materials. I sincerely thank to my lab chef Aurélie and my dear colleagues Méghan, Lise, Camille, Mikael, Simon, Pauline, Julie, Fanny, Patrick, Mathilde, Steph and my ex-chef of the lab Emanuel.

I thank to the LN0 lab team in the Atalante facility notably to Julien and Guillaume for their availabilities and helps during the thermal treatments.

I appreciate all Atalante facility employees, especially the hardworking SPR team (Christine, Agnes, Antony x2, Djemal, and Donut), along with Herve Largillier and Hafid Kapouch. Their dedication in work have made life easier in Atalante.

Special thanks to Damien Prieur of ESRF, as well as to Myrtille Hunault and Pier-Lorenzo Solari of the Soleil Synchrotron for accepting our proposals and their helps throughout the beamtime.

Deepest gratitude to my French language tutors notably to Nathalie Daguet and Jean-Philippe Wamengwa Diasivi for not only the French language, but also for all the good memories that we shared over the three years.

Being the sole representative of my family in France had its challenges, but the support of special people made it feel like I never left my country.

I express sincere thanks to the Didier Family for their acceptance, love, care and endless supports notably to Marc, Françoise, Louis, Aline, Simon, and Iseur Didier.

I'm grateful to little brother Baptiste Macias and his family. Et oui, je suis pour OM.

Special gratitude to the Bourbon Family: Paul, Özlem, Menekşe, and Kerem Bourbon.

My family in Paris: Alexia Dechaux, Aure Luce, Tenko and Ava.

Friends at the Atalante facility: Yann Seillier, Bruno Charles, Sergio Da Cunha, Duc Tri, and Hamza Karim.

Friends at the Radiochemistry lab at Orsay: Alexandre Chmakoff and Hugo (ve Tolga Abi) Sauzet.

Thanks to friends in Avignon: Anas, Mustafa Abi, Hasret, Yahya, Ali Abi, Kadir, Antony and Natalia Perez.

I deeply appreciate the Kılıç Family of Ankara. Notably Gökhan, Tanya, Akay and Nisa Kılıç for their endless support during my journey in Ankara and in France.

Endless gratitude for the Güvenli family of Izmir for their unconditional love and support. Notably to Şerife, Osman, Samet, İlknur, Elisa and Tony Güvenli.

Tacettin Amca and Selahattin Amca for the cherished memories.

My friends Alper, Sultan, Saime, Mustafa Saleh, Aslı, Zeki, Ezgi, Şükrücan, Veysi (as always), Batuhan, Üsame, Farooq, Bazil, Bahtiyar and of course Hacımehmet Özgün Uluğoğullarından.

Lastly, my deepest appreciation goes to my parents for their unwavering and unconditional support.

Table of Contents

Introduction

Among different ways we produce energy, nuclear power is a strong and clean source of electricity, with the potential to sustain our energy needs. So far, nuclear power plants are operational in 31 countries worldwide with more than 18,000 reactor years of experience [1]. The current status of the energy demand, however, brings the necessity of continuous development of the nuclear technology and to optimize the use of nuclear fuels. Today, we predominantly rely on Light Water Reactors (LWR) and Heavy Water Reactors (HWR) for nuclear energy, with LWRs being the common choice.

LWRs commonly rely on UOx (uranium dioxide (UO_2) fuels) as their primary fuel source, enriched in ^{235}U between 3 and 5 wt%. Nevertheless, for a better waste management and to optimize the use of natural resources, a closed fuel cycle is adapted by several countries. Such strategy allows valorizing plutonium with its use as a reactor fuel. For more than 30 years, France has implemented spent fuel reprocessing at the industrial scale, notably to extract the Pu from the UOx spent fuel. The Figure 1 illustrates a simplified representation of the current French version of closed fuel cycle. The recovered plutonium, mainly composed of fissile ^{239}Pu, is mixed with depleted uranium (U), both as oxides, to produce $(U,Pu)O_2$ Mixed Oxide fuel (MOX). This fuel has a Pu/(U+Pu) content ranging between 6% and 10% and is optimized for the current French LWR fleet. The commercial fabrication of this fuel takes place in the Orano Melox facility in France.

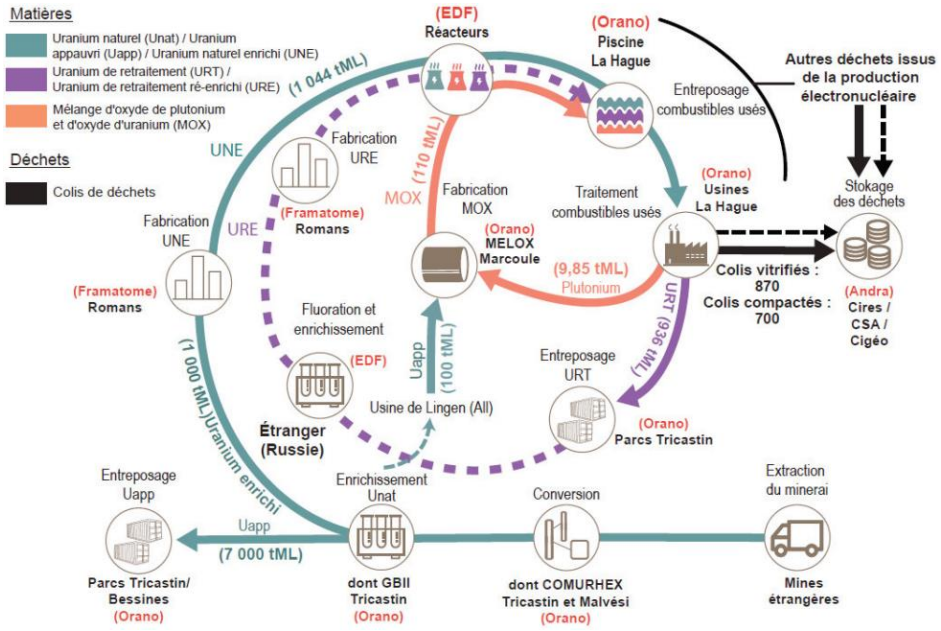

Figure 1 Simplified diagram of a closed fuel cycle adapted for the French nuclear program [2]

Presently, spent nuclear fuel is cycled only once, *i.e.* only UOx spent fuels are routinely reprocessed. The accomplishment of a fully closed fuel cycle, however, relies on the multi-recycling of Pu, *i.e.*, the extraction of Pu from spent MOX fuels [3]. This technology is under development in the French nuclear program.

In the currently employed MOX fuels, the Pu isotopic composition primarily consists of ^{239}Pu, which represents more than 50 wt% of the composition. However, the isotopic composition of multirecycled Pu will be different, as further recycling enriches the isotopy toward ^{238}Pu, ^{240}Pu, and ^{241}Pu (which decays into ^{241}Am) at the cost of the ^{239}Pu isotope. Given the significantly higher alpha (α) activities of ^{238}Pu (633.4 GBq/g), ^{240}Pu (8.4 GBq/g), and ^{241}Am (127 GBq/g) in comparison to that of ^{239}Pu (2.3 GBq/g), these new fuels will be subjected to stronger alpha self-irradiation. The latter will accelerate the accumulation of defects in the fuel's crystal structure and microstructure. This phenomenon is one of the challenges associated with Pu-multirecycling. Consequently, it becomes crucial to carefully assess this

defect accumulation, notably because of the possible consequences on the fuel's state evolution during the period between manufacturing and irradiation.

At the macroscopic level, alpha self-irradiation is known to result in lattice swelling (lattice parameter increase of up to 0.29% for $(U,Pu)O_2$ materials) due to the recoiling nuclei that cause damage cascades and/or the accumulation of helium atoms over time [4]. Until now, the lattice parameter increase of $(U,Pu)O_2$ due to the α-decay of the Pu isotopes and its evolution with time has been rather well documented, but this knowledge largely relies on empirical observations [5]–[9].

Hence, a comprehensive understanding of the underlying mechanisms at the microscopic scale remains incomplete. The identification and the description of the point or extended defects, their stability vs time and temperature, and the mechanisms that lead to the swelling are yet to be revealed and described. In this context, this thesis work focuses on characterizing and understanding the defects generated through alpha self-irradiation in uranium-plutonium mixed oxides and their impact in the fuel microstructural properties. Within this scope, one LWR type MOX fuel and two Sodium Fast Reactor (SFR) type MOX fuels are analyzed in this study. Here, the two type of MOX fuels here have inherent differences in terms of homogeneity and overall Pu contents due to their different fabrication routes.

Some advanced characterization methods such as Transmission Electron Microscopy (TEM) [10], [11], Electron Energy Loss Spectra (EELS) [10] and Molecular Dynamics (MD) [12], [13] studies have been conducted in the literature to have insights about the swelling in the atomic scale. The observations of the first two techniques suggests that the cationic and oxygen sublattice are not affected in the same way, which makes it necessary to use several techniques that will be sensible to modification of these specific sublattices. Furthermore, given the inherent heterogeneity of the materials studied, it is evident that a complementary use of global and local scale characterization will be necessary to obtain information in the samples. Considering all these facts, four methods are principally used in this study, which are X-ray Diffraction (XRD), Raman spectroscopy, Electron Microprobe Analysis (EPMA), and X-ray Absorption Spectroscopy (XAS).

In this essence, in such compounds, XRD probes the cationic sublattice only and provides insights into changes in lattice parameters, also offering information on the overall Pu content and O/M ratio. In contrast, Raman spectroscopy is used for investigating the oxygen sublattice. XAS enables us to probe the short-range order through providing evolution of distances of the first oxygen and first cation coordination shells. The evolution in the Debye Waller factor is used to observe the changes in the structural disorder within these shells. Moreover, the oxidation states of each cations and their evolution could be followed. Furthermore, Electron Microprobe Analysis (EPMA) is also used to have information on the local Pu content at the µm scale.

Within the scope of the thesis, the Raman spectroscopy technique was given more emphasis than other methods. This technique is particularly valuable for revealing structural deformations and detecting alterations in local symmetry. The current literature include a significant number of studies of actinides mixed oxides, but their Raman spectra are not yet fully understood. In this work, Raman spectroscopy will thus not only be used as a tool for characterizing the self-irradiation induced-damage but also to get a better understanding of the structural information contained in these spectra. Moreover, an advantage of this method is that the spectrometer used in this study is coupled with a confocal microscope, allowing for Raman imaging. Given the chemical heterogeneity of the samples at the µm scale, this will allow Raman data to be correlated with the local plutonium content. We will thus be using the sample heterogeneity to our advantage, using it to study a whole range of plutonium contents, rather than having to deal with averaged data.

This manuscript is divided in five chapters.

The first chapter gives a literature review, offering an overview of the thermodynamics and crystallography of the materials examined in this thesis, all of which exhibiting a common fluorite –type symmetry. The chapter continues with the alpha self-irradiation effect and the resulting defect generation mechanisms in the actinide oxide materials. The chapter also includes the previous research that focuses on identification of these defects using different characterization methods notably: XRD, Raman spectroscopy, TEM and MD.

The second aims at introducing the experimental approach used for this study. It comprises two primary sections. The first introduces the MOX materials used in this thesis, providing their chemical and isotopic compositions. Additionally, this section outlines the methodology applied, which is based on the annealing of the samples and the subsequent accumulation of the defects. The second section of the chapter aims at describing the characterization techniques employed in our study. Notably, a dedicated sub-section is included for the resonant Raman scattering and the utilization of Raman spectroscopy in the analysis of actinide oxide materials.

The third chapter involves the application of the characterization techniques described in the previous chapter for the examination of the samples after annealing *i.e.* the defect free samples. The analysis of the samples includes their local plutonium content, average lattice parameters, mean atomic distances in the first oxygen and cation shells, Debye Waller factors as well as the oxidation states of the cations, including uranium, plutonium, and americium. Considering the microstructure of the materials studied in this work, which are inherently heterogeneous, the results are analyzed under some assumptions that are detailed in this chapter. This also helped us to understand the extent and limits of the characterization methods on these specific materials.

The fourth chapter is dedicated to analyze of the self-irradiation effects in the MOX samples. For this purpose, samples that accumulated different levels of self-irradiation damages on their microstructure are characterized by means of XRD, Raman spectroscopy, and XAS. The evolution of the interatomic distances will thus be described, both at the global scale (but only for the cationic sublattice) using XRD, as well as the local symmetry around cations using EXAFS. These methods will also bring information on the structural disorder building up in the materials under self-irradiation. The evolution of the Raman spectra under self-irradiation will also be described, taking advantage of Raman imaging to correlate these evolution with the local Pu content.

Up until this final chapter, the results will have been presented in a descriptive manner, primarily focusing on the obtained results and their comparisons with values found in the literature. The discussion was intentionally reserved for this concluding part. Within this chapter, a comprehensive analysis is provided for interpreting the impact of the self-irradiation effect on the Raman spectrum of the MOX samples. In the end, using the findings obtained in this study as well as the data available in the literature, potential scenarios are given to understand the lattice swelling and the changes in the physicochemical properties of MOX resulting from self-irradiation defects.

Three appendix sections have been included to provide readers with additional information. Appendix A covers details related to sample fabrication, their preparation, annealing. In Appendix B, optical and selfradiography images of the sample surfaces used in the study are presented. Appendix C describes the experimental conditions for all the characterization techniques employed in this work

Chapter 1. Literature Review

This chapter is divided into three main sections. In the first section, a thorough description of the U-O and Pu-O binary systems and their related thermodynamics are given. For these systems, the crystallographic structures of the phases of interest for this study are detailed. Then, the U-Pu-O ternary system and the crystal structures of the related oxide phases are discussed.

The second section begins with the generalities concerning defects within crystalline solid materials. Following this, it engages into an analysis of the literature regarding the alpha self-irradiation effect in MOX materials, along with the corresponding mechanisms generating defects.

The third and last section of this chapter presents the characterization techniques used in the literature to identify the self-irradiation defects in MOX materials. It includes XRD (X-ray diffraction), Raman microscopy, TEM (transmission electron microscopy) and MD (molecular dynamics) studies.

1.1 Crystallographic structures and thermodynamics of Actinide Oxides

From a crystallographic point of view, $(U,Pu)O_2$ fuel can be described as the incorporation of Pu in the UO_2 crystal structure. As a result, a good comprehension of the U-Pu-O ternary system and its corresponding phase diagram is necessary, with a focus on the domain of interest for the fuels (Pu/(U+Pu) contents lower than 40 at% and O/M (oxygen to metal, M = U, Pu, Am…) ratio close to 2). This section first starts with presenting the U-O and Pu-O binary systems, before discussing the U-Pu-O ternary system.

1.1.1 U-O Binary System

1.1.1.1 General description

The U-O binary system has been studied for decades and several review documents are available in the literature providing experimental and modelling results [14]–[16]. Figure 2 shows the thermodynamic modelling of the U-O phase diagram developed by Guéneau *et al.* [17] using the CALPHAD method. Figure 2b, where experimental data are also plotted, concentrates on the region of interest for this study, *i.e.* the range of O/U ratio between 1.90 and 2.40 corresponding to U oxidation states of +3, +4, +5 and +6.

For the O/U ratio ranging between 2 and 3, the oxides UO_{2+x}, U_4O_9, U_3O_7, U_3O_8, and UO_3 are formed. Despite $UO_{2.00}$ and $UO_{3.00}$ which are pure U^{4+} and U^{6+}, the phases UO_{2+x}, U_4O_9 and U_3O_7 consist of U^{+4} and U^{5+} oxidation states that co-exist with different ratios, while for U_3O_8 the oxidation state is a mixture of U^{+5} and U^{+6} [17].

The particularity of the U-O system is the large stability domain of the $UO_{2\pm x}$ phase both in temperature and oxygen stoichiometry. From stoichiometric conditions (O/U=2.00) until slight departure from stoichiometry ~2.03, this phase exists as a single phase from the ambient temperature until its melting point which is above 3000 K [14].

Upon further increase of O/U ratio from 2.03 until 2.25, the phase diagram shows that the UO_{2+x} phase exists in equilibrium with the U_4O_{9-y} phase, while their discrimination in XRD is rather difficult due to their close crystal structure in cubic symmetry, as later described in Section 1.1.1.2. At ambient temperature,

for an O/U ratio between 2.25 and 2.33, U_4O_{9-y} co-exists with the metastable U_3O_7 phase, while at O/M between 2.33 and 2.67, the U_3O_8 phase prevails and coexists with, yet again the metastable U_3O_7 phase. For 2.67 < O/U < 3.00, on the other hand, U_3O_8 coexists with UO_3 and beyond that UO_3 is present as a single-phase in equilibrium with gaseous O_2 in the system [18].

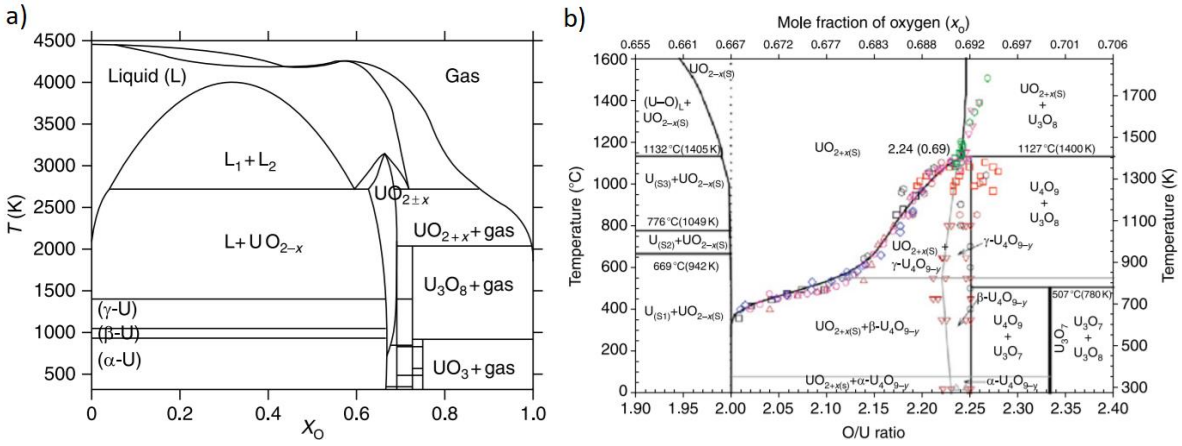

Figure 2 a) U-O system phase diagram at P = 1 atm pressure, x(O) represents oxygen molar concentration, b) U-O diagram centered on the region of interest for this thesis [17], [19].

1.1.1.2 Crystallographic data

Almost all studies on nuclear fuels, and thus for this study, concerns the U-O system with an oxygen stoichiometry between 2.00 and 2.25. At the ambient temperature, the equilibrium conditions show that the phases that exist in this range are UO_{2+x} and U_4O_9. In the following sub-sections, their crystal structures are thus described, as well as those of U_3O_7 and U_3O_8 as they can bring some understanding of the defects that can be present in the oxygen sublattice. A summary of the crystallographic data for the U-O phases is given in Table 1.

1.1.1.2.1 UO_2

UO_2 crystallizes in a fluorite-type structure (space group $Fm\bar{3}m$, n°225). In this structure, the cations occupy the regular sites of a face-centered cubic (FCC) structure, while the oxygen atoms reside in the eight tetrahedral interstitial sites of the cationic sublattice, thus forming a simple cubic sublattice. A representation of the UO_2 fluorite-type structure is given in Figure 3. At room temperature, the lattice parameter of the stoichiometric $UO_{2.00}$ unit cell was recently reported as 5.47127 ± 0.00008 Å [20] (after having been considered for a long time equal to 5.470 Å [21]).

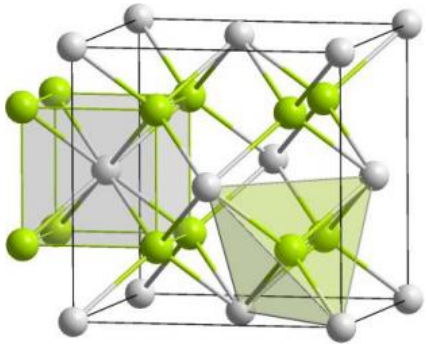

Figure 3 Schematic representation of the UO_2 fluorite-type crystal structure. The grey balls are the U atoms, the green balls are the oxygen atoms [22]

As illustrated by the UO_{2+x} stability domain, the fluorite UO_2 structure can incorporate additional oxygen atoms. For a range of x (deviation in stoichiometry) between 0 and 0.24, the fluorite geometry is conserved in the cationic sublattice. The only modification is a progressive decrease of the lattice parameter with x. For x lower than 0.125, Lynds *et al.* reported a coefficient of -0.094Å per x [23].

The positions of the incorporated oxygen atoms were first analyzed by Willis through a neutron scattering experiment at high temperature (1073 K) using an $UO_{2.13}$ sample [24]. The results indicate that the incorporated oxygen atoms do not find their position at the high-symmetry octahedral sites but are displaced by about 1 Å in the <110> and <111> directions, which are labeled as O' and O'' atoms respectively [24]. The incorporation of this new oxygen pairs is later followed by the creation of an oxygen vacancies nearby as shown in Figure 4a. This model is later referred as the (2:2:2) defect cluster model or Willis clusters in the literature, containing two O' atoms, two oxygen vacancies and two O'' atoms [25] as illustrated in Figure 4b.

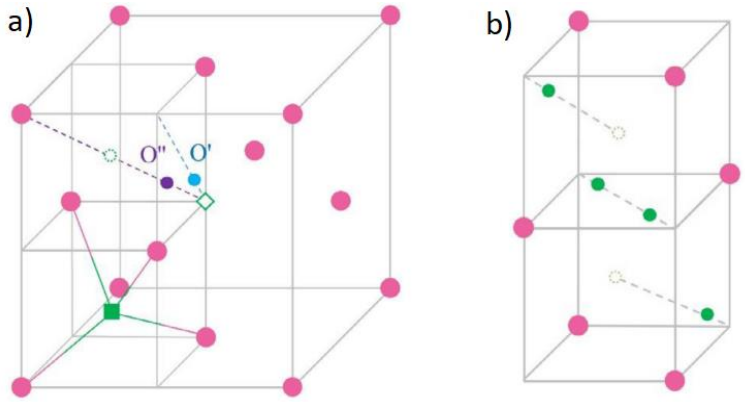

Figure 4 Incorporating additional oxygen atoms at the UO_2 structure. a) Positions of the O' and O'' atoms and formation of oxygen vacancy b)The (2:2:2) Willis cluster model (Pink dots denote normal U atom, green cube denotes normal O atom, green dots denote O interstitial, green open diamond denotes the octahedral site and green open dots denote O vacancies [26].

When the oxygen stoichiometry increases, the Willis cluster agglomerate into the cuboctahedral clusters as shown in Figure 5. This defect is composed of 8 oxygen vacancies, 12 oxygen atoms in the O' position and 1 oxygen atom in the O'' position and thus denoted as (8:12:1). These cuboctahedral defects accumulate in the UO_{2+x} structure without modifying the uranium sublattice. When the O/U ratio gets close to 2.25, the accumulation of cuboctahedral clusters leads to small distortions of the cationic sublattice and the formation of the U_4O_{9-y} phases.

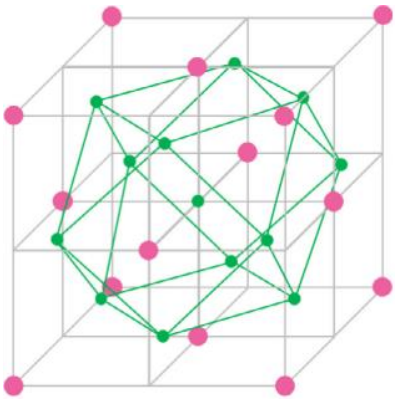

Figure 5 The cuboctahedral cluster of O atoms and first shell of U atoms. The oxygen vacancies are not shown for simplicity [26].

1.1.1.2.2 U_4O_9

Three allotropes exist for the U_4O_9 crystal structure (α, β and γ) that become stable within specific temperature ranges: α-U_4O_9 (for temperatures below 50°C), β-U_4O_9 (for temperatures between 50°C and 600°C), and γ-U_4O_9 (for temperatures between 600°C and 1250°C). These allotropes are associated with changes in the fluorite arrangement of the cationic sublattice, which evolves with varying temperatures. [26]. At temperatures above 1250°C, on the other hand, γ-U_4O_9 decomposes to UO_{2+x} (with a value of *x* close to 0.25) [27].

The β-U_4O_9 phase structure is a 4×4×4 superstructure of the UO_{2+x} fluorite structure ($I\bar{4}3d$ space group, N° 230) with a lattice parameter of 21.77 Å [28]. This value is very close to four times that of UO_{2+x} for at the same O/U ratio, *i.e.* an *x* value of 2.25 (considering the dependency of the lattice parameter to the oxygen stoichiometry of Lynds *et al.* given in 1.1.1.2.1).

The reorganization of the oxygen anions in the oxygen sublattice leads to changes in the U-O distances from those found in UO_2 [29]. Besides, the cationic sublattice is also affected by the presence of the cuboctahedrons resulting in some of the uranium cations being slightly displaced relative to their position in a fluorite like structure (as shown in Figure 6b) [30].

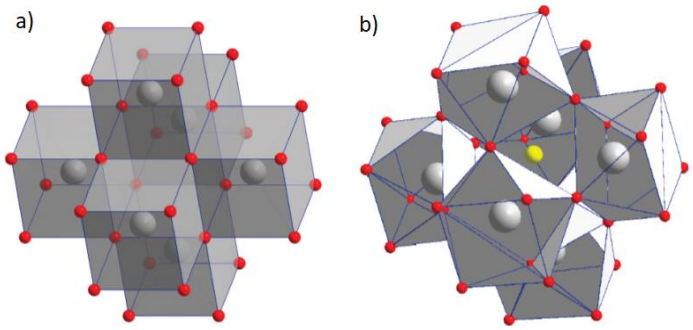

Figure 6 Comparison between the a) UO_2 lattice and b) a cuboctahedron of anions formed from six square antiprisms of the β-U_4O_9 structure according to Desgranges et al. [31]

The structure of the α-U_4O_9 phase (<50°C) is considered as closely related to the β-U_4O_9 phase, differing only by small distortion in the α angle, being 90.08° [32]. It has a trigonal rhombohedral crystal structure, corresponding to the *R*3*c* (N° 161) space group [28]. Regarding the γ-U_4O_9 crystal structure, on the other hand, it is considered to have a cubic structure, nevertheless its space group is not yet clearly defined in the literature [33].

The composition ratio of (pure) U_4O_9 is known to be close to O/U~2.24 [27], thus slightly below than its nominal stoichiometric ratio O/U=2.25 [34]. Regarding this, Van Lierde *et al.* suggests that at room temperature the O/U ratio of U_4O_9 is between 2.235 and 2.240 [27].

The distribution of the uranium oxidation states were studied by Kvashnina *et al.* [35] and Leinders *et al.* [36]. According to them, the XANES experimental data acquired for U_4O_9 provides indications a combination of U^{+IV} and U^{+V} and the absence of U^{+VI}.

1.1.1.2.3 U_3O_7

When the ratio of oxygen to uranium (O/U) surpasses 2.234, the symmetry is lowered [37], yet the atomic structure maintains a close connection to the fluorite arrangement until the creation of U_3O_8, which possesses a distinct crystal structure[38], [39]. The compounds that lie between $U_4O_{9-\varepsilon}$ and U_3O_8 have been provisionally designated with formulas such as U_3O_7 or U_2O_5, relying on thermogravimetric data [40], [41]. For the case of O/U ratio close to 2.333, the structure is commonly referred to as U_3O_7, which is an intermediate product formed during the oxidation of UO_2 or U_4O_9 to the U_3O_8 phase [33].

The crystal structure of U_3O_7 has similar characteristics with the U_4O_9 structure, differing mainly with the increased quantity in cuboctahedral clusters bringing them closer to each other (even sharing edges) which causes distortions in the cubic lattice. Subsequently, the c/a ratio becomes no longer equal to unity [42] and thus a tetragonal structure prevails. The first investigations documented the presence of two polymorphs, notably the α-U_3O_7 (with a c/a ratio ~0.986) and β-U_3O_7 (with a c/a ratio ~1.031) [43]. Nevertheless, the recent investigation had some difficulties with differentiating the α-U_3O_7 phase from the cubic $U_4O_{9-\varepsilon}$ phase, which emerges during the earlier stage of oxidation [44]. Fluctuations in the axial

ratio (with 1 < c/a ≤ 1.031) are frequently documented, yet they consistently remain below c/a ≈ 1.031, corresponding to the value attributed to β-U_3O_7 , which is the most referred polymorph [45].

The most recent explanation of its crystal structure was done by Leinders *et al.* [45], stating that the U_3O_7 exhibits a long-range ordered structure that bears a strong resemblance to the fluorite-type configuration seen in UO_2 [45]. The cations maintain the same arrangement found in the fluorite structure, while surplus anions create deformed cuboctahedral oxygen clusters, intermittently substituting the fluorite's anion pattern. In relation to the oxidation states of the cations, the XANES experiments conducted by Leinders *et al.* [36], indicated a mixture of U^{+IV} and U^{+V}.

1.1.1.2.4 U_3O_8

All the phases described previously can be explained through making analogies to the fluorite structure. Nevertheless, for an O/U ratio above 2.33, the fluorite structure cannot hold more oxygen ions and transforms into U_3O_8 with a unique crystal structure particularly with differences in the cationic sublattice [46], where this difference is linked to the emergence of the U^{+VI} state in the crystal structure. As indicated by Kvashnina *et al.* [35] and Leinders *et al.* [36] the XANES experimental data acquired for U_3O_8 provides indications of a mixture of U^{+V} and U^{+VI} oxidation states.

Three polymorph phases are identified for the U_3O_8 structure, which are α-U_3O_8, α'-U_3O_8 and β-U_3O_8 phases. The α-U_3O_8 phase (*C2mm* (Nº 35)) and the β-U_3O_8 phase (*Cmcm* (Nº 63)) have similar crystal structures both being orthorhombic [39]. The α-U_3O_8 phase transforms to the α'-U_3O_8 phase at higher temperatures (between 150-200°C) becoming a truly hexagonal crystal structure corresponding to $P\bar{6}2m$ space group (Nº 189) [47].

Table 1 Summary of the crystallographic data of uranium oxides of interest [48]

Phase	O/U ratio	Space Group	Symmetry	Lattice parameters (Å)	Ref.
UO_{2+x}	2.00→2.25	$Fm\bar{3}m$	Cubic	a=b=c=5.471→5.445	[23]
α-U_4O_9	2.235→ 2.240	*R*3*c*	Rhombohedral	a= b=c=4 × (5.441→5.444); α=90.078° (T=20°C)	[27]
β-U_4O_9	2.25	$I\bar{4}3d$	Cubic	a= b=c=4 × 5.438 (T=65°C)	[28]
γ-U_4O_9	2.25	Not reported	Cubic	a=b=c=4 × (5.47→5.50) (T>600°C)	[28]
α-U_3O_7	2.33	*I*4/*m*	Tetragonal	a=b=5.472, c=5.397	[43]
β-U_3O_7	2.33	$I\bar{4}2$d	Tetragonal	a=b=5.363, c=5.531	[43]
γ-U_3O_7	2.33	Not reported	Tetragonal	a=b=5.41, c=5.49	[40]
α-U_3O_8	2.67	*C2mm*	Orthorhombic	a=6.715, b=11.96, c=4.146	[47]
α'-U_3O_8	2.67	$P\bar{6}2m$	Hexagonal	a=b=6.812, c=4.146	[47]
β-U_3O_8	2.67	*Cmcm*	Orthorhombic	a=7.07, b=11.45, c=8.30	[39]

1.1.2 Pu-O Binary System

1.1.2.1 General Description

The Pu-O phase diagram has been studied since the late fifties [49]–[51]. Figure 7a is the Pu-O phase diagram calculated by Guéneau *et al.* [17] using the CALPHAD method, where the Figure 7b focuses on the region of interest for this study with an O/Pu ratio between 1.5 and 2.00.

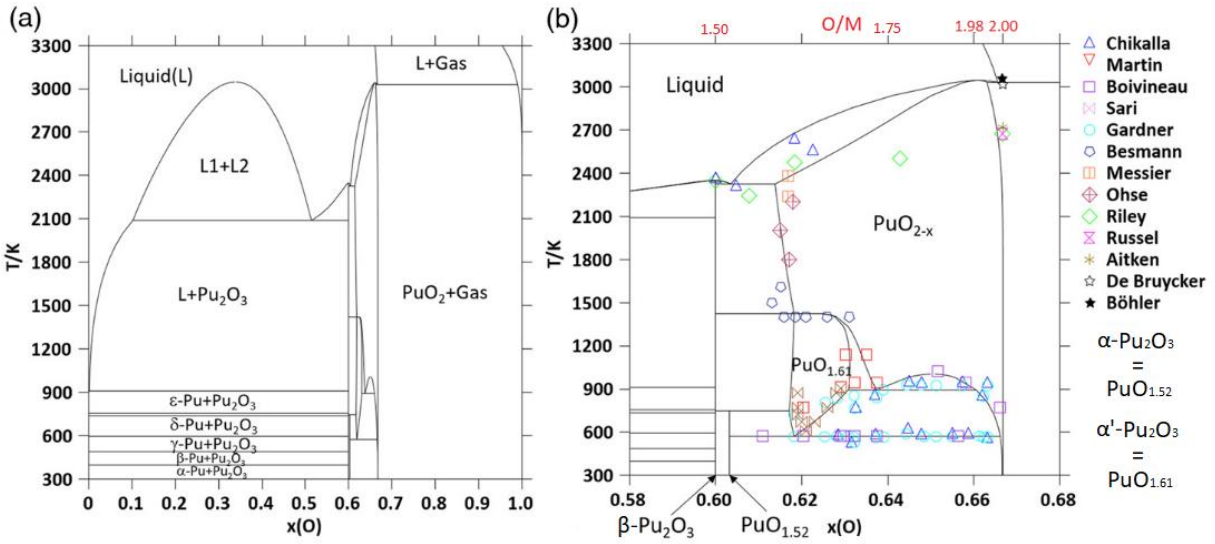

Figure 7 a) Representation of the Pu-O phase diagram b) centered on the given range of oxygen molar fraction (0.58 < x (O) < 0.68) calculated by Guéneau *et al.* [17], the same figure also displays the experimental data provided by various authors

In the Pu-O binary system, plutonium can only have two oxidation states: +3 and +4 meaning that only oxygen hypostoichiometry exists, contrarily to the U-O system [17]. Four solid phases are identified in the region of interest: β-Pu_2O_3, α-Pu_2O_3 ($PuO_{1.52}$), α'-Pu_2O_3 ($PuO_{1.61}$) and PuO_{2-x}, from which only the β-Pu_2O_3 phase has hexagonal symmetry, while the three others are cubic.

The PuO_{2-x} phase can accept oxygen hypostoichiometry over a larger range with increasing temperature, down to an O/Pu of 1.7 at temperatures above 923 K. The other three phases described in the phase diagram are the reduced phases for PuO_{2-x} that exist at rather lower temperatures compared to the stability domain of PuO_{2-x}. The β-Pu_2O_3 and the α-Pu_2O_3 are the two definite phases having fixed O/Pu ratios slightly above 1.50 [50]. Up to a temperature of 873 K, the body-centered cubic (bcc) α-Pu_2O_3 phase coexists in equilibrium with PuO_2 and the sesquioxide β-Pu_2O_3 phase [52]. For temperatures above 573 K, the α-Pu_2O_3 phase takes up more oxygen and forms a new body centered cubic phase with a range of O/Pu from 1.61 to 1.69 and denoted as the α'-Pu_2O_3 phase [49].

Furthermore, a narrow miscibility gap is reported in the fluorite phase in a limited domain (between 900 and 1000 K and for 1.78 < O/Pu < 1.94) leading to the simultaneous presence of two fluorite-type PuO_{2-x} phases with different stoichiometry [49], [50].

1.1.2.2 Crystallographic Data

The crystal structure of the phases present in the Pu-O phase diagram are detailed in this section. A summary of the crystallographic data for the Pu-O phases is later given in Table 2.

1.1.2.2.1 PuO_2 Phase

The PuO_2 phase crystallizes in the same fluorite-type structure as UO_2, which is described in section 1.1.1.2.1 (space group $Fm\bar{3}m$, n°225) and its crystal structure is illustrated in Figure 3. The lattice parameter of freshly annealed $PuO_{2.00}$, *i.e.* free from alpha self-irradiation damage, is reported as

5.396±0.001 Å by Gardner *et al.* [50]. As described in the previous section, the crystal structure accepts oxygen hypostoichiometry, which results in oxygen vacancies and a lattice parameter increases while plutonium is partially reduced to Pu^{+III}.

1.1.2.2.2 α-Pu_2O_3 Phase ($PuO_{1.52}$)

Decreasing the oxygen content in PuO_{2-x} causes an ordering of the oxygen vacancies, leading to a re-arrangement of the fluorite structure into a superstructure. This new crystal structure is composed of eight fluorite unit cells and corresponds to the C-type rare-earth sesquioxide structure ($Ia\bar{3}$, space group Nº 206), as shown in Figure 8. Its lattice parameter is about twice that of PuO_2. This rearrangement of the oxygen vacancies causes a distortion in the structural symmetry and form a second cationic site as illustrated more clearly in Figure 8b, where the cations shifted from their initial position are colored in blue [53].

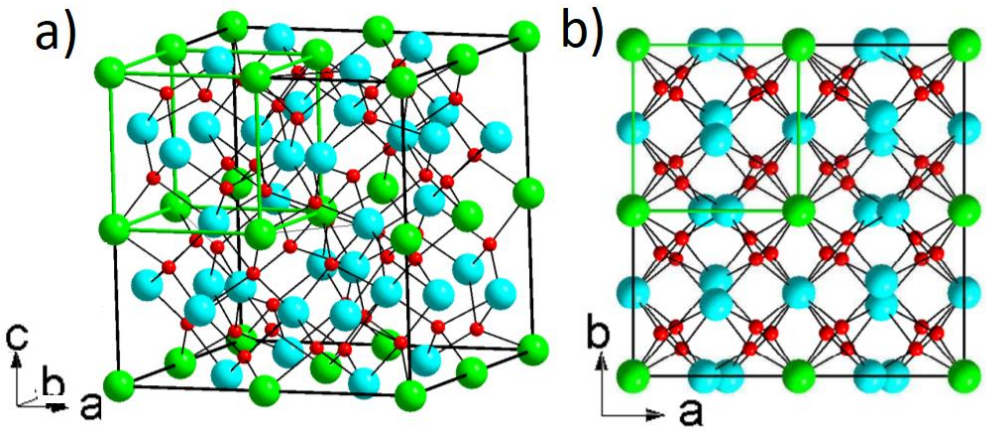

Figure 8 a) The representation of the α-Pu_2O_3 phase (C-type sesquioxide structure) b) View along the [001] axis [53]

1.1.2.2.3 α'-Pu_2O_3 Phase ($PuO_{1.61}$)

The structure of α'-Pu_2O_3 has not been definitely resolved but is believed to be closely related to that of the α-Pu_2O_3 [54].

1.1.2.2.4 β-Pu_2O_3 Phase ($PuO_{1.5}$)

Hexagonal Pu_2O_3, frequently termed as β-Pu_2O_3, exhibits the A-type rare-earth sesquioxide structure with the $P\bar{3}1m$ space group (Nº 164) as illustrated in Figure 9 [54]. Its upper limit oxygen content has been reported as O/Pu = ~1.510 by Gardner *et al.* [50]. In this structure, each cation is surrounded by seven oxygen atoms forming an octahedral shape around the metal atom and there is one oxygen atom placed above one of the octahedral faces [55].

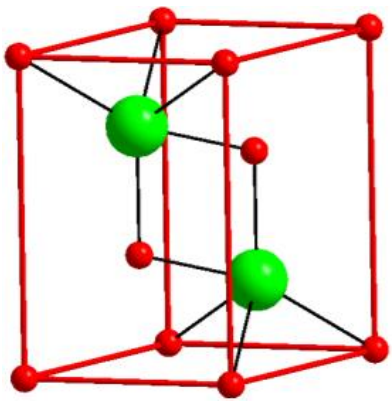

Figure 9 The representation of the La_2O_3 sesquioxide structure of type A [53]

Table 2 Summary of the crystallographic data of of plutonium oxides

Phase	Structure Type	Space Group	Symmetry	Lattice parameters (Å)	Ref.
β-Pu_2O_3 ($PuO_{1.5}$)	La_2O_3	$P\bar{3}1m$	Hexagonal	a=b=3.841, c=5.958	[54]
α-Pu_2O_3 ($PuO_{1.52}$)	Mn_2O_3	$Ia\bar{3}$	BCC	a=b=c=11.050	[54]
α'-Pu_2O_3 ($PuO_{1.61}$)			BCC	a=b=c=11.00	[54]
PuO_2	CaF_2	$Fm\bar{3}m$	FCC	a=b=c=5.3960	[50]

1.1.3 U-Pu-O Ternary System

The U-Pu-O ternary system has been studied with the interest of fabrication of MOX fuels. It is inherently a complex system due to differences between the U-O and Pu-O phase diagrams and several aspects are still to be revealed. The corresponding phase diagram will be discussed in this section.

1.1.3.1 U-Pu-O Phase Diagram

Markin et Street [56] and Sari *et al.* [57] were the first to propose a U-Pu-O phase diagram which was later modelled by Guéneau. Figure 10 gives the representation of the U-Pu-O phase diagram at room temperature as proposed by Sari et al. [57]. The latter is centered on the region of interest for this study which is located around an O/M ratio of 2.

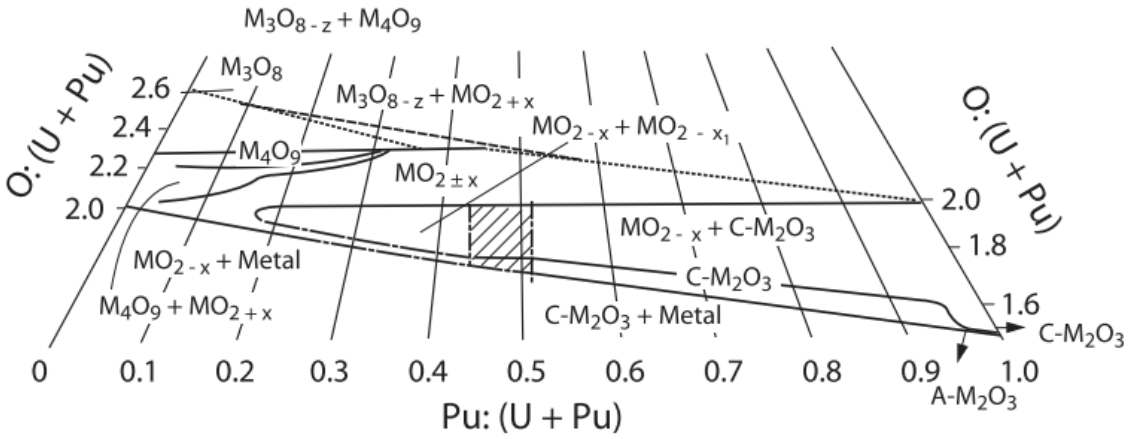

Figure 10 U–Pu–O phase diagram at room temperature for the composition range 1.5 < O/M < 2.7 [57]

1.1.3.1.1 Phase at stoichiometric conditions (O/M = 2)

At stoichiometric conditions (O/M=2.00), plutonium is soluble in the UO_2 structure in the whole composition range. A monophasic $MO_{2.00}$ phase is thus present for the whole range of Pu/(U+Pu), *i.e.* from UO_2 to PuO_2. With the increasing Pu content, the uranium atoms are randomly replaced by the plutonium atoms forming $U_{1-y}Pu_yO_{2.00}$ [58].

In this phase, both U and Pu are mostly in their +4 oxidation state. Thermodynamic modelling suggests that co-existence of reduced Pu state (+3) with the oxidized U state (+5) is possible at high temperature even at the stoichiometric conditions, as shown in Figure 11. Recent measurements performed at room

temperature even showed that all these cations (Pu^{+III}, Pu^{+IV}, U^{+IV} and U^{+V}) seem to coexist even at oxygen stoichiometry in a single phased $(U,Pu)O_2$, in proportions that keep the O/M ratio equal to 2.00 [59].

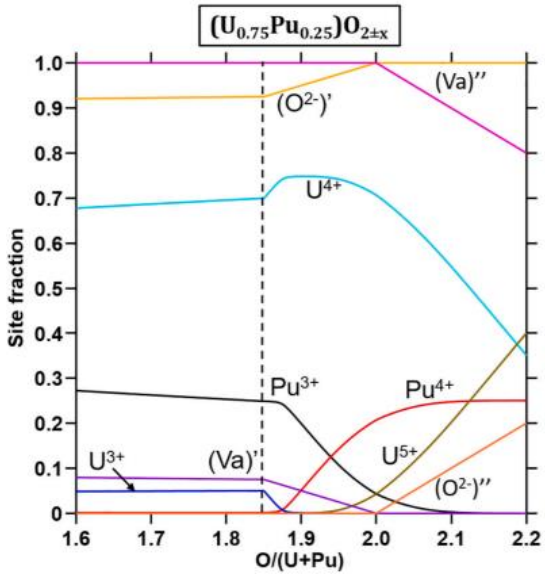

Figure 11 Calculated site fraction of the species at 1773 K in $U_{0.75}Pu_{0.25}O_{2\pm x}$ as function of O/M ratio [60].

1.1.3.1.2 Deviations from stoichiometry

The fluorite structure of the mixed oxide $(U,Pu)O_{2\pm x}$ has the ability to tolerate both oxygen hyperstoichiometry and hypostoichiometry, leading to the formation of a wide stability domain for monophasic $MO_{2\pm x}$, which corresponds to the region around the parabolic area in Figure 10 [17].

For hypostoichiometric conditions (O/M < 2.00), the charge compensation is mostly done through the partial reduction of Pu^{+IV} to Pu^{+III}. For hyperstoichiometric conditions (O/M > 2.00), the partial oxidation of U^{+IV} to U^{+V} takes place to balance the charges.

For the scope of the thesis and the material of interest that are under investigation, we will be mostly interested in the stoichiometric and hypostoichiometric domain of $U_{1-y}Pu_yO_{2-x}$ materials. We will thus not describe in details the phases and crystallographic changes existing and occurring in the hyperstoichiometric domain.

1.1.3.1.3 Miscibility gap

In slightly hypostoichiometric conditions (2.000 > O/M > 1.985), the monophasic MO_{2-x} domain is still present for the whole Pu/(U+Pu) range. For O/M < 1.985, on the other hand, a single phase with the fluorite-type structure is observed only for y < 0.17, and the system becomes biphasic for values of y higher than 0.17, which corresponds to a miscibility gap observed as the large parabolic region in Figure 10. The presence of these two-phase regions is correlated to the complex phase interactions observed within the Pu_2O_3–PuO_2 phase diagram at temperatures lower than 1400K in Figure 7b [17].

In the 0.17 < y < 0.45 range, this miscibility gap contains two fluorite structures with different oxygen stoichiometries (MO_{2-x1} and MO_{2-x2}), one with a O/M ratio close to 2.00, while the second has a lower oxygen content [61]. At high temperatures, the gap undergoes a shrinkage and disappears completely at a temperature in the order of 1273 K, as illustrated in Figure 12.

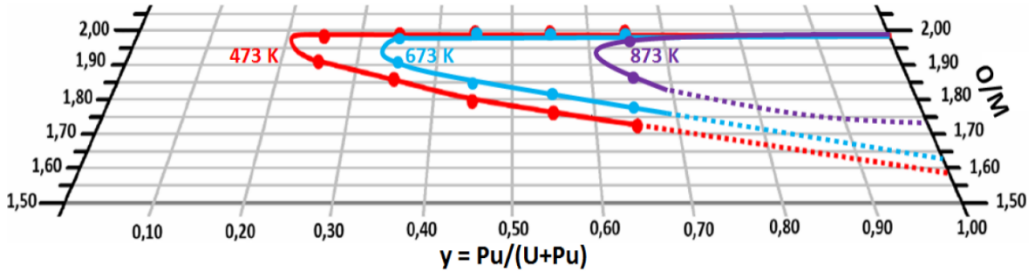

Figure 12 the U-Pu-O miscibility gap limits [62].

A comparison of the lattice parameters of the hypostoichiometric $U_yPu_{1-y}O_{2-x}$ samples in the biphasic region is reported by Vigier *et al.* [61] as shown in Figure 13. The results indicate that the experimental and predicted cell parameters for the phase that is close to stoichiometry are in very good agreement. For the low oxygen content phase, the reported lattice parameters show significant differences between different experimental studies, as shown in Figure 13b, some of them being close to what the model predicts.

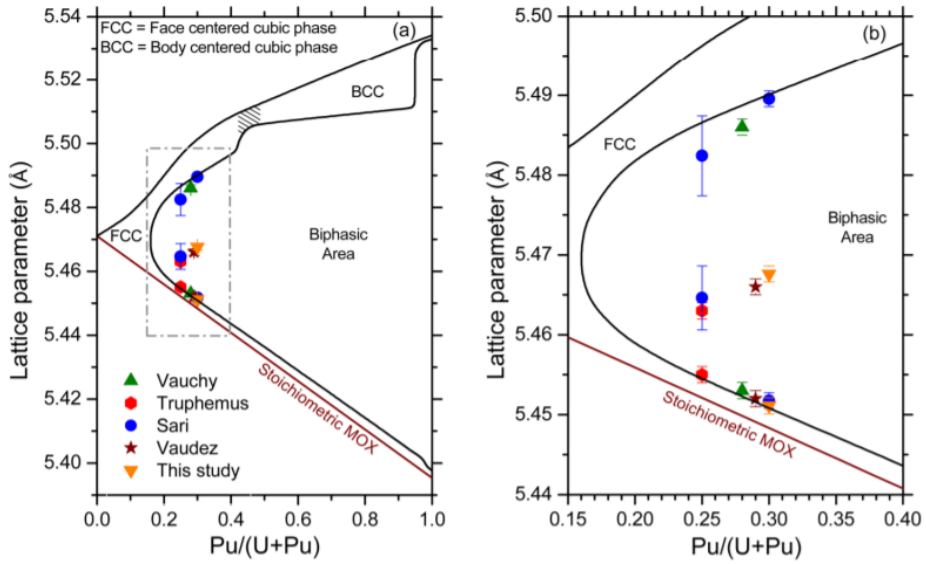

Figure 13 Comparison of lattice parameters of the stoichiometric $U_{0.7}Pu_{0.3}O_{2.00}$ and biphasic $U_{0.7}Pu_{0.3}O_{2-x}$ with the experimental values indicated in the literature (a) Full phase diagram. (b) Focused on the region indicated with dashed rectangle [61]

Upon further increase in the Pu/(U+Pu) content from y=0.45 until y=0.55, the system enters a three-phase region indicated with the shaded area in Figure 10. The three phase region was initially proposed by Markin et Street [56] and later experimentally observed by Truphemus *et al.* [58], where two fluorite-type $(U,Pu)O_{2-x}$ phases and one BCC M_2O_3-type phase coexist. For higher Pu contents (y > 0.55), on the other hand, another two-phase regions is observed in which a fluorite-type $(U,Pu)O_{2-x}$ coexists with a Pu_2O_3 phase.

Finally, in the case of oxygen hyperstoichiometry (O/M>2.00), at room temperature, the oxidation of mixed oxides with a Pu content lower than y=0.5 results in either a single phase fluorite MO_{2+x} with a maximum O/M ratio of 2.27, or in biphasic regions composed of MO_{2+x} M_4O_9 or M_3O_8 phases [17].

1.1.3.2 Change in the $(U_y,Pu_{1-y})O_{2\pm x}$ lattice parameter with Pu content and oxygen stoichiometry

1.1.3.2.1 Effect of Pu content

Several studies [57], [58] have reported that stoichiometric $U_{1-y}Pu_yO_{2.00}$ is an ideal solid solution and its lattice parameter follows a Vegard's law. Based on lattice parameters often reported for stoichiometric $UO_{2.00}$ and $PuO_{2.00}$, *i.e.* 5.470 Å and 5.396 Å respectively, the Vegard's law for the $(U,Pu)O_{2.00}$ is:

$$a(U_{1-y}Pu_yO_{2.00}) = 5.470 - 0.074y \qquad \text{Eqn (1)}$$

Where y is the molar ratio of Pu/(U+Pu) and a the lattice parameter (Å).

This relation has been used for years for the study of $(U,Pu)O_2$ compounds, even though an updated value was recently reported for UO_2, as discussed in Section 1.1.1.2.1. The comparison of the Vegard's law Eqn 1 with the experimental values reported in the literature is shown in Figure 14.

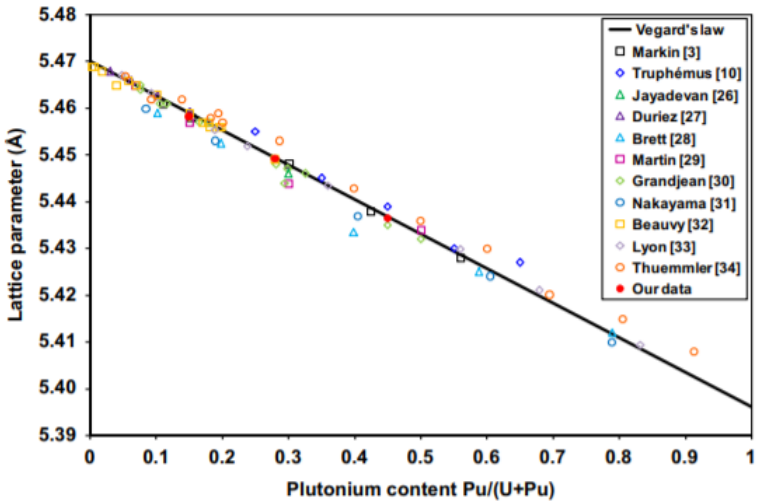

Figure 14 Experimental lattice parameters plotted versus Pu content and compared with Vegard's law (black line) and literature values [63].

A reminder can be given to the fact that it can be difficult to compare the lattice parameters available in the literature as several factors influence the lattice parameter such as the O/M ratio, impurities (e.g. americium, lanthanides…) and the age of the samples (self-irradiation effect) which are not always provided in the articles.

1.1.3.2.2 Effect of variations from oxygen stoichiometry

For non-stoichiometric samples, the change in the lattice parameter due to variation in oxygen stoichiometry (Δa/Δx) must be taken into account. Ohmichi *et al.* [64] proposed an estimation of this ratio through the ionic radii of the ions composing the fluorite lattice. The equation considers the charge balance between the cations and the formation of the oxygen vacancies in the solid solution. For the case of $U_{1-y}Pu_yO_{2-x}$ solid solution, the equation proposed by Ohmichi *et al.* reduces to Eqn 2

$$\frac{da}{dx} = \frac{4}{\sqrt{3}}\left\{2(r_{Pu^{3+}} - r_{Pu^{4+}}) + \frac{1}{2}(r^*_{ov} - r_{O^{2-}})\right\} \qquad \text{Eqn (2)}$$

Where $r_{Pu^{4+}}$, $r_{Pu^{3+}}$ and $r_{O^{2-}}$ are the ionic radius of Pu^{4+} (0.96 Å in eight-coordination), Pu^{3+} (approximated as 1.10 Å for six and seven-coordination) and O^{2-} (1.38 Å in four-coordination) respectively. r^*_{ov}, on the other hand, is the corrected radius of the oxygen vacancy. The details can be found in the related article [64].

By employing the ionic radii list corresponding to the presented coordination numbers in Shannon's paper [65], the calculation yields a value of da/dx as 0.33 ± 0.06 Å.

Duriez *et al.*[66] combined XRD and thermogravimetric analysis to calculate the lattice parameter and the O/M of $(U,Pu)O_{2\pm x}$ samples and derived a value in close agreement with this estimation, reporting a da/dx of 0.32 ± 0.01 Å. This empirical assessment was then integrated in the Vegard's law. This integration expands the correlation linking lattice parameters with both Pu content and deviations from stoichiometry within the range of $0.00 < x < 0.05$ for a hypostoichiometric $U_{1-y}Pu_yO_{2-x}$, as described by the following Equation 3.

$$a(U_{1-y}Pu_yO_{2-x}) = 5.470 - 0.074y - 0.32x \quad \text{Eqn (3)}$$

Where x is the negative deviation from stoichiometry, y the molar ratio of Pu/(U+Pu) and a is the lattice parameter (Å).

This relationship is further validated by Vauchy *et al.* [67] for a range of Pu content $0<y<0.45$ (x range remains unchanged).

1.1.4 Influence of americium

Americium is often present in plutonium and uranium-plutonium oxides as ^{241}Am is a product of ^{241}Pu decay. The dioxide samples studied are thus often rather $(Pu,Am)O_{2-x}$ or $(U,Pu,Am)O_{2\pm x}$ in which americium is fully soluble. In these compounds, americium can be present as Am^{+III} or Am^{+IV}.

However, when uranium is the major cation present, only Am^{+III} is observed even at oxygen stoichiometry or in some cases of hyperstoichiometry [59]. The influence of Am^{+III} on the lattice parameter is a subject of debate in the literature. All reported values show a decrease of the lattice parameter with the increasing amount of americium, but the values are not all consistent with each other [59].

1.2Irradiation defects in actinide dioxides

In this section a general introduction to the defects in the crystalline solid materials will be given. The effect of alpha self-irradiation in the Pu-bearing compounds will be introduced as well as the associated defect generation mechanism. The lattice swelling of the fuel matrix and its mathematical description will be discussed for different isotopes and for MOX fuel (composed of several isotopes). Lastly, the defect recovery studies that are available in the literature will be revisited. This section serves as the foundation for the subsequent discussion of defect types in the thesis.

1.2.1 Defects in Crystalline Solids

The defects in the crystal can be classified according to their dimensions.

- 0-D defects
  - Point defects (vacancy, interstitials, impurity atoms, etc.)
- 1-D defects
  - Linear defects (dislocations)
- 2-D defects
  - Plane defects (breaking stack of atomic planes)
- 3-D defects
  - Volume defects (precipitates, voids, etc.)

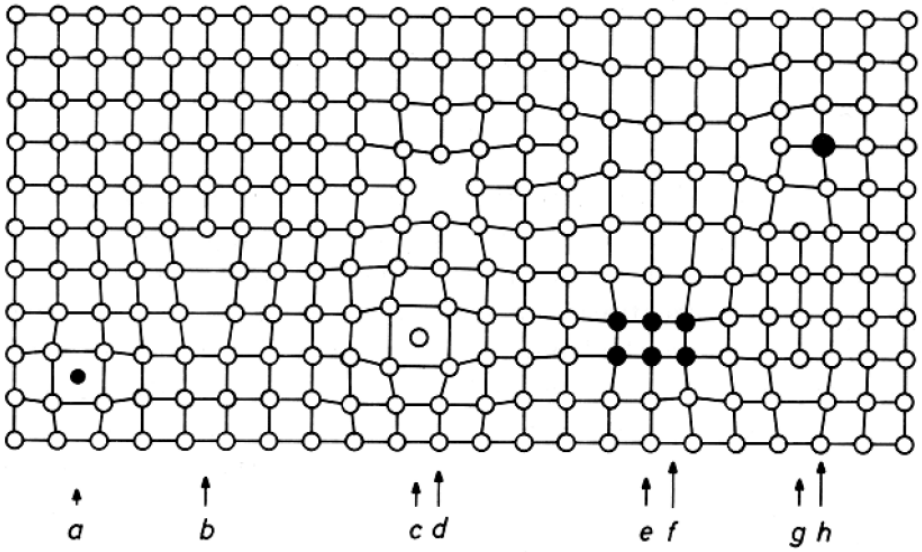

Figure 15 Some of the defects in crystalline solids: a) interstitial impurity, b) edge dislocation, c) self-interstitial, d) vacancy, e) precipitate, f) vacancy dislocation loop, g) interstitial dislocation loop, h) substitutional impurity atom [68]

The point defects involve one lattice position and influence their immediate vicinities. A missing atom from a lattice position is called a vacancy, while an atom standing outside of the normal lattice positions of the defect-free structure is called an interstitial. These two types of point defects are called intrinsic defects, and a small concentration of them is thermodynamically favored at temperatures other than 0 K.

Foreign atoms can also be included in the lattice and are called extrinsic point defects in the crystalline solids. These impurities (or dopants) can be substitutional if they replace an atom of the original lattice, or interstitial, in the case of occupying another position in the lattice. In ionic solids, the point defects cannot be generated independently one from another (except the accumulation of noble gases such as helium formed due to radioactive decay). The electroneutrality of the material must be conserved leading to the formation of Frenkel or Schottky defects, as illustrated in Figure 16.

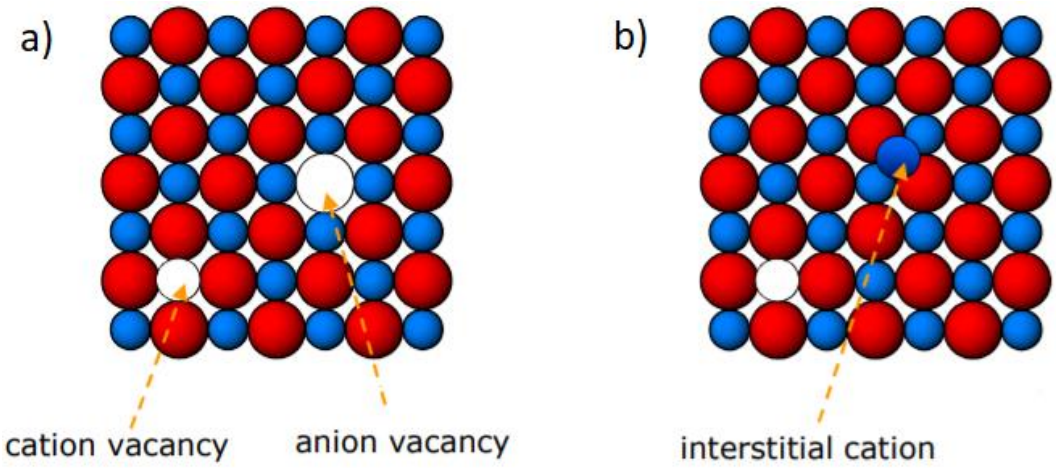

Figure 16 Intrinsic point defects: a) Schottky defect, b) Frenkel defect

Briefly, when a vacancy is compensated by an analogue interstitial atom, the combination of the two defects is called a Frenkel pair, whereas when the vacancy is balanced by one or more vacancies of the oppositely charged ion (for a binary compound), the assembly is labelled as a Schottky defect. In our case it corresponds to UO_2 or PuO_2. More complicated arrangements and interactions of defects result in extended defects [68].

1.2.2 Alpha Self Irradiation, Defects and Lattice Swelling

In this section, the alpha self-irradiation in MOX materials is introduced with the defect generation mechanism and its macroscopic consequence, which is the lattice swelling.

1.2.2.1 Alpha Self-Irradiation Damage

The alpha decay forms a recoiling nucleus and an alpha particle, where the two products share the decay energy indirectly proportionally to their respective masses. Figure 17 presents the alpha decay of a ^{239}Pu nucleus in a $(U,Pu)O_2$ material forming a ^{235}U nucleus and an alpha particle. The values and consequences indicated in the figure are however representative of any actinide alpha decay in any mixed actinide dioxide.

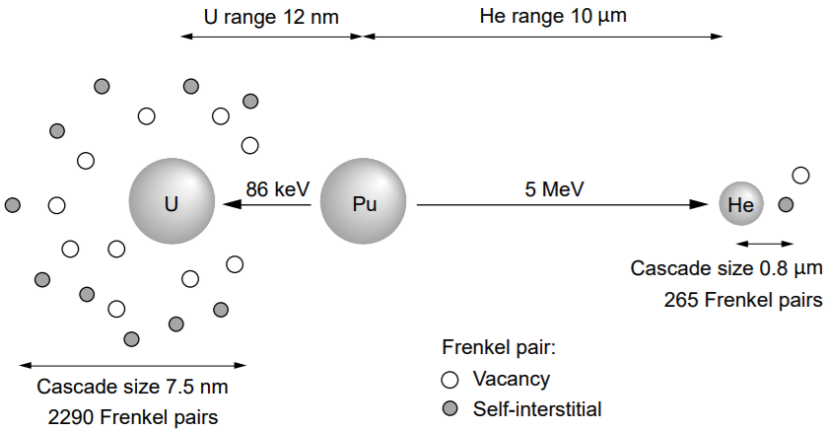

Figure 17 ^{239}Pu alpha decay and the defect generation in $(U,Pu)O_2$ [69].

The recoil nucleus has an energy of ~86 keV and a mean free path of ~12 nm in the UO_2 matrix [70]. Considering the displacement energy calculated as 40 eV for U and Pu atoms, as well as 20 eV for O atoms [71], the energy and the mass of the recoil nucleus has enough momentum to create displacement cascades and knock the surrounding atoms from their sites through inelastic collisions. Through this phenomenon, a single decay creates approximately 2300 Frenkel pairs [72]. Although, ~90% of these Frenkel pairs return to their initial lattice sites within the first 200 nanoseconds, the remaining ~10% remain in the lattice in the form of either free interstitials and vacancies or clusters of interstitials or vacancies [69], [70].

The alpha particle, on the other hand, is identical to the nucleus of the ^4He atom. It has an approximate energy of ~5.1 MeV and a range of about 10 µm in the microstructure, significantly longer than that of the recoiling nucleus. It loses its energy mostly through electronic stopping and create a lower number of defects (about 265 Frenkel pairs) compared to the recoiling nucleus (about ten times less) [72]. Along its path, it captures two electrons and eventually comes to rest as a helium atom. Having a low solubility in the matrix (in UO_2 single crystal is reported as between 10^{22} and 10^{23} atoms/m^3 (*i.e.*, close to 1 ppm/mol) for temperatures between 1073-1473 K [73]) its accumulation over time [69] will lead to the formation of bubbles.

In most of the materials, the displacement cascades due to the alpha self-irradiation leads to amorphisation. Nevertheless, no amorphisation has ever been reported in the literature for the actinide oxides due to alpha self-irradiation [74].

1.2.2.2 Alpha Self-Irradiation in MOX material

1.2.2.2.1 Specific activities of plutonium isotopes

The radioactive decay data of the Pu isotopes of interest for MOX fuel are tabulated in Table 3. According to this data, the α specific activities of ^{238}Pu and ^{241}Am are significantly larger than those of the other Pu isotopes, being 633.9 and 127.0 GBq/g respectively. The MOX material will thus suffer from self-irradiation effect mainly due to these isotopes. The contribution of the U isotopes is negligible. ^{241}Am are initially present in the spent fuel but is separated from plutonium during the spent fuel reprocessing operations that are performed for the fabrication of PuO_2 powders. It although accumulates in the later due to the ^{241}Pu decay.

Table 3 Plutonium isotopes and their corresponding decay data.

Isotope	α decay half-life (years)	β decay half-life (years)	Main decay type	α-specific activity (GBq.g^{-1})	β-specific activity (GBq.g^{-1})
^{235}U	$7.04 \cdot 10^{8}$	-	α	$7.90 \cdot 10^{-5}$	-
^{238}U	$4.47 \cdot 10^{9}$		α	$1.24 \cdot 10^{-5}$	
^{238}Pu	87.7	-	α	**633.9**	-
^{239}Pu	$2.4 \cdot 10^{4}$	-	α	2.31	-
^{240}Pu	$6.6 \cdot 10^{3}$	-	α	8.35	-
^{241}Pu	$3.2 \cdot 10^{5}$	14.1	β$^-$	0.17	$3.9 \cdot 10^{3}$
^{241}Am	432.2	-	α	**127.0**	-
^{242}Pu	$3.7 \cdot 10^{5}$	-	α	0.15	-

As some of the considered isotopes have relatively short half-file compared to the duration of this work (about 3 years), it will be necessary to calculate the evolution in the isotopic composition as a function of time. This can be done using the H. Bateman equation [75]. In the case of a chain of three isotopes $A \xrightarrow{\lambda_A} B \xrightarrow{\lambda_B} C$, which will be the case for the calculating the ^{241}Am composition, the solution of the H. Bateman equation reduces to Eqn 4.

$$N_B = \frac{\lambda_A}{\lambda_B - \lambda_A} N_{A_0} \left(e^{-\lambda_A t} - e^{-\lambda_B t}\right) \qquad \text{Eqn (4)}$$

Where:

- t is the time (in s),
- N_X is the number of the corresponding X isotope,
- λ_X is the X isotope constant decay (in s^{-1}).

1.2.2.2.2 Isotopic composition of plutonium extracted from spent fuel

At this moment, it is a good practice to examine the temporal evolution of the Pu isotopic composition in an irradiated fuel. As an example, we use the isotopic plutonium composition obtained in spent UOX fuels irradiated in a French commercial LWR reactors in standard conditions. Table 4 gives the quantity of plutonium and its composition calculated using the Origen 2 code [76] just after irradiation as well as after a span of 10 years. The main plutonium isotope is ^{239}Pu, whereas the strong alpha emitters of interest for this work (^{238}Pu and ^{241}Am) are present at relatively low contents. As ^{241}Pu makes for about 20 % of the initial plutonium however, the plutonium isotopic composition undergoes a drastic change over the first ten years: the quantity of ^{241}Am builds up, reaching a Am/(Pu+Am) ratio of 7.4% after ten years. This americium will however mostly be separated from the plutonium during spent fuel reprocessing after which it will start build up again, but from a smaller ^{241}Pu quantity.

Table 4 Evolution of the Pu isotopic composition of a neutron-irradiated UO_2 fuel calculated with ORIGEN 2 code [76]. These numbers are calculated with an initial uranium comprising 957.5 kg of ^{238}U, 42.5 kg of ^{235}U, and 0.293 kg ^{234}U and a burn-up of 50,000 MW-days (per metric ton) [76]

Isotope	Weight at discharge (kg)	Pu/(Pu+Am) (%)	Weight after 10 years cooling (g)	Pu/(Pu+Am) after 10 years (%)
^{238}Pu	0.236	2.44	0.242	2.47
^{239}Pu	4.900	50.8	5.000	50.97
^{240}Pu	2.070	21.4	2.130	21.71
^{241}Pu	1.820	18.9	1.130	11.52
^{241}Am	0.048	0.50	0.728	7.42
^{242}Pu	0.579	6.00	0.579	5.90

The exact plutonium isotopic composition of the sample that will be used in the present work will be given and discussed in Section 2.1.1. Because the sample were all prepared from reprocessed plutonium (hence separated from americium at least once) and because they are now "old" enough, these compositions will not undergo significant changes during the timeframe of this work (3 years). The compositions will thus be considered as constant in this study.

1.2.2.2.3 Quantification of accumulated doses in α-emitters-bearing materials

To quantify the self-irradiation damage in materials, two units are commonly used, which are the dpa (displacement per atom) and the cumulated dose (α-decay event.g^{-1}).

The dpa is the average amount of atoms that have been displaced in the lattice due to the accumulated alpha decay events.

E. De Bona [11] suggested the following equation to calculate dpa as a result of alpha self-irradiation damage in UO_2. Because of the similarities between UO_2 and $(U,Pu)O_2$ MOX fuels. This relation is notably Equation 5

$$\mathrm{dpa} = \frac{\mathrm{displacement}}{\mathrm{atoms}} = \frac{(1650 \cdot \mathrm{a} \cdot \mathrm{t} \cdot \mathrm{m_{Pu}})}{3 \cdot \mathrm{N}_a \cdot \frac{\mathrm{m_{MOX}}}{\mathrm{M_{MOX}}}} = \frac{1650 \cdot \mathrm{a} \cdot \mathrm{t} \cdot \mathrm{m_{MOX}}}{3 \cdot N_a} \cdot (\mathrm{Pu\%}) \qquad \text{Eqn (5)}$$

Where:

- a (GBq.g^{-1}) is the specific activity of the α-emitting isotopes,
- t (s) is the self-irradiation time,
- M_{MOX} (g.mol^{-1}) is the molar mass of the MOX sample,
- N_a is the Avogadro's number (mol^{-1}),
- m_{Pu} (g) is the mass of the alpha emitter isotopes in the matrix,
- m_{MOX} (g) is the mass of the MOX sample,
- Pu% is the mass percentage of the alpha emitters in the MOX fuel,
- The factor 1650 corresponds to the average number of atom displaced in a single decay event. The number is calculated using SRIM code [77] for a displacement energy of 40 eV for the U and Pu atoms and 20 eV for the O atoms [11].

The cumulated dose (α.g^{-1}), on the other hand, is the measure of the alpha decay accumulated per gram of material. To calculate this for the Pu and Am within the MOX material, it is necessary to calculate the effective specific activity in the material as described in equation 6 below.

$$Sp' = C_{Pu} \sum Sp_i C_i \quad \text{Eqn (6)}$$

Where:

- Sp' ($\alpha.g^{-1}.s^{-1}$) is the effective specific activity of the Pu and Am within the MOX material,
- Sp_i ($\alpha.g^{-1}.s^{-1}$) is the specific activity of each isotope,
- C_i is their corresponding isotopic fraction (over Pu+^{241}Am) in the material,
- C_{Pu} is the mass Pu+^{241}Am content in the material.

Cumulated dose ($\alpha.g^{-1}$) is then calculated through multiplying the effective specific activity ($\alpha.g^{-1}.s^{-1}$) of the material by the time (s) passed for the self-irradiation as shown in Eqn 7.

$$\text{Cumulated dose} = Sp' \times \text{time} \quad \text{Eqn (7)}$$

1.2.2.3 Lattice Swelling due to Alpha Irradiation Damage

Several authors have investigated the lattice swelling through observing the cell parameter increase over time using various samples such as $^{238}PuO_2$, $^{239}PuO_2$, $^{241}AmO_2$ and $^{243}CmO_2$ [5]–[9].

Figure 18 shows the experimental results of the cell parameter increase for different samples. For all the materials, a rather fast swelling in the earlier period is observed and progressively reaches a saturation value at which further radiation damage will no longer increase the lattice parameter. An explanation of this saturation phenomenon was given by W.J. Weber [78]–[80], who suggested an equilibrium between the defect formation from alpha self-irradiation and defect self-healing. The rate of self-healing being considered proportional to the number of accumulated defects, it progressively increases as the defects accumulate until an equilibrium with the rate of defect formation is reached.

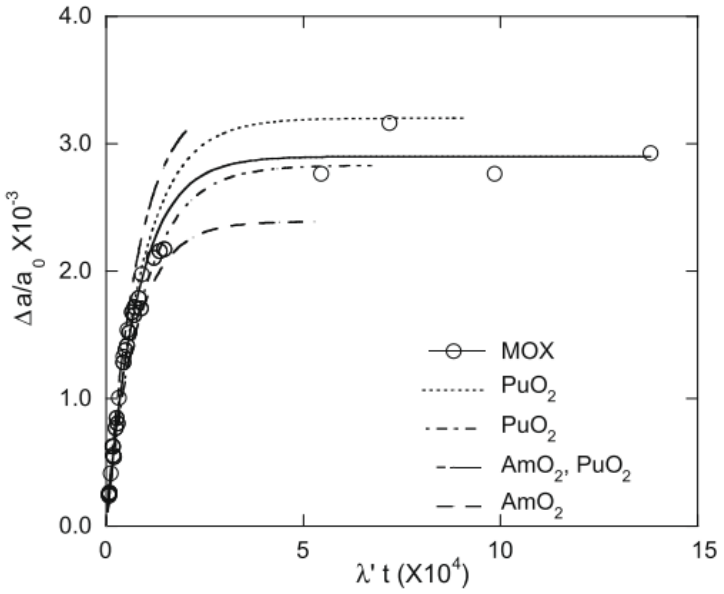

Figure 18 Lattice swelling of different samples due to self-irradiation effect [4].

In the literature, the following empirical relationship is reported as shown in Equation 8. The equation correlates the lattice parameter increase to the sample storage time.

$$\Delta a/a_0 = A[1 - e^{(-B \cdot \lambda \cdot t)}] \quad \text{Eqn (8)}$$

Where:

- a_0 (Å) is defect free initial lattice parameter,
- Δa (Å) is the increase of lattice parameter caused by self-irradiation,
- λ (s^{-1}) is the decay constant of the alpha-decaying isotope,
- t (s) is self-irradiation time,

- A and B are dimensionless constants.

A and B parameters are usually obtained after fitting the experimental lattice swelling data to the Equation 8. The parameter A corresponds to the maximum $\Delta a/a_0$ (saturation) value, while the parameter B is related to the unit cell swelling kinetics [4]. The reported values for the A and B parameters in the literature using different actinide oxide samples are tabulated in Table 5.

In the case of MOX materials, which includes several isotopes as damage sources, an effective decay constant λ' (s^{-1}) must be defined (see Equation 9) and re-introduced in Equation 8.

$$\lambda' = C_{Pu} \sum \lambda_i C_i \qquad \text{Eqn (9)}$$

The effective decay constant λ' (s^{-1}) is defined for:

- i number of Pu isotopes in the system,
- λ_i (s^{-1}) is the decay constant of each Pu isotope,
- C_i its corresponding mass fraction over Pu+^{241}Am,
- C_{Pu} is the (Pu+^{241}Am)/(U+Pu+^{241}Am) mass percentage.

The Equation 7 is hence remodified with the effective decay constant to represent the increase of the lattice parameter when several alpha decaying isotopes coexist, yielding Equation 10.

$$\Delta a/a_0 = A_1[1 - e^{(-B_1 \cdot \lambda' \cdot t)}] \qquad \text{Eqn (10)}$$

Kato *et al*. [4] has reported the lattice swelling behavior of several MOX samples with various Pu contents and isotopic compositions. As illustrated in Figure 18, for $(U,Pu)O_2$ samples, the swelling reached at saturation is approximately 0.29% of the initial lattice parameter. The time required to reach this amount of damage depends on the isotopy of the material and the Pu content.

Horlait *et al.* [81] investigated similar behavior with $(U,Am)O_2$ samples and reported that the saturation takes place after an accumulation of the alpha self-irradiation dose in the order of $8.0 \cdot 10^{17}$ alpha.g^{-1}, which corresponds to an approximate damage level of 0.20 dpa. Similarly, according to Wiss *et al.* [82] for the actinide oxides, the saturation of lattice parameter increase is reached at 0.6 dpa.

A study of external irradiation of UO_2 single crystals was undertaken by W.J. Weber[78], using a $^{238}PuO_2$ source. The material was exposed to a dose up to $3 \cdot 10^{16}$ alphas/cm^2, which according to the author, corresponds to 0.05 dpa of damage. The fitted data shows that the saturation of the lattice parameter increase ($\Delta a/a_0$) is observed at 0.84% increase, which is almost three times higher than the saturation point observed for the MOX. This difference between the two results could be attributed to the localized heating of the crystal lattice due to self-irradiation damage, which does not occur in the case of an external source. This heating process can be associated with the sample annealing, and thus facilitating the healing of defects. Another reason could be that the alpha dose was accumulated faster in Weber's study. This faster accumulation was due to a larger dose rate resulting from the use of ^{238}Pu as a source.

Table 5 The list of the fitted A and B parameters indicated in the literature

Material	A (%), *i.e.* $\Delta a/a_0$ at saturation	B	Ref
MOX	0.290	$1.22 \cdot 10^4$	[4]
$^{238}PuO_2$	0.283	$1.08 \cdot 10^4$	[7]
$^{239}PuO_2$	0.390	$0.87 \cdot 10^4$	[83]
$^{241}AmO_2$	0.239	$1.34 \cdot 10^4$	[9]
$U_{0.925}Am_{0.075}O_{2\pm x}$	0.278(5)	$1.8 \cdot 10^4$	[81]
$U_{0.85}Am_{0.15}O_{2\pm x}$	0.284(5)	$3.3 \cdot 10^4$	[81]
$U_{0.7}Am_{0.3}O_{2\pm x}$	0.272(5)	$6.9 \cdot 10^4$	[81]
$U_{0.6}Am_{0.4}O_{2\pm x}$	0.271(5)	$8.4 \cdot 10^4$	[81]
$U_{0.5}Am_{0.5}O_{2\pm x}$	0.242(5)	$11.0 \cdot 10^4$	[81]
UO_2 (external irrad.)	0.45-0.79	--	[78]

1.2.3 Defect Recovery: lattice swelling and Helium Release

Damage accumulated through alpha (internal or external) irradiation can be recovered through thermal annealing. Thermal recovery studies, *i.e.* the observation of the lattice parameter of the damaged material after annealing at different temperatures, provide insights about the types of defects present in the damaged lattice through analyzing their healing kinetics.

As the continuation of the previous study, W.J. Weber [78]–[80] examined the thermal recovery behavior of irradiated UO_2 single crystal. The sample was exposed to isochronal annealing in an Ar-4% H_2 atmosphere maintaining the oxygen stoichiometry constant at $UO_{2.00}$. The lattice parameter is reported throughout the annealing from 323 to 1323 K with 50 K of increments kept for 30 min. The author indicates that the thermal recovery of lattice defects is complete at 1323 K.

Three recovery stages are observed as shown in Figure 19. The attribution of these stages to different types of point defects can be done through comparing the activity energy of the thermal recovery stage (calculated assuming that each recovery stage has first order reaction kinetics) to the migration and recovery activity energies of point defects found in the literature. W.J. Weber attributed each stage to the annealing of a different type of defects: anion Frenkel pair (*i.e.* anti-Frenkel) for stage I (573 K), cation Frenkel (*i.e.* Frenkel) defects for stage II (850 K) and vacancies, where the isolated He atoms are trapped, for stage III (1200 K).

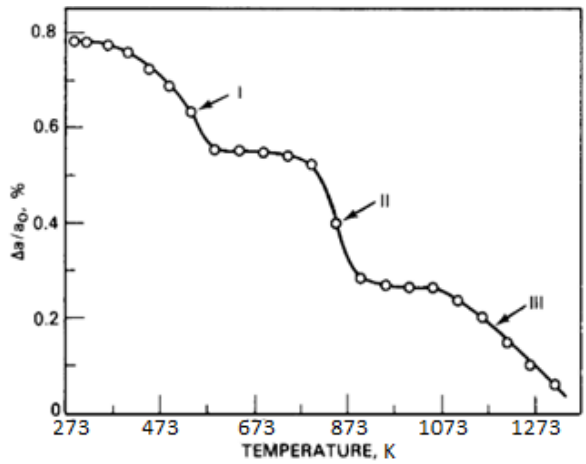

Figure 19 Isochronal defect recovery stages of alpha irradiated $UO_{2.00}$ single crystal at saturation (0.8% $\Delta a/a_0$ increase) [79].

Similarly, Kato *et al.* [4] investigated the thermal recovery of self-irradiated MOX samples whose lattice parameters already swelled by 0.29% due to self-irradiation (at the saturation). The thermal recovery of three MOX samples of different Pu contents is shown in Figure 20. The samples were heated from 473 to 1473 K in an $Ar/H_2/H_2O$ controlled atmosphere keeping the O/M ratio constant. According to the study, no Pu content dependence is observed on the thermal recovery and the lattice expansion is completely recovered at 1473 K [4].

Table 6 compares the activation energies of these three thermal recovery stages to thermal recovery of point defects in UO_2 and diffusion of oxygen, uranium and plutonium atoms in MOX material. The first stage can thus be associated with the recovery of anion Frenkel defects. Due to their low activation energy, these defects can be easily annihilated and completely recovered at temperatures below 673 K. The second recovery stage is associated with the cation Frenkel defects which is completed at 1073 K. Lastly, the third recovery stage with an activation energy of 1.2 eV, corresponds to the release of isolated helium trapped in vacancies, which is experimentally detected starting from 1273 K [4]. These results show that these three stages are the same as those reported by W. J. Weber for $UO_{2.00}$ [79].

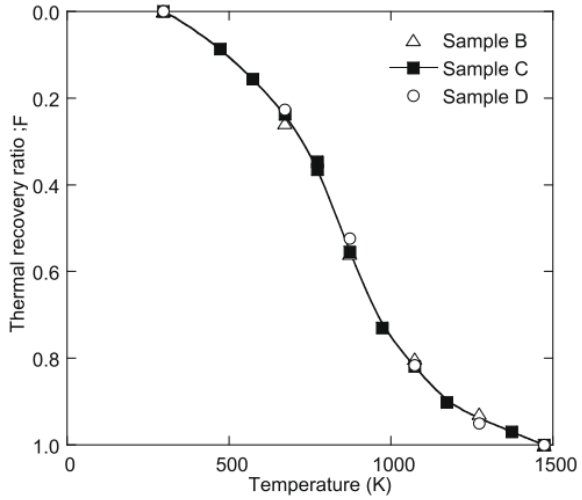

Figure 20 The thermal recovery behavior of the lattice parameter of the MOX samples with the increasing temperature [4]. Samples A, B and C have respective Pu/(U+Pu) ratios of 29.7, 39.9 and 45 wt%.

Table 6 Comparison of MOX sample thermal recovery activation energy for each stage to the activation energy of the point defects in the irradiated UO_2 and the diffusion of atoms in the MOX material [4]

	Temperature (K)	Activation energy (eV)	Ref
Thermal recovery of lattice expansion in MOX			
Stage I	<673	0.12	[4]
Stage II	673-1073	0.73	[4]
Stage III	1073-1573	1.2	[4]
Thermal recovery of point defects in irradiated UO_2			
I_U in UO_2	<763	0.1-0.4	[84]
V_U in UO_2	853-1023	2.0-2.4	[84]
I_O in UO_2	373-673	0.9-1.4	[85]
V_O in UO_2	973-1073	1.7-2.8	[84]
Diffusion in MOX			
O in $MO_{2\pm x}$	473-1273	0.2-0.7	[86]
U in $MO_{2\pm x}$	1173-1873	1.6	[87]
Pu in $MO_{2\pm x}$	1173-1873	1.42	[87]

Finally, the degree of lattice recovery at each stage with respect to the total lattice expansion is summarized in Table 7. The available data for the thermal recovery studies of UO_2, $(U,Th)O_2$, PuO_2 and $(U,Am)O_2$ are also given for comparison. The table illustrates the impact of the three distinct defect types: oxygen Frenkel pairs (stage I), cation Frenkel pairs (stage II) and trapped He atoms in the vacancies (stage III) on the overall lattice swelling observed in different samples. According to the results, the increase of the lattice parameter would be mainly caused by creation of the cation Frenkel pairs for the MOX material, which is similar to what is observed in the case of UO_2.

In contrast, for a $(U,Am)O_2$ sample, the majority of the recovery occurs during the stage linked to helium release. This suggests that in this material, there is a greater presence of vacancy defects capable of trapping helium bubbles compared to the MOX material.

Table 7 The lattice parameter recovery ratio in each stage for different actinide oxides.

Sample	Swelling at saturation (%)	Stage I	Stage II	Stage III	Ref
MOX	0.29	28 %	52 %	20 %	[4]
UO_2 (external irradiation)	0.84	35 %	36 %	30 %	[79]
$(U,Th)O_2$	0.55	45 %	40 %	15 %	[88]
PuO_2	0.32	40 %	44 %	16 %	[7]
$U_{0.8}Am_{0.2}O_{2-x}$	0.31	25 %	30 %	45 %	[89]

1.3Self-irradiation effects in the (U,Pu)O_2 system: previous studies

This section is dedicated to the experimental and calculation methods that have been used to study self-irradiation effects in MOX materials. This literature includes results from various characterization techniques such as X-Ray Diffraction (XRD), µ-Raman imaging, Transmission Electron Microscopy (TEM), as well as Molecular Dynamics (MD) calculations.

1.3.1 X-ray Diffraction

The increase of the strain $\Delta a/a_0$ due to the self-irradiation effect in the MOX materials was already indicated in Section 1.2.2.3. Recently, De Bona et al. [90] has studied the evolution in the XRD pattern for the UO_2 sample doped with 2.5 wt.% ^{238}Pu. The resulting shift in the (111) reflection that indicates the cell parameter increase is shown in Figure 21. The results range from the first day of the self-irradiation effect until 564 days, which corresponds to a damage level of 0.102 dpa.

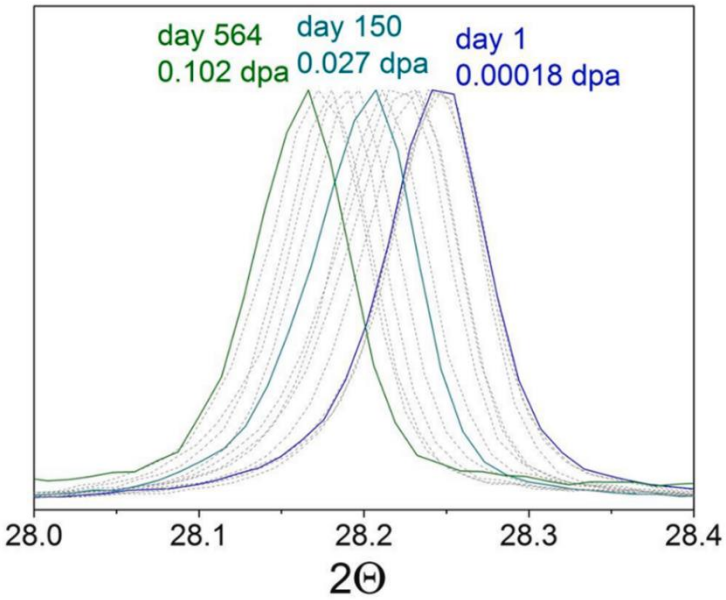

Figure 21 Change in the (111) XRD peak position with respect to time and dose in a UO_2 sample doped with 2.5 wt% Pu. The changes are attributed to the lattice swelling caused by the self-irradiation damage [90].

Continuing with their investigation, the same researchers conducted a comparison involving UO_2 samples doped with 1.25% and 5.0% Pu/(U+Pu). The authors note that the lattice swelling only depends on the irradiation damage but not on the irradiation rate. This is evident from the analogous behavior exhibited by both the 1.25% and 5.0% Pu/(U+Pu) samples [91].

The authors also studied the evolution of microstrain with the accumulated self-irradiation dose. The values are calculated with the Williamson-Hall method [92] and the authors claim that there is a decreasing trend in the microstrains as illustrated by Figure 22b. This latter phenomenon would be connected to the recombination of point defects into dislocation loops. This behavior was also identified through TEM results, even at a low damage level of 0.072 dpa, as observed by the same research group. The details are given in Section 1.3.3.

It has however to be noted that the uncertainties given for these microstrain measurements appears to be too small. Note for example that the grey point at around 0.001 dpa has a microstrain value lower than $1.8 \cdot 10^{-4}$ whereas the points just before and after both present microstrain values around $2.4 \cdot 10^{-4}$, while

the uncertainty given on these values are about $0.1 \cdot 10^{-4}$. If larger (and more reasonable) uncertainties had been used, the decreasing trend would not be as evident.

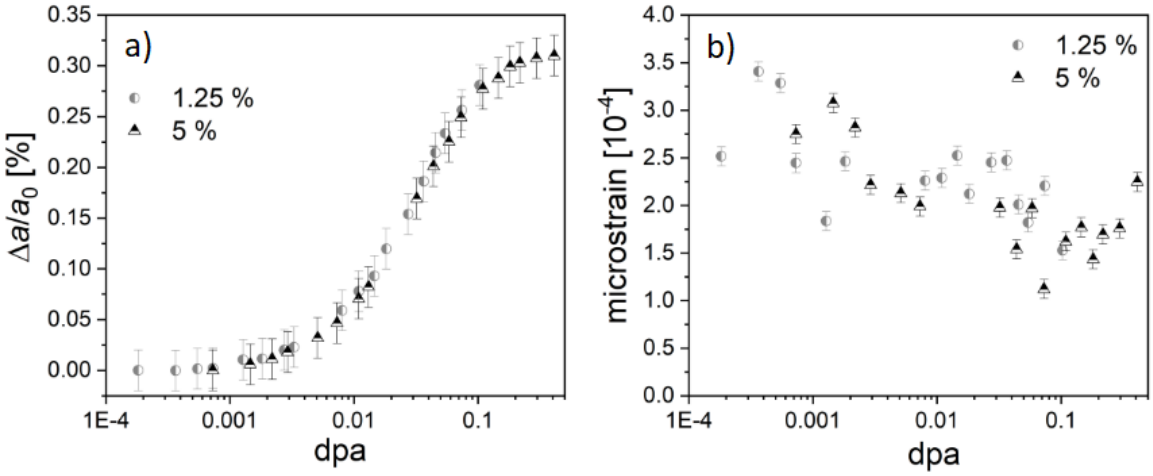

Figure 22 a) Relative lattice parameter increase ($\Delta a/a_0$) of the two UO_2 samples doped with 1.25 % and 5.0% Pu, b) microstrain as calculated from the corresponding XRD patterns of the same samples [91].

Conversely, Horlait *et al.*[93] indicated for $(U,Am)O_2$ samples that the evolution in the microstrains remained within the uncertainty of the measurements (Figure 23), except for the first 100 hours in which variations are related to an oxidation of the samples). As a result, the authors concluded that no evolutions of the microstrain was observable by XRD.

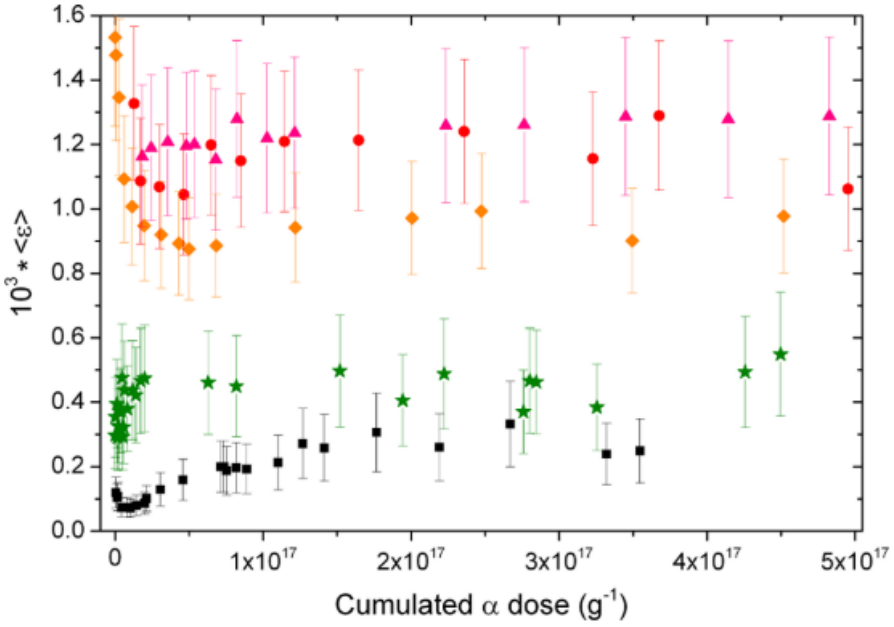

Figure 23 Evolution of the microstrain <ε> as a function of the cumulated α dose for (■)$U_{0.925}Am_{0.075}O_{2\pm\delta}$, (green ★) $U_{0.85}Am_{0.15}O_{2\pm\delta}$, (orange ◆)$U_{0.7}Am_{0.3}O_{2\pm\delta}$, (red ●)$U_{0.6}Am_{0.4}O_{2\pm\delta}$, and (magenta ▲)$U_{0.5}Am_{0.5}O_{2\pm\delta}$ [93]

1.3.2 Raman Spectroscopy

The current understanding of the components observed in the Raman spectra of actinide dioxide will be described in details in the dedicated Section 2.2.3.5 of Chapter 2. This section is thus only dedicated to the description of the main modifications that are observed with (self)-irradiation.

The Raman spectra of (self) irradiated samples of MO_2 (M = actinides) were studied by several authors ([72], [94]–[97]). Mohun *et al.* [94] studied the Raman spectra of UO_2 disks irradiated with 21 MeV He^{2+} ions and a PuO_2 sample (2.5 years old) that had already accumulated a certain level of alpha self-irradiation damage. The resulting spectra and their comparison are shown in Figure 24.

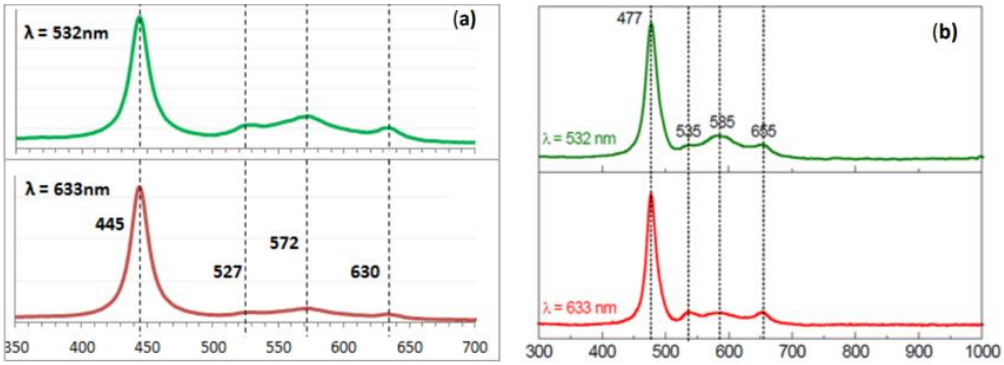

Figure 24 Raman spectra of irradiated (a) UO_2 (b) PuO_2 samples analyzed using 532 nm (green) and 633 nm (red) excitation wavelength [94]

Besides the T_{2g} band in the first order spectrum (at around 445-480 cm^{-1}), three additional peaks are present in the 500-700 cm^{-1} range (as shown in Figure 24). This particular region is often reported as the defective region and the three corresponding bands are called the defect bands (U_1, U_2 and U_3).
In the literature, different authors mostly agree on the interpretation of the defect bands:

- The U_1 band is mostly associated with oxygen vacancy defects, as observed by Li et al [98] and Medyk et al [99].
- The second band (U_2) observed at ~575 cm^{-1}, which will be detailed in the Chapter 2, becomes Raman active by the presence of defect in the crystal (loss of the translational invariance, detailed in Section 2.2.3.4.2) [100]. Naji *et al.* [96] associated it with the presence of oxygen Frenkel defects.
- The assignment of the third band (U_3), observed at ~630 cm^{-1} is associated with the cuboctahedral cluster defects [32]. However, this last hypothesis seem impossible for PuO_2 Raman spectrum as the highest oxidation state of plutonium is +IV in the Pu-O system(as mentioned in Section 1.1.2) and oxygen cuboctahedrons were only observed together with an actinide at the +V oxidation state [101].

For the U_1 band, L. Medyk [95] and Talip et al. [97] both observed an increase in intensity with self-irradiation. Harker and Puxley studied [102] the evolution of the U_2 and U_3 bands within damaged PuO_2 samples over a time span of 3.8 to 7.1 years. The experiments were performed using an excitation wavelength of 633 nm. This investigation involved annealing the samples at temperatures ranging from 673 to 1073 K, while closely observing changes in both band intensity and shape [102]. It was shown that the U_2 and U_3 peak intensities remain only weak between 873 and 1073 K. This outcome suggests that the origin of these bands are related to cation Frenkel pairs considering the insights gained through the thermal recovery studies of Kato *et al.* [4] explained in section 1.2.3. However, the observed phenomenon was exactly the opposite *i.e.* an increase in the intensity of the defect bands is observed for annealing temperatures up to 773 K. This observation suggested a possible defect migration mechanism from the bulk to the surface of the material. Conversely, Guimbretiere *et al.* [103] observed the complete disappearing of the U_2 and U_3 peaks for a temperature between 650 and 800 K in a MOX sample. As a result, no consensus has yet been reached on this subject.

Regarding the position of the T_{2g} band, as it is known to be related to the lattice parameter (as will be discussed in details in Section 2.2.3.5.2), a shift in the T_{2g} position towards lower frequencies could be expected. Regarding this, Talip *et al.* [97], [104] reported a shift in the order of 1-2 cm^{-1} in their $(U,Pu)O_2$ samples that had reached saturation due to self-irradiation. However, in a recent publication, Medyk *et al.* [99] observed no shifts in the T_{2g} position between the self-irradiated (at saturation) and annealed

samples. According to the latter, this contradiction seems to indicate that the lattice parameter increase observed with XRD mostly concerns the cationic sublattice, and is not linked with a change in the oxygen sublattice (O-O distance) which would be observed through a shift in the T_{2g} position. Besides the position of the T_{2g} band, its broadening with the increased self-irradiation damage is also reported in De Bona et al. [91]. Based on these discrepancies in the literature, additional data is required before a consensus can be reached.

1.3.3 Transmission Electron Microscope (TEM)

Wiss *et al.* [10] performed TEM observation on self-irradiated $(U,Pu)O_2$ samples doped with different concentrations of ^{241}Am and ^{238}Pu. As tabulated in Table 8, a wide range of samples were investigated having different damage levels ranging from 10^{-4} to 88 dpa [10]. The same samples were later thermally treated to heal the damage and TEM images of the annealed samples were compared to the damaged ones.

Table 8 List of the samples investigated by Wiss et al. in [10]

Sample	Dpa	Cumulated alpha dose of the samples (g^{-1})
$(U_{0.999}{}^{238}Pu_{0.001})O_2$	10^{-4}	$4.175 \cdot 10^{15}$
$(U_{0.9}{}^{238}Pu_{0.1})O_2$	0.5	$2.088 \cdot 10^{18}$
$(U_{0.9}{}^{238}Pu_{0.1})O_2$	1	$4.175 \cdot 10^{18}$
$(U_{0.9}{}^{238}Pu_{0.1})O_2$	1.1	$4.593 \cdot 10^{18}$
$(U_{0.9}{}^{238}Pu_{0.1})O_2$	2.5	$1.044 \cdot 10^{19}$
$(U_{0.9}{}^{238}Pu_{0.1})O_2$	3.4	$1.42 \cdot 10^{19}$
$(U_{0.9}{}^{238}Pu_{0.1})O_2$	4	$1.67 \cdot 10^{19}$
$(Am_{0.94}Np_{0.06})O_2$	36	$1.4 \cdot 10^{20}$
$(U_{0.4}{}^{238}Pu_{0.6})O_2$	88	$3.674 \cdot 10^{20}$

At first, the TEM image of the $(Am,Np)O_2$ sample which accumulated a dose of 36 dpa is shown in Figure 25. According to the authors, in this particular TEM image, He bubbles of different sizes could be evidenced up to 30 nm illustrating the low solubility of He in the material.

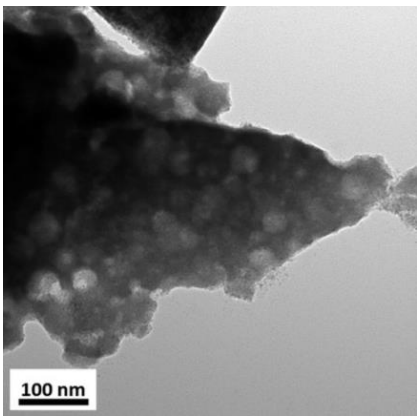

Figure 25 TEM image of AmO_2 showing a high concentration of large He bubbles (white spots) after 36 dpa of damage [10].

Furthermore, the TEM images of the eight $(U,^{238}Pu)O_2$ samples for various range of cumulated doses are compared in Figure 26. First, the dislocation loops (dark circular marks) appear at very low dpa values

and their concentration increases with the alpha dose (between 10^{-4} and 4 dpa). In this range, no significant increase in their size is observed and their concentration appears to reach a saturation. At a much higher damage dose of 88 dpa, the defects has evolved from isolated dislocation loops to tangles of dislocation.

Despite the absence of data between 4 and 88 dpa, the authors conclude that the evolution of point defects toward the extended defects plays a role in minimizing the overall strain and lattice swelling in the sample's crystal structure. This behavior could thus appear to be directly correlated to the saturation of the lattice parameter increase after a certain level of self-irradiation damage [10]. Nevertheless, as shown in Section 1.2.2.3, the saturation in the lattice swelling is reached at a damage level of 0.6 dpa for the MOX, *i.e.* before dislocation tangles were observed by TEM. This data thus do not yet provide a comprehensive description of the relation between the defects observed by TEM and the lattice parameter swelling.

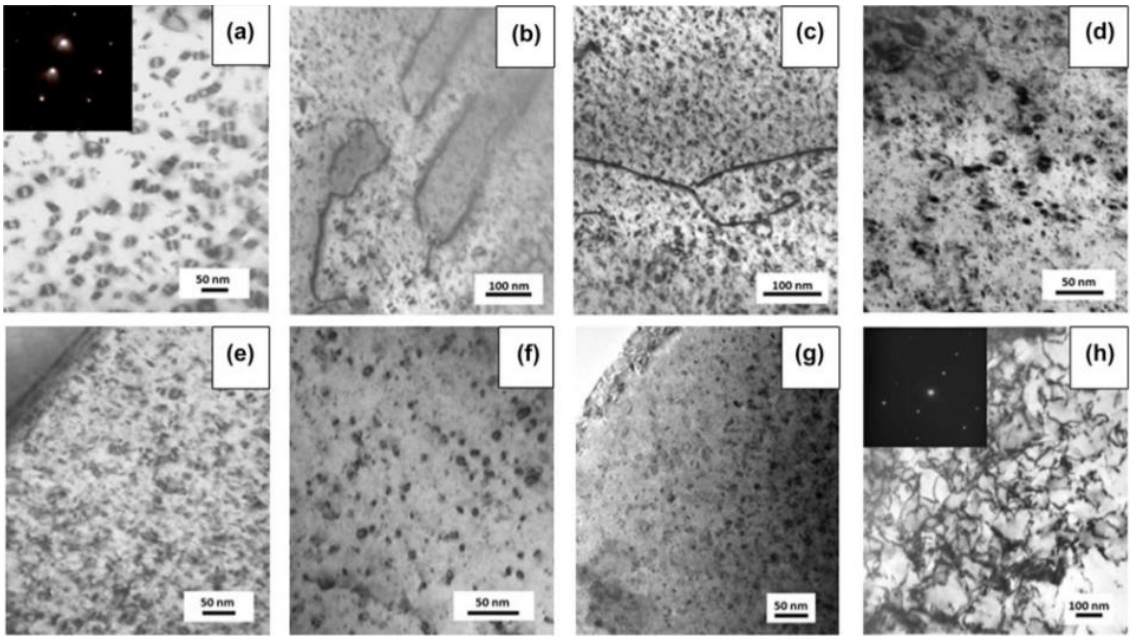

Figure 26 Defects in the $(U,Pu)O_2$ samples as a function of alpha - damage: (a) 10^{-4} dpa, (b) 0.5 dpa, (c) 1 dpa, (d) 1.1 dpa, (e) 2.5 dpa, (f) 3.4 dpa, (g) 4 dpa, and (h) 88 dpa [10].

To distinguish the effect of the annealing on defect concentration and on helium desorption, TEM micrographs of an annealed $U_{0.9}{}^{238}Pu_{0.1}O_2$ sample are shown in Figure 27. In the first set of images taken on the sample annealed at 1400 K (a–c), the dislocation loops can be seen along with the He bubbles (the latter are observed as white spots in the images). The second set of images (d–f) are from the sample after annealing at 1800 K, in which, according to the author, the number of bubbles decreased, whereas their size is increased and the dislocation loops are no longer observed [10]. This finding suggests that the stability of the He bubbles extends all the way up to 1800K, even though these bubbles could be empty after the annealing.

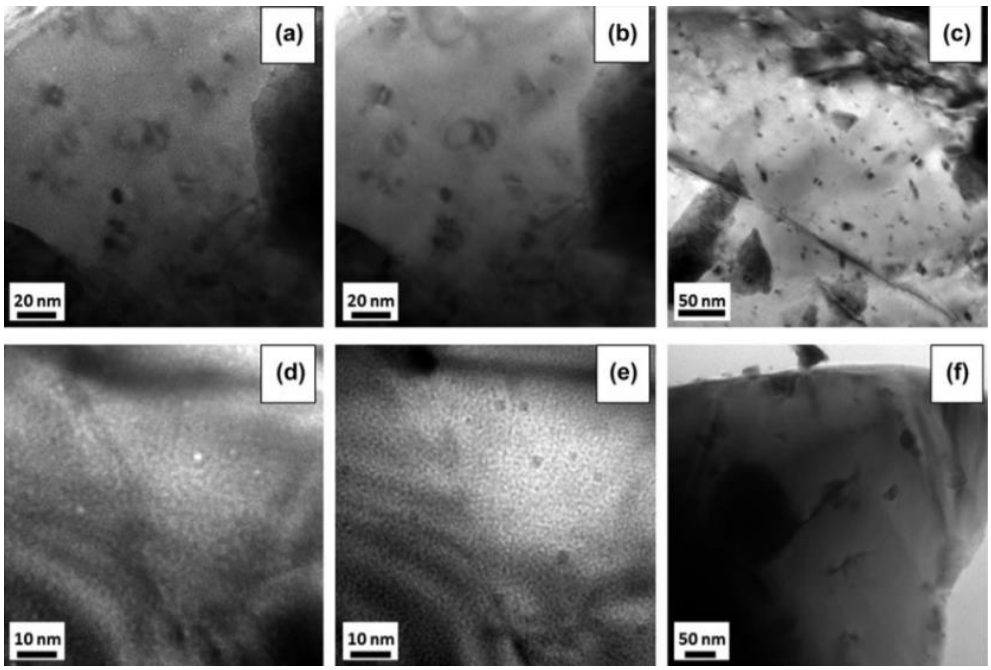

Figure 27 Micrographs of the 0.1 wt% ^{238}Pu-doped UO_2 sample: (a–c) bubbles and dislocation loops after annealing at 1400 K; (d–f) bubbles after annealing at 1800 K [10]

1.3.4 Molecular Dynamics Studies

Van Brutzel *et al.* performed MD simulations to investigate the primary self-radiation damage in U_{1-y},Pu_yO_2 solid solution [12], [13]. In their model, Frenkel pairs are continuously introduced in the system to simulate the radiation damage caused by self-irradiation. The simulation initiates the collision sequence by choosing a cation (Pu or U), which is labeled as PKA (Primary Knock-on Atom) to mimic a recoil nucleus. The evolution of the number of cation Frenkel pairs and anion Frenkel pairs are reported in Figure 28 for three PKA energies: 5, 10 and 75 keV and three different systems having Pu/(U+Pu) contents of 0, 50 and 100 at% [12].

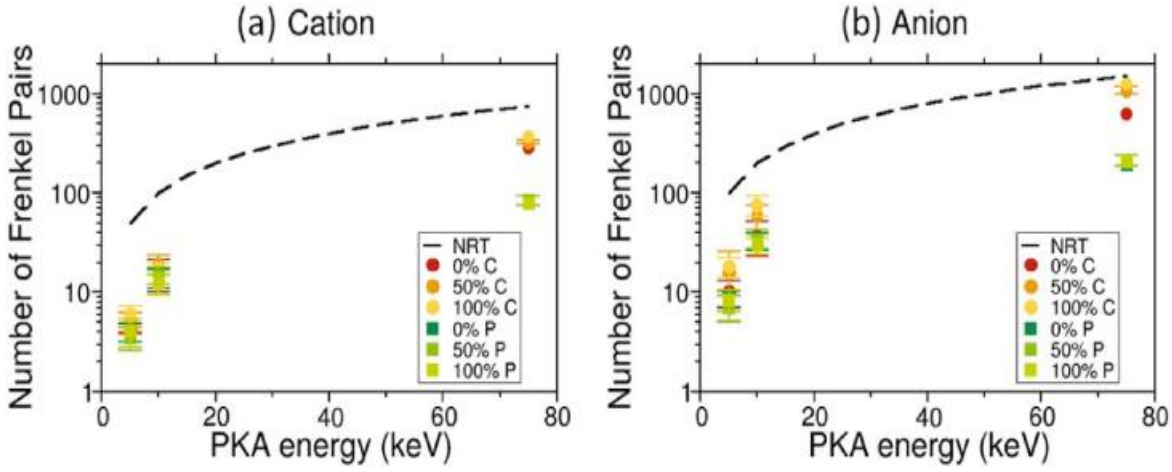

Figure 28 Evolution of the number of (a) cation and (b) anion Frenkel pairs present at the end of the displacement cascades as a function of PKA energy for two kinds of potentials (C for Cooper and P for Potashnikov) and for Pu/(U+Pu) contents of 0, 50 and 100 at% [12]

These results are compared with the NRT (Norgett, Robinson, and Torrens) model, which calculates the number of Frenkel pairs as function of the displacement energy (E_d), set as 40 eV for the cations and 20 eV for the anions, along with the initial kinetic energy of the projectile (E_{PKA}) [105] as presented in Equation 11.

$$N_{FP}^{NRT} = \frac{0.4E_{PKA}}{E_D} \quad \text{Eqn (11)}$$

Where,

- N_{FP}^{NRT} is the number of Frenkel pairs produced,
- E_{PKA} is the initial kinetic energy of the projectile (eV),
- E_D is the displacement threshold energy (eV).

According to the simulation results, the number of Frenkel pairs found at the end of the cascades is significantly lower than the one estimated with the NRT law. This difference resides from the fact that realistically the NRT law does not include the defect recombination. Indeed, the atomic displacements induce a temporary local disorder of the crystal in the core of the cascade. Subsequently, the system evolves releasing energy in the form of thermal vibrations, causing a drastic increase of the local temperature, which triggers numerous recombination events in the system. This phenomenon mainly leads to the reconstruction of the fluorite lattice leaving only a few remaining point defects [12].

The evolution of the microstructure was also modeled in the same work. Figure 29 corresponds to the damage behavior at 1600 K as a function of the dose expressed in dpC (displacement per cation) for a $(U_{0.5}Pu_{0.5})O_2$ material. The evolution of the microstructure follows three main stages:

- Until a damage level of 0.2 dpC (0.067 dpa), the concentration of the point defect increases without forming dislocations.
- Until a damage level of 0.5 dpC (0.167 dpa), the point defects form Frank loops that nucleates from interstitial clustering.
- As the dose further increases to 2 dpC (0.67 dpa), these loops transform into perfect loops.

For a further increase of the number of accumulated Frenkel pairs, on the other hand, the density of perfect loops stabilizes and a steady state is reached. The information gathered from the MD studies thus closely matches the TEM observations by by Wiss *et al*. [10].

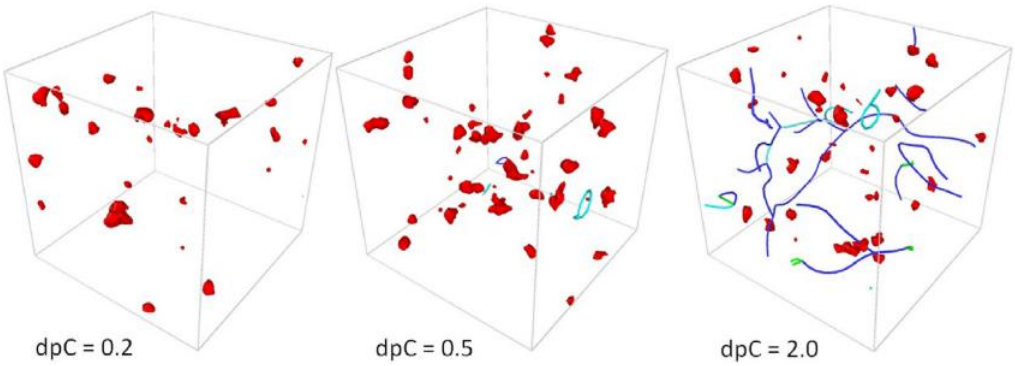

Figure 29 Evolution of extended defects as a function of dose (expressed in dpC) at 1600 K for a Pu/(U+Pu) content of 50 at%. Size of the system includes 40×40×40 fluorite unit cells. The red zone marked the regions where structure departs from perfect fluorite structure. The cyan lines are Frank loops, the green lines are Shockley partial dislocations, and the blue lines are perfect dislocations [12].

Chapter 2. Materials and Methods

In the first chapter, we described the so-called "closed" nuclear fuel cycle, which involves the reprocessing of spent fuel to recover its reusable materials (uranium and plutonium in particular), while its other components (fission products and minor actinides) constitute the ultimate waste. In particular, this brief literature review focused on the main effects of self-irradiation on fuels synthesized from the recycling of MOX-type materials: defect injection and material lattice swelling. Still in this first chapter, we summarized a number of works that have been devoted to describe the structural effects of this self-irradiation, along with the use of some associated characterization techniques. We have not gone into the description of the samples, nor into the description of the characterization methods used. This is the purpose of this second chapter.

MOX materials are rather heterogeneous in nature, which means that materials and the associated self-irradiation effects are to be described at different spatial scales. In this context, the micron scale seems relevant for our needs to a certain extent.

The guiding idea behind this work was to consider fuels synthesized more than 15 years ago: as in terms of swelling, they already reached the saturation level. These fuels were designed for use in PWR or FNR, meaning that they were manufactured through different fabrication routes and have differences in Pu content. Annealing of these materials allows healing (at least partially) of the defects, and the material to be returned to its (virtually) original state. Starting from annealed materials, self-irradiation effects may be analyzed.

Knowledge of material isotopy is a first prerequisite. Knowledge of material heterogeneity in terms of local Pu content is a second prerequisite. One also needs information on lattice swelling and the presence/evolution of structural defects *vs* storage time.

To derive this information, we used four characterization techniques, some of which are available in the L26 laboratory of the ATALANTE facility in Marcoule (namely electron probe microanalyser (EPMA), X-ray diffraction (XRD) and Raman spectroscopy), while X-ray absorption spectroscopy (XAS) results were collected at the SOLEIL and ESRF synchrotron facilities.

The rationale behind this second chapter is therefore to briefly describe the materials, the isotopy of the samples, and the principles and the contribution of the characterization methods used. The purely experimental aspects will be covered in the appendix part of this document.

2.1 Materials

Three different MOX samples are used for this study. Among them, one of the samples is the PWR MIMAS (MIcronized - MASter blend) type MOX material, while the remaining two are SFR (Sodium Fast Reactor) type MOX materials. The samples were stored at room temperature in an inert (N_2) atmosphere. The particularities of these samples are explained more in details in the Appendix A that involves their fabrication routes as well as the handling techniques for the nuclear materials.

The MIMAS sample that is used in this study was taken from a batch synthesized in 2007. It has a global Pu+Am/(U+Pu+^{241}Am) content of about 10 wt.%, while the initial O/M ratio of the sample is ≈ 2.00. The fabrication process of this sample (see Appendix A.1.1.1.1) leads to a sintered ceramic material consisting in three observable "phases" as function of the Pu content. These phases can be described as agglomerates of UO_2, agglomerates of a PuO_2 with an average Pu/(U+Pu) content close to 28 wt% and a third phase, referred to as “coating” with an intermediate Pu content, which is located between the agglomerates of the other two phases.

The two remaining SFR type MOX samples are named as Capra4 and Trabant40. Due to their fabrication processes, they have a rather more homogeneous microstructure than the MIMAS type MOX fuel, which is mainly composed of a matrix phase. The Capra4 sample had an initial global Pu/(U+Pu) content of 29% and an initial O/M ratio close to 1.97. One particularity of this sample is the high Am content that accumulated over the years due to its relatively high amount of ^{241}Pu in its initial isotopy. Considering the current isotopic composition that is calculated for the year 2023, the global stoichiometry of the sample can be designated as $U_{0.69}Pu_{0.285}Am_{0.025}O_{2.00}$. The Trabant40 sample, on the other hand, has a little higher Pu/(U+Pu) content, which is in the order of 40% Pu/U+Pu. The isotopic contents of the samples are tabulated in the following section.

2.1.1 Isotopy of the samples

The initial and the present year (2023) isotopic composition of the samples are summarized in this section with the tables below, where the calculation for the actual values were done using the Eqn 4.

The samples were initially fabricated in the year 2007, 1996 and 1997 respectively for the MIMAS, Capra4 and the Trabant40 samples. The initial and final isotopic composition of the three samples are shown in Table 9, Table 10 and Table 11. An important evolution in the Am enrichment over the years for the MIMAS and the Capra4 samples can be noted, which is more than a factor of four for the former and factor of six for the latter. This is due to the beta decay of ^{241}Pu isotope. The spatial distribution of this element in the sample is expected to follow that of Pu. It is, thus, expected that the main consequences of this Am enrichment are to be found in the Pu-rich clusters for the MIMAS type sample.

Table 9 Initial (2007) and present (2023) isotopic composition (Isotope/(Pu + Am) or isotope/U) of the MIMAS MOX fuel used in this study.

Isotope	MIMAS Isotopic Composition (wt %) in 2007	MIMAS Isotopic Composition (wt %) in 2023
^{238}Pu/(Pu+Am)	2.41	2.11
^{239}Pu/(Pu+Am)	53.9	54.1
^{240}Pu/(Pu+Am)	25.8	25.8
^{241}Pu/(Pu+Am)	8.91	4.13
^{241}Am/(Pu+Am)	1.48	6.20
^{242}Pu/(Pu+Am)	7.50	7.52
^{235}U/U	0.30	0.30
^{238}U/U	99.74	99.74

Table 10 Initial (1996) and the present (2023) isotopic composition (Isotope/(Pu + Am) or isotope/U) of the Capra4 MOX fuel used in this study.

Isotope	Capra4 Isotopic Composition (wt %) in 1996	Capra4 Isotopic Composition (wt %) in 2023
^{238}Pu/(Pu+Am)	1.92	1.60
^{239}Pu/(Pu+Am)	55.2	55.5
^{240}Pu/(Pu+Am)	25.3	25.4
^{241}Pu/(Pu+Am)	9.77	2.70
^{241}Am/(Pu+Am)	1.38	8.30
^{242}Pu/(Pu+Am)	6.50	6.50
^{235}U/U	0.30	0.30
^{238}U/U	99.7	99.7

Table 11 Initial (1997) and the present (2023) isotopic composition (Isotope/(Pu + Am) or isotope/U) of the Trabant40 MOX fuel used in this study.

Isotope	Trabant40 Isotopic Composition (wt %) in 1997	Trabant40 Isotopic Composition (wt %) in 2023
^{238}Pu/(Pu+Am)	0.14	0.12
^{239}Pu/(Pu+Am)	74.4	74.5
^{240}Pu/(Pu+Am)	21.8	21.8
^{241}Pu/(Pu+Am)	1.59	0.48
^{241}Am/(Pu+Am)	1.44	2.48
^{242}Pu/(Pu+Am)	0.71	0.71
^{235}U/U	0.30	0.30
^{238}U/U	99.7	99.7

2.1.2 Sample Preparation and Annealing

The samples were exposed to a series of ceramographic preparation that mainly involves cutting, coating and polishing prior their characterization. The details of the preparation of the samples are given in Appendix A.1.1.1

All samples in the study were initially in the pellet form. Hence, small pieces sections were cut from the pellets and subjected to thermal treatment (annealing) in order to heal the defects that were accumulated over the years. Once the annealing is done, the accumulation of the self-irradiation defects starts from the beginning.

Here the expected lattice swelling over about 3 years for Capra4, Trabant40 and MIMAS sample with its average Pu content and in the Pu-rich agglomerates are shown in Figure 30. The calculation is done with the empirical correlation indicated in Eq 10.

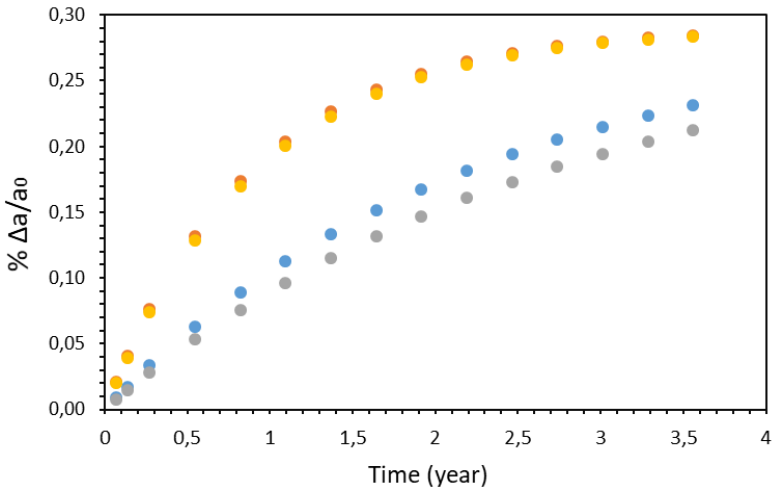

Figure 30 The expected lattice parameter increase of the samples used in this thesis calculated with the Kato's empirical correlation [4]. The red: Capra4 sample, the blue: Trabant40 sample, the yellow: Pu-rich agglomerates of the MIMAS sample, the grey: MIMAS sample calculated for the average Pu content (10% Pu/U+Pu).

Within the time scale of the study, several specimens of each initial samples were annealed at different times (see Appendix A.1.1.2 for conditions). To give an example, for the Capra4 sample, the first thermal treatment was done at 15/06/2021 and within the time scale of the thesis, it was possible to have information from this sample until a time range of 600 days that corresponds to an order of 0.25% increase of the initial lattice parameter. This approach made it possible to obtain a certain number of specimens having different levels of accumulated self-irradiation damages within each batch. As a function of the isotopy and the Pu content of the selected samples, the corresponding cumulative α-activity of the samples were high enough to increase the lattice parameter to some reasonable extents within the time scale of the thesis as seen in Figure 30. This methodology allowed us to analyze the samples at states corresponding to varying levels of self-irradiation damage accumulated in the samples. For the EPMA, XRD and Raman Microscopy experiments, it was possible prepare only one specimen for each sample and analyze it at different states after waiting for some certain time period once it is annealed. Nevertheless, for the XAS campaigns it was obligatory to prepare different pieces of these samples that have accumulated different damage levels, as the measurements had to be done in the synchrotron facility once for all the specimens. The date of the annealing and the extent of damage that is accumulated in each sample at the time of characterization will be detailed on a case-by-case basis in the following chapters.

2.2 Experimental Techniques used in this Study

The introduced techniques are used to probe the microstructure in the short and long-range order as well as its homogeneity. The main adapted strategy of this study is based on the complementary use of these techniques. The information sought will be successively: (i) the local Pu content, (ii) the swelling of the lattice parameter, (iii) the injection and the presence of structural defects. To this end, four methods will be used: EPMA, XRD, Raman spectroscopy and X-ray absorption techniques (XANES and EXAFS). As we shall see below, this “multiscale” approach of involving the complementary use of these four methods will collectively enable us to describe materials at various spatial scales.

2.2.1 EPMA

The electron microprobe is a non-destructive characterization technique based on the surface analysis using the WDS (Wavelength dispersive spectrometer), which gives access to the chemical composition of the samples, with µm spatial resolution. Briefly, EPMA works with bombarding the sample surface with a focused electron beam that continuously excite the atoms. The de-excitation mechanism that returns the atoms to their ground state release photons in the X-ray energy range that are characteristic of these atoms. The sample composition can be then identified based on the energy of the peaks in the WDS spectra and quantified using standards of known compositions. For example, UO_2 and PuO_2 were respectively used for U and Pu. In our case, the measurements were performed at the M lines of the actinides (energies around 3.5 keV) using a 20 kV electron beam. The probed volume in $(U,Pu)O_2$ in these conditions has a diameter and a depth of about 0.8 and 0.5 µm, respectively. In our work EPMA, was mostly use to obtained mappings (of up to about 1mm²) of the Pu/(U+Pu(+Am)) content at the micron scale.

Even though the measurements are non-destructive in nature, it requires a dedicated sample preparation both to ensure the accuracy of the measurements and the safe handling of the radioactive samples. Only samples mounted in a polyester resin, polished, decontaminated and coated with about 20 nm of carbon could be analyzed which sometimes limited the feasibility of some measurements (directly on a piece of pellet for example, as could be done by Raman or µ-XAS).

2.2.2 X-ray Diffraction (XRD)

The technique is based on irradiating the material with an X-ray source and then measuring the scattering angles and their intensities. The scattering phenomenon of the incident X-ray follow the Bragg's law (Eqn 12), which relates the diffraction angle and the X-ray wavelength. The intensity of the scattered X-rays is plotted as a function of the scattering angle, which gives the diffraction pattern of the sample. The structure of the material (space group, cell parameters, atomic positions) is determined through the analysis of the diffraction angle and the intensities of scattered peaks.

$$n\lambda = 2d_{hkl} \cdot \sin\theta \qquad \text{Eqn (12)}$$

Where:

- d_{hkl} (Å) distance between two crystallographic (hkl) planes
- θ is the angle between the incident X-ray beam and the crystallographic plane
- λ (Å) is the X-ray wavelength
- n is the diffraction order.

Subsequently, the lattice parameter of the crystal structure is determined. For a cubic unit cell the following equation is used:

$$d_{hkl} = \frac{a_O}{\sqrt{h^2 + k^2 + l^2}} \qquad \text{Eqn (13)}$$

Where h,k,l are the miller indices of the particular lattice plane and a_0 is the lattice parameter of the cubic unit cell.

As introduced in Chapter 1, UO_2, PuO_2 and $(U,Pu)O_2$ solid solution crystallize in the FCC fluorite-type structure and thus yields the same diffraction pattern whose peak positions are shifting with the lattice parameter, e.g. as a function of the Pu content, the O/M ratio, or the amount of self-irradiation damage accumulated in the crystal matrix. A typical XRD diffraction pattern of a monophasic $(U,Pu)O_2$ sample is shown in Figure 31.

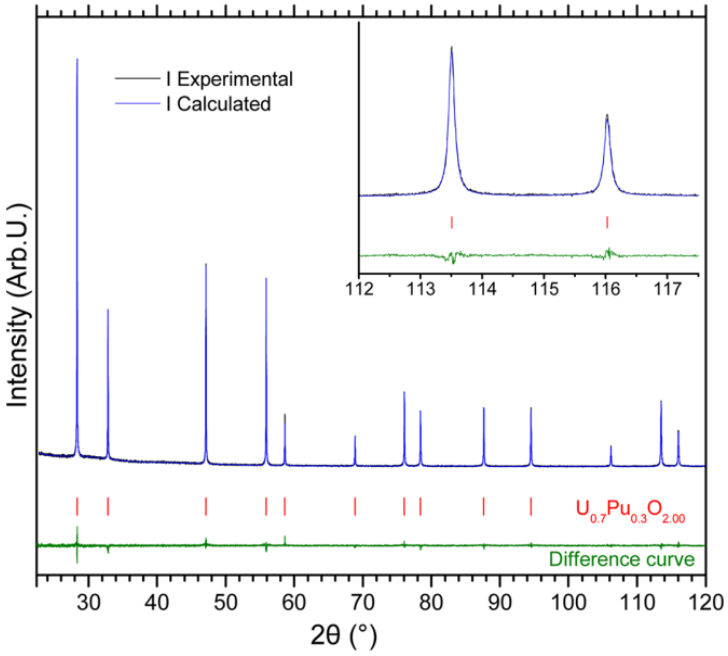

Figure 31 XRD pattern (Cu K-alpha irradiation) of freshly sintered $U_{0.7}Pu_{0.3}O_{2.00}$ sample [61]

As explained in Section 1.2.3, self-irradiation leads to a gradually increase the lattice parameter until the saturation level. This phenomenon is recorded with a gradual shift of the XRD peaks toward lower 2θ angles (as explained by Eqn 12 and 13).

Due to the conditions used and the materials under investigation, an uncertainty of 0.001-0.002 Å can be given on the value of the lattice parameter determined in this study. This accuracy of lattice parameter measurement is, however, good enough to see the change in the lattice parameter due to self-irradiation effects considering the maximum increase of the initial lattice parameter ($\Delta a/a_0$) is in the order of 0.29% for the MOX materials, which corresponds to a maximum increase of roughly 0.016 Å [81]. Besides, the uncertainty of ± 0.001 Å on the lattice parameter gives an estimated error of ±0.01 for calculation of the O/M ratio of the $(U,Pu)O_2$ using Equation 3 [106]. The details in the diffractometer used for this study are given in Appendix C.2.

Besides the shift in the 2θ angle, the XRD peak can also undergo broadening as consequence of different factors. The peak broadening can be, at first, due to the apparatus characteristics and has to be calibrated using a microcrystalline standard (such as LaB_6 SRM660b microcrystalline standard). However, several factors leading to peak broadening are also often encountered as seen in Figure 32. The smaller the finite size of the coherent domains (and hence directly related to the crystallite size), the broader the peaks. Similarly local micro distortions (*i.e.*, microstrain), in other words, the local variations of interatomic distances around a mean value (and thus the unit cell parameter) also contribute to this broadening [81]. To dissociate the line broadening due to crystallite size and microstrain, the Williamson−Hall method can be employed [107]. The latter is based on the fact that microstrains provoke a Gaussian-type diffraction line broadening, while decreased crystallite size induces a Lorentzian-type broadening. The two contributions can then be separated by writing the following equation, for one individual XRD peak [81].

$$\beta_{mat} = \beta_G + \beta_L = \lambda/(L\cos\theta) + 4\tan\theta\varepsilon \qquad \text{Eqn (14)}$$

Where:

- β_{mat} is the integral breadth of the considered diffraction peak after subtraction of the instrument contribution,
- β_G and β_L, respectively are the Gaussian and Lorentzian contributions to integral breadth
- L is the crystallite size (in nm),
- λ is the X-ray wavelength (in nm),
- θ is the angular position of the considered X-ray reflection,
- ε is the microstrain.

Plotting of $\beta_{mat}\cos\theta$ values for each diffraction line as a function of sinθ gives access to the mean value of microstrain <ε> and to the crystallite size L, as the slope and the intercept of the straight line correspond to ε and to λ/L respectively. An example is shown in Figure 32.

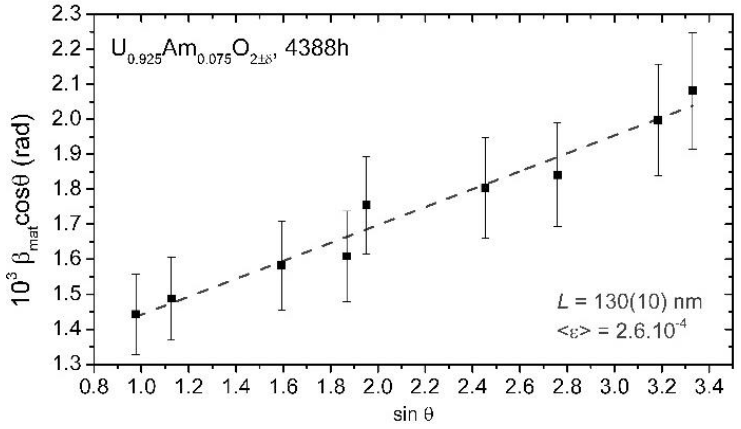

Figure 32 Example of application of Williamson−Hall plot for the determination of microstrain <ε> and the crystallite size L, obtained, respectively, from the slope and the intercept of the linear fit [81]

It is also crucial to address the phenomenon where multiple phases of the same crystal structure and similar compositions, such as $(U,Pu)O_2$ with slight variations in Pu content and/or O/M ratio co-exist in the matrix. This induces a lattice parameter distribution with peak positions too close that cannot be separated

easily. When this happens, the resulting diffraction pattern may present as if it belongs to a single phase but with broader peaks. This occurrence is especially notable when these phases are closely related in composition.

2.2.3 Raman spectroscopy

Raman Spectroscopy makes an important part of our study. To be able to evaluate the results and have an eventual discussion some notions related to the theory of Raman scattering are essential.

To give a brief introduction, the Raman effect was predicted and experimentally observed by C.V. Raman. The original paper was published in 1928, in which a new type of secondary, or emitted radiation, different than fluorescence, was described for the first time [108]. The Raman effect is an inelastic light scattering phenomenon. It is based on the interaction of monochromatic light, in the near UV (~220 nm) - near IR (~ 1 µm) spectrum, with matter (gas, liquid or solid). In this inelastic scattering process, an incident photon may lose or gain some energy, corresponding to the so-called Stokes and Anti-Stokes radiations respectively, by creation or annihilation of an elementary excitation in the matter. Most of the time, this elementary excitation is a specific vibrational mode, which is why the method is usually considered as a vibrational spectroscopic technique [109]. However, this denomination can be rather restrictive because electronic (plasmons, individual excitation) or magnetic (magnons) or even coupled (phonon-plasmon) excitations can also be observed. Thus, there are different degrees of description of the method. The simplest ones are the “energy transfer model” and the “electromagnetic (classical)” description, which is outlined in the following sub sections. In the frequency range considered, roughly speaking an enlarged “visible” spectral range, and far from any electronic transition, the incident field will mostly “see”, or slightly “shake” the electrons at the same frequency. As a matter of fact, the ions cannot follow the incident field in this frequency range.

2.2.3.1 The energy transfer model

As a first simplistic quantum approach, an energy level diagram for different processes (in particular, the photo-excitation of an electron) is presented in Figure 33. In such a simplified scheme, the energy of the incident photon is compared to the energy levels available in the molecule or the crystal. In this diagram, two different electronic levels (ground state and first excited state) are drawn, along with some vibrational levels. In this diagram, one can first recognize the absorption processes between two consecutive vibrational levels (infrared spectroscopy) and electronic levels (UV-visible spectroscopy). These are one-photon techniques. On the other hand, Raman spectroscopy is a two-photon technique. In the figure, it is shown that the Stokes and Anti-Stokes processes imply so-called “virtual levels” that do not correspond to any particular allowed energy level of the molecule. Without going into details, the virtually excited states have very low lifetimes and can emit a photon. We then recognize on the Figure 33 the Rayleigh (the emitted photon has the same frequency as the incident photon), Stokes (the emitted photon is of lower energy) and anti-Stokes processes (the emitted photon is of higher energy). For the last two, the difference in energy between the incident and emitted photons corresponds to the Raman shift.

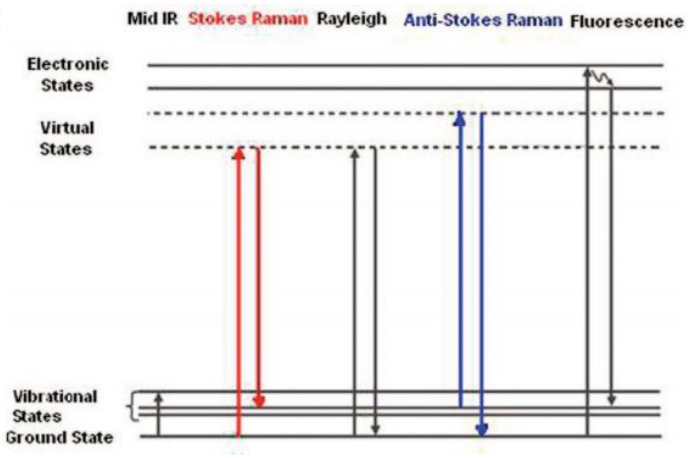

Figure 33 Energy level diagram for different processes [110]

As already mentioned, when analyzed with a spectrometer, the scattered radiation exhibits lines in a symmetric way on both sides of the excitation frequency as shown in Figure 34. As such, these vibrational spectra are a definite fingerprint of the molecule or the material.

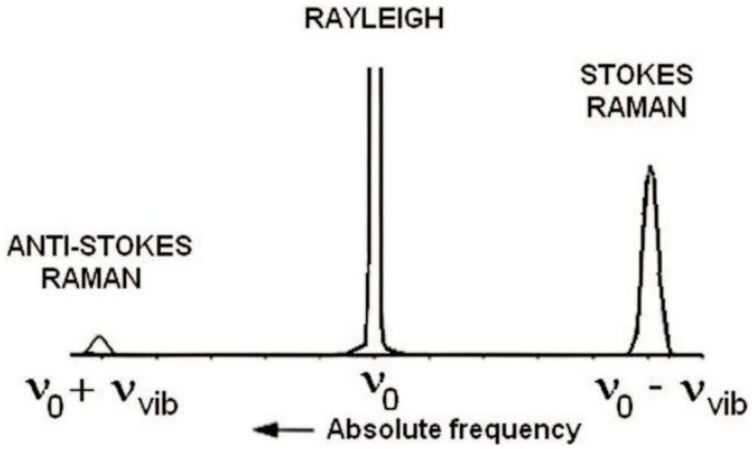

Figure 34 Raman and Rayleigh scattering of excitation at a frequency ν_0. The molecular vibration in the sample is of a frequency ν_{vib} [110]

2.2.3.2 The electromagnetic description of Raman scattering in solids

According to this theory, also known as the classical theory of Raman scattering in solids, within the linear approximation, the polarization **P** (the induced dipole moment per unit volume) of the material in response to an applied electric field **E** writes:

$$\mathbf{P} = \varepsilon_0 \chi \mathbf{E} \qquad \text{Eqn (15)}$$

Where χ is the electric susceptibility, a macroscopic quantity that represents the ability to deform of all electronic clouds. In the most general case (anisotropic or non-cubic materials), the electric susceptibility is a second-rank tensor, with non-zero components determined by the symmetries of the unit cell. As a rule, the number of independent coefficients of these tensors reflects the crystal symmetry.
The electric susceptibility is related to the relative permittivity ε_r (dielectric function) as described in Eqn 16

$$\chi = \varepsilon_r - 1 \qquad \text{Eqn (16)}$$

Both the electric susceptibility and the permittivity are expressed as complex variables that are related to the refraction index n and the extinction coefficient κ according to:

$$\epsilon_r = \epsilon_r + i\tilde{\epsilon}_r = n^2 = (n + i\kappa)^2 \qquad \text{Eqn (17)}$$

The dielectric function of a solid is a function of the frequency. A first and direct consequence is that the volume of the material that is probed may strongly depend on the excitation wavelength, in particular close to characteristic electronic transitions: once again, in this frequency range, this spectroscopy technique first probes electrons. Thus, in the frequency range considered here, the dielectric function is sensitive to optical properties from various electronic energy band processes. Here one understands the link between the optical properties of the solid and its "Raman" response, the resonant scattering in particular, which will be detailed in the Resonant Raman scattering section.

The movement of atoms around their equilibrium positions (*i.e.* atomic lattice vibrations) can modulate the electronic susceptibility. What are these vibration modes? A solid possessing within a scattering volume V a number N of atoms can be first considered as one “giant molecule”: 3N vibrational modes are expected, including the three translational ones. In a crystalline material, for which the translational invariance is preserved over larges dimensions, using Bloch's theorem and the so-called harmonic approximation, vibrational modes, in other words phonons, can be described in terms of plane waves, which will be further detailed in this Chapter.

Vibrational modes in crystalline solids are first discussed at the scale of the primitive cell. Considering a crystal with p atoms in the primitive cell ($p \geq 2$), 3p branches are expected, 3 of them are acoustical modes (one longitudinal acoustic mode and two transverse acoustic modes), 3p-3 are optical modes. In the optical mode two adjacent different atoms move against each other (anti-phase motion), while in the acoustic mode they move together (in-phase motion). If a crystal has n unit cells, then each branch has n normal modes (number of $\boldsymbol{q}$-points for each dispersion curve). As a result, the total number of normal modes of the whole crystal is 3pn, *i.e.* the total Degree of Freedom of atoms in this crystal. These modes are represented by dispersion relations that specify a frequency $\omega(\boldsymbol{q})$ for each value of $\boldsymbol{q}$, where $\boldsymbol{q}$ corresponds to the crystal momentum, pseudomomentum, or wave vector of the mode. The vibrational modes are therefore linked by a simple phase relation from one primitive cell to another.

For low vibration amplitudes Q, the time modulation of the electric susceptibility can be described as using a power series, for which we will restrict ourselves to the first two terms:

$$\chi = \chi_0 + \frac{\partial \chi}{\partial \mathrm{Q}} \mathrm{Q} + \cdots \qquad \text{Eqn (18)}$$

With

$$Q = Q_0 \cos\left(\boldsymbol{q}.\boldsymbol{r} - \omega_{vib} t\right) \qquad \text{Eqn (19)}$$

The incident electric field writes:

$$E = E_0 \cos\left(\boldsymbol{k_{exc}}.\boldsymbol{r} - \omega_{exc} t\right) \qquad \text{Eqn (20)}$$

The combination of the above equations allows the induced dipole moment to be expressed as:

$$\begin{aligned} P = {} & \varepsilon_O \chi_O E_O \cos(\boldsymbol{k_{exc}}.\boldsymbol{r} - \omega_{exc} t) \\ & + \frac{\varepsilon_O E_O Q_O}{2} \left(\frac{\partial \chi}{\partial Q}\right) \{\cos[(\boldsymbol{k_{exc}} + \boldsymbol{q}).r - (\omega_{exc} + \omega_{vib})t] \\ & + \cos[(\boldsymbol{k_{exc}} - \boldsymbol{q}).r - (\omega_{exc} - \omega_{vib})t]\} \end{aligned} \qquad \text{Eqn (21)}$$

The first term is associated with a radiation of frequency ω_{exc} that corresponds to Rayleigh scattering. The second term reflects the emission of two radiations of frequencies equal to ω_{exc}-ω_{vib} (Stokes radiation) and ω_{exc}+ω_{vib} (anti-Stokes radiation). This very simple approach highlights the conservation laws that govern first-order Raman scattering in a crystal:

$$\omega_{exc} = \omega_{scat} \pm \omega_{vib} \quad and \quad \boldsymbol{k_{exc}} = \boldsymbol{k_{scat}} \pm \boldsymbol{q} \qquad \text{Eqn (22)}$$

Where:

- ω_{exc} and $\boldsymbol{k_{exc}}$ characterize the incident radiation,
- ω_{scat} and $\boldsymbol{k_{scat}}$ the scattered radiation,

- ω_{vib} and $\boldsymbol{q}$ a lattice vibrational mode.

Thus, a vibrational mode will be Raman active providing:

$$\frac{\partial \chi}{\partial Q} \neq 0 \qquad \text{Eqn (23)}$$

In other words, inelastic scattering is induced by time fluctuations in χ. On the other hand, it may be shown that Rayleigh (elastic) scattering is induced by density fluctuations in the matter. It will be noted here that the infrared activity supposes that:

$$\frac{\partial \mu}{\partial Q} \neq 0 \qquad \text{Eqn (24)}$$

Where μ is the dipole moment.

This is the first "Raman scattering selection rule", as explained by the classical approach. Such a simple description effectively allows to describe the interaction between radiations and matter, but does not allow to compute to the scattered intensities.

At this point, it must one must take into account the population of phonons *n(ω,T)* in the material at thermal equilibrium which is given by the Bose-Einstein distribution function:

$$\mathrm{n}(\omega, \mathrm{T}) = \left(\mathrm{e}^{\left(\frac{\hbar\omega}{\mathrm{k_B T}}\right)} - 1 \right)^{-1} \qquad \text{Eqn (25)}$$

Where:

- n is the average number of phonons
- ω is the frequency of the phonon
- T is the temperature
- k_B is the Boltzmann's constant
- $\hbar$ is the reduced Planck's constant.

The intensity of the Stokes radiation is proportional to *(n+1)* while the intensity of the anti-Stokes radiation is proportional to *n*. This means that far from resonances1, the ratio between stokes to anti-stokes intensity is proportional to exp(ħω/kBT) and at "low to moderate" temperatures, the Stokes signal is expected to be much stronger than the anti-Stokes signal. Thus, for any practical, routine purpose, only the Stokes side of the spectrum is analyzed by the Raman spectroscopy [111].

Because of the translational invariance, one important selection rule for light scattering processes in crystals is the wavevector conservation, see Eqn 22. The energies of crystalline vibrations probed by Raman are usually lower than 250 meV (about 2000 cm^{-1}) and those of the exciting visible laser light are about 1.5 – 5 eV, corresponding to the infra-red or deep UV excitations that can be *a priori* used. Therefore, we get $\omega_{scat} \approx \omega_{exc}$ and the wavevector in a typical backscattering experiment will be on the order of $q \approx 4\pi n/\lambda_{exc}$, much smaller than the wavevector $q = 2\pi/a$ at the boundary of the Brillouin zone, where a is a lattice constant and *n* denotes the refractive index of the sample. For most materials, its value is about 1/100 of the size of the Brillouin zone. Therefore, this selection rule implies the contributions of phonons at (more exactly very close to) the center of the Brillouin zone (Γ point). Another way to understand the $\boldsymbol{q} \approx 0$ rule is to consider that the excitation wavelength is always very large

[1] Resonance: The state when the incident photon energy is close to the electronic transition energy, this scattering process is known as resonant scattering. In such a case, the scattering cross-section is increased by several orders of magnitude.

compared to the interatomic distances, thus the lattice parameter: the photo-excitation of electrons is nearly "vertical" in the reciprocal space. Physically, the vibrations from one primitive cell to another one are in phase.

Hence one-phonon Raman scattering probes only zone-center phonons. In such experiments, ***q*** can usually be assumed to be zero. One also sees that the "geometric" observation conditions "select" a particular scattering wave vector.

2.2.3.3 Some aspects of Raman scattering

In this current section some aspects of the Raman scattering will be detailed, which will be essential for analyzing the Raman spectra of the actinide oxide materials. These insights will be further used for subsequent discussions aimed to understand the self-irradiation effects on the MOX materials that are analyzed in this thesis.

2.2.3.3.1 First-order spectrum: the scattered intensity

Stokes and anti-Stokes radiation are created by a fluctuating electric-dipole in the scattering medium induced both by the action of the incident light beam and the vibrational modes in the solid. As previously mentioned, the effect may be understood as that from an induced polarization ***P*** (the dipole moment per unit volume induced by a given vibrational mode) that oscillates at the frequency ω_{scat}. This polarization is represented by a modulation of the electric susceptibility of the medium induced by the vibrational modes. Here, for a given vibrational mode, one can introduce a modulated Raman susceptibility most often denoted as $R_{\alpha\beta}$, *i.e.* a "Raman tensor", which is defined by:

$$P_\alpha(\omega_{scat}) = \sum_\beta R_{\alpha\beta} E_\beta(\omega_{exc}) \qquad \text{Eqn (26)}$$

Where $\boldsymbol{E}(\omega_{exc})$ is the exciting electric field, α, β are related to the crystal axis. The scattered intensity, proportional to $|P(\omega_{scat})|^2$ writes:

$$I(\omega_{exc}, \omega_{escat}, q) \propto \left|\boldsymbol{E_{scat}} R_{\alpha\beta} \boldsymbol{E_{exc}}\right|^2 \qquad \text{Eqn (27)}$$

Here, note that the above equation obscures the fact that the scattered intensity is proportional to the vibration amplitude *Q* squared.

The form of the $R_{\alpha\beta}$ Raman tensors for crystals with different symmetries can be determined from group theory considerations. For crystals of cubic symmetry, they write as:

$$R_x = \begin{pmatrix} 0 & 0 & 0 \\ 0 & 0 & d \\ 0 & d & 0 \end{pmatrix}, R_y = \begin{pmatrix} 0 & 0 & d \\ 0 & 0 & 0 \\ d & 0 & 0 \end{pmatrix}, R_z = \begin{pmatrix} 0 & d & 0 \\ d & 0 & 0 \\ 0 & 0 & 0 \end{pmatrix} \qquad \text{Eqn (28)}$$

Here, x, y and z refer to the crystal axis of the cubic system, with x//(100), y//(010) and z//(001).

This is the triply degenerate representation whose three components can be denoted as x, y, and z. In this particular case we can regard these three components as equal to the projections of the relative displacement of the atoms in the unit cell along the crystallographic axes. This representation can be used for actinide oxides, which crystallize in the cubic form. We will come back to this below.

These equations are used to determine the selection rules for the polarization of the incident and scattered light: the scattered intensity *a priori* depends on the observation conditions. As a rule, the observation conditions are usually defined in a "laboratory reference frame" X, Y, Z. When the analysis is performed

under a microscope, meaning a backscattering geometry, the wavevector of both the incident and scattered radiations are along Z, the polarization vector of the incident radiation is usually along X. Without any knowledge of the response of the instrument in terms of polarization, the scattered light is *a priori* analyzed along X and Y with different responses. When the analysis of the scattered intensity is required, the physical properties of the samples (here Raman tensors) are to be expressed in the laboratory reference frame, using known laws of axis rotation.

The result of these symmetry requirements is that the scattered radiation may vanish for particular choices of the polarizations E_{exc} and E_{scat} and scattering geometries. These so-called Raman selection rules are very useful for determining the symmetry of Raman-active phonons. Since these selection rules are dependent on the scattering geometry, a specific notation (Porto's notation) is used for describing scattering geometries, which can be specified by four vectors: $\boldsymbol{k_{exc}}$ and $\boldsymbol{k_{scat}}$ (the directions of the incident and scattered photons, respectively) and E_{exc} and E_{scat} (the polarizations of the incident and scattered photons, respectively). These four vectors define the scattering configurations usually represented as $\boldsymbol{k_{exc}}$ (E_{exc}, E_{scat}) $\boldsymbol{k_{scat}}$.

2.2.3.3.2 Second-order scattering

Throughout this work, the second-order spectrum will be considered. The observation of this second order spectrum is a consequence of the anharmonicity of the internuclear potential energy of the vibrational motion.

Considering lattices with more than one (p) atom in the primitive cell and n unit cells, e.g., 3pn frequencies, the electric susceptibility may be written as:

$$\chi = \chi_0 + \sum_i \frac{\partial \chi}{\partial Q_i} Q_i + \frac{1}{2} \sum_{i,j} \frac{\partial^2 \chi}{\partial Q_i \partial Q_j} Q_i Q_j + \cdots, \qquad \text{Eqn (29)}$$

taking into account the second term of the Taylor expansion of the electric susceptibility. Thus, scattered radiations are also expected at the frequencies $\omega_{exc} \pm 2\,\omega_i$ (overtone scattering), $\omega_{exc} \pm \omega_i, \pm\ \omega_j$ (difference and combination scattering). The conservation laws now write:

$$\omega_{scat} = \omega_{exc} \pm \omega_l \pm \omega_j \qquad \text{Eqn (30)}$$

$$\boldsymbol{k_{scat}} = \boldsymbol{k_{exc}} \pm \boldsymbol{q_i} \pm \boldsymbol{q_j} \qquad \text{Eqn (31)}$$

While in first-order, the spectra display a discrete set of peaks that are associated with zone-center modes, higher-order spectra give continua that probe modes of wave vectors that span the whole Brillouin zone of the crystal: the selection rule for $\boldsymbol{q}$ conservation now implies that the sum or difference of the $\boldsymbol{q}$ vectors of the two phonons involved is approximately zero. Hence, in principle, all phonons can be observed. Therefore, at least far from resonance, the second order spectrum usually more or less reflects twice the phonon density of states (PDOS), although modified by a factor dependent on the phonon occupancy and the scattering efficiency. Thus, prominent spectral features are related to structure in the density of states of the respective modes. However, this may not be exactly the case, because of specific resonance conditions.

Far from resonance conditions, the second-order spectrum is of low intensity.

2.2.3.4 Resonant Raman scattering

Resonant Raman scattering is observed when the excitation is tuned on a specific electronic transition. In such a case, the scattering cross-section may be increased by several orders of magnitude. For the

case of molecules, discrete electronic levels are concerned, while for solids, the electronic band structure (inter-band processes) is to be considered as the corresponding energy level [111].
When visible photons are used to excite Raman scattering in a solid, they couple to electrons via the so-called electron-radiation interaction [111]. In a more quantum description, the light scattering proceeds in three steps:

- the incident photon excites the material into an intermediate state (virtual or real) by creating an electron-hole pair,
- the electron-hole pair is scattered into another state by emitting (Stokes) or absorbing (anti-Stokes) a phonon via the electron-phonon interaction,
- the electron-hole pair recombines radiatively with emission of the scattered photon.

Again, electrons are seen to mediate the Raman scattering of phonons, although they remain unaffected after the scattering process. Thus, the scattering cross section contains, at least in principle, information on electron-phonon interaction, electron-radiation interaction and the electron band structure. Again, one way to retrieve some of this information is to tune the excitation wavelength to resonate with an inter-band transition, to create resonant conditions.

Still within an electromagnetic description, the dielectric function and the susceptibility usually exhibits some structure as a function of frequency, usually due to so-called “critical points” in the density of states of electronic inter-band transitions. For non-polar compounds, as a first crude approximation, the expansion of the susceptibility in terms of the phonon coordinates suggests that the shape of the first-order resonance can be described in part with the Eqn 32, where the scattering resonances follow simply the square of derivative of the frequency-dependence of the linear susceptibility [112]

$$R_{\alpha\beta} \propto \left| \frac{\partial \chi_{\alpha\beta}}{\partial \omega} \right|^2 \qquad \text{Eqn (32)}$$

as it was observed for silicon as an example [112]. Two different processes, namely ingoing (outgoing) resonances are to be considered, that correspond to situations for which the incident (scattered) photon energy approaches or equals the energy of the optical transition. Finally, what has been described above is valid for second order as well. A complete description of resonance effects can be found in Ref. [111].

The resonance conditions of the system can be modified by certain external parameters such as temperature, pressure or simply by the presence of structural defects in the crystal lattice.

The resonance Raman scattering comes in handy in the case of analyzing very thin layers in the order of ten nm or even less, or chemical compounds with very small concentrations. On the other hand, resonance-related effects must always be considered alongside with effects resulting from the decrease in penetration depth of the probing radiation.

2.2.3.4.1 Polar compounds: the “Fröhlich” interaction

There is an important distinction between lattice vibrations which do or do not produce an electric dipole moment in the lattice, and are thus respectively active or inactive in first-order infra-red absorption The frequencies of infra-red-inactive phonons are determined mainly by short-range forces in the lattice: optical phonons can be regarded as "microscopic distortions" within the primitive unit cell. No variations in the Raman shift can be produced by variation of the scattering angle or of the relative orientation of the light beams and the crystal axes.

In a polar crystal, the frequency of an optical phonon is split into longitudinal (LO) and transverse (TO) components by the macroscopic electric field associated with the longitudinal phonon [111]. This electric field serves to stiffen the force constant of the phonon and thereby raises the frequency of the LO over

that of the TO. In cubic crystals with large LO-TO splitting, the phonon spectrum consists of an LO mode and a twofold-degenerate TO mode. The situation is by far more complicated in uniaxial crystals, as it becomes necessary to consider simultaneously two independent forces: the long-range electrostatic forces responsible for the LO-TO splitting, and the short-range inter-atomic forces, which exhibit some anisotropy in the force constants [113]. This effect leads to frequency variations with the direction of the phonon wave vector $\boldsymbol{q}$ in non-cubic crystals. A thorough description of LO-TO splitting can be found in Ref. [113].

Optical phonons can change the energy of an electronic band in two ways. In nonpolar crystals optical phonons alter the electronic energies only by changing the bond lengths and/or the bond angles. This electron-optical-phonon interaction is known as the deformation-potential interaction. On the other hand, as already mentioned, in polar crystals a long-wavelength longitudinal optical (LO) phonon involves uniform displacements of the charged atoms within the primitive cell. Such relative displacement of oppositely charged atoms generates a macroscopic electric field. This electron (electro-optical) longitudinal-optical-phonon interaction is known as the Fröhlich interaction [111].

Thus, for polar LO phonons, the scattering efficiency depends on both the strengths of the "mechanical" (deformation potential) to electro-optic (Fröhlich interaction) coupling in the electron-phonon interaction.
Besides the possible enhancement of the first-order LO mode discussed above, a strong enhancement of the scattered light intensity is usually observed near resonance. This is true for (forbidden) scattering by one LO-phonon and for scattering by 2 LO-phonons near the Brillouin zone center (Γ). Electron-phonon coupling via the Fröhlich interaction can actually produce multiphonon scattering near resonance (in some particular cases, CdS for example, up to about 10 LO-phonons are observed, see [114]. Several theories of this particular scattering phenomenon have been proposed, for a review see for example [114]). In such conditions, the scattering is polarized, observed for parallel incident and scattered polarizations. These phenomena have been discussed in [114], and references herein.

2.2.3.4.2 Effect of structural defects. Progressive or complete loss of the translational invariance. Expected consequences

There are many ways to introduce disorder in a crystal lattice: point defects (vacancies, interstitials, impurities, alloying…), planar defects (dislocations, stacking faults, grain boundaries…). In addition to point and line defects, there are defects that are composed of a small number of point defects. These are referred to as complexes. In each case, the net result is a modification the local arrangement of the atoms in the crystal lattice, which leads at least to both a mass disorder and/or a bond length disorder. Another effect may be a partial (point and planar defects) or complete (amorphization) loss of the translational invariance that characterizes the “idealized” perfect crystal. As a direct consequence, the presence of defects in the crystal lattice may induce a partial or a complete relaxation of the $\boldsymbol{q} \approx 0$ selection rule. In other words, there is some “uncertainty” on the phonon wavevector.

Depending on the amount of defects, the consequences on the line shape in the Raman spectra can be quite different:

- The appearance of Raman-forbidden modes, or impurity-induced modes. Out of resonant conditions, relatively large concentrations of defects are needed (≈ 10^{18}/cm^3) to detect these vibrational modes. Their position in the spectrum depends in particular on the mass difference between the impurity and the atom it substitutes in the lattice. Some of these (lighter impurities) are known as local modes.
- A possible modification of the lattice symmetry. This effect may be analyzed as a phase transition.
- When the amount of defects is quite large, inducing small characteristic lengths or mean coherent sizes below ≈ 15 nm, these effects are usually discussed according to the phenomenological “phonon confinement model” [115]. Depending on the dispersion of the optical branches in the Brillouin zone, a shift and asymmetrical broadening of the Raman-allowed line may be observed. The disorder transforms the sharp Raman lines, resulting from wavevector conservation in

crystals, into phonon densities of states (PDOS). Thus, the range of phonon wave vectors that contribute to the Raman line shape is determined in part by the crystallite size and is given by $\Delta \boldsymbol{q} = 2\pi/l$, where *l* is a characteristic length.

- When the amount of defects is quite large, the translational symmetry does not exceed three or four lattice parameters. In such a case, the $\boldsymbol{q} \approx 0$ is completely relaxed, and the Raman (and IR) spectra reflects the PDOS. Obviously, the knowledge of the PDOS is here a prerequisite for a complete understanding of the vibrational spectra.
- Finally, it is expected that the disorder also affects the electronic states responsible for the polarizability. The effect of disorder on the electronic states is most probably to "blur" sharp resonances.

Here, the issue is to establish whether the spectroscopic analysis allows effectively discriminating between these different effects, or not. In the latter case, this may mean that any cause of loss of translation invariance leads to equivalent spectroscopic signatures.

2.2.3.4.3 The mass and isotopic disorder

Throughout this work, $(U,Pu)O_2$ solid solutions (sometimes referred as mixed crystals) will be examined. In a first approximation, it is generally assumed that the spatial distribution of the intermixing atomic species is nearly random. This randomness obviously removes the translational symmetry of the crystal, so that Raman spectra from mixed crystals might be expected to be similar to the Raman spectra from amorphous materials. Nevertheless, alloying is in general a much "gentler" perturbation than amorphization, as it can be seen from diffraction studies, which clearly indicate the existence of a remaining order and a well-defined average lattice constant. In all cases, these almost-crystalline structural properties are reflected in their Raman spectra, which turn out to be dominated by relatively narrow peaks.

Different situations can then be encountered, depending on the mass and/or force constant contrasts between the two extreme compositions of the solid solution. Without going into detail, these different situations lead to so-called "one-mode", "two-mode" or even "three-mode" behaviors [116]. Throughout this work, only the one-mode behavior will be considered, which is simply characterized by a continuous evolution of the frequencies between those of the two end-member compositions.

In a first approximation, this "mean lattice cell" can be analyzed according to the Virtual Crystal Approximation (VCA). The VCA is usually introduced for a crystal containing heteroelements or even isotopes to recover the translational invariance lifted by the disorder. In the case of an isotopic disorder, masses are simply replaced by their average weighted relative abundances.

Within the framework of the harmonic approximation, each vibrational mode may be described as a simple mass and spring system. Such a description comes from the analysis of the vibration properties in terms of normal modes. This description consists in diagonalizing the so-called dynamic matrix, which can be written according to:

$$(\Phi - \omega_i^2 M) e(i) = 0 \qquad \text{Eqn (33)}$$

Where:

- Φ and *M* are the force constant and mass matrices respectively,
- ω_i and e*(i)* the eigenvalues and eigenvectors of Eqn 33, that give the vibrational frequencies and the atomic displacement patterns of the vibrational mode i.

The harmonic approximation allows to decouple all the vibrational modes meaning they do not interact with each other [117]. Thus, the frequency of each particular mode *i* becomes proportional to $\sqrt{K_i / \mu_i}$,

where K_i is an effective force constant and μ_i an effective mass. The effective force constant brings some structural information, while the effective mass naturally brings chemical information.

Deviations from the perfect lattice, *i.e.* mass and/or force constant disorder, perturbations will change the force constant and mass matrices, so that Eqn 33 becomes:

$$(\Phi + \Delta\phi - \omega_i^2(M + \Delta M))e(i) = 0 \qquad \text{Eqn (34)}$$

This simple model can be used to explain the compositional dependence of the main peaks in Raman spectra of alloys or mixed crystals. According to this model, one can write the shift in the Raman frequencies as the sum of a "mass perturbation" and "bond perturbation" term:

$$\Delta\omega_i^2 = \Delta\omega_{mass}^2 + \Delta\omega_{bonds}^2 \qquad \text{Eqn (35)}$$

Eqns 34 and 35 can be used to analyze isotopic disorder (in which case $\Delta\Phi = 0$), stress as we will see below (for which $\Delta M = 0$), and alloying, for which in principle there are changes in both the force constant and mass matrices. In the case of an isotopic disorder, using the VCA approximation, masses may be simply replaced by their average weighted relative abundances, as a first approximation.

2.2.3.4.4 Strain effects

Because of the anhamonicity of the crystal potential, the response of lattice dynamics (mode frequencies) follows the response of the static lattice induced by the changes in the unit cell volume. The latter are usually induced by temperature and/or pressure. However, heteroelements, vacancies, interstitials, may also induce changes in the volume of the lattice cell. In this last case, additional changes in the "mean lattice cell" are to be taken into account.

Generally, strain effects can be computed through a modification, most often linear in terms of strain, of the spring constant. This hypothesis is the so-called quasiharmonic approximation, which allows the volume (strain) dependence of the phonon wavenumbers to be taken into account, but still consider them to be harmonic.

Different approaches have been used to relate strain to Raman shifts and the one which is useful in this work is the so-called Grüneisen parameter. In its microscopic formulation, the Grüneisen parameter $\boldsymbol{\gamma(q, s)}$ is a measure of how a specific phonon frequency $\boldsymbol{\omega(q, s)}$ is altered under a small change in the geometry of the crystallographic unit cell. Here, $\boldsymbol{q}$ is a specific wave vector in the first Brillouin zone and $\boldsymbol{s}$ an index that refers to a specific mode. For isotropic materials, or materials with cubic lattice symmetry, *i.e.* the most commonly discussed situation, the Grüneisen parameter is simply a scalar that refers to an isotropic change in the volume V, according to:

$$\gamma(\boldsymbol{q}, s) = -\frac{V}{\omega(\boldsymbol{q}, s)}\left(\frac{\partial\omega(\boldsymbol{q}, s)}{\partial V}\right)_T = -\left(\frac{\partial \ln\omega(\boldsymbol{q}, s)}{\partial \ln V}\right)_T \qquad \text{Eqn (36)}$$

For a constant temperature, introducing the bulk modulus $K = -V(\partial P/\partial V)$, and the compressibility $\kappa = 1/K$, Eqn 36 reduces to:

$$\gamma_T(\boldsymbol{q}, s) = = -\left(\frac{\partial \ln\omega(\boldsymbol{q}, s)}{\partial \ln V}\right)_T = \frac{1}{\kappa\omega(q, s)}\left(\frac{\partial\omega(\boldsymbol{q}, s)}{\partial P}\right)_T \qquad \text{Eqn (37)}$$

Where γ_T is the isothermal Grüneisen parameter. Note that $\boldsymbol{K}$ is not a strictly a constant, but is *a priori* a function of pressure ($\boldsymbol{P}$) and temperature ($\boldsymbol{T}$).
For a temperature-induced strain (lattice expansion), one can define an isobaric Grüneisen parameter according to:

$$\gamma_P\,(\boldsymbol{q},s) = = -\left(\frac{\partial \ln \omega\,(\boldsymbol{q},s)}{\partial \ln V}\right)_T = \frac{-1}{\alpha_T \omega\,(q,s)}\left(\frac{\partial \omega\,(\boldsymbol{q},s)}{\partial T}\right)_P \qquad \text{Eqn (38)}$$

Where α_T is the volumetric thermal expansion coefficient.

When the isobaric and isothermal Grüneisen parameter coincide in a given T or P range, it is considered that the vibrational mode of interest has a quasi-harmonic behavior. Such a case is rather unusual in its ideality. In this specific case, the mode Grüneisen parameters can be determined under isostatic stress conditions. Usually, the Grüneisen mode parameters are positive and lie in the range 1.5 ± 1. In a first rough approximation, this means that one expects line up-(down-) shifts of a few reciprocal centimeters for a lattice contraction (expansion) of an order of magnitude close to 10^{-3}. Self-irradiation-induced lattice swelling is therefore *a priori* observable using Raman spectroscopy.

Finally, non-isotropic strains obviously lead to a modification of the cubic lattice symmetry, and to a modification of the number of observable modes.

2.2.3.5 Actinide oxides with the fluorite structure.

2.2.3.5.1 Infrared- and Raman-allowed modes

As described in Chapter 1, close to oxygen stoichiometry, the main actinide oxides (MO_2) considered in this study (UO_2 and PuO_2 as well as their solid solutions) crystallize in the fluorite symmetry. In this symmetry, there is an inversion center, meaning that the mutual exclusion rule holds. Group character analysis of the long-wavelength ($\boldsymbol{q} \approx 0$) lattice vibrations shows that the phonon dispersion curves consist of three acoustic branches and six optic branches. At $\boldsymbol{q} \approx 0$ three of the latter are infrared-active modes of vibration of T_{1u} symmetry (in fact one doubly degenerate TO mode and one LO mode for $\boldsymbol{q}$ not strictly equal to 0, because of the long range polarization field). The remaining three optic modes are Raman-active and triply degenerate, of T_{2g} symmetry. The triple degeneracy arises from the fact that all three crystal directions are equivalent in a cubic symmetry. The Raman mode frequency is obviously given directly by the Raman measurements, whereas the TO and LO frequencies are given indirectly by fitting the infrared reflectivity. The atomic displacement patters of both the infra-red- and Raman-active modes are given in Figure 35.

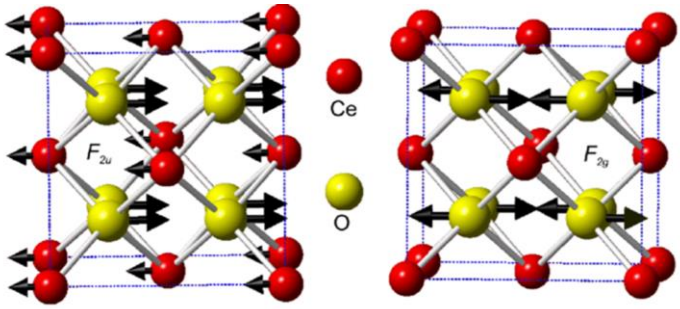

Figure 35 The normal modes of the infrared (F_{1u}) and Raman (F_{2g}) active lattice vibrations of the fluorite structure, here CeO_2. Reproduced from Ref [118].

For the zone-center Raman-active normal mode, the two O sub-lattices move against each other, while the M sub-lattice is stationary. This mode involves both the nearest-neighbor M-O and O-O force constants, the O-O contribution being larger than the M-O stretching one [119]. Its reduced mass is that of the two oxygen atoms involved in the atomic displacement pattern. Thus, purely isotopic disorder is expected to have no effect on the frequency of this mode.

The infra-red mode only requires the M-O force constant, along with the force induced by the effective electric field which acts on the effective ionic charges of both the O and M ions. Its reduced mass involves both oxygen and metal atoms, and writes as:

$$\mu = \frac{2m_O m_M}{(2m_O + m_M)} \quad \text{Eqn (39)}$$

where m_O and m_M are the oxygen and metal masses respectively.

The second-neighbor force constant between the M ions does not appear in the equations of motion since cations do not move relative to each other at q = 0. Here, one effectively expects isotopic disorder to have an effect on the frequency of infrared modes. However, a simple computation shows that this effect will be very weak, lower than 1 cm^{-1}, when for example considering ^{238}Pu and ^{242}Pu isotopes. Since the force constants in the harmonic approximation is a constant, the relative shift in the frequency due to isotopy is proportional to the following equation as already explained in Section 2.2.3.4.3

$$\omega \propto \frac{1}{\sqrt{\mu}} \quad \text{Eqn (40)}$$

Sarsfield *et al.* [120] compiled the band positions of several MO_2 fluorite-type structures (ThO_2, UO_2, NpO_2 and PuO_2) as tabulated in Table 12.

Table 12 Band position of some of the MO_2 fluorite structures reported until 2012 [120]

Compound	T_{2g}(cm^{-1})	1LO(cm^{-1})	2LO(cm^{-1})	Other bands (cm^{-1})	Ref
PuO_2	476±2	578±8	1158±8	2116±10, 2611±10	[120]
	478	-	-	639-645[a]	[121]
	463-475	580	1160	-	[122]
	475	-			[123]
ThO_2	465				[121]
	466	-	-		[124]
	461	565	1155	610	[125]
UO_2	-	578±2	-	-	[126]
	445	-	-	-	[121]
	445	575	1150	-	[127]
	445	598[b] – 618[c]	1149	1343[c],1630[b]	[128]
NpO_2	463-468	568	1150	-	[120]
	466				[121]
	467				[124]

a Possibly assigned to $^{234}UO_{2+x}$ // b 514.5 nm laser used //c 785 nm laser used

Two different points stand out from Table 12:

- the Raman and infra-red frequencies of these oxides are rather similar, see in particular the observed frequencies of LO infra-red active mode,
- excluding UO_2, there is a large scatter in the Raman data.

2.2.3.5.2 The Pu content relationship with the T_{2g} band position in the fluorite symmetry

In the case of a stoichiometric $(U,Pu)O_{2.00}$ sample, the position of the T_{2g} band varies between those of UO_2 and PuO_2 *i.e.*, 445 cm^{-1} and 478 cm^{-1}.

Elorrieta *et al.*, [129] studied the T_{2g} band positions with increasing Pu content for a series of $(U_{1-y}Pu_y)O_2$ samples, as shown in Figure 36. They suggest there is a linear behavior of the T_{2g} position as a function of the Pu content.

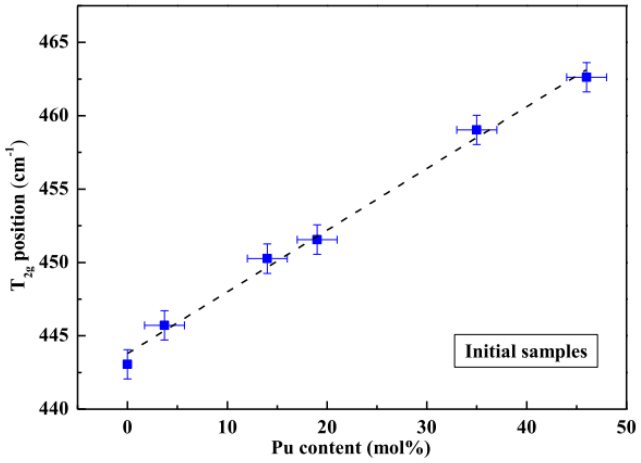

Figure 36 Position of the T_{2g} band vs. Pu/(U+Pu) for $(U_{1-y}Pu_y)O_2$ samples with 0< y< 0.46 [129]

Recently, Medyk *et al.* showed that this relation is not linear, as shown in Figure 37 (which includes also the Elorrieta's data).

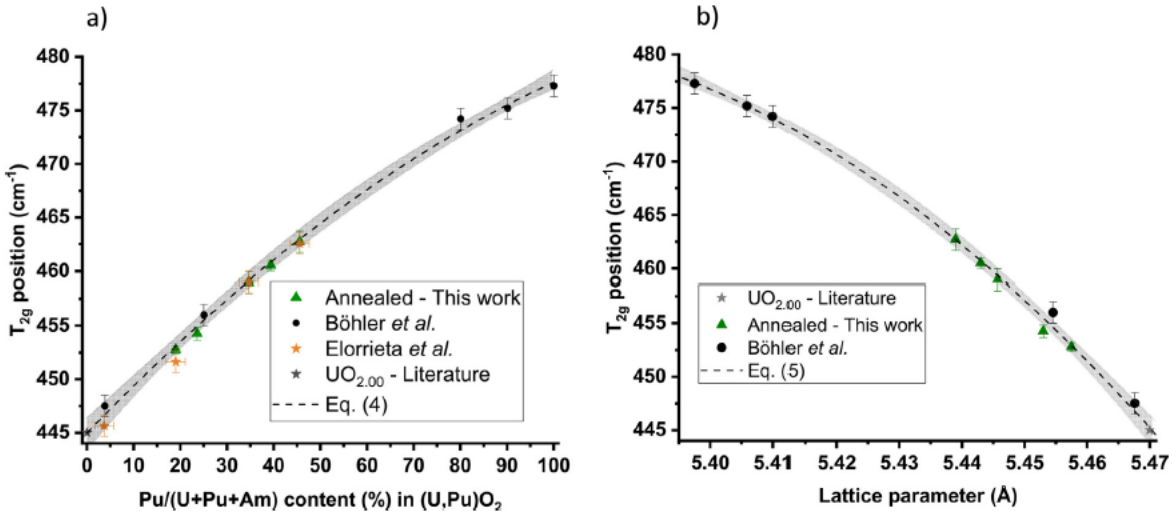

Figure 37 T_{2g} position of $(U,Pu)O_{2.00}$ samples as a function of a) the Pu/(U+Pu+Am) content (mol.%) and b) the lattice parameter [99]

The relation proposed by Medyk *et al.* is given in Equations 41 and 42.

$$y = k_1 \, x \sqrt{k_2 - \omega} + k_3 \qquad \text{Eqn (41)}$$

$$a = h_1 \, x \sqrt{h_2 - \omega} + h_3 \qquad \text{Eqn (42)}$$

Where:

- y is the the Pu/(U+Pu+Am) molar ratio in $U_{1-y-z}Pu_yAm_zO_{2.00}$

- a (Å) the lattice parameter
- ω (cm^{-1}) the T_{2g} band position

and the constants variables are as the following:

- k_1 = (−28.2±1.0) $cm^{-1/2}$
- k_2 = (485.7±1.9) cm^{-1}
- k_3 = (180.0±8.4)
- h_1 = (1.861±0.040)×10^{-2} $cm^{1/2}$·Å
- h_2 = (482.1±1.0) cm^{-1}
- h_3 = (5.3569±0.0024) Å.

Following these equations, the T_{2g} position is calculated using the two following Equations 43 and 44. The first is based on the Pu/(U+Pu+Am) content with Equation 41 and the second is based on the lattice parameter with Equation 42.

$$\omega = A \times y^2 + B \times y + C \quad \text{Eqn (43)}$$

Where the constant variables:

- A = -1.2559x10^{-3} cm^{-1}
- B = 4.5215x10^{-1} cm^{-1}
- C = 4.4498x10^{2} cm^{-1}

$$\omega = A' \times a^2 + B' \times a + C' \quad \text{Eqn (44)}$$

Where the constant variables:

- A' = -2.8874x10^{3} cm^{-1}.$Å^{-2}$
- B' = 3.0935x10^{4} cm^{-1}.$Å^{-1}$
- C' = -8.2376x10^{4} cm^{-1}

Finally, linking the Vegard's law (Eqn 1) and Equation (42), the equation that links the T_{2g} position to the Pu/(U+Pu+Am) content can be derived with the following relation.

$$\omega = h_2 - \left(\frac{(5.47 - 0.074 \times y - h_3)}{h_1}\right)^2 \quad \text{Eqn (45)}$$

2.2.3.6 Raman Microscope Instrumentation and Raman Imaging

The Raman spectroscopy can be coupled with a confocal microscope, where the probe size is reduced down to an order of one micrometer (~ 1µm^2). This coupling is called the Raman microscope. In this context, the numerical aperture of the objective, its focusing ability as well as its quality have an impact on the probe size of the spectrometer, which, in turn, affects the spatial resolution and sensitivity of Raman measurements. Here, the "Confocal" is simply defined as "having the same focus" and describes an optical microscope in which the sample is illuminated with a point source and the image of this point is detected through a pinhole in front of the detector [130]. This technique is used extensively in this study and the details for the Raman Microscopy installed in the ATALANTE facility is given in the Section C.3 of the Appendix C.

Figure 38 shows a sketch of a typical Raman Microscope. As an overall description, the system consists of an excitation laser, a microscope and a spectrometer with CCD detector.

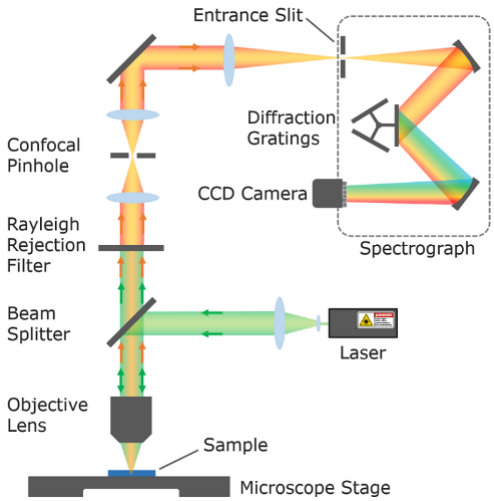

Figure 38 : Typical layout of a Raman microscope with a fiber-coupled laser source and spectrometer (image from Edinburgh instruments)

In a more general description of the instrumentation, the sample to be analyzed is placed on the microscope stage and the excitation light from a laser is reflected and focused down onto the sample through the objective lens of the microscope. The Rayleigh and Raman scattered light are collected by the objective lens, which then transmitted through the beam splitter and passed through the rejection filter, which removes the Rayleigh scattered light. The scattered beam is then analyzed using holographic grating (600, 1200, 1800 or 2400 lines/mm) which disperses the photons according to their wavelength. A high number of grooves/mm (lines/mm) results in a high dispersion and thus a high resolution. At the output of the holographic grating is the detector, which is most often multichannel (like CCD cameras). CCD's consist of an array of tiny light-sensitive elements called pixels (short for "picture elements"). Each pixel can detect and measure the intensity of light. They simultaneously collect photons of different wavelengths and forms the Raman spectrum [130].

2.2.4 X-ray Absorption Spectroscopy (XAS)

XAS is a powerful technique to investigate the electronic and geometric information in the short-range order of a chosen element independent of the sample physical state. XAS spectra are divided into two distinct regions, each providing distinct information. The first region, known as the X-ray Absorption Near Edge Structure (XANES), characterizes the fine details of the absorption edge and is sensitive to the oxidation state and the electronic structure of the absorbing atoms, while EXAFS (Extended X-ray Absorption Fine Structure provides information about the local atomic structure and coordination of the absorbing atoms [131].

2.2.4.1 The Principle of the XAS

The technique is based on irradiation of the sample with a monochromatic X-rays of varying energy. One simply scans in radiation energy and observes the change of the sample's absorption cross section. The absorption of the X-ray obtained with the Beer-Lambert law given in Eqn 46.

$$I = I_0 e^{(-\mu t)} \qquad \text{Eqn (46)}$$

Where:

- I is the intensity that is transmitted through the sample,
- I_0 the incident X-ray intensity,
- t the thickness of the sample
- μ the sample absorption coefficient.

The absorption coefficient μ(E) here is a function of the sample density (ρ), its atomic number (Z), atomic mass (A) and the energy of the incident X-ray (E), which is defined with the equation 47 below.

$$\mu(E) \approx \frac{\rho Z^4}{AE^3} \qquad \text{Eqn (47)}$$

In the applied energy range of the absorption spectroscopy, the photoelectric effect is the main interaction of the photon with the matter. This phenomenon is due to the interaction of the incident photon with the core electrons of the atom. More precisely, when the energy of the incident X-ray is higher than the binding energy of a core electron. The electron is then ejected from its quantum level. In this case, the X-ray is absorbed and the excess energy is given to the photoelectron as kinetic energy. The mean free path of the photoelectron, which represents the average distance that it can travel before undergoing inelastic scattering or before the core hole is filled, typically spans a range of 5 to 30 Å.

When the incident X-ray has an energy equal to that of the binding energy of a core-level electron, a sharp increase in the absorption is observed: *i.e.* the absorption edge. This phenomenon indicates the core transition of the core electrons into vacant valence levels and the continuum. Briefly, for the XAS, the primary focus is the variation of the absorption as a function of energy, near and at energies above these absorption edges. Each element have their characteristic absorption edges corresponding to a specific electronic orbital. As an example, the K-edge corresponds to the bonding energy of the 1s orbital, while the L_1, L_2 and L_3 edges correspond to the bonding energies of the 2s, $2p_{1/2}$, and $2p_{3/2}$ orbitals, respectively.

Alternative to the transmission mode, the X-ray absorption spectrum can also be measured with the fluorescence emission (Auger mode is not considered here), where the core-hole due to the ejected photoelectron is compensated with one of the electrons from the upper shells, emitting energy in the form of X-ray fluorescence photons as shown in Figure 39a. These fluorescence photons are characteristic of the element that emitted them and have discrete energies as shown in Figure 39b.

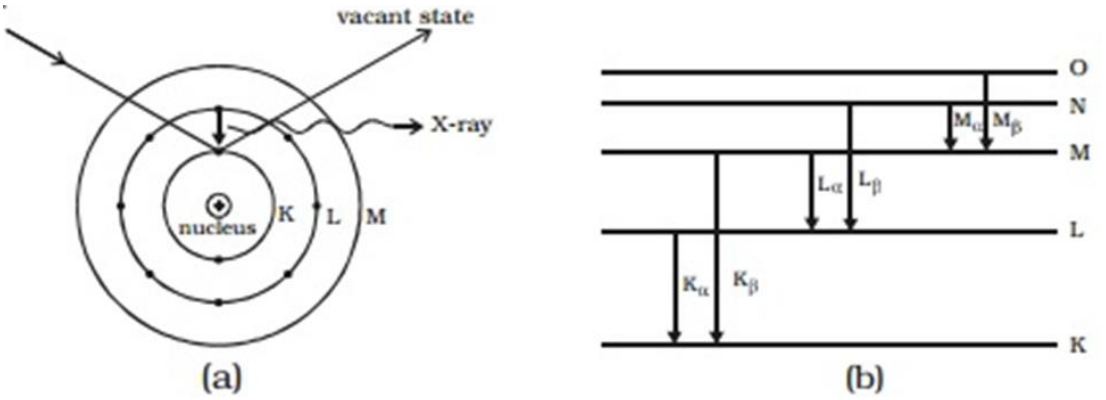

Figure 39 a) X-ray fluorescence generation mechanism b) diagram of possible transitions for an electron when there is a hole in the K layer (K_α, K_β) and a hole in the L layer (L_α, L_β series) and hole in the M layer (M_α, M_β series) [132]

The emitted X-ray with an intensity proportional to the absorption coefficient of the material μ(E). Thus, μ(E) can be measured both in transmission geometry, according to Eqn 46, or in the fluorescence geometry, according to Eqn 48, where I_f is the fluorescence intensity.

$$\mu(E) \propto \frac{I_f}{I_0} \qquad \text{Eqn (48)}$$

These measurements require a fine-tuning of the selection of the region of interest (ROI) from the fluorescence spectrum as well as correction of self-absorption effects when the probed elements concentration in the samples is larger than 10 at%. Here, the ROI refers to the specific energy range or

wavelength range where we choose to monitor the emitted X-ray fluorescence signal after X-ray excitation. The Figure 40 is an example for the selection and optimization of ROI for the Si K emission line in a fluorescence spectrum.

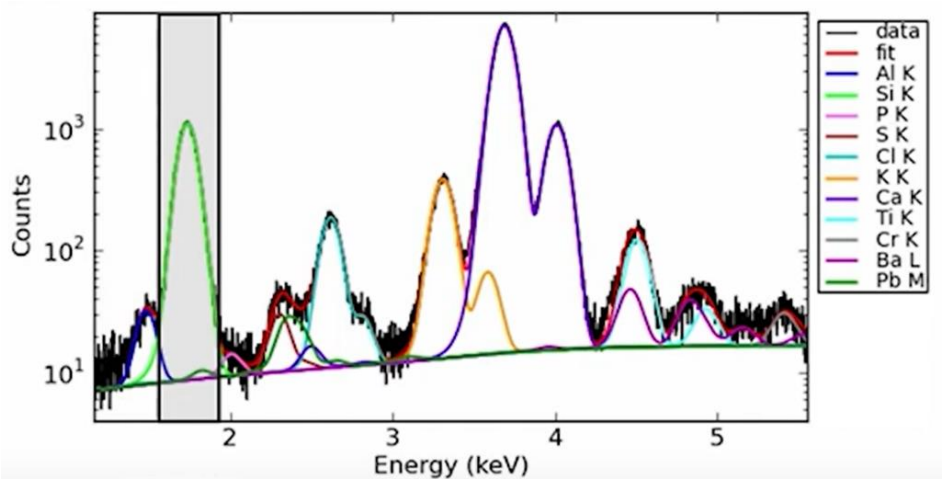

Figure 40 Fluorescence spectra of several elements with their corresponding emission lines. Here the Si K region is selected as ROI (as highlighted in the spectrum)

Here the Figure 41 illustrates how the absorption coefficient evolves when a metallic copper sample is exposed to X-rays with varying energies up to 12 keV. This energy level corresponds to the Cu L and K-edge regions. The same figure also clearly shows the XANES and EXAFS part of the spectrum in the close-up region.

The absorption edge (designated as E_0) is typically measured relative to the Fermi level, which represents the highest occupied energy level in the material at absolute zero temperature. Its position is defined in the XAS spectra as the first zero crossing of the second derivative of the absorption spectrum. The XANES part of the spectrum corresponds to the region -30/+30 eV relative to the absorption edge.

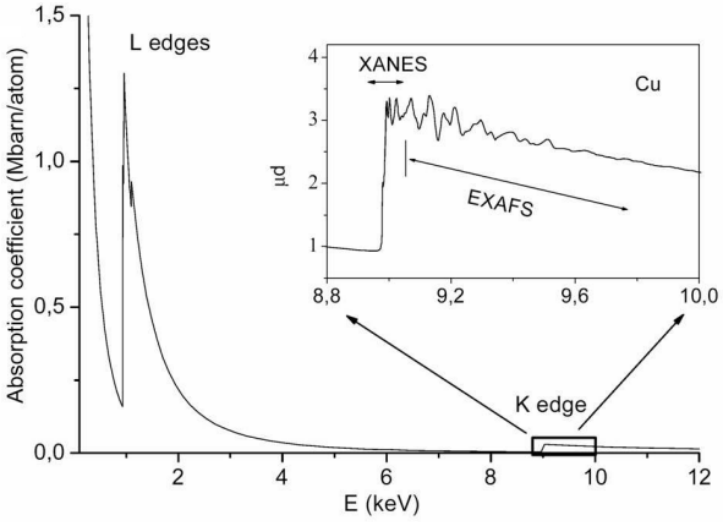

Figure 41 X-ray absorption coefficient of copper in the region of the L and K edges. The inset shows an expanded view of the K -edge region with the separation into a XANES and an EXAFS range. [133]

The EXAFS part of the spectrum, on the other hand, can continue for ~1 keV ahead the absorption edge. The oscillations in the EXAFS part of the spectrum, hence, correspond to the wave interactions between the ejected photoelectron and the atoms surrounding the absorbing atom. Thus, EXAFS is better understood through the wave-like behavior of the photoelectron generated during the absorption process. It is hence, practical to convert X-ray energy into k, representing the wave number of the photoelectron, denoted in the units of distance^{-1} as shown in Equation 49.

$$\mathrm{k} = \sqrt{\frac{2m(E - E_0)}{\hbar}} \qquad \text{Eqn (49)}$$

Where E_0 is the absorption edge energy, m the mass of an electron, and ħ the Planck's constant.

Here, the primary parameter of interest in EXAFS is the χ(k), which signifies the isolated variation in the absorption coefficient relative to the wave number of the photoelectron. In this scope, the χ(k) parameter is simply referred to as "the EXAFS." In Figure 42a, the EXAFS obtained from the Fe K-edge for a FeO sample is displayed. The EXAFS exhibits clear oscillations and rapidly diminishes with further increasing k. To emphasize these oscillations, χ(k) is often multiplied by a power of k for the purpose of a better visualization, typically k^2 or k^3, which is also the case in the Figure 42a. Furthermore, employing the Fourier Transform of the EXAFS enables us to make transition from the frequency domain (k) to the distance domain (R), allowing us to visualizing the different coordination shells as shown in Figure 42b. Note that the distance values obtained in this domain cannot be directly extracted. For this a phase correction term (δ (k)) is used.

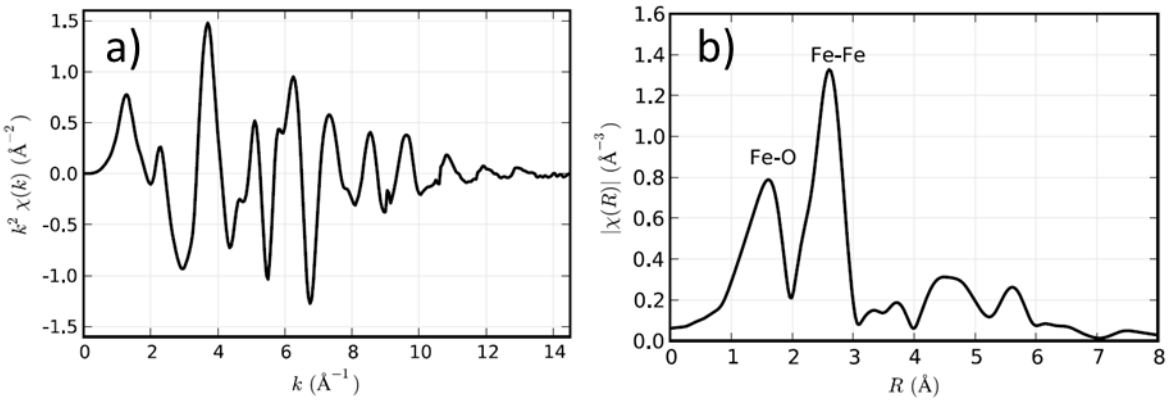

Figure 42 The EXAFS spectrum obtained for the Fe K edge of FeO, with a) k^2 weighting applied to EXAFS spectra b) the Fourier transform of the k-weighted XAFS, revealing the contributions originating from neighboring atoms of both Fe-O and Fe-Fe [134].

The parameters that influence scattering by various neighboring atoms can be explained using the so-called EXAFS Equation, where a simplified version is shown in the Equation (50) as follows:

$$\chi(\mathrm{k}) = \sum_j \frac{N_j f_j(k) e^{-2k^2\sigma_j^2} e^{-2R_j/\lambda(k)}}{kR_j^2} \sin\left[2kR_j + \delta_j(k)\right] \qquad \text{Eqn (50)}$$

In this equation, 'j' signifies the shell of neighboring atoms. In accordance with that, 'N_j' represents the count of neighboring atoms in that shell, 'R_j' indicates the distance between the absorbing atom and the respective neighboring atom in that shell, and 'σ_j^2' denotes the Debye Waller factor, which reflects the variations in distances among neighbors and relates to the disorder within the j-th atomic shell. 'f (k)' represents the scattering factor for shell 'j,' and 'δ(k)' is a phase correction term. The λ refers to the photoelectron's mean free path, and its range (5 to 30 Å) varies as a function of k.

In this context, due to the λ(k) and the $1/R^2$ term in Equation (50), the EXAFS is essentially a local probe and capable of examining the surroundings of the absorbing atom within a range of only in the order of 5 Å.

The EXAFS equation is further corrected using the S_0^2 parameter, which represents the amplitude reduction factor due to various factors, including electronic relaxation and multiple scattering effects. It accounts for the reduction in the intensity of the EXAFS oscillations compared to what would be expected

based solely on the simple scattering of a photoelectron by a single atom. In our study, the adapted S_0^2data for different edges used in this study are given in the Appendix C.4.5.2.

While it may seem somewhat complex, the EXAFS equation is straightforward enough to effectively model the EXAFS data. Consequently, we can fit the values for N, R, and σ² (while keeping S_0^2 as constant) once we have accurate information on the scattering amplitude f(k) and phase-shifts δ(k). Here, the f(k) and δ(k) values are modelled using the FEFF software [135]. The created FEFF model for the samples in this study are explained in the Appendix C.4.5.2.

2.2.4.2 XAS spectrum collection

In most of the synchrotron beamlines, both the transmission and the fluorescence geometry measurements can be performed, even simultaneously if the sample allows it. A disposition of a typical X-ray absorption experimental setup is shown in Figure 43. In the arrangement, the energy of the incident X-ray is tuned with a two crystals monochromator (Si crystal). The varying beam intensity is monitored prior and after the interaction with the sample, using the first and second ionization chambers (measuring I_0 and I respectively). This gives the absorption information of the sample in the transmission geometry. The fluorescence detector is typically placed at 45° to the sample surface to maximize the fluorescence signal. It is also a common practice to measure the transmission of a reference sample using the second and a third ionization chambers to correct the incident energy [136].

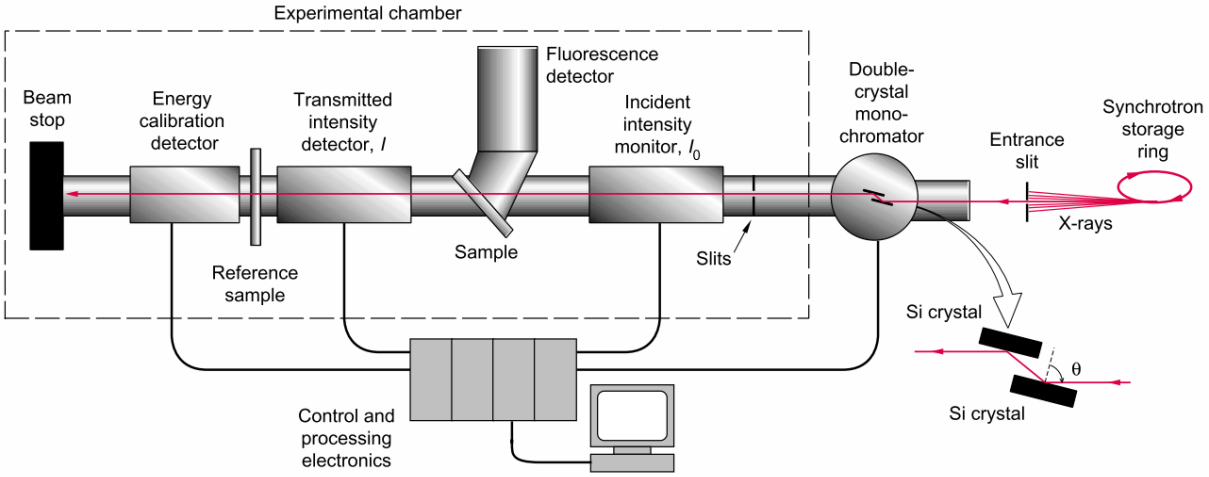

Figure 43 Arrangement of a typical X-ray absorption experiment [137]

Chapter 3. Examination of the annealed samples

In the previous two chapters, we have described the samples and the methodology used in this work, both from a theoretical and a practical point of view. In particular, we have shown that a high-temperature annealing in a controlled atmosphere can be used to heal the self-irradiation-induced defects and to retrieve virtually defect-free samples. Such annealed samples can thus be considered as “defect-free” replica of the aged, self-irradiated samples.

The aim of this chapter will be to describe the three MOX samples as accurately as possible, quite immediately after annealing. For this purpose, characterization methods such as EPMA, XRD, Raman microscopy and XAS will be employed. As already mentioned, these MOX materials are heterogeneous in nature, which means they will have to be examined at different spatial scales.

In essence, it is crucial to determine the O/M (Oxygen-to-Metal) ratio of the annealed samples. While the annealing process is expected to bring the samples close to stoichiometry under the employed thermal treatment conditions, we will rely on XRD (X-ray diffraction) and XAS (X-ray absorption spectroscopy) results to assess their O/M values. The samples at stoichiometry will help us simplify the study by eliminating the defects arising from non-stoichiometry. The characterization techniques will be further employed to identify: (i) the local Pu content, (ii) the average lattice parameters, (iii) the oxidation states of U, Pu and Am atoms in the lattice, (iv) interatomic distances in the first and second coordination spheres (metal-oxygen, metal-metal distances). We will attempt, as far as possible, to get this information redundantly.

At this point, it should be underlined that a certain number of assumptions and approximations are necessary to present and interpret the results as accurately as possible. These will be introduced progressively in this chapter. In particular, the presence of americium, albeit in small quantities, is not taken into account. This will be discussed when analyzing the X-ray absorption results and more in detail in the final chapter of this document.

From these samples, it will be seen that it will be possible to revisit in part the $(U,Pu)O_2$ solid solution in the 0 – 40 at% Pu concentration range. While the behavior of the solid solution in terms of lattice parameter was already described from diffraction techniques, it is probably not yet the case for Raman spectroscopy, although the main trends have been discussed in the litterature [97], [99], [129], [138]. For such a purpose, a few additional samples, available as part of another study [139], will be used to extend the Pu/(U+Pu) concentration range in between 0 and 100 at%. In particular, this will enable us to examine the Raman spectra of these materials in more details, including some possible effects due to excitation wavelength.

3.1 EPMA

EPMA was used to collect mappings of the plutonium distributions in the samples. These measurements were performed on both the annealed and old samples. In each samples, several regions (1024 × 1024 pixels with a pixel size of 1×1µm^2) were randomly selected for these analyses and no discrepancies were observed between these regions. Only one map per sample will thus be presented in this section. These samplings are large enough to give a representative description of the plutonium distribution of the samples and to locate suitable regions for the Raman mapping. In this section, we will thus describe the plutonium distribution of the three annealed samples. We will also discuss the EPMA images obtained for the aged samples, in order to analyze and/or exclude any effect of the annealing on the plutonium distribution in the samples.

3.1.1 The MIMAS sample

Examples of pseudo-quantified Pu mappings for the annealed and the old MIMAS samples are shown in Figure 44. The provided image consists of both the full image and a close-up image on the bottom. This helps determining the average agglomerate sizes and better distinguishing the different phases.

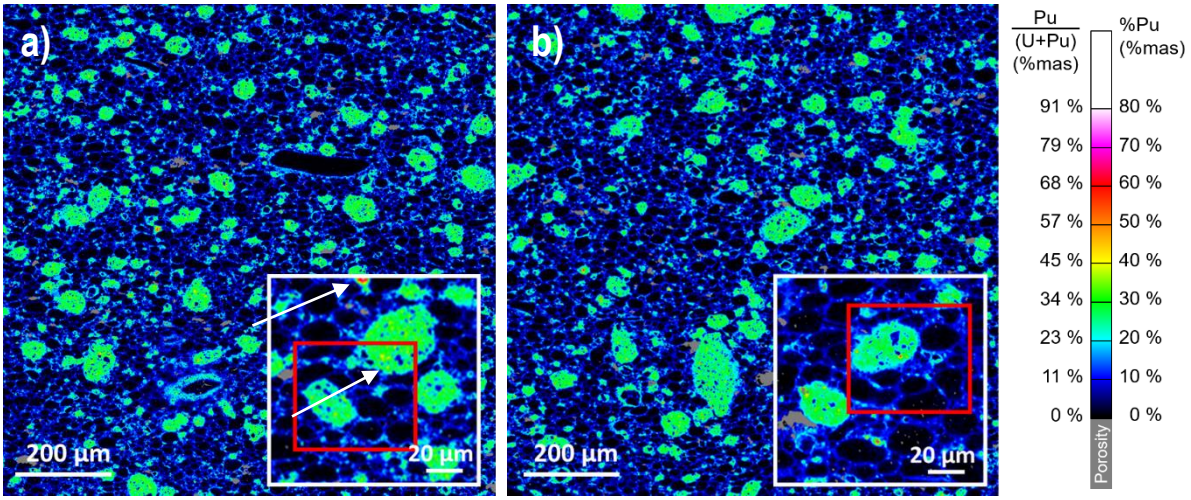

Figure 44 EPMA pseudo-quantified Pu large mapping in the annealed MOX MIMAS specimen a) annealed sample, b) old sample. The white square is a detailed mapping of a particular region in the sample. The red square highlights a region in which the Raman analyses were conducted. The color scale on the right indicates the associated Pu content.

By analyzing the image, three distinct phases are visually distinguishable by their respective black, green, and blue colors corresponding to Pu local content. They correspond, respectively, to U-rich agglomerates, Pu-rich agglomerates, and an intermediate Pu content region known as the coating phase. The U-rich agglomerates have sizes ranging mostly smaller than 30 µm, while the Pu-rich agglomerates are larger; with size mostly distributed between 10 and 100 µm.

The Pu is primarily distributed between the Pu-rich agglomerates and the coating phase, which respectively contain about 35 and 65 % of the sample Pu. The average Pu/(U+Pu) content in the Pu-rich clusters is approximately 30 wt%. The Pu/(U+Pu) content in the coating phase varies, but is primarily in the 5-20 wt% range. For the U-rich agglomerates, however, the estimated Pu/(U+Pu) content is mostly lower than 1 wt%. Yet, the quantitative line scans (as seen in Figure 45) demonstrate that this low Pu content is also not constant within these regions and observed in the 0-4 wt% range close to the edges of the agglomerates. This can be attributed to the interdiffusion phenomenon that occurs during sintering between the U-rich agglomerates and the PuO_2 present in the coating phase. However, it is worth noting that (as observed here), the sintering conditions only allow for a partial interdiffusion, rather than achieving a complete interdiffusion of the cations.

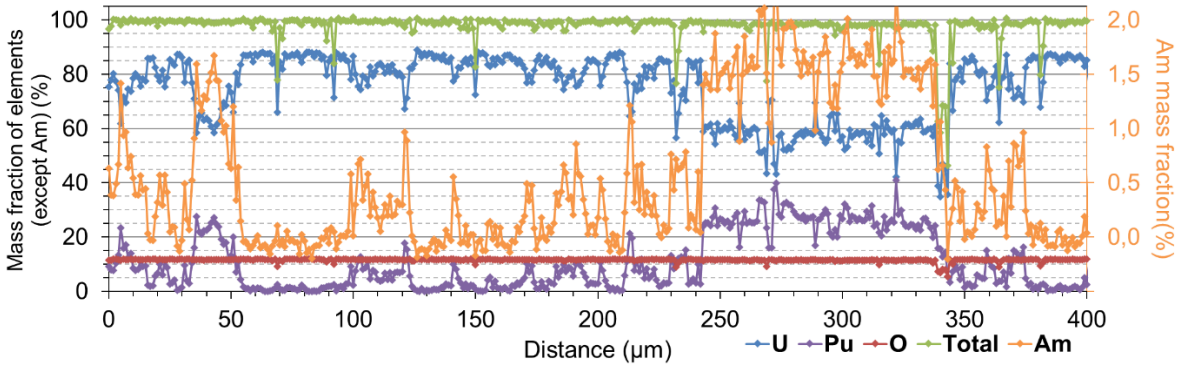

Figure 45 Quantitative line scan across the selected zone in the old MIMAS sample

The Pu content histograms derived from the EPMA images give another description of the distribution of this element in the sample, as shown in Figure 46. The histograms were constructed from the 1024 x 1024 pixels EPMA images of the samples before and after annealing. Three different regions, more or less identified as apparent local maxima, that can be distinguished in the histograms, centered at about 1, 9 and 29 wt%. These three phases are not discrete and separate peaks, but rather indicate a large Pu content distribution in each. Here, the comparison of the Pu content histograms of both aged and annealed samples also confirms that the thermal treatment used for the defect healing did not significantly modify the Pu spatial distribution. The latter is an essential observation before going any further in characterization of the samples.

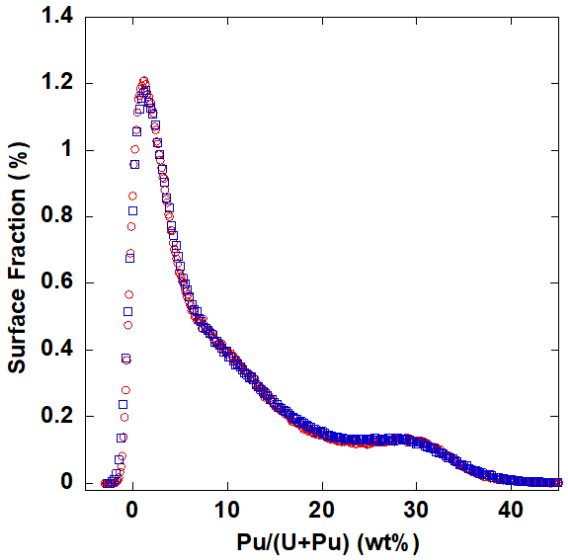

Figure 46 Pu content histograms extracted from the Pu distribution images. Blue and red open circles correspond to the aged and annealed samples, respectively.

It has to be noted that the apparent widths of the peaks of these phases observed in these histograms are not truthful representation of the plutonium distribution. One can see in particular that the U-rich agglomerates have only a low average Pu content. The width of this first distribution cannot give any relevant information about the sample as it is mostly due to experimental noise in the data (considering that an area with a low plutonium content give a low signal to noise ratio in a plutonium mapping and is thus affected by a large relative uncertainty).

3.1.2 The Capra4 and Trabant40 samples

3.1.2.1 Capra4

With a similar approach, the EPMA images of the Capra4 specimens before and after annealing are shown in Figure 47. Apparently, due to their fabrication process, which involves a single cogrinding step instead of the two-step process used for the MIMAS sample, the SFR samples exhibit a notably more homogeneous distribution of cations. Nevertheless, small UO_2 rich zones (in blue) are observed, as well as very small Pu hotspots (in red), where the Pu/(U+Pu) ratio can go up to 100%. The majority of the microstructure, is however, composed of a matrix with an average Pu/(U+Pu) content of 25-35% in mass.

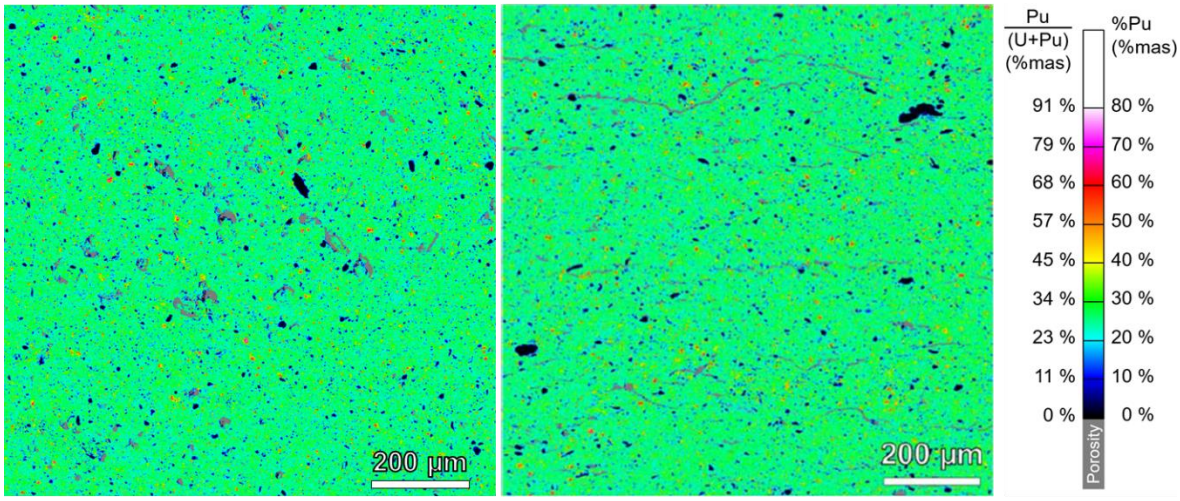

Figure 47 EPMA pseudo-quantified Pu large mapping in the annealed Capra4 specimen a) Annealed sample, b) Old sample

Figure 48 presents a quantitative line scan measured across the annealed Capra4 sample. The scans reveal the average contents of the cations in the fuel matrix as in the order of 20-25% for Pu, 55-65% for U, and 2-3% for Am, respectively. Following the Am lines, as expected, we can observe that the Am results coincide with that of Pu.

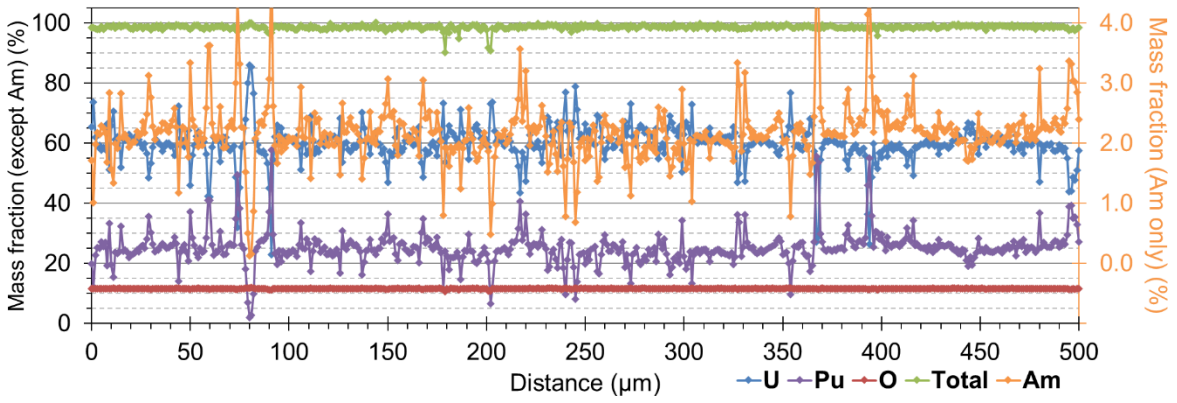

Figure 48 Quantitative line scan across the selected zone in the annealed Capra4 sample

Concerning the line scans, some deviations from a total mass fraction of 100% (as indicated by the green line in Figure 45 and Figure 48) are observed (following the green line). These are primarily due to the presence of porosity within the probed volume. It is also worth noting that the uncertainty associated with the Am mass fraction is higher than that of U or Pu. This is due to the absence of a suitable Am sample for use as a reference in this measurement.

Similarly to the case in the MIMAS sample, the comparison of the Pu content histograms of the samples before and after annealing are analyzed but the details are given in Section 3.1.2.3 where it is compared to the Trabant40 sample.

3.1.2.2 Trabant40

The EPMA image of the annealed Trabant40 sample is given in Figure 49. The microstructure of this particular sample resembles that of Capra4. This was expected, given that both samples were fabricated using a single-step co-grinding method. The main differences between the two, however, are the larger Pu content in the Trabant40 sample, which is centered at 38.5% Pu/(U+Pu) in the matrix phase and the scarcity of the UO_2 rich spots, which are fewer and smaller compared to the Capra4 as can be seen visually in Figure 47 and Figure 49. The details with the Pu content histogram of the sample before and after annealing is detailed in Section 3.1.2.3.

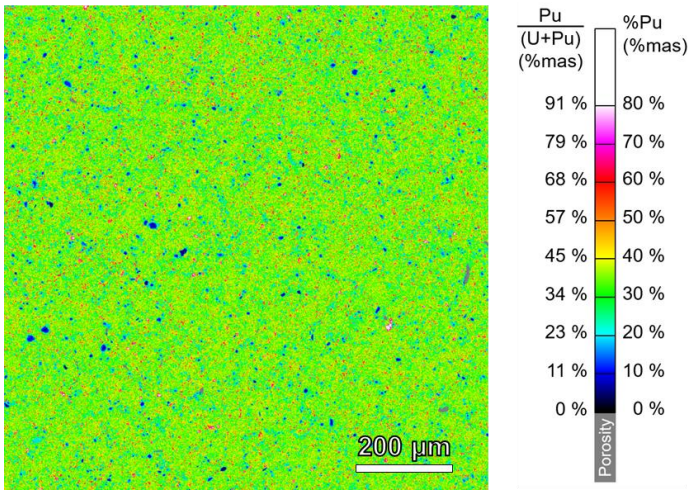

Figure 49 EPMA pseudo-quantified Pu large mapping in the annealed Trabant40 specimen

For the EPMA histogram of the aged sample, the measurements performed during the Pauline Fouquet-Metivier's thesis work [59] is used.

3.1.2.3 Comparison of the SFR samples

The comparison of the Pu content histograms of the two SFR type samples are shown in Figure 50. The log scale shows a more detailed look to the U-rich and the Pu-rich zones. Apart from the difference in plutonium content in the matrix (resulting from the difference between the samples' average compositions), the main difference between the two samples is that the U-rich zones exist in a larger quantity in Capra4 than in Trabant40. A peak centered close to a Pu/(U+Pu) content of 0 % is thus clearly visible in the log-scaled Capra4 red line.

The results from the fits (obtained using the method described in Appendix C.1.6) are also presented in these figures Figure 50 and Figure 51. The parameters obtained by the fit are presented in Table 13.

As evidenced by the logarithmic scale used for Figure 51, this fit is not reliable to reproduce the distributions in Pu-rich zones (Pu/(U+Pu+Am) ratios higher than 55 and 60 wt%, respectively for the Capra4 and the Trabant40 samples). For the Capra4 samples, the contribution centered on a Pu/(U+Pu+Am) ratio close to 0 wt.% (U-rich zones) is also obviously not reproduced by the fit. The area fractions corresponding to U-rich and Pu-rich zones were thus extracted from the residue of the fits. For Capra4 and Trabant40 samples, the Pu-rich zone area fractions were calculated as the cumulative residue for Pu/(U+Pu) ratios larger than 55 and 60 wt%, respectively. U-rich area fractions were calculated for Pu/(U+Pu) ratios lower than 10 wt%, for the Capra4 samples only, as this contribution was close to 0 % for the Trabant40 samples. The calculated values are also given in Table 13.

As evidenced by these parameters, even if both samples can be roughly described as composed of a single mode centered on a Pu content close to the sample average, they present some differences. The main mode of the distribution is larger in Trabant40 than in Capra4 in absolute values. When expressed

in relative values (normalized by the Pu content of the distribution center), these widths are similar in both samples. In terms of U-rich zones, they are only quantifiable from the histograms in the Capra4 sample but not for Trabant40 samples. Quantified Pu-rich zones are in similar proportions in both samples. As seen in the Figure 51 and Table 13, they have a larger Pu content in the Trabant40 sample (average Pu/(U+Pu+Am) content of 73 wt% against 66 wt%).

The data show only small discrepancies between the samples before ("old") and after annealing ("annealed"). This confirms that the annealing heat treatment did not change the cationic distribution in the samples.

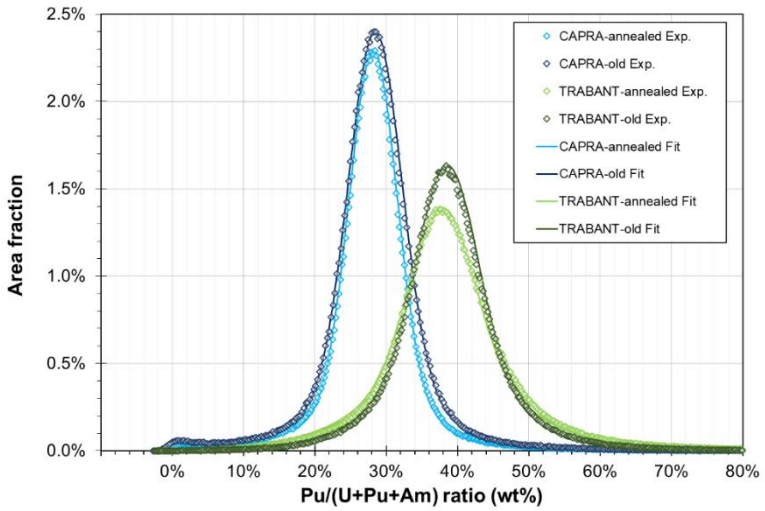

Figure 50 Comparison between the distributions extracted from the EPMA mappings of the old an annealed Capra4 and Trabant40 samples and fits performed with two Gaussian components both centered on the mode of the experiment data.

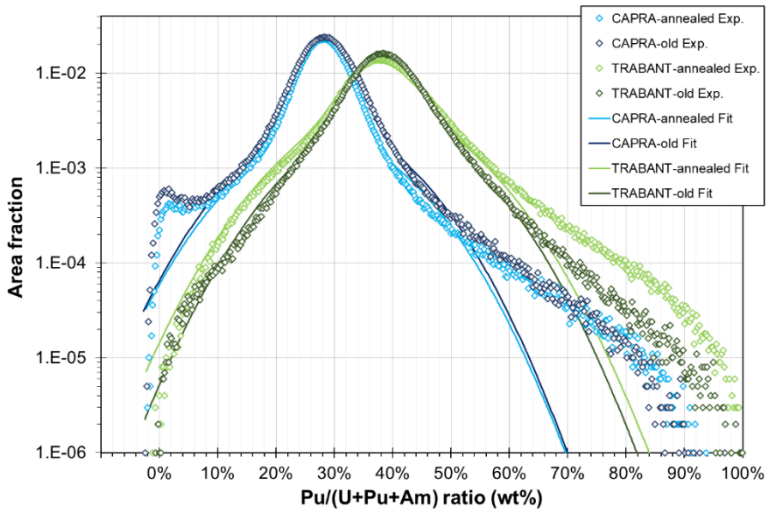

Figure 51 Comparison in logarithmic scale between the distributions extracted from the EPMA mappings of the old an annealed Capra4 and Trabant40 samples and fits performed with two Gaussian components both centered on the mode of the experiment data.

Table 13 Characteristics of the plutonium content distribution extracted from the EPMA mappings of the Capra4 and Trabant40 old and annealed samples. All vales given in wt% are Pu/(U+Pu+Am) weight ratios

Sample	Capra4		Trabant40	
	Old	Annealed	Old	Annealed
EPMA mapping average	28.3 wt%	28.1 wt%	38.7 wt%	39.0 wt%
First Gaussian component of the fit				
Weight	89%	91%	82%	73%
Center	28.4 wt%	28.2 wt%	38.5 wt%	37.9 wt%
FWHM	8.8 wt%	7.9 wt%	10.3 wt%	10.8 wt%
FWHM of the instrumental contribution	6.9 wt%	6.2 wt%	7.1 wt%	7.1 wt%
FWHM of the sample contribution	5.5 wt%	4.9 wt%	7.5 wt%	8.1 wt%
Relative FWHM of the sample contribution	31%	28%	27%	28%
Second Gaussian component of the fit				
Weight	11%	9%	18%	27%
Center	28.4 wt%	28.2 wt%	38.5 wt%	37.9 wt%
Fit FWHM	24.6 wt%	25.0 wt%	25.5 wt%	26.7 wt%
FWHM of the instrumental contribution	6.9 wt%	6.2 wt%	7.1 wt%	7.1 wt%
FWHM of the sample contribution	23.6 wt%	24.3 wt%	24.5 wt%	25.8 wt%
Relative FWHM of the sample contribution	87%	89%	66%	71%
U-rich zones	Pu/(U+Pu+Am) < 10 wt%		-	
Area fraction	1.0%	0.9%	-	-
Pu/(U+Pu+Am) content in U-rich zones	2.9 wt%	3.8 wt%	-	-
Pu-rich zones	Pu/(U+Pu+Am) > 55 wt%		Pu/(U+Pu+Am) > 60 wt%	
Area fraction	0.5%	0.5%	0.5%	1.6%
Pu/(U+Pu+Am) content in Pu-rich zones	65.0 wt%	66.0 wt%	73.0 wt%	72.4 wt%

For both SFR samples, the EPMA results suggest that probing the U and the Pu-rich hotspots will be rather difficult. The main reason behind this is that the size and plutonium (Pu) content of the hotspots can vary significantly, leading to uncertainties in the local plutonium content when attempting to investigate similar areas across different specimens. Additionally, the limited number of available spots (especially when compared to the Raman mapping dimensions) will make it challenging to employ statistical approaches. The focus for these materials is, hence, going to be the matrix phase, *i.e.* the green region observed in the corresponding EPMA images.

3.2XRD

The XRD patterns of the samples after annealing are shown and discussed in this section. For comparison purposes, a characteristic diffraction pattern of $UO_{2.0}$ is also systematically given in the same figures. Here, the lattice parameter of $UO_{2.0}$ has been determined to 5.4708 Å, which is in close agreement with

all previous works [20]. As expected, all XRD patterns obtained in this study shows that all samples can be indexed exclusively in the expected *Fm*-3*m* fcc structure, which will not be questioned after this point.

3.2.1 The MIMAS sample

The XRD pattern of the annealed MIMAS specimen is given in Figure 52, as well as that of the $UO_{2.0}$ pellet. As expected from the EPMA analysis, the diffraction line maxima are close to those observed for $UO_{2.0}$, see in particular the inset in the figure that focuses of the (422) reflection, for which the two $K\alpha_1$ and $K\alpha_2$ reflections are almost resolved. Nevertheless, on the first reading, these diffraction patterns are to be adjusted by at least two different sets of lines, see in particular the asymmetric broadening of the (422) reflection towards the high 2θ angles.

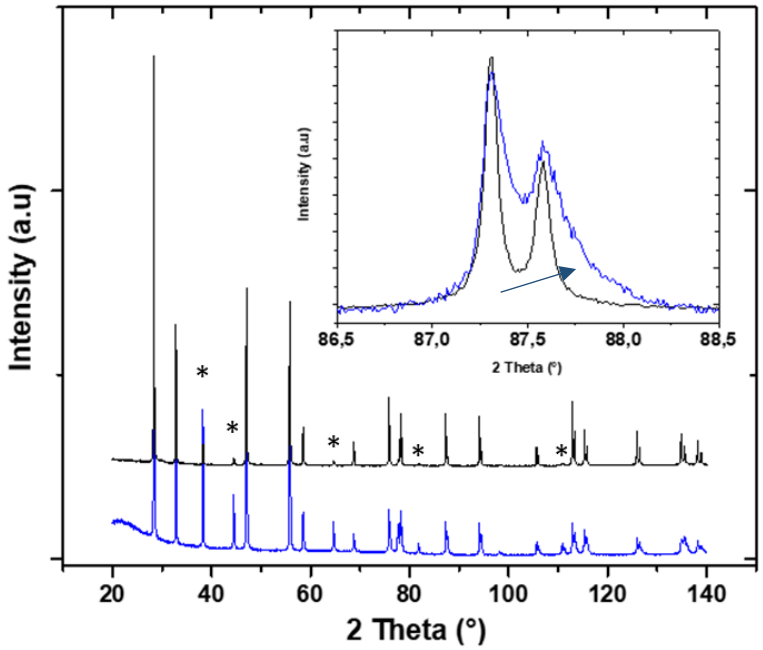

Figure 52 XRD diffraction patterns of the annealed MIMAS sample (blue line) and $UO_{2.0}$ (**black line**) specimens. The inset is a close-up on the (422) reflection. The asterisks indicate some of the reflections of the Au standard used for 2θ calibration purposes. The arrow indicates the asymmetry observed in the annealed MIMAS sample.

The observed asymmetry is towards higher angles, which suggests the presence of at least one phase with a smaller lattice parameter. This is indeed a clear indication of the existence of Pu-rich phases within the specimen. Considering the heterogeneous Pu content distribution evidenced by EPMA (see Figure 46), and the resulting heterogeneous distribution in lattice parameters, the observed line widths are not significantly increased when compared to that of the UO_2 reference sample. This is an indication that micro-strains, in other words a distribution of local lattice parameters, remain rather low on average in the sample.

For the refining of the diffraction patterns, several fluorite-type phases with close but different lattice parameters have to be used. Table 14 shows the influence of the number of phases used in the fitting quality of this sample. The use of only two phases proved to be insufficient to reproduce correctly the experimental data, with a residue systematically indicating the presence of at least one another phase, whereas adding a fourth phase did not significantly improve the fit. Thus, three phases were further used for the refinements, assuming that the three different lattice parameters correspond to three different "mean" Pu contents. Figure 53 shows an example of the fit obtained with these three phases.

Table 14 Influence of the number of phases on the fitting quality of the MIMAS sample XRD pattern

Number of phases in the fit	Rexp	Rwp	Rp	GoF
1	4.10	17.70	13.55	4.31
2	4.10	10.57	8.41	2.58
3	4.10	8.44	6.47	2.06
4	4.09	8.45	6.48	2.06

For the visualization of the accuracy of the fitting, diffraction lines were mostly examined in the high 2θ angle range of the diffraction pattern, for example that corresponding to the (422) reflection in the cubic structure, as shown in Figure 53. The doublet in the peaks is due to the Cu $K\alpha_1$ and Cu $K\alpha_2$ lines from the X-ray source. This figure confirms that the three-phase fit, described by the green, magenta and yellow curves in the figure, allows reproducing the experimental data, see in particular the residuals of the computation. The figure illustrates that each three phases exhibits different parameters, the linewidths in particular. These results are in good agreement with the EPMA results, reflecting the different Pu distributions in at least three phases as shown in Figure 46. Indeed, the clearest indicator is that the line corresponding to the UO_2 rich agglomerates has the smallest width compared to the other two, which is consistent with the homogeneous looking black agglomerates in the Pu mappings in Figure 44.

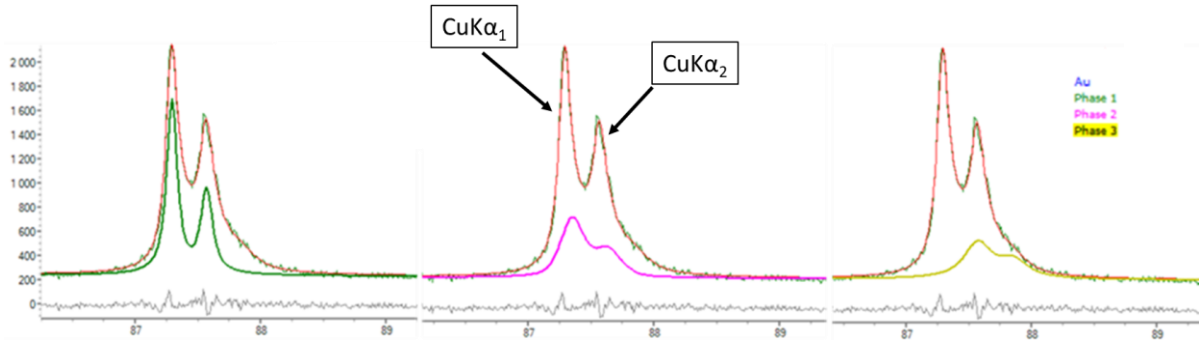

Figure 53 The (422) reflection of the MIMAS sample XRD pattern obtained with a Cu $K\alpha_1/K\alpha_2$ source (green line: experimental data, red line: global fit, grey line: residue). A) U-rich agglomerates, b) intermediate phase, c) Pu-rich agglomerates. Fitting is performed using the Topas software.

This way of proceeding is clearly a first approximation. As seen by EPMA, the MIMAS sample presents a wide distribution of Pu contents, thus resulting on a distribution of many lattice parameters that are very similar to each other. The fit with three phases allows for a relevant reproduction of the experimental data, but each phase is only an average of domains with close lattice parameters. This results in numerous possibilities for fitting with several closely related phases. Nevertheless, one can see that the lattice parameters obtained by this three-phase fit is satisfying, since it reproduces the trends extracted from the EPMA images and their associated composition histograms, see Table 15. Assuming oxygen stoichiometry, the "mean" Pu content of the three phases *i.e.* U-rich agglomerates, coating phase and Pu-rich agglomerates were found to be close to 0, 5.4 and 22 at%, respectively. One can see, however, that the composition of the Pu-rich agglomerates is somewhat low comparing to the EPMA values.

Because of the closeness of the three phases, once again for the three different phases, we only give the different lattice parameters with an accuracy of 0.001 Å for the U-rich phase but 0.003 Å for the other two. Using Eqn 1, these accuracies roughly respectively correspond to about 1 and 4 at% in terms of Pu/(U+Pu) content.

One should be aware that the Pu/(U+Pu) content used in Eqn 1 is an atomic ratio (at%.), while the EPMA results are presented as mass values (wt%). However, because of the small difference in average mass

between U and Pu isotopes, the difference between these two values is below the uncertainties of the extracted quantities and they can be roughly directly compared.

Table 15 Mean lattice parameters extracted from the refinement of the XRD patterns. The Pu/(U+Pu) content was computed for the annealed sample lattice parameters using Eqn 1.

	U-rich agglomerates (Å)	Coating phase (Å)	Pu-rich agglomerates (Å)
Annealed	5.470(1)	5.466(3)	5.454(3)
Pu/(U+Pu) (wt%)	≈ 0 (±1)	5.4 (±4)	22 (±4)
EPMA (wt%) Mean values	1 (±1)	9 (±1)	29 (±1)

3.2.2 Capra4 and Trabant40 samples

The diffraction patterns of the Capra4 and Trabant40 samples are shown in Figure 54, along with that of the UO_2 sample. Likewise, the inset in the figure focuses of the (422) reflection. One might think that analysis would be easier because the samples are much more homogeneous. Nevertheless, both Capra4 and Trabant40 display a minor peak near the anticipated position for UO_2, with the latter exhibiting a more pronounced peak in comparison. Furthermore, the primary peak in Capra4 diffraction pattern appears to have a symmetrical profile. In contrast, the Trabant40's pattern exhibits peculiar shoulders at both lower and higher angles, along with a pronounced midpoint between $K\alpha_1$ and $K\alpha_2$. These observations would suggest that Trabant40 exhibit a significantly lower crystallinity or a less uniform distribution of lattice parameters than Capra4, which is in contradiction with the EPMA results. Another explanation could originate from sampling, as only a small fraction of the material (lower than 100 mg) is used for the XRD analysis. This sample was not available in enough quantity to study this hypothesis, and its XRD will not be further analyzed in this section.

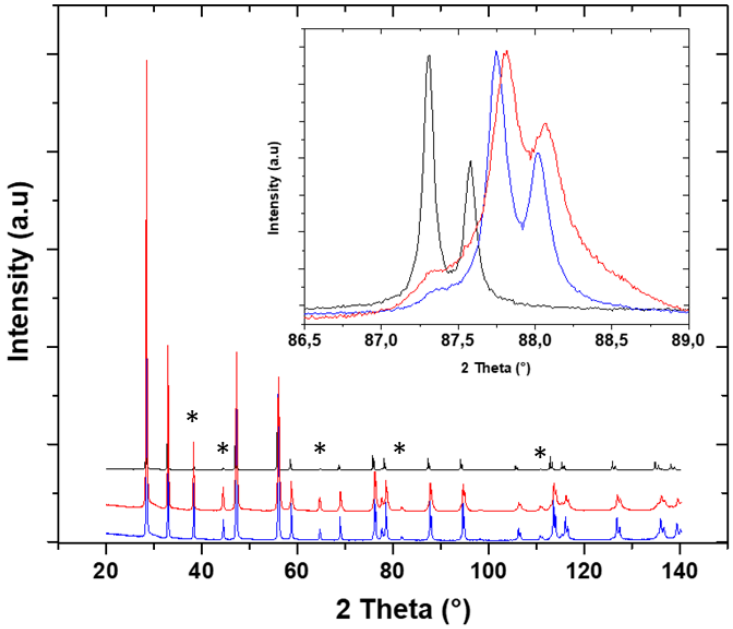

Figure 54 XRD diffraction patterns of the annealed Capra4 sample (blue line), annealed Trabant40 sample (red line) and $UO_{2.0}$ (**black line**) specimens. The inset is a close-up on the (422) reflection. The asterisks indicate some of the reflections of the Au standard used for 2θ calibration purposes

A similar approach to that employed for the MIMAS sample was used to fit the XRD patterns of the Capra4 and Trabant40 samples. Table 16 displays the influence of adding phases during the XRD pattern fitting, with up to four phases. Taking into account the quality of the fit and information derived from EPMA data,

it was determined that employing three phases for the fitting yielded the best results. While a small improvement in fitting quality was observed upon adding a fourth phase, it did not align with the EPMA data. These three phases corresponded to the U-rich spots, Pu-rich spots, and the matrix phase, whose traces in the fitting are shown in Figure 55. However, for this particular sample, only the matrix phase will be considered in the XRD analysis.

Table 16 Influence of the number of phases on the fitting quality of the Capra4 sample XRD pattern

Number of phases in the fit	Rexp	Rwp	Rp	GoF
1	4.30	13.76	10.30	3.20
2	4.30	10.63	7.71	2.47
3	4.29	9.42	6.90	2.20
4	4.29	9.38	6.80	2.18

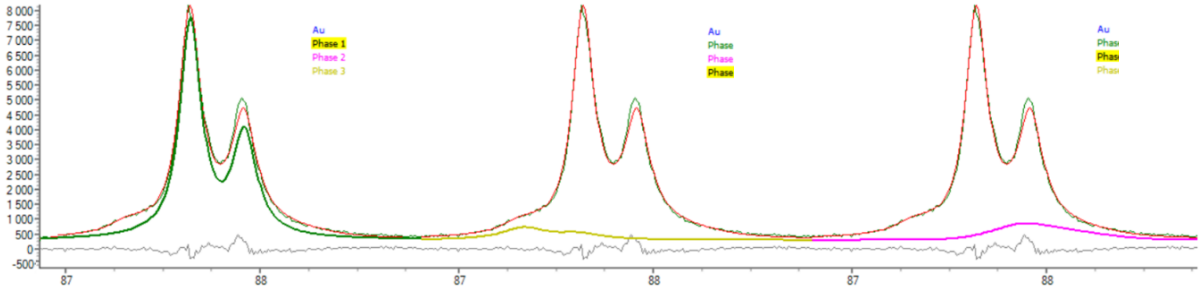

Figure 55 The (422) reflection of the Capra4 sample XRD pattern obtained with a Cu Kα1/Kα2 source (green line: experimental data, red line: global fit, grey line: residue). a) The matrix phase, b) U-rich spots, c) Pu-rich spots. Fitting is performed using the Topas software

The main results of the fit are summarized in Table 17. For both samples, there is a relatively large discrepancy between the Pu/(U+Pu) contents determined from EPMA and XRD measurements, notably for Capra4, for which it is close to 3 wt%. The explanation of this relatively large difference between the two outcomes are not settled clearly. This discrepancy could be related to the relatively high Am content (^{241}Am/(Pu+Am) ratio of 8.3%) in the Capra4 sample which will have an influence in the lattice parameter obtained with this sample.

Table 17 Mean lattice parameters obtained from the refinement of the XRD patterns for both the Capra4 and Trabant40 samples, alongside the corresponding values derived from EPMA. The Pu/(U+Pu) content was computed for the annealed sample lattice parameters using Eq. 1.

	Capra4 Matrix Phase	Trabant40 Matrix phase
Annealed lattice parameter (Å)	5.446(1)	5.443(1)
Pu/(U+Pu) calculated from the lattice parameter (wt%)	31.6 ±1	36.2±1
Pu/(U+Pu+Am) (wt%) obtained from EPMA for the matrix phase	28.2±1	37.9±1

Here the XRD Pu/(U+Pu) content is calculated using Vegard's law (Eqn 1) under the assumption of O/M = 2.00. This calculation does not include the effect of the Am content. The lattice parameter of AmO_2 reported as 5.3755 ± 0.0005 Å [140] in the literature, suggesting that the presence of Am will lower the lattice parameter of the solid solution. Therefore, if the Capra4 sample had contained no Am, the lattice parameter obtained from XRD would be larger, resulting a lower calculated Pu/(U+Pu) content. Therefore, the Am content in this sample is at least partially responsible for the 3 wt% discrepancy between the calculated Pu/(U+Pu) content values obtained from EPMA and XRD measurements.

3.3Raman Spectroscopy, Raman imaging

The expected spectrum of the $(U,Pu)O_2$ solid solution is *a priori* particularly simple, as only one single T_{2g} symmetry mode is expected. It was shown in Section 2.2.3.5.2 that the frequency of this mode, in the absence of other external stresses, is sensitive to the Pu content. This means that it will be essential to have as precise information as possible on the frequency of this mode. As already mentioned, this information is already available in part from the literature, in particular in the Pu/(U+Pu) 0 - 40 at% range [97], [99], [129], [138]. However, we now have access to additional samples that can assist us in enhancing the existing data.

As already mentioned, all the results obtained in this work were exclusively acquired using an excitation wavelength of 532 nm. As is already know from the recent literature, strong resonance effects are expected at this excitation wavelength [100], [141]. This wavelength effect will be explained gradually, especially in the final chapter of this document. As we shall see, the effect of the excitation wavelength can seem drastic.

Throughout this work, Raman imaging was employed, necessitating the acquisition of a substantial volume of data. The results obtained will be utilized well beyond a simple visualization aspect. Again, this chapter is intended to be completely descriptive for the annealed samples; hence, the main discussion is postponed to the last chapter of this document.

3.3.1 Analysis using a 532 nm excitation. Some consequences

Throughout this work, we have deliberately chosen to use only one excitation wavelength, *i.e*. 532 nm. This choice is not without consequences, which will be addressed progressively in this chapter. To initiate the discussion, the spectra of UO_2 and PuO_2 are displayed in Figure 56.

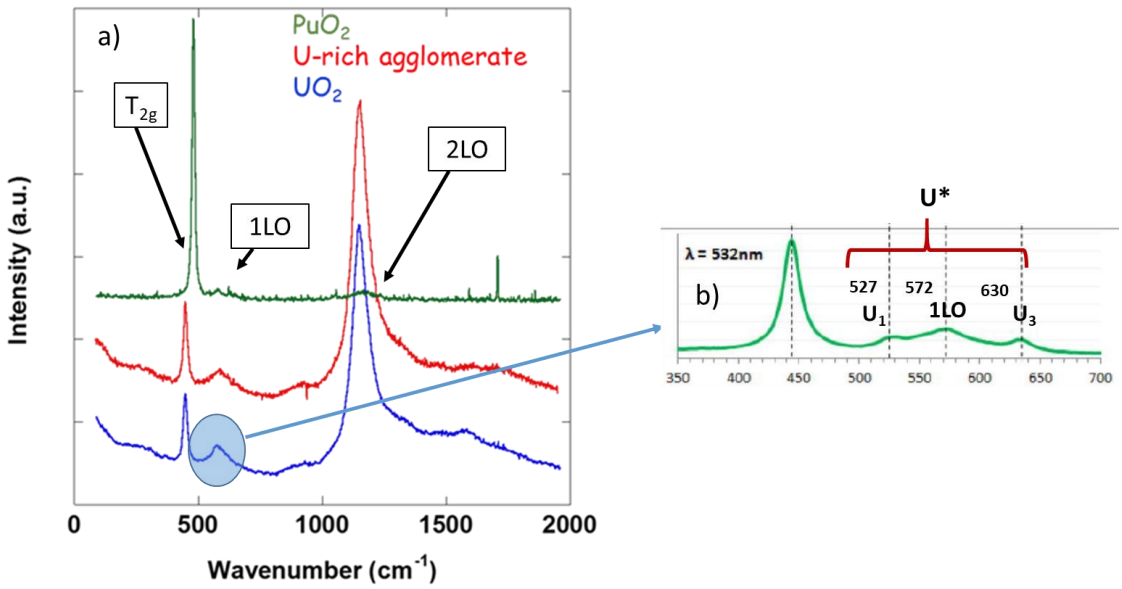

Figure 56 Examples of Raman spectra in the fluorite structures a) The full spectra: Green line: recorded in PuO_2 rich zone, red line: recorded within a U-rich agglomerate of the annealed MIMAS sample. **Blue** line: characteristic Raman spectrum of stoichiometric $UO_{2.0}$, recorded using similar acquisition conditions on a single crystal. The peak at ≈ 1700cm^{-1} is due to Ne used for calibration purposes (see Section C.3.2 of Appendix C), b) Close up region to the first order spectrum showing the U* region (defect bands)

This figure immediately shows that the spectrum obtained for PuO_2 corresponds to what one would expect: a single mode is dominantly observed, *i.e.* the Raman-active mode of the fluorite structure with T_{2g} symmetry (~475 cm^{-1}), while the other very strong band (~1150 cm^{-1}) can be interpreted in part as second-order signals. The spectra obtained for UO_2 appear much more complex than what is foreseen by group theory considerations. Two spectra are displayed for UO_2, corresponding respectively to pure UO_2 (blue trace) and a UO_2-rich agglomerate (red trace) in the MIMAS sample. Apparently, the two spectra match quite perfectly and correspond in every respect to those found in literature obtained with an excitation in the green spectral range (514 or 532 nm).

From Figure 56 up to 1200 cm^{-1}, five different bands and/or shoulders may be observed at about 445, 535, 576, 630, and 1150 cm^{-1}. We will not discuss the other signals (weak maxima at about 250, 900, and 1300 cm^{-1}) that most probably arise from second- or higher-order scattering. Moreover, their intensities are too weak to be used for the construction of the Raman images, as we shall see below.

The first band is the Raman-allowed first-order mode with T_{2g} symmetry, while the prominent line at about 1150 cm^{-1} is known to be a specific second-order feature. As this line is the second of a series of six lines (overtones) peaking at about 575, 1150, 1725, 2312, 2910, and 3470 cm^{-1} [100], it is thus the first overtone of the 575 cm^{-1} line. This frequency (575 cm^{-1}) corresponds perfectly to the expected Raman-forbidden, IR-allowed LO line, see, for example, the computed dispersion curves available in Refs [142]–[144] and the forbidden scattering explanation in the section 2.2.3.4 of Chapter 2. Briefly, the line at 1150 cm^{-1} will be labeled 2LO, as it is the first overtone (resonant) mode of the IR active 1LO band. In the vicinity of the 1LO band, however, two distinct shoulders are noticeable which are at 530 and 630 cm^{-1}. These two bands, together with the 1LO band are sometimes referred to, as a whole, as the U* line, or as the triplet defect band (U_1, U_2, and U_3, respectively), see Figure 56b. The origin of these two shoulders on both sides of the 1LO mode in UO_2 and UO_2-based mixed oxides is still being debated [31], [32], [104], [129], [138], [141], [145], [72], [95]–[100], [102]. The presence of the Raman-forbidden 1LO mode in the spectra is usually explained by the introduction of structural defects that lead to the loss of the inversion center of the fluorite lattice (violation of the mutual exclusion rule). Again, this point will be discussed later in this document.

We now need to investigate how these signals evolve in the $(U,Pu)O_2$ solid solution. For that purpose, we need samples covering the whole Pu concentration range. Here, we use some of the spectra available for the MIMAS, Capra4 and Trabant40 samples. We also use other samples with a higher Pu content, available from another project in the laboratory [139]. At this point, we do not need to know Pu contents with a high accuracy: just an order of magnitude within a few wt.% uncertainty is necessary. Finally, we need to examine the effect of the excitation wavelength. To our knowledge only one study is available in the literature [129]. It covers the 0 - 46 wt% Pu/(U+Pu) concentration range, with spectra recorded at 647 nm. All these spectra are given in Figure 57.

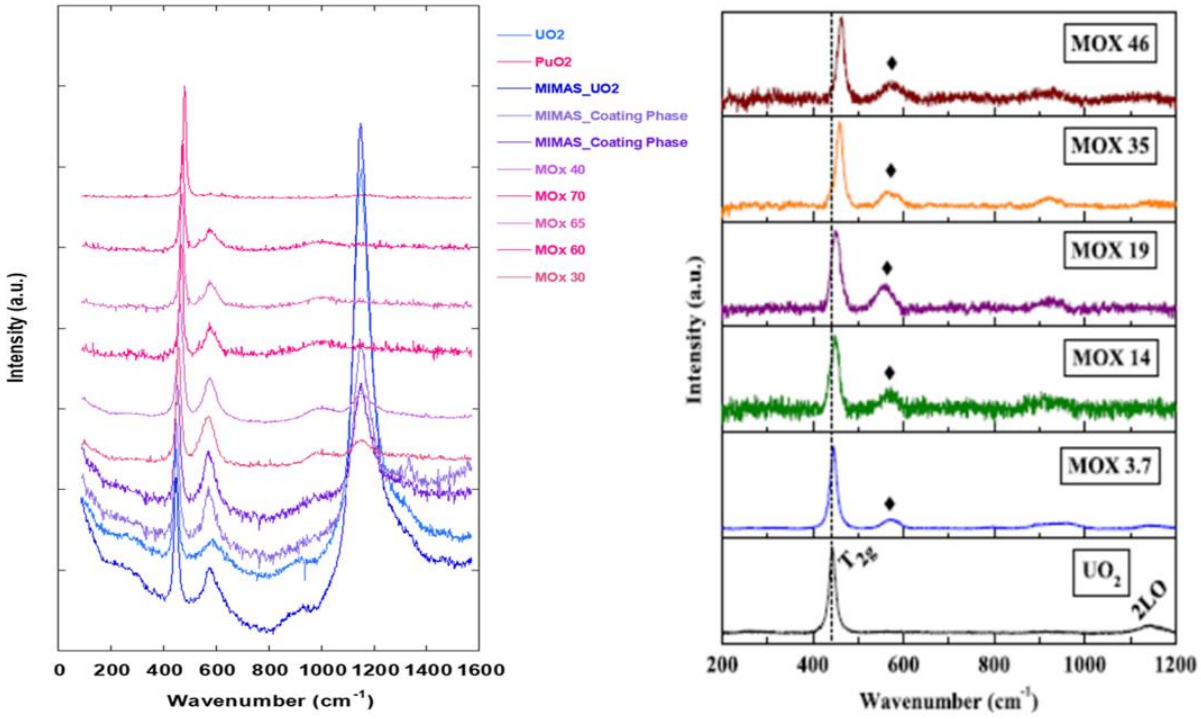

Figure 57 Raman spectra recorded at different Pu/(U+Pu) contents at, a) a 532 nm and , b), a 647 nm excitation wavelength (Elorrieta's work) [129] (in these two figures, the spectra have been roughly normalized to the amplitude of the T_{2g} mode).

Several conclusions can be drawn from the evolution of the spectra with the Pu content:

- the 2LO mode is not observed at 647 nm, regardless of the Pu content,
- the 2LO mode vanishes progressively with the Pu content at 532 nm,
- the U* group of lines is not clearly observed in the UO_2 spectrum recorded at 647 nm, whereas it is observed at 532 nm,
- the U* group of lines seems to be observed whatever the Pu content, within the exception of pure and annealed PuO_2.
- A closer examination of the spectra tends to indicate some broadening of the T_{2g} mode for Pu compositions quite far from any of the two endmembers.

These observations can be explained in part considering that the excitation is exactly resonant for UO_2 at 532 nm. Again, we will come back to this in the final chapter of this document. As a result, the analysis at 532 nm will therefore be less straightforward than might have been anticipated.

3.3.2 Extraction of the Pu content. Main hypothesis and their consequences.

As discussed in Section 2.2.3.5.2, the Pu content of $(U,Pu)O_2$ solid solutions can be extracted from their Raman spectra. [99]. Here, the key point is that this quantity can be derived at the µm scale, *i.e.* at a relevant scale for the study of agglomerates present in these samples. This information is therefore

comparable to what was obtained in the EPMA analysis. As shown in Figure 56, the spectra of the $(U,Pu)O_2$ solid solution exhibit a one-mode behavior, *i.e.* a continuous evolution of the spectra between those of the two endmembers. Therefore, the frequency of the T_{2g} mode depends on the Pu content, which is what is discussed below.

Again, little work has been devoted to the quantification of this dependency [99], [129], [138]. The main results are summarized in Figure 58. In the figure, additional data points were added, in the high Pu content range, see the red full circles. The T_{2g} position we obtained for the lower Pu contents were not added, as they were consistent with those previously reported.

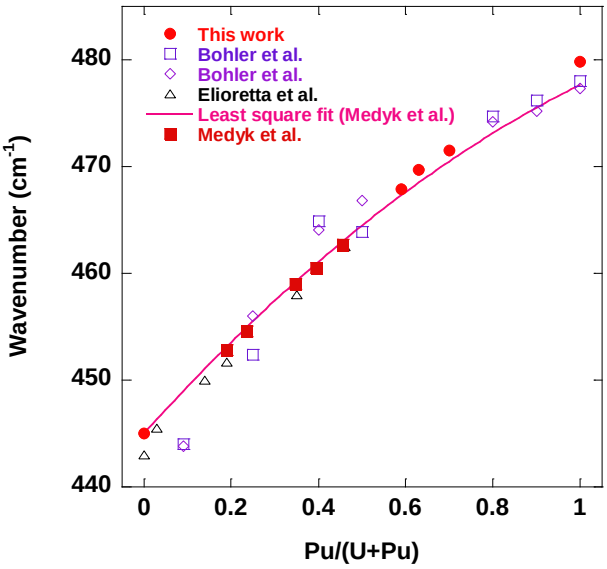

Figure 58 T_{2g} position recorded for the $(U,Pu)O_{2.00}$ samples as a function of the Pu/(U+Pu+Am) content (mol.%), combination with the literature and this work

In the figure, all symbols correspond to experimental data, while the solid line corresponds to the quadratic fit of the data, as proposed by Medyk *et al.* [99]. The figure provides a number of information:

- (i) a rather strong scattering of the data points,
- (ii) the presence of data points both above and below the mean trend,
- (iii) a marked difference (upshift) from a simple Vegard's law-like behavior.

First of all, how to explain this large scatter in the data? Based on the references used to draw Figure 58, apparently the Pu contents were mainly derived from the XRD patterns. Although there is some uncertainty in the determination of the lattice parameter, it does not allow for a comprehensive explanation of the dispersion. To go further in the discussion, one can first mention the effects of deviation from the exact stoichiometry. Again, they were described and discussed in [99]. For the $(U,Pu)O_2$ solid solution, hypo-stoichiometry is known to induce an increase of the lattice parameter. This effect results in a downshift of the T_{2g} frequency of more than two reciprocal centimeters (cm^{-1}) for a deviation from the exact stoichiometry close to 0.02. In the same spirit, one can evoke self-irradiation effects that lead to an increase of the lattice parameter. Again, a downshift of the T_{2g} mode is expected, although it was not clearly observed in [99]. On the other hand, at this stage, it is difficult (or even impossible) to explain the presence of experimental data well beyond the average trend. We will therefore have to accept a certain uncertainty on the calculated Pu content, which can be quantified with some margin to about +/- 1 wt%, or even more.

Still assuming oxygen stoichiometry, the mean trend for the T_{2g} band position can be fitted with a quadratic function, according to:

$$\omega(U_{1-y}Pu_yO_2) = -12.21256\times10^{-3} \times y^2 + 0.452 \times y + 445.0 \quad \text{Eqn (51)}$$

Where y is the Pu/(U+Pu) molar ratio. This equation may not be completely representative of the results for the highest Pu contents, especially for y above 50 at%. Nevertheless, we will use it as it is. The analysis of our results will enable us to discuss it in more details, in particular in the 0 - 40 at% composition range.

This quadratic correlation was derived for samples whose Am/cations contents were in the 0.5–1.5 at% range, close to the values effectively found for the samples considered in this study (about 2 at% in the Pu-rich agglomerates of the MIMAS sample or in the matrix phase of the SFR sample. Due to this very low content, the Am impact on the T_{2g} mode frequency can be safely ignored here; it can be considered that the quadratic equation refers to an Am-free material [146].

Finally, as already mentioned, there is an apparent bowing in the frequency of the T_{2g} mode *vs* composition. The deviation from a simple linear law seems to be maximum for Pu/(U+Pu) contents close to about 50 at%, where it is about 2.5 cm^{-1}. Such a deviation will also be discussed in the Chapter 5.

3.3.3 Raman Imaging

From Figure 59, it appeared that four different spectral features can be used to construct the Raman images: the frequency and width of the T_{2g} mode as well as the intensities of the U* and 2LO bands. In what follows, the intensity of both the U* and 2LO modes will be normalized to the intensity of the T_{2g} mode, which is acceptable according to the low polarization dependence of the spectrometer used in this work. These intensity ratios will be referred to as U^*/T_{2g} and $2LO/T_{2g}$ respectively.

During the analysis of the Raman images, the T_{2g} mode frequency in particular, we continue to consider stoichiometric samples. More, the samples are now assumed “defect-free” and “strain-free,” still for simplicity and comparison purposes. One can mention that this is a rather crude approximation as local micro-strains are unavoidable for this type of ceramics, especially close to the grain boundaries. However, both assumptions and approximations are necessary to enable the conversion of the T_{2g} mode frequency in terms of composition.

As mentioned in the experimental part, the size of the images (70 × 70 µm) and a point of spacing (2 µm) were chosen to analyze a representative area of the samples, including the different agglomerates detected in the corresponding EPMA images, while looking for a compromise between acquisition time and signal quality.

3.3.3.1 Analysis of the MIMAS sample

The four different Raman images of the MIMAS sample are given in Figure 59. The region selected for the Raman images was earlier analyzed by EPMA.

First, one can observe from Figure 59 that three of the Raman images immediately allow identifying the different phases in the microstructure:

- Figure 59 (a) *i.e.*, the map of the T_{2g} mode frequency, directly translated in terms of Pu/(U+Pu) content, here given as a percentage,
- Figure 59 (b) *i.e.*, the map of the line width of the T_{2g} line
- Figure 59 (d) *i.e.*, the map of the $2LO/T_{2g}$ intensity ratio maps.

Here these Raman images give the first trends regarding the sample. The different agglomerates already observed in the EPMA images are clearly detected. Accepting the simplifying assumptions given above, one can see that Pu/(U+Pu) concentrations are low, or even close to zero for the U-rich agglomerates

and about 30 at% for the Pu-rich agglomerates. In the last case, small clusters with higher concentrations are also evidenced. On the other hand, one can see that the Pu content is not completely homogeneous in the different agglomerates, as evidenced by EPMA. Furthermore, as expected from mass disorder considerations, the width of the T_{2g} mode is sensitive to the Pu content, even if the T_{2g} mode width image does not exhibit a very strong contrast. Quite surprisingly, the U^*/T_{2g} intensity ratio tends to highlight the coating phase. This could be (as a first hypothesis) due to the increased disorder in the crystal with the increased Pu content which will result in an increase of the U* intensity and a broadening of the T_{2g} band. Moreover, it appears that further increase of the Pu content leads to a reduction of U* intensity, particularly noticeable within the Pu-rich agglomerates. This phenomenon will be explored in a more detail in the last chapter concerning the effects of the resonance phenomenon.

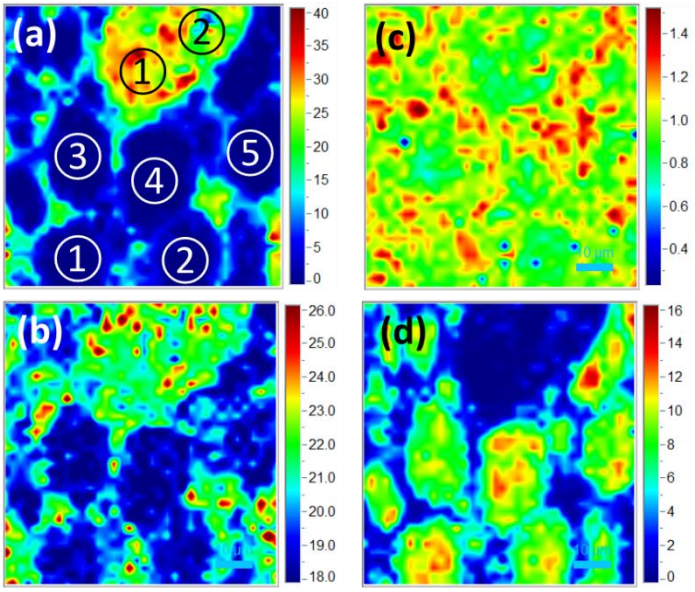

Figure 59 Images constructed from the Raman mapping of the annealed MIMAS sample. The size of the images is 70 x 70 μm^2. (a): frequency of the T_{2g} mode, translated in terms of Pu/(U+Pu) content (at%). (b): line width of the T_{2g} mode (cm^{-1}). (c): U^*/T_{2g} intensity ratio. (d): $2LO/T_{2g}$ intensity ratio. The white and black circles in (a) indicate the agglomerates or regions for which spectra were averaged.

The Pu content histogram obtained from the Raman image is compared to that obtained from the EPMA analysis in Figure 60. One can see that the agreement between the two data sets is satisfactory: the shape of the EPMA histogram is rather well reproduced. Hence, the quite small Raman image dimensions compared to EPMA are sufficient to observe the main characteristics of the sample microstructure. More, Eqn 51 effectively provides a description of the data in terms of Pu composition, within an acceptable uncertainty range.

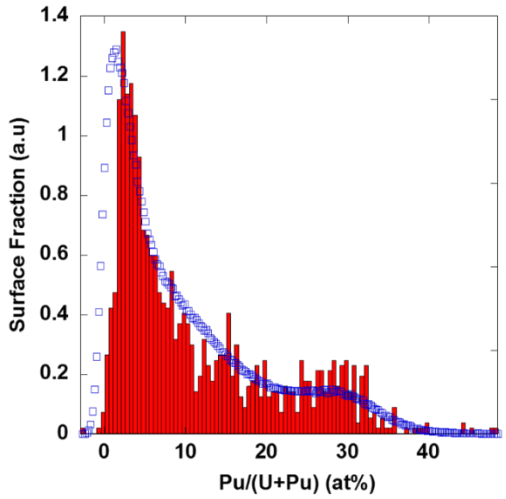

Figure 60 Pu content histograms extracted from the EPMA (blue circles) and Raman (red bar graph) images.

Both methods (Raman and EPMA) give an average Pu/(U+Pu) content in the overall sample of ≈ 10%. The small differences between the two histograms are not completely surprising considering the uncertainties of the two measurements, the scale of the cationic heterogeneities in the sample and the comparatively small size of the Raman mapping. Other reasons, most probably of more fundamental origins, can also be evoked to understand the slight differences between the two methods, lattice strains in particular, or the very low statistics in the low Pu contents in the EPMA data.

Another way to analyze the data sets is to plot the width, U^*/T_{2g} and $2LO/T_{2g}$ parameters determined for each pixel as a function of the Pu content calculated from the T_{2g} position of that pixel. The 2LO mode frequency can also be examined in this way. Thus, one can examine the evolution of those parameters, at least their mean trends, as a function of the Pu content. In other words, the evolution of these quantities can be completely examined in the 0 – 40 wt% Pu/(U+Pu) concentration range using a single sample to analyze the effects of Pu substitution. We will see that such an approach enables a better quantification of the self-irradiation effects. The main trends are given in the Figure 61 and Figure 62.

First the evolutions of the $2LO/T_{2g}$ and U^*/T_{2g} intensity ratios as a function of the Pu content are given in Figure 61a and Figure 61b, respectively. For both data sets, some spread is observed, unavoidable here because of the heterogeneity of the sample, the assumptions used and the short acquisition time of the individual spectra. Nevertheless, rather clear trends are observed. In particular, Figure 61b shows a strong variation of the intensity of the 2LO mode as a function of Pu content. The intensity of this mode seems to be the highest for the lowest Pu contents, and decreases gradually thereafter. Above a Pu/(U+Pu) content of about 15 wt%, the 2LO mode intensity is quite low and its decrease tends to slow down, while above 30%, it is very close to 0, the 2LO band then being almost not distinguishable in the individual spectra anymore. The behavior of the U* mode seems to be different as it tends to remain almost constant independently of the Pu content. One can also see that its dispersion is very large for a given Pu content. A similar finding was already obtained in Figure 59c, but these two figures clearly quantify the data.

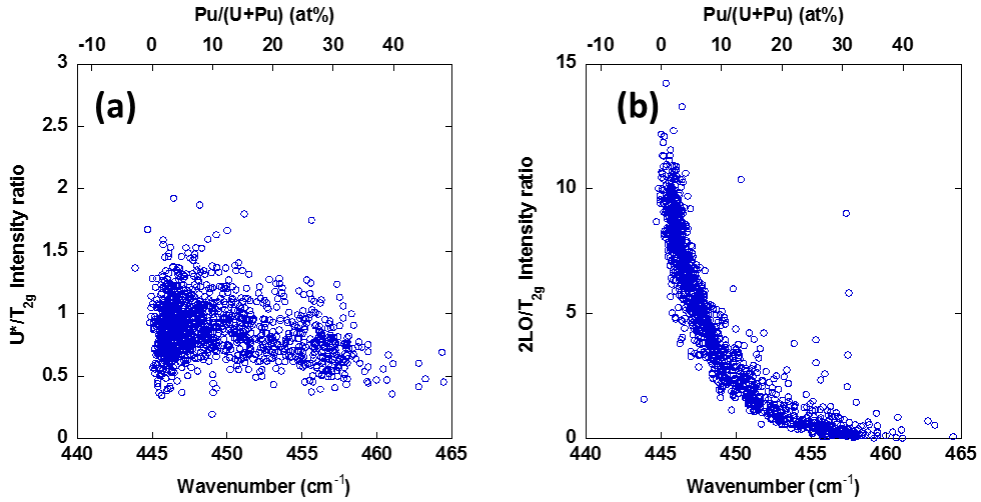

Figure 61: evolution of (a) the U^*/T_{2g} and (b) the $2LO/T_{2g}$ intensity ratios vs the Pu/(U+Pu) content or the T_{2g} mode frequency in the annealed MIMAS sample

In a similar way, one can focus on the evolution of two other variables, the T_{2g} mode width and the 2LO mode frequency, see Figure 62a and Figure 62b. A small broadening of the T_{2g} mode is observed as a function of the Pu content, which probably reflects the mass disorder introduced by the Pu doping, see Figure 62. Indeed, this line width was found to be close to 13 cm^{-1} for a freshly annealed $PuO_{2.0}$ sample on the same experimental setup. It should be noted here that only the trend is to be considered, the absolute values of the line widths depending on the spectrometer used and the measurement conditions. From Figure 62b, a small upshift of the 2LO mode, of about 3 cm^{-1} for a Pu/(U+Pu) content close to 30 wt%, can be discussed. This upshift remains weak compared to that of the T_{2g} mode, close to 12 cm^{-1} for a similar Pu content. The 2LO mode is effectively peaking at about 1160 cm^{-1} for PuO_2. One consequence of this smaller frequency variation is that it will be almost unobservable on the 1LO mode, which is what is generally observed.

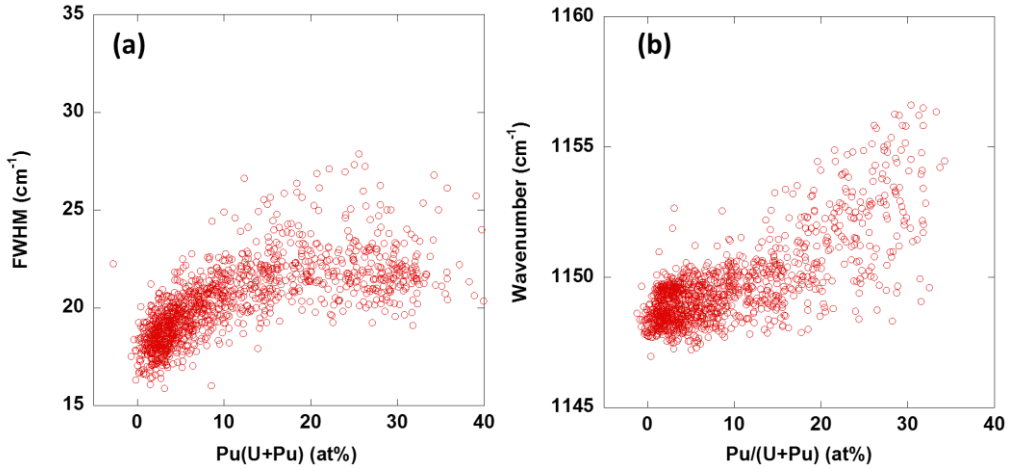

Figure 62: evolution of (a) the width of the T_{2g} mode and (b) the frequency of the 2LO mode in the annealed MIMAS sample vs the Pu content

To retrieve the last information, it is necessary to analyze the spectra in more details. For such a purpose, it first seems convenient to use average spectra obtained on predefined areas, or particular agglomerates that were already evidenced and identified in the frequency images, at least to increase the signal to noise ratio of the signals. These agglomerates are highlighted in Figure 59. Examples of such averaged spectra are given in Figure 63. They correspond in all respects to those already shown in Figure 57 for similar compositions.

Focusing on the U- and Pu-rich agglomerates, one can see that these spectra are more or less constant from one agglomerate to another. In addition to some more heterogeneity effects within the agglomerates,

one can also detect a small amount of carbon pollution that is detected in the second-order region. It seems to be mostly observed for Pu-rich agglomerates. The U* mode cannot be clearly resolved into three components.

Further analysis of these spectra can be achieved by line fitting, which will not be performed in this chapter but will be extensively used in the next chapter, as an attempt to analyze the self-irradiation effects.

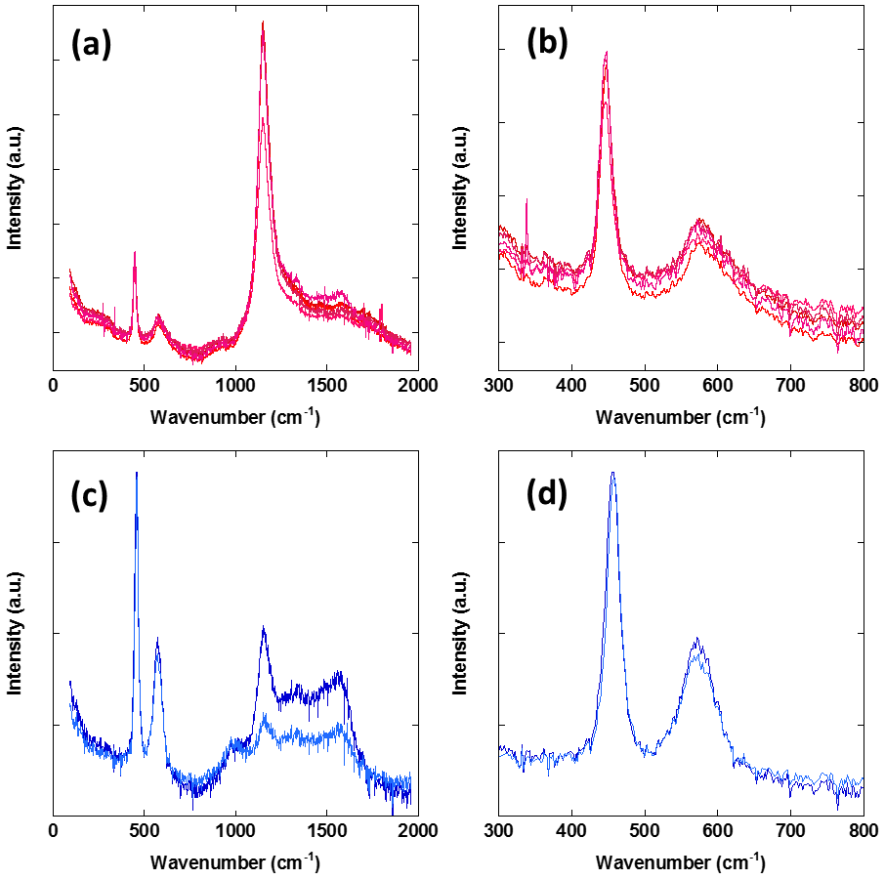

Figure 63 Examples of averaged Raman spectra for Pu (a and b) and U- rich (c and d) agglomerates. The zones from which these signals have been extracted are indicated in Figure 59. Reddish lines correspond to the U-rich agglomerates; bluish line correspond to the Pu-rich agglomerates. (a) and (c): complete spectra, between ≈ 100 and ≈ 2000 cm^{-1}. (b) and (d): close-up of the first order region.

3.3.3.2 Capra4 and Trabant40 Samples

Due to their similar manufacturing process (single step co-grinding), the microstructures of the Capra4 and Trabant40 samples are quite similar, as shown by the EPMA images. We will therefore examine them simultaneously. The corresponding Raman images are first given in Figure 64 and Figure 65. As shown in the composition images (derived from the T_{2g} in images (a) of both figures), these SFR-type samples are mostly made of a rather homogeneous matrix phase. However, one can still observe U- and Pu- rich clusters (or rather spots). As for the MIMAS sample, these clusters are identified using the mappings of the T_{2g} position (Figure 64a and Figure 65a) and of the $2LO/T_{2g}$ intensity ratio (Figure 64d and Figure 65d). In this case though (and contrarily to the MIMAS sample), the information contained in the T_{2g} width mapping (Figure 64b and Figure 65b) does not seem very efficient to locate the U- or Pu-rich clusters, whereas that of the U^*/T_{2g} intensity ratio (Figure 64c and Figure 65c) is somewhat sensitive to the presence of U-rich clusters.

At first glance, the images obtained for Trabant40 may seem more contrasted than those obtained for Capra4, especially in the matrix phase. However, as the comparison of EPMA- and Raman-composition histograms show, this is more a false color scaling effect than a real composition effect. A comparison of

these two histograms is shown in Figure 66. These two histograms describe the two samples in a fairly similar way. The EPMA histograms appear systematically wider than the Raman histograms, but this is mostly due to the instrumental contribution to that width, as discussed in Section 3.1.2.3 and Appendix C.1.6. When this instrumental contribution is removed, the difference in FWHM (tabulated in Table 18) between the EPMA histogram and the Raman histogram is less than 0.5 wt% in Pu/(U+Pu) ratio. The zones analyzed by Raman thus appears to be fairly representative of the overall sample as analyzed by EPMA.

Table 18 The width of the Raman and EPMA histograms of the SFR samples calculated after fitting with Gaussian function

Sample	Sample contribution to the EPMA histogram FWHM	Raman histogram FWHM
Capra4	8.6±0.2	4.3±0.2
Trabant40	12.1±0.2	7.7±0.2

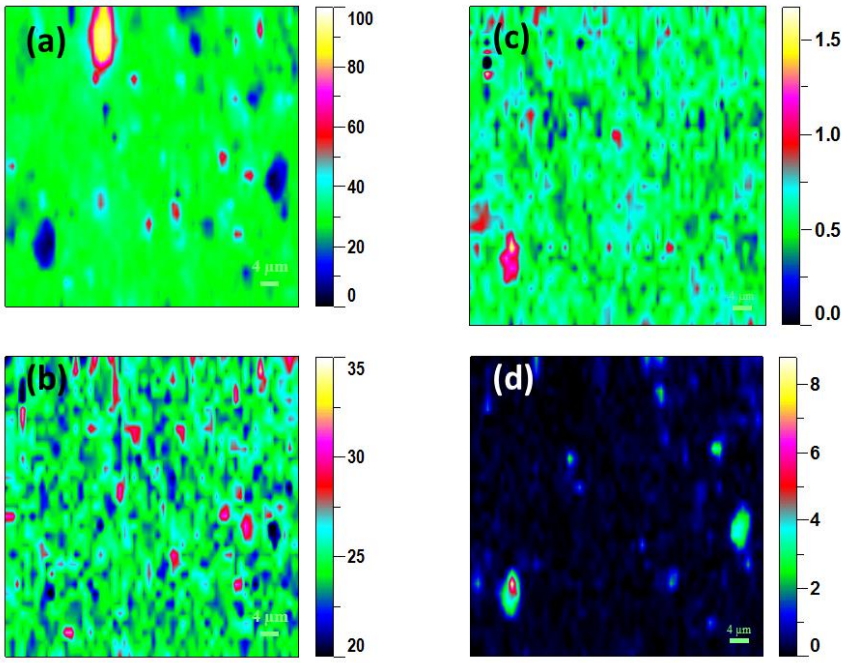

Figure 64 Images constructed from the Raman mapping of the annealed Capra4 sample. The size of the images is 35 x 50 µm^2. (a): frequency of the T_{2g} mode, translated in terms of Pu/(U+Pu) content (at%). (b): line width of the T_{2g} mode (cm^{-1}). (c): U*/T_{2g} intensity ratio. (d): 2LO/T_{2g} intensity ratio.

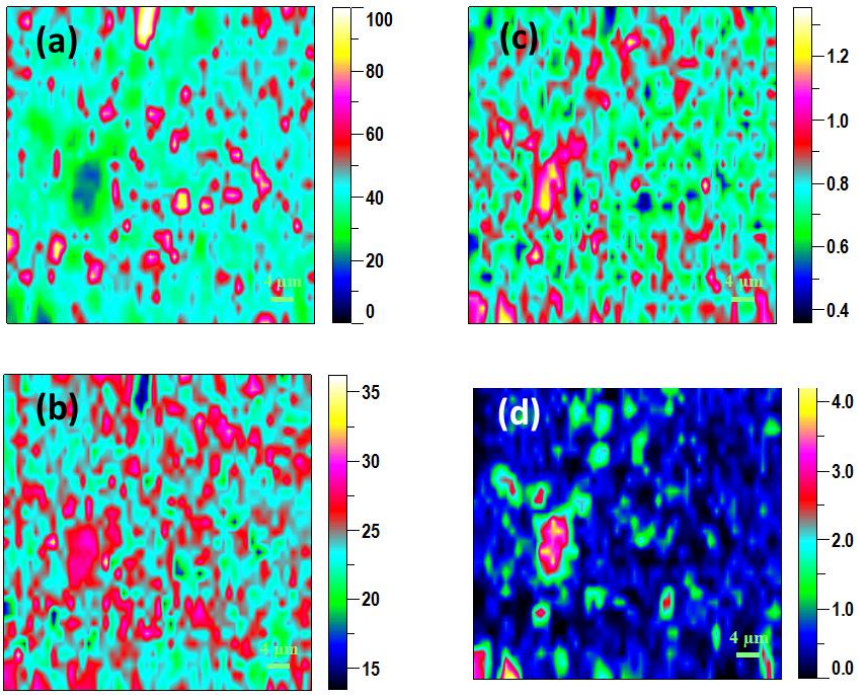

Figure 65 Images constructed from the Raman mapping of the aged Trabant40 sample. The size of the images is 35 x 50 µm^2. (a): frequency of the T_{2g} mode, translated in terms of Pu/(U+Pu) content (at%). (b): line width of the T_{2g} mode (cm^{-1}). (c): U*/T_{2g} intensity ratio. (d): 2LO/T_{2g} intensity ratio

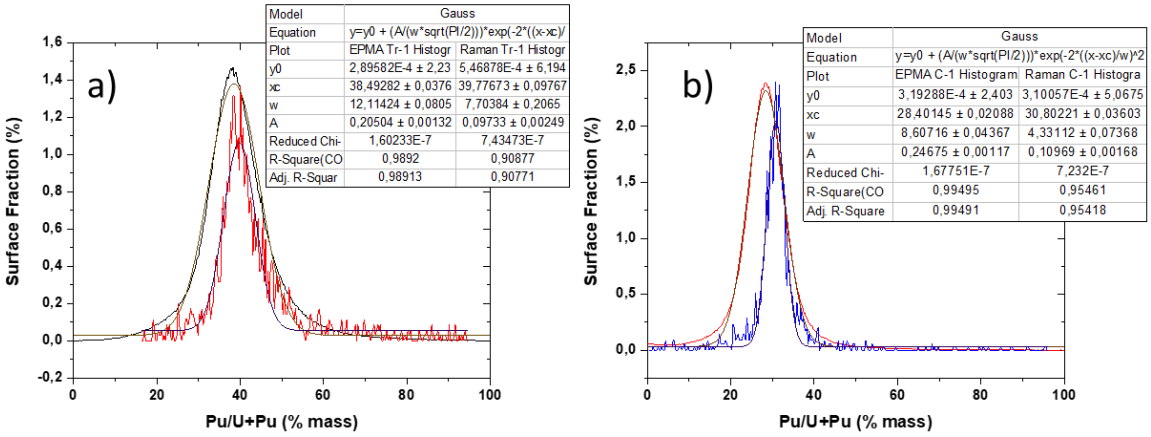

Figure 66 The Pu content histogram comparison a) Trabant40 sample, **black** histogram (EPMA data), red histogram (Raman spectroscopy data), b) Capra4 sample, red histogram (EPMA data), blue histogram (Raman spectroscopy data)

Variations in T_{2g} mode width and U^*/T_{2g} ratio as a function of Pu content are plotted in Figure 67a and Figure 67b respectively. In the figure, all the data points of the two Raman images are given, as well as the data obtained for the MIMAS sample. It is worth noting that the number of points available for Figure 67b is lower than for Figure 67a, as it was more often impossible to achieve a reasonable fit of the U* band than of the T_{2g} band. There is still a high degree of dispersion in the data. Nevertheless, the trend observed for the evolution of the T_{2g} mode width seems clear. The line width is the highest for Pu/(U+Pu) contents in between 20 and 80%. The evolution of the U^*/T_{2g} ratio is more difficult to discuss, in part due to the dispersion of the data. There is no very clear trend, and the U* band is observed whatever the composition. The main characteristics observed in Figure 61are therefore, at least partially reproduced. As expected, the characteristics of the spectra for high Pu contents seem to converge towards those of PuO_2 as seen in Figure 56a. The only slight difference is that the U* band is always observed for the highest Pu contents. The 2LO mode is not analyzed here, as its intensity is always very low for Capra4 and Trabant40 samples, except in the vicinity of U-rich agglomerates.

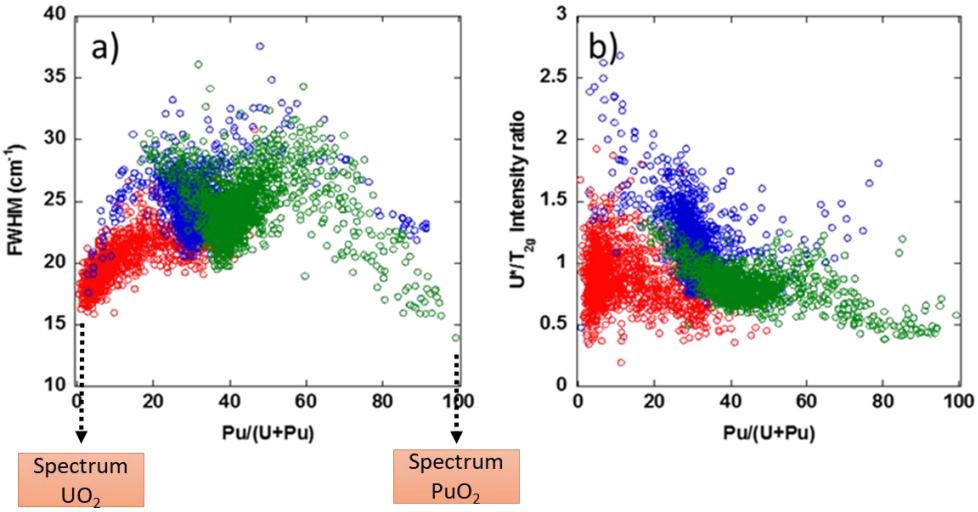

Figure 67 a) evolution of the width of the T_{2g} mode in the annealed sample vs the Pu content, (b): evolution of the U^*/T_{2g} intensity ratio vs the Pu/(U+Pu) content. (Annealed MIMAS sample, red open circles); (Capra4 sample, blue open circles); (Trabant40 sample, green open circles)

Some characteristic spectra of the samples are shown in Figure 68. They were recorded in U- and Pu-rich agglomerates as well as randomly in the more homogeneous matrix. Figure 68a and Figure 68c give an overview of the spectra as a whole, while Figure 68b and Figure 68d focus on the first-order region. Each spectrum was simply extracted (without any intensity normalization) from a single pixel in the

images. Thus, they were recorded under exactly the same conditions allowing for direct comparisons with other spectra within the same figure.

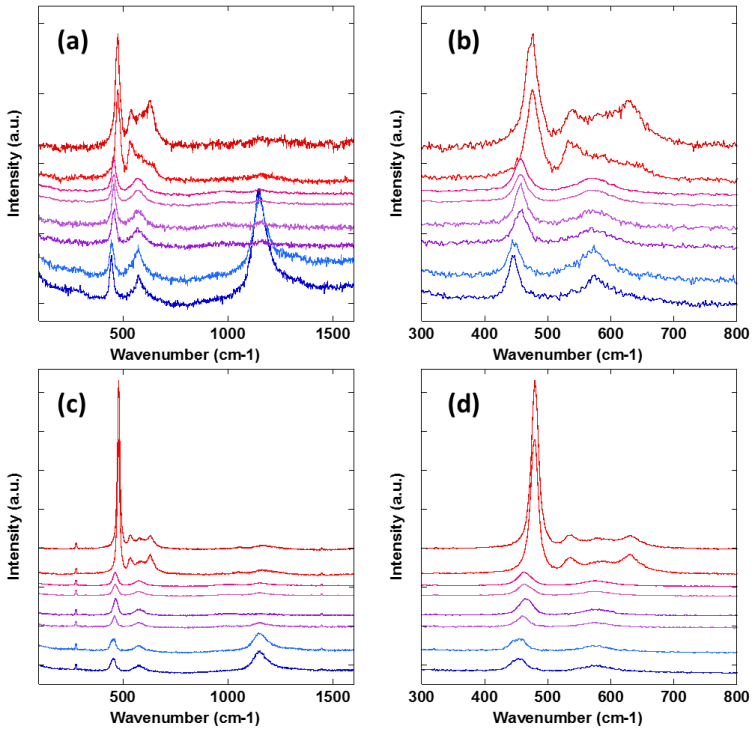

Figure 68 Examples of Raman spectra for Capra4 (a and b) and Trabant40 (c and d) annealed samples. Reddish lines correspond to the Pu-rich spots; bluish lines correspond to the U-rich spots; the violet lines correspond to the matrix phase (a) and (c): complete spectra, between ≈ 100 and ≈ 2000 cm^{-1}. (b) and (d): close-up of the first order region.

Spectra from U- and Pu-rich spots are highlighted in blue and red in Figure 68, respectively. The examination of the spectra provides a number of useful insights:

- (i) The intensity of spectra characteristic of U-rich zones is systematically lower than that of Pu-rich zones. This is most obvious in the Trabant40 sample. Without anticipating the discussion too much, this is most probably a probing depth effect, much higher for the PuO_2 than UO_2 for this specific excitation wavelength.
- (ii) The 2LO mode is always observed for U-rich agglomerates. However, its intensity is much lower than that observed for pure UO_2. U-rich agglomerates undoubtedly contain a small but significant Pu content, as shown by the Raman composition images. The UO_2 spots detected in the EPMA images are therefore not present in the Raman images, a consequence of the small size of the areas analyzed.
- (iii) The U* band is never resolved for either the U-spots or the matrix. However, it is clearly resolved for Pu-rich spots. For these agglomerates, the composition images tend to show unalloyed PuO_2 (exception made of americium, present in different contents between the two samples, which will be detailed in Section 5.1.2 of Chapter 5). For both samples, the lines identified as U_1, U_2 and U_3 are clearly detected. One can clearly see that their intensity ratios are not constant.

3.3.4 First overview of the results

Through analyzing these three samples, we were able to review the main features of the Raman spectra of the $(U,Pu)O_2$ solid solution. All the spectra were acquired at 532 nm and are different from those acquired at other excitation wavelengths. The effect of composition (Pu content) has therefore to be taken into account in the analysis of the resonant Raman scattering.

Raman imaging was used to examine all three samples. Four different spectral characteristics can be used to immediately the different agglomerates, at least the U-rich zones. The T_{2g} mode frequency could be used to extract local Pu content with fair accuracy, in particular in the 0-40 at% Pu/(U+Pu) composition range. The agreement with EPMA was satisfactory, as shown by the comparison of composition histograms obtained by the two methods. Above 50%, the quadratic law proposed by Medyk et al. [99] may be somewhat questionable, but this does not call into question the orders of magnitude obtained in the different composition images. The rather strong bowing observed for the evolution of the T_{2g} mode frequency vs composition remains to be explained.

The triplet defect band (U_1, U_2, and U_3), widely discussed in the literature has never been spectrally resolved, with the exception of a few Pu-rich clusters. Finally, the 2LO band is analyzed in over a wide range of Pu content, whose intensity decreases progressively until a Pu/(U+Pu) content of 15 wt%. Beyond this threshold, the band intensity remains very low and gradually converges to zero at around 30 wt%.

3.4XAS

Finally, the samples were also analyzed during two XAS measurements campaigns performed at the ESRF and Soleil synchrotrons. As mentioned in the two previous chapters, the aim of these measurements was to obtain more additional information: the oxidation degrees of the cations, the distances between first and second neighbor atoms in the cubic lattice, as well as some possible disorder-induced parameters.

This part of the chapter begins with the presentation of results from fluorescence mappings conducted at the SOLEIL synchrotron, focusing on the MIMAS sample only. Subsequently, we delve into the findings of the XANES analysis performed for both the annealed SFR and MIMAS samples, providing insights into the oxidation states of the cations. Lastly, we explore the EXAFS results obtained for these same samples.

3.4.1 Fluorescence Mapping at the MARS beamline (SOLEIL)

Considering the heterogeneity in the Mimas sample microstructure, only XAS spectra recorded with a microbeam could be of interest. Fluorescence mappings were first collected to locate the three phases (U-rich, Pu-rich and the matrix phase), using an incident X-ray beam of 19 keV (with a 15×16 μm^2 size). Various maps were collected at the same locations as that used for EPMA and µ-Raman. Example of fluorescence maps of the annealed MIMAS sample are shown in Figure 69a and Figure 69b, where the former shows the uranium mapping and the latter shows the plutonium mapping. Combination of these two maps helps identifying the three phases in the selected zone. As examples, the regions labeled as x_1 and x_3 represent U-rich agglomerates, x_2 and x_4 Pu-rich agglomerates, and x_5 and x_6 the coating phase. The XANES and EXAFS spectra at U L_{III}, Pu L_{III} and Am L_{III} edges (only XANES at the latter) were collected in these zones of interests. Americium mapping (not shown here) is similar to that of plutonium, which confirms what was observed by EPMA (see Figure 45).

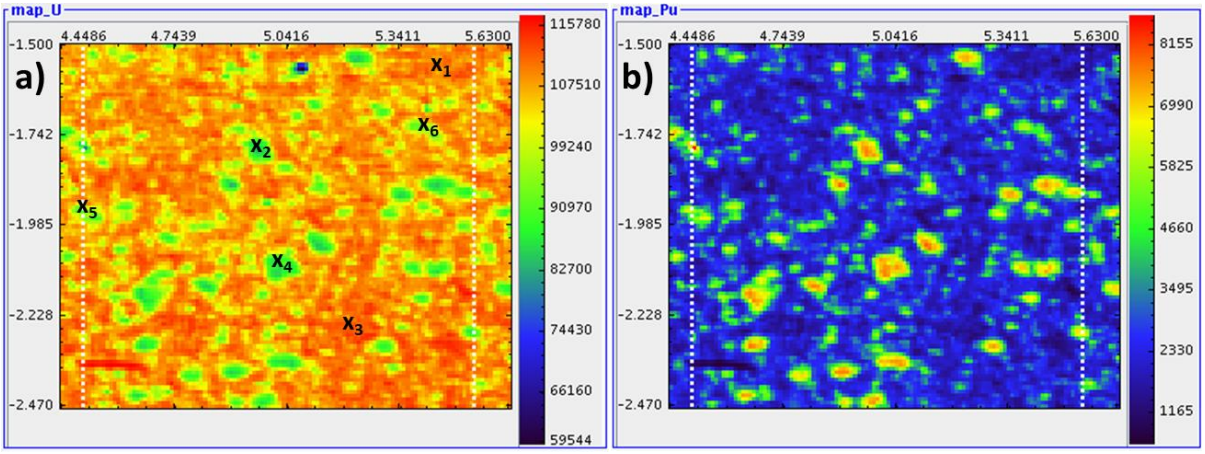

Figure 69 X-ray Fluorescence map of a selected zone in the annealed MIMAS sample, a) Uranium mapping, b) Plutonium mapping. For the mappings, the x- and y- axis are shown in mm scale and the color scale corresponds to the number of counts of the fluorescence emission.

As previously noted, some of the fluorescent imaging zones had been previously analyzed using EPMA and μ-Raman. Figure 70 illustrates the integration of EPMA and Raman microscope images with the fluorescence map.

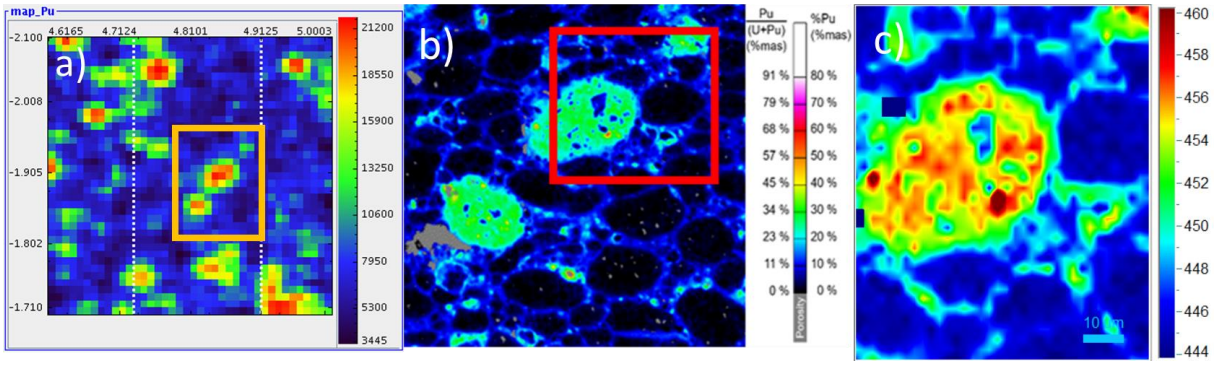

Figure 70 a) Plutonium X-ray fluorescence mapping, the x- and y- axis are shown in mm scale and the color scale corresponds to the number of counts of the fluorescence emission. b) Pseudo-quantified plutonium mapping obtained by EPMA, c) T_{2g} Raman band position mapping, the color scale corresponds to the T_{2g} position in cm^{-1}. All of the three figures are obtained from the same selected spot on the aged MIMAS sample.

3.4.2 XANES analysis

Based on the XANES spectra collected from the annealed samples, we investigate the average oxidation states of various cations at the U L_{III}, Pu L_{III}, and Am L_{III} edges.

3.4.2.1 XANES results (SFR Samples)

The results from the analysis of annealed SFR samples are illustrated in Figure 71 (for Capra4) and Figure 72 (for Trabant40). To determine the average oxidation states of the three cations, a linear combination fitting approach was employed using XANES spectra from reference compounds, as outlined in Section C.4.5.1 of Appendix C. The results of this analysis indicate that, in line with expectations after the annealing process, the majority of U and Pu cations exist in their +4 states. However, it is worth noting that amounts of U^{+5} and Pu^{+3} were also detected in the samples. It is important to note that Am was identified only in the Am^{+3} state. The global O/M ratio of the sample is calculated based on the average oxidation states of the three cations and considering the actual chemical composition of the samples. Here, despite all Am being in its +3 state, its influence on the O/M ratio remained very low. This was the case even for the Capra4 sample, which has a $^{241}Am/(Pu+Am)$ ratio of 8.30 wt%. This limited influence

was also compensated by the presence of a small quantity of U^{+5} within the material. The results for these samples are tabulated in the first two columns of Table 19 and demonstrate that the samples are at oxygen stoichiometry, within the measurement uncertainties.

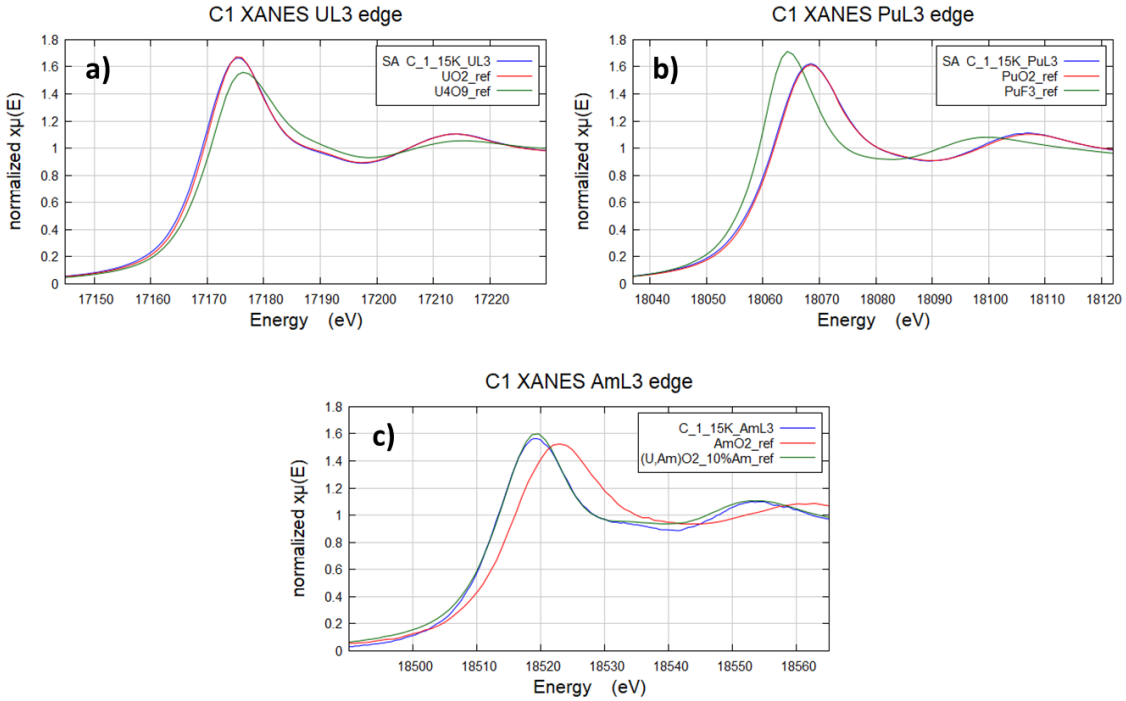

Figure 71 XANES spectra at the a) UL_{III}, b) Pu L_{III}, c) Am L_{III} edge collected from annealed Capra4 sample (denoted as C-1)

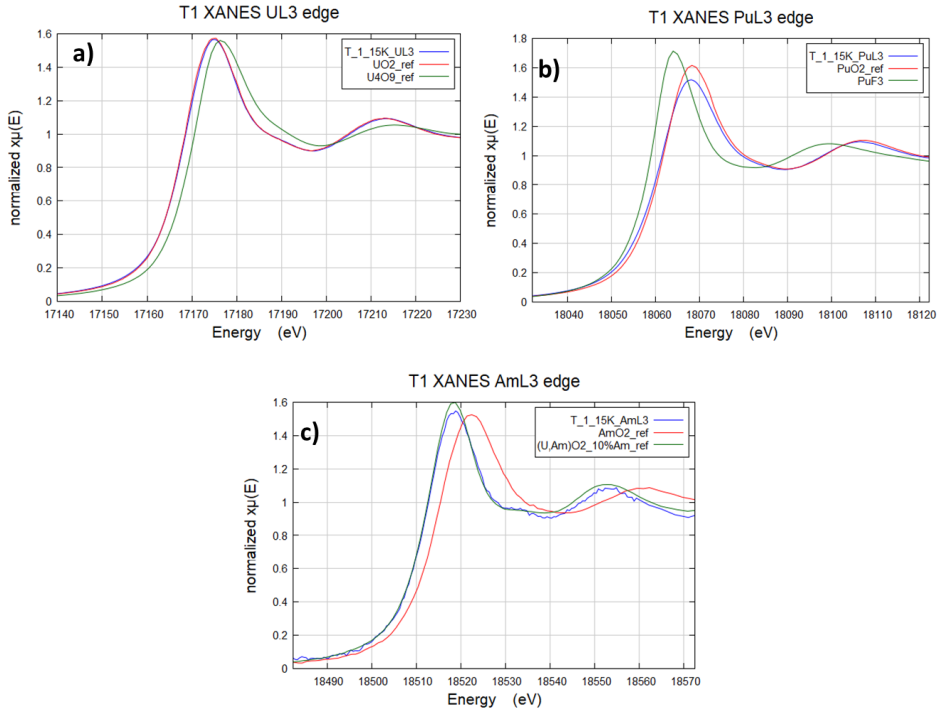

Figure 72 XANES spectra at the a) UL_{III}, b) Pu L_{III}, c) Am L_{III} edge collected from annealed Trabant40 sample (denoted as T-1)

3.4.2.2 XANES results (MIMAS Samples)

The results obtained from the analysis of annealed MIMAS samples are presented in Figure 72. This particular sample's spectra were collected from three distinct phases as indicated. Spectra from the U-rich agglomerates were exclusively collected at the U L_{III} edge, considering the limited presence of Pu

and Am in those agglomerates. Conversely, all three edges (U L_{III}, Pu L_{III}, and Am L_{III} edges) were collected from both the Pu-rich agglomerates and the matrix phase.

Figure 72 exclusively shows representative results, where (a) corresponds to the U L_{III} edge of the U-rich agglomerate, while (b), (c) and (d) correspond to the (U L_{III}, Pu L_{III}, and Am L_{III} edges) collected from the Pu-rich agglomerates.

In Section C.4.5 of Appendix C, we address the challenges related to the continuous collection of energy calibration spectra for the reference material due to the beamline setup. Consequently, there is an associated uncertainty of ~2 eV in the position of the absorption edge in the XANES spectra of the MIMAS sample. Given this inherent uncertainty, we will rely on the findings obtained from the analysis of the annealed SFR samples to support our conclusions regarding the oxidation state of the cations and the overall O/M ratio in the annealed MIMAS sample.

The examination of the SFR samples revealed that uranium is made of a mixture of +4 and +5 oxidation states, while plutonium exhibits a mixture of +4 and +3 oxidation states. These observations align with the trends we observed in the MIMAS sample, as indicated in Figure 73. Furthermore, the presence of trivalent Am in the SFR samples did not deviate the sample from stoichiometry as it is present in a low amount and is compensated by the presence of U^{+5}. Thus, we anticipate a similarly insignificant influence on the O/M ratio in the MIMAS sample, particularly when considering that MIMAS possesses a lower Am content compared to Capra4.

Besides, considering that all samples in this study underwent the same thermal treatment conditions, and the uncertainty given for the O/M ratio (0.01), we can reasonably conclude that the annealed MIMAS samples are also close to stoichiometry.

From now on, we will adopt this hypothesis for the MIMAS samples, particularly when evaluating the aged MIMAS samples in Chapter 4. We will analyze these samples under the assumption that the annealed MIMAS sample has a global O/M ratio of 2.00 based on the oxidation states specified in the last two columns of Table 19, where uranium is in the +4 oxidation state, plutonium is also in the +4 oxidation state, and americium is in the +3 oxidation state.

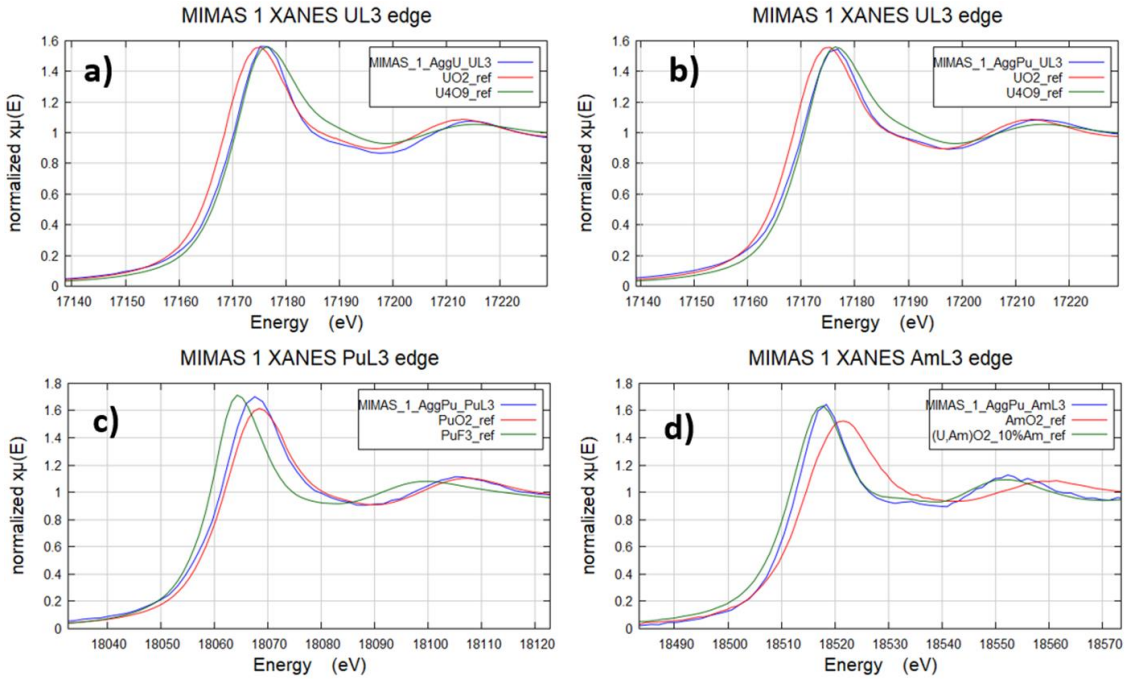

Figure 73 XANES spectra at the a) U L_{III} edge in U-agglomerate b) U L_{III} edge, c) Pu L_{III} edge d) Am L_{III} edge in Pu agglomerate collected from the annealed MIMAS sample

Table 19 Calculated O/M ratios of the annealed samples

Sample	T-1	C-1	MIMAS U-Rich (assumed)	MIMAS Pu-Rich (assumed)
U	4.03(5)	4.07(5)	4.00	4.00
Pu	3.96(5)	3.95(5)	-	4.00
Am	3.0	3.0	-	3.0
O/M	2.00(1)	2.01(1)	2.00(1)	2.00(1)

3.4.3 EXAFS

The EXAFS data of the annealed samples are presented in this section. The fits were all performed using the fluorite model described in the Appendix C.4.5.2.1 and C.4.5.2.2.

Here, the results of the fit in the EXAFS and the FT spectra are first compared in the same figures for all samples. Figure 74 corresponds for the U-L_{III} edge for each sample and Figure 75 to the Pu-L_{II} edge of the SFR samples and the Pu-L_{III} edge of the annealed MIMAS sample.

In this section, the fit results for both the EXAFS and Fourier Transform spectra are presented. Figure 76 and Figure 77 show the results for the annealed Capra4 samples at the U-L_{III} and Pu-L_{II} edges, respectively. While, Figure 78 and Figure 79 show it for the annealed MIMAS sample within a Pu-rich agglomerate. At the U-L_{III} and Pu-L_{III} edges. For simplicity, only the Capra4 spectra are presented here to represent the SFR-type samples.

For all the samples, the Fourier transforms show two main peaks, the first around 1.9 Å and the second around 3.8 Å, where the first peak corresponds to the first coordination shell, constituted by 8 oxygen anions, while the second peak corresponds mainly to the second neighbor shell, constituted by 12 cations. One hypothesis that was tested during the fitting of the EXAFS spectra involved performing initial fits using only one cation-cation shell. Subsequently, the use of two cation shells (cation-Pu and cation-U) was experimented, but no improvements were observed in terms of the R factor. This suggests that the incorporation of the two cation shells did not lead to any noticeable improvements in the fit quality, and the single cation-cation shell configuration was found to be sufficient for accurately representing the data. Furthermore, it was also seen that allowing the coordination numbers to vary during the fitting did not improve the quality of the results. Simply, when they were allowed to change, the differences in coordination numbers were always within the uncertainty of the measurements.

The calculated interatomic distances for the annealed samples are tabulated in Table 20, as well as the corresponding Debye Waller factors in Table 21.

For comparison purposes, we also give the data obtained for UO_2 and PuO_2, extracted from references [147], [148].

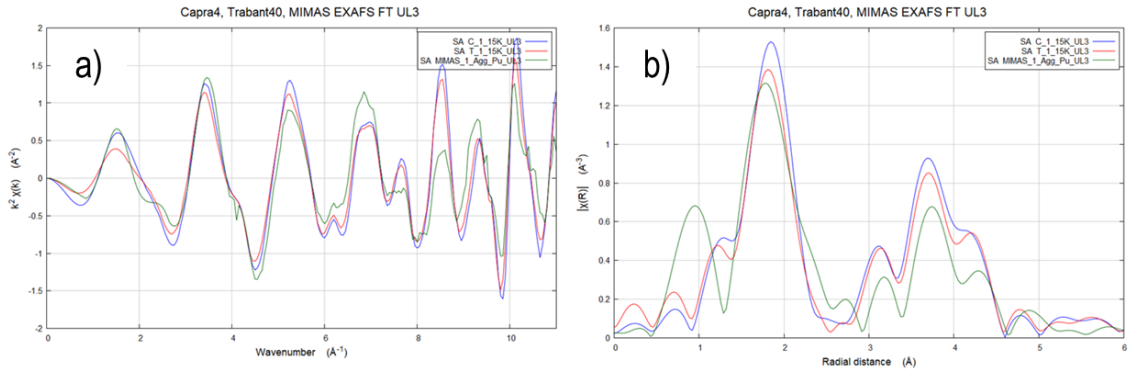

Figure 74 Comparison of the FT spectra of the annealed samples in the U-L_{III} edge for all samples. a) EXAFS spectra, b) Fourier Transform spectra k range 3-10 A^{-1} for each spectrum. Blue is the annealed Capra4 sample, red is the annealed Trabant40 sample, green is the annealed MIMAS sample (taken from a Pu-rich agglomerate).

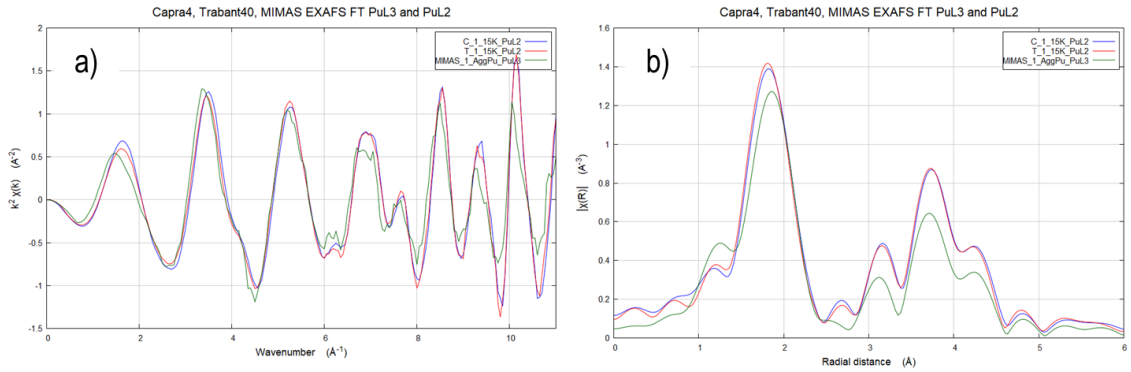

Figure 75 Comparison of the FT spectra of the annealed samples in the Pu-L_{II} edge for the SFR samples, Pu-L_{III} edge for the MIMAS sample a) EXAFS spectra, b) Fourier Transform spectra k range 3-10 A^{-1} for each spectra. Blue is the annealed Capra4 sample, red is the annealed Trabant40 sample, green is the annealed MIMAS sample (taken from a-Pu rich agglomerate).

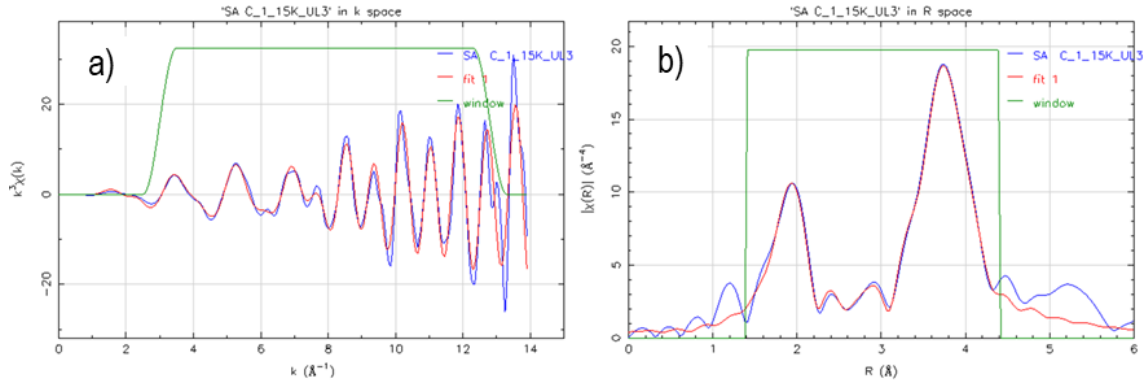

Figure 76 Experimental and fitted a) EXAFS spectra, b) Fourier transform of sample C-1 at U-L_{III} edge (fitted k range 3-12.5 $Å^{-1}$). The blue correspond to the experimental data and the red corresponds to the fitted data. R factor is 0.0012.

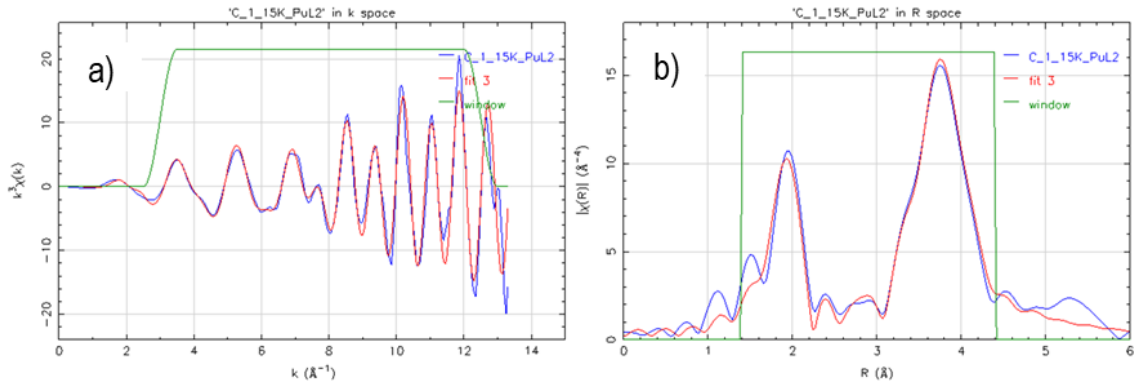

Figure 77 Experimental and fitted a) EXAFS spectra, b) Fourier transform of sample C-1 at Pu-L_{II} edge (fitted k range 3-12.5 Å^{-1}). The blue correspond to the experimental data and the red corresponds to the fitted data. R factor is 0.004.

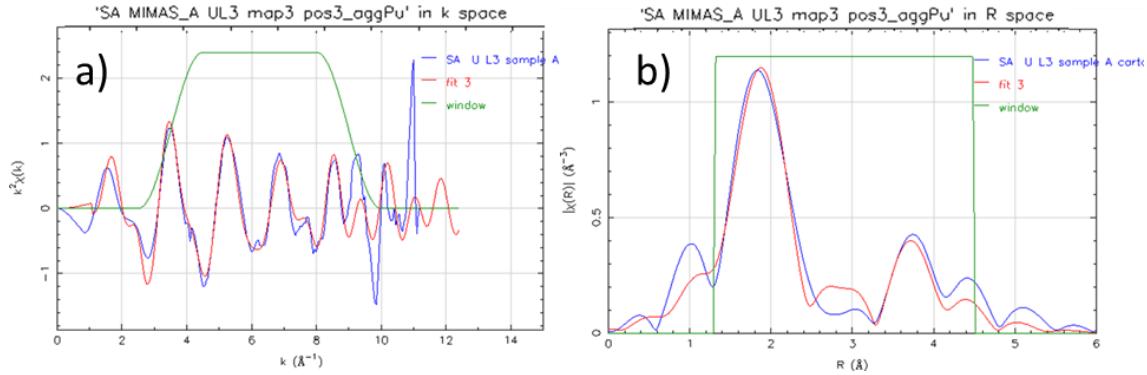

Figure 78 Experimental and fitted a) EXAFS spectra, b) Fourier transform of spectra obtained from a Pu-rich agglomerate of a MIMAS sample at U-L_{III} edge (fitted k range 3-9 Å^{-1}). The blue correspond to the experimental data and the red corresponds to the fitted data. R factor is 0.011.

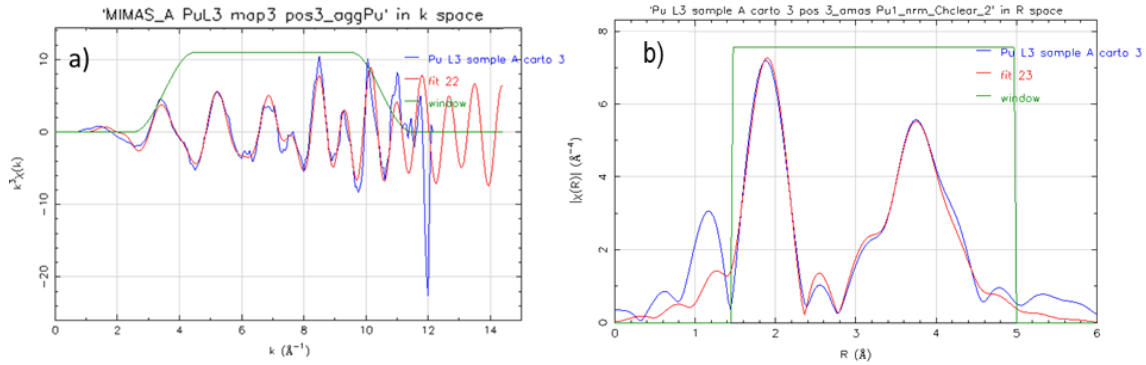

Figure 79 Experimental and fitted a) EXAFS spectra, b) Fourier transform of spectra obtained from a Pu-rich agglomerate of a MIMAS sample at Pu-L_{III} edge (fitted k range 3-10.5 Å^{-1}). The blue correspond to the experimental data and the red corresponds to the fitted data. R factor is 0.030.

It is accepted that EXAFS leads to reliable measurement of interatomic distances. Typically, for nearest neighbors this can be 0.02 Å or even better. From that point, it is useful to compare the equilibrium crystallographic positions, and the time-averaged positions, which are detected by EXAFS. These values are given in brackets in Table 20, assuming a perfect fluorite structure with cations at the (0 0 0) position, and O atoms at the (¼, ¼, ¼) positions in the cubic cell (corresponding to the 4a and 8b Wyckoff positions), according to the virtual crystal approximation. For the calculation, we do not take into account the fact that some measurements were conducted at 15K. Furthermore, we use average Pu contents of 30 wt. % (Capra4, MIMAS Pu-rich) and 40 wt% (Trabant40), for simplicity. These values are given in brackets in Table 20. For UO_2 and PuO_2, one can see that these values rather coincide, taking into account the measurement accuracy. This is no longer the case for MOX samples. Quite clearly from Table 20, the cation-O distances in the samples are shorter than those calculated by XRD. On the other hand, it is seen that the EXAFS cation-cation shell, close to 3.85 Å, leads to lattice parameters in satisfying

agreement with diffraction data. The agreement would undoubtedly have been even better taking into account the thermal expansion, which is not completely known at such low temperatures due to lack of data in the literature. The second information is that the mean Pu-O and U-O distances are always equivalent, perhaps in a non-intuitive way. The graphical demonstration of the Table 20 are shown in Figure 80, Figure 81 and Figure 82. These figures illustrate the cation-O distance in the first coordination sphere, the M-M distance in the first coordination sphere, and the cation-O distances in the second coordination sphere, respectively.

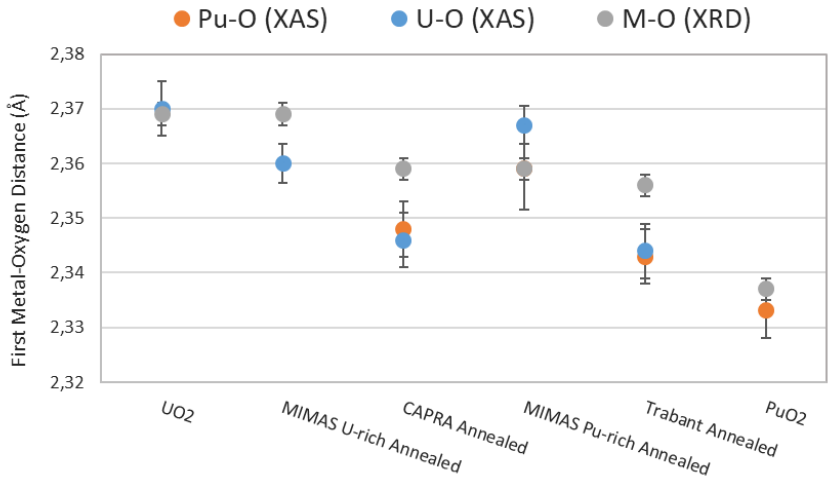

Figure 80 Cation-O distances calculated for the first coordination sphere using EXAFS compared to the distances calculated from the XRD.

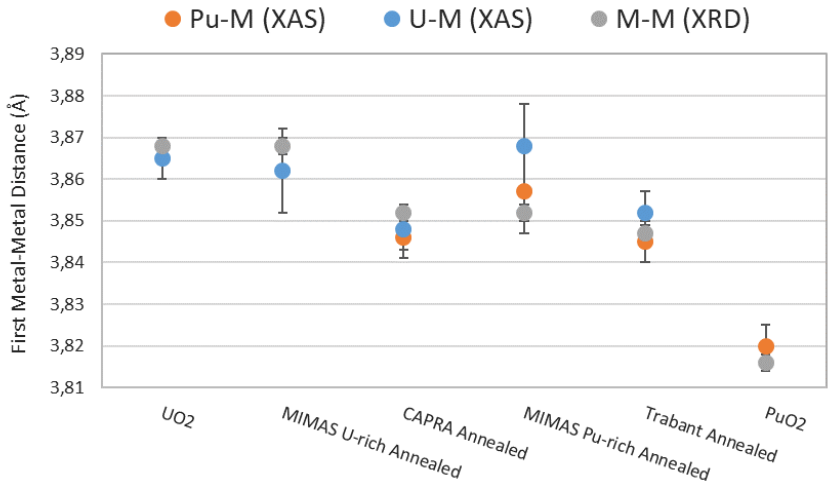

Figure 81 Cation-cation distances calculated for the first coordination sphere using EXAFS compared to the distances calculated from the XRD.

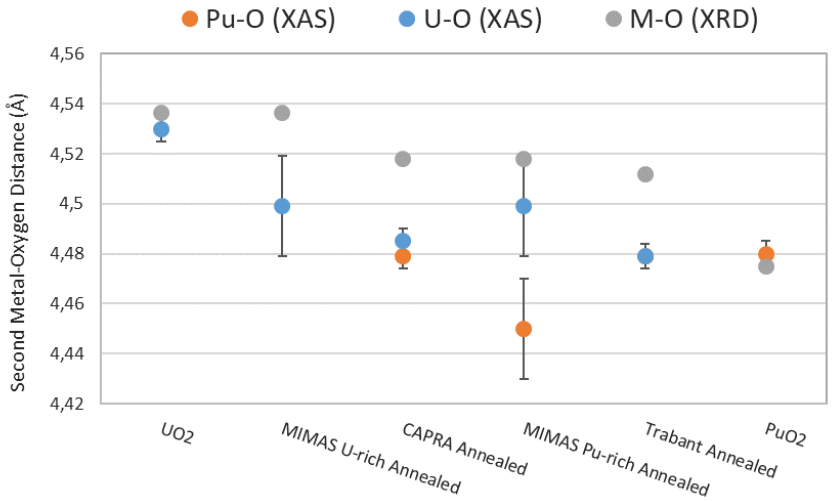

Figure 82 Cation-O distances calculated for the second coordination sphere using EXAFS compared to the distances calculated from the XRD.

Table 20 The interatomic distances of the annealed samples. The red values correspond to the XRD data from virtual crystal approximation. Two references [147], [148] are used for the interatomic distances calculated for UO_2 and PuO_2 former being recorded at room temperature, the latter is recorded at 10K.

Sample	Pu-Oxygen (1st shell) Å	Pu-Cation (1st shell) Å	Pu-Oxygen (2nd shell) Å	U-Oxygen (1st shell) Å	U-Cation (1st shell) Å	U-Oxygen (2nd shell) Å
C-1 (5.4488) (20)	2.348 (5) (2.359)	3,846 (5) (3.852)	4,479 (5) (4.518)	2,346 (5) (2.359)	3,848 (5) (3.852)	4,485 (5) (4.518)
T-1 (5.4414) (20)	2.343 (5) (2.356)	3,845 (5) (3.847)	4,479 (5) (4.512)	2,344 (5) (2.356)	3,852 (5) (3.847)	4,479 (5) (4.512)
MIMAS U-rich (5.4710) (20)	--	--	--	2,360 (8) (2.369)	3,862 (10) (3.868)	4,499 (20) (4.5363)
MIMAS Pu-rich (5.4488) (20)	2.359 (8) (2.359)	3,857 (10) (3.852)	4,450 (20) (4.518)	2,367 (8) (2.359)	3,868 (10) (3.852)	4,499 (20) (4.518)
UO_2 (5.471)				2.370(5) [147] 2.365(5) at 10K [148] (2.369)	3.865(5) [147] 3.86(1) at 10K [148] (3.868)	4.53(2) [147] 4.54(2) at 10 K [148] (4.5363)
PuO_2 (5.40)	2.333(5) [147] 2.335(1) at 10K [148] (2.337)	3.820(5) [147] 3.81(1) at 10K [148] (3.816)	4.48(2) [147] 4.47(2) at 10 K [148] (4.475)			

A third information is given by the Debye–Waller (DW) factor, in other words the variance of the distance distributions. Here, the DW factor includes the effects of both the static and dynamic disorder. The static disorder is a configuration disorder, while the dynamic disorder is caused by thermal vibration of atoms (zero-point energy plus the thermal motion). The static disorder must also take into account the Pu distribution of the samples, which necessarily leads to a distribution of lattice parameters and of the distances between atoms.

Focusing first on Capra4 and Trabant40 samples, for which the contribution of temperature is negligible (measurements performed at 15 K), it appears that the DW factor is always much lower for cation-cation distances than for cation-O distances. This suggests a relatively organized cationic sub-lattice, the distance disorder naturally induced by the difference in the lattice parameters of UO_2 and PuO_2 being absorbed or compensated by some disorder in the oxygen sub-lattice. The data for the MIMAS sample are more difficult to comment on, perhaps due to the effect of thermal agitation, which can no longer be neglected.

Therefore, a more complex local environment for both actinides are observed than what is suggested by the perfect virtual crystal approximation. More, the interatomic distances of the parent UO_2 and PuO_2 materials do not appear to be preserved, as it is generally the case with materials with a strong covalent character, even accepting some relaxation from perfectly rigid bonds.

Table 21 Calculated Debye Waller factor of the annealed samples (Å^2)

Sample	Pu-O (1st shell)	Pu-Cation (1st shell)	Pu-Oxygen (2nd shell)	U-O (1st shell)	U-Cation (1st shell)	U-Oxygen (2nd shell)
C-1	0.0049 (2)	0.0018 (2)	0.0060 (2)	0.0034 (2)	0.0012 (2)	0.0050 (2)
T-1	0.0052 (2)	0.0020 (2)	0.0057 (2)	0.0042 (2)	0.0018 (2)	0.0060 (2)
MIMAS U-rich	--	--	--	0.0030 (10)	0.0069 (10)	0.0135 (10)
MIMAS Pu-rich	0.0046 (10)	0.0041 (10)	0.0080 (10)	0.46 (10)	0.57 (10)	0.0103 (10)
UO_2				0.0080(5) [147] 0.0035(5) at 10 K [148]	0.0050(5) [147] 0.0013(5) at 10K [148]	0.007(2) [147] 0.006(2) at 10K [148]
PuO_2	0.0064(5) [147] 0.0063(5) at 10K [148]	0.0033(3) [147] 0.0028(5) at 10K [148]	0.010(2) [147] 0.007(2) at 10K [148]			

3.5 Conclusion

This fourth chapter has been dedicated to the examination of the three selected samples, after high temperature annealing. This annealing was carried out to heal the samples, as much as possible, from the self-irradiation effects and to bring them to a composition close to exact oxygen stoichiometry. The required information included: (i) the local Pu content, (ii) the average lattice parameters, (iii) the oxidation states of U, Pu and Am atoms in the lattice and (iv) the mean cation – O distances.

Assuming an exact oxygen stoichiometry, as confirmed for all samples by the different XANES spectra, and strain-free materials, XRD and Raman spectroscopy could be used to extract a mean or a local Pu content, to be confronted to the chemical analysis (EPMA). For all samples, the Raman data were rather similar to the EPMA data within an estimated error margin close to +/- 1% in Pu/(U+Pu) ratios, or slightly greater. Comparable composition images were accordingly obtained using both techniques. Surprisingly, the diffraction data, although considered reliable, were further away from the chemical data.

Examining the EXAFS data, some distortion from the perfect fluorite structure were evidenced. The data, in particular those obtained at low temperature (15K), suggest a rather organized cationic sub-lattice, and a more disordered oxygen sub-lattice.

The next chapter will examine the effects of self-irradiation. The task will perhaps be simplified, since the aim will be to highlight any deviation from the reference signals obtained in this chapter. Nevertheless, one can expect these deviations to be small, which means we will need robust measurement protocols.

Chapter 4. Self-irradiation Effects: time analysis of annealed samples

4.1Introduction

In the previous chapter, the three MOX samples (MIMAS, Capra4 and Trabant40) were characterized as accurately as possible immediately after annealing, using various characterization techniques and different spatial scales. These spatial scales both derive from the probe sizes used (*e.g.* Raman, XRD) and the physical principles involved in the analysis (*e.g.* XAS). This approach was essential due to the heterogeneous microstructure of the MOX materials. The samples were analyzed for their local Pu content, average lattice parameters, mean atomic distances (cation-oxygen and cation-cation) and the cation oxidation states (*i.e.* U, Pu, and Am) within certain assumptions and approximations. The obtained results were also compared in part with the information available in the literature.

In the present chapter, we analyze the effect of self-irradiation on the microstructure of the samples. Such an analysis obviously involves a periodic examination of the samples over time. Here, considering the α decay of the Pu (and Am) isotopes involved, and their relative low concentration, the time scale covers the whole duration of this work. The same three characterization methods (XRD, Raman imaging and XAS) will be used. As in the previous chapter, we still remain as descriptive as possible. Results will be discussed in more details in the final chapter of this document.

For all samples, EPMA showed that there was no significant variation in local Pu contents upon annealing, which we will not further discuss here.

For reasons that will be gradually introduced, we will start analyzing these effects for the Capra4 sample, and partially for the Trabant40 sample. Indeed, the analysis of the Trabant40 sample could not be fully completed due to a probable sampling issue as described in Chapter 2. The more homogeneous microstructure of these samples makes it easier to analyze the results. More, the Raman analysis is also easier to tackle, as it is carried out far from the strict resonance conditions observed for pure and stoichiometric UO_2. Finally, the analysis of Capra4 samples should be similar to that of Pu-rich agglomerates from MIMAS samples, considering that the average Pu content is similar, which provides another means to examine some of the data.

There are different ways to plot and understand the following data (time, cumulated dose, DPA). Concerning the results given in this chapter, we preferred to use the time scale.

4.2Capra4 and Trabant40 samples

4.2.1 XRD

The time evolution of the XRD patterns of the Capra4 and Trabant40 samples is described in this section. Here, the relative uncertainty of the measurements discussed in the previous chapter does not appear as a strong issue, as only the relative evolution of the signals is considered. Potential instrumental deviations were continuously monitored by adding a gold powder as an internal standard on the sample plate. This standard was mainly used as a reference for 2θ positioning. It could also be used for a first normalization

of the diffraction line intensities. However, this second approach will not be used here, in particular for the Capra4 sample, as it had to be re-prepared during analysis. In the figures, the background was subtracted from all patterns while the secondary peaks that comes from the diffraction of the Cu $K\alpha_2$ radiation are kept for each pattern so as not to distort the information. For visualization purposes, we use the (420) reflection of the fluorite symmetry, which is close enough to the (311) gold reflection.

4.2.1.1 Capra4 sample

The evolution of the (420) diffraction line since the annealing of the sample is shown in Figure 83. In the figure, eight diffraction patterns have been selected and displayed. The date of recording is given in the caption. The last data was recorded 569 days after the first annealing, which corresponds to a damage level of 0.8 dpa, see Section 1.2.2.2.3. For each pattern, the 2θ scale was corrected to set the gold (311) reflection to its expected position, according to JCPDS file n° 00-004-0784. According to the figure, the progressive shift of the diffraction line towards the lower 2θ is obvious. This observation lies in accordance with a swelling of the lattice and has thus been observed in many previous studies [4], [79], [81], [90], [91].

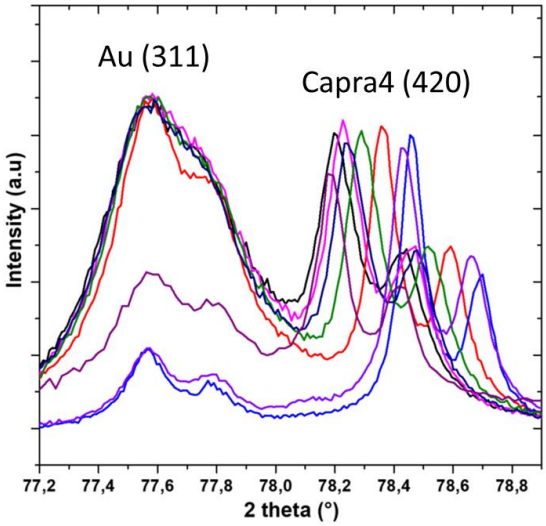

Figure 83 Evolution of Capra4 sample (420) diffraction peak after annealing, (**blue**: 3 days after annealing, **violet**: 19 days after annealing, red: 112 days after annealing, **olive**: 224 days after annealing, **navy**: 321 days after annealing, **magenta**: 495 days after annealing, **black**: 569 days after annealing, **purple**: before annealing.

Perhaps more subtle is the progressive broadening of this line. Figure 84 illustrates the broadening of the (420) diffraction line by comparing it with XRD patterns taken at three different ages: 3 days after annealing, 224 days after annealing and the sample before annealing. Table 22 shows the FWHM values of the same diffraction line (420) of the patterns shown in Figure 84. The values indicate a progressive broadening of this line.

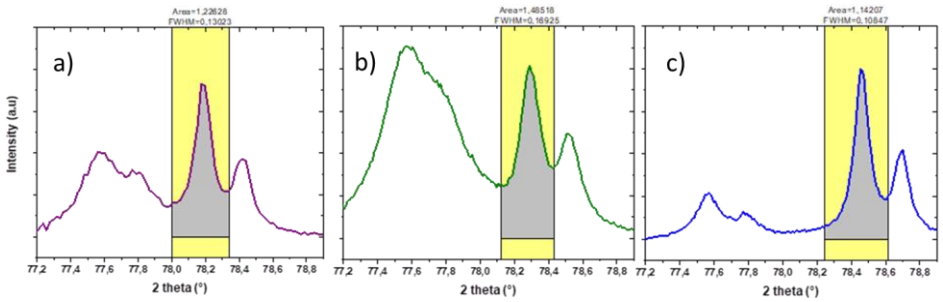

Figure 84 FWHM measurements for the (420) diffraction peaks. Violet: before annealing, green: 224 days after annealing, blue: 3 days after annealing.

Table 22 The FWHM values of the (420) diffraction peak of the patterns shown in Figure 83

Day after annealing	3	19	112	224	321	495	569	Sample before annealing
FWHM of (420) reflection	0.108 ± 0.01	0.137 ± 0.01	0.13 ± 0.018	0.170 ± 0.01	0.184 ± 0.01	0.184 ± 0.01	0.212 ± 0.01	0.130± 0.01

The interpretation of the broadening of the lines is rather challenging due to several factors. Here, in these extracted patterns, three different sample plates were used. One plate is used for the patterns from day number 3 and 19. Another plate is used for the patterns from day number 112, 224, 321, 495 and 569. While a third plate was prepared for the sample before annealing. The consequence of this (the use of different plates) is also visible in the intensity of the corresponding Au (311) peak in the Figure 83, as different quantity of Au is used for each plate preparation (see Appendix C.2.2 for XRD sample preparation). This makes it rather difficult to compare the results as we lack a reference peak for each pattern.

Considering the available data shown in Table 22, although we have a more or less progressive increasing in the line broadening since the first annealing of the sample, the recorded data of the sample before annealing is almost as thin as the sample after annealing. The observed difference might result from sampling-related issues or effects related to the XRD sample preparation (as described in paragraph above). Thus, after excluding this last point, it is possible to fit the available data with Equation (52), as shown in Figure 85.

$$y = y_0 + (1 + A \cdot (1 - e^{(-B \cdot t)})) \qquad \text{Eqn (52)}$$

Where:

- y is the FWHM value,
- T is the time in days
- A and B are dimensionless constants, where the y0·(1+A) corresponds to the FWHM at saturation.

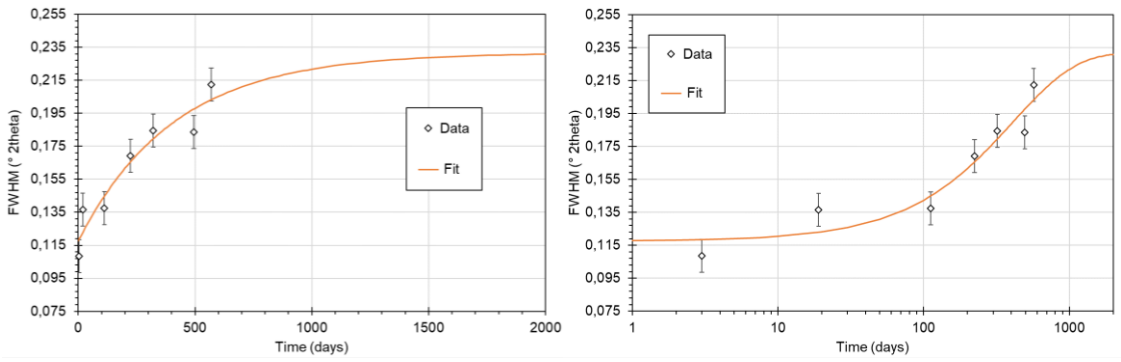

Figure 85 The resulting fit of the FWHM data of the (420) lines tabulated in Table 22, the last data (old sample) excluded. Figure on the left, linear scale, on the right: log scale in the x-axis focused on first 1000 days.

The fitting equation gives a maximum FWHM value of 0.232 at the saturation state and the increasing behavior follows the lattice parameter increase as explained hereafter.

Figure 86 gives the self-irradiation-induced strain calculated from the lattice parameter obtained by XRD. This data follows the expected behavior and was thus fitted with the expected function and using the effective decay constant (λ') estimated through Eqn (9). The dotted line gives the best fit. Based on the fit, the maximum strain A is close to 0.3% (horizontal dashed line in the figure) and the B.λ' value is $5.86 \cdot 10^{-8}$ s^{-1}. In the figure, the blue solid line corresponds to the expected swelling based on the data reported by Kato, which gives a B.λ' product of $3.51 \cdot 10^{-8}$ s^{-1}. The difference between these two values is rather significant and cannot be explained only by some imprecision in the measurements as shown in Figure 86 (in which the uncertainty on the lattice parameter in included in the size of the dots).

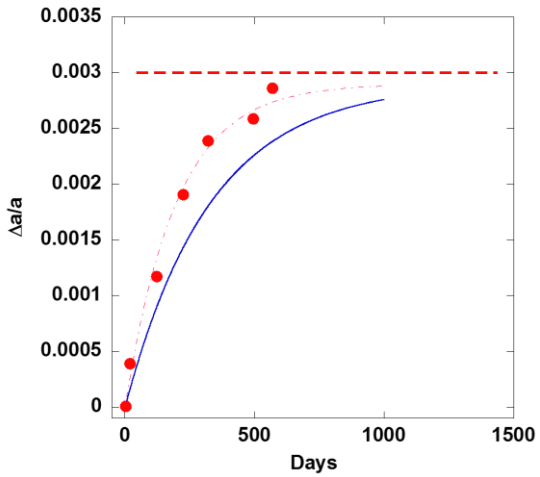

Figure 86 Lattice parameter swelling vs time. Full circles: XRD data. Blue full line: calculation according to the Kato's empiric law. The decay constant is $-3.51 \cdot 10^{-8}$ s^{-1}. Dashed line: fit of the experimental data, with a time constant close to $-5.86 \cdot 10^{-8}$ s^{-1}. The strain saturation level is indicated by the horizontal dashed line.

4.2.1.2 Trabant40 sample

The same analysis was performed for the Trabant40 sample. The observed shift in the XRD pattern is shown in Figure 87. Due to its lower alpha dose rate despite its higher Pu content (see Table 11), the shift in the XRD pattern (and thus the lattice parameter increase) is slower in this sample compared to the Capra4 sample.

Figure 88 shows the behavior of the lattice parameter increase of this sample with the time, which is compared to a fit using Equation 10 and to Kato's data [4]. The fit results are in a good agreement with the evolution calculated with the Kato's data. Here, the calculated B.λ' value after the fitting yields $1.76 \cdot 10^{-8}$ s^{-1}, compared to $1.42 \cdot 10^{-8}$ s^{-1} for Kato.

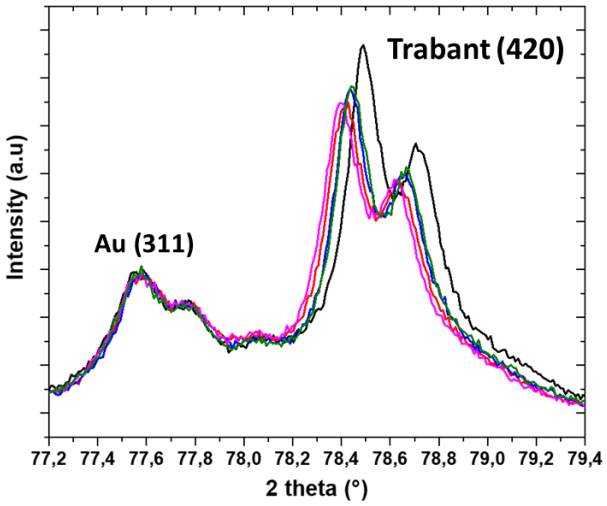

Figure 87 Evolution of Trabant40 sample XRD patterns after the first annealing through the representative (420) diffraction peak. The **black** 70 days after annealing, **olive** 247 days after annealing, blue 336 days after annealing, red 424 days after annealing, **magenta** 483 days after annealing.

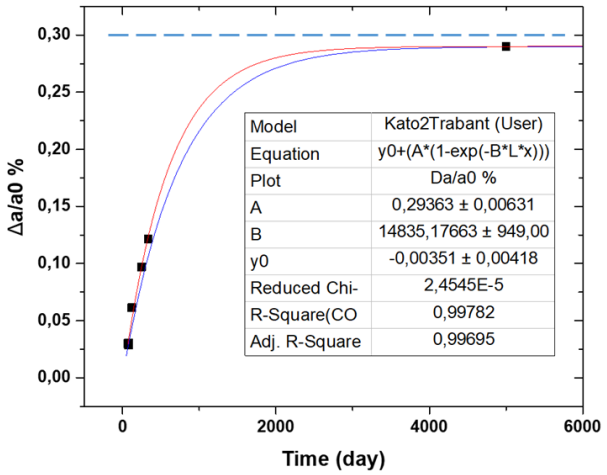

Figure 88 Trabant40 lattice parameter increase comparison with the Kato's empirical formula. The **black** scattered points are the experimental data of the Trabant40 calculated lattice parameter; the blue curve is the calculated lattice parameter increase using Kato's empirical formula.

An analysis for the FWHM evolution within the (420) diffraction line was also conducted for the Trabant40 sample, similar to the approach taken for the Capra4 sample. However, it was observed that the FWHM values obtained were significantly influenced by the choice of the region of interest (see the yellow zones in Figure 84), resulting in a very large uncertainty in the values. Hence, given this inherent variability, no attempts were made to fit the values, and no further analysis was made related to this observation.

Table 23 The FWHM values of the (420) diffraction peak of the patterns shown in Figure 87

Day after annealing	70	247	336	424	483
FWHM of (420) reflection	0.255 ± 0.02	0.265 ± 0.02	0.259 ± 0.02	0.285 ± 0.02	0.265 ± 0.02

4.2.2 Raman Spectroscopy analysis of the Capra4 sample

The time evolution of the Raman signals of the Capra4 sample is described in this section. Here, six samples are compared. The first one is freshly annealed (one day after annealing), four others are 44, 75, 421 and 582 days old and the last one is to the aged sample (~ 8000 days old).

4.2.2.1 Sampling strategy

At first, the main information sought here is an average information, *i.e.* an average spectrum with a sufficient signal-to-noise ratio for small spectral variations from one sample to another to be noticeable. To ensure that the measurement statistics are sufficient, it is necessary to record a minimum number of spectra, since the signal-to-noise ratio vary as the square root of the number of spectra.

At first, the main information sought here is an average spectrum with a satisfactory signal-to-noise ratio, which allows us to observe minor spectral differences between various samples. To be able to ensure that our measurement statistics are sufficient, it is essential to acquire a minimum number of spectra, given that the signal-to-noise ratio improves as the square root of the number of spectra increases.

As an attempt to reduce the acquisition time, a Raman image on a sample was first recorded. This image contained about 1500 acquisition points. Different average spectra were extracted from the image, from regions where the Pu content (*i.e.* the position of the T_{2g} band) appeared to be rather homogeneous. The size of these averaged regions was progressively increased until all the average spectra were indistinguishable from each other. These identical averaged spectra were considered as representative of the matrix phase.

Subsequently, different line profiles were recorded on the same sample. Similarly, average spectra were obtained, excluding the points obtained for areas of high or low Pu contents, that lie outside the main frequency histogram. It was shown that about 200 spectra were needed to retrieve an average spectrum similar to the representative spectrum extracted from the Raman image. Hence, for the remaining acquisitions, line profiles of 400-500 spectra were collected and averaged (after removal of the U- and Pu-rich spectra) for observing the spectral evolutions.

The second information we are looking for is the evolution of signals characterizing Pu-rich and U-rich clusters. For such a purpose, we will simply use the Raman images of the annealed and old samples, in which it is possible to observe several of them.

4.2.2.2 Analysis of average spectra

The average Raman spectra of the six Capra4 samples are reproduced in Figure 89. Here, we focus only on the first order region, where the T_{2g} and the U* bands are present. Considering the high average Pu content of the sample, the 2LO mode is indeed no longer clearly observed, nor does it brings any particular information see Figure 68 of Chapter 3).

For an initial and purely visual examination, a first means to examine the data was to normalize all the average spectra to the amplitude of the T_{2g} mode. Figure 89a immediately shows that self-irradiation causes little change in the line shape of the spectra. The T_{2g} band is progressively shifting to the lower frequencies, increasing in its width (FWHM) and developing some asymmetry on its lower frequency side as shown in the inset in the figure. This asymmetry is clearly detectable after 421 days of self-irradiation. Concerning the U* frequency range of the spectrum, *i.e.* the defect bands, the U_1, U_2 and U_3 bands appears to have some intensity increase, perhaps with some differences in magnitude. Still concerning the U* signal, one can also normalize the signal to the amplitude of the 1LO mode see Figure 89b. This way of proceeding, still purely visual, tends to confirm the progressive increase in intensity of the U_1 and U_3 signals compared to the 1LO. This perception would have required to be confirmed by fitting the signal

with three components. We will not go any further in this analysis, as the U* signal is not sufficiently resolved to allow the use of the fit results without ambiguity considering that a minimum of twelve parameters have to be adjusted.

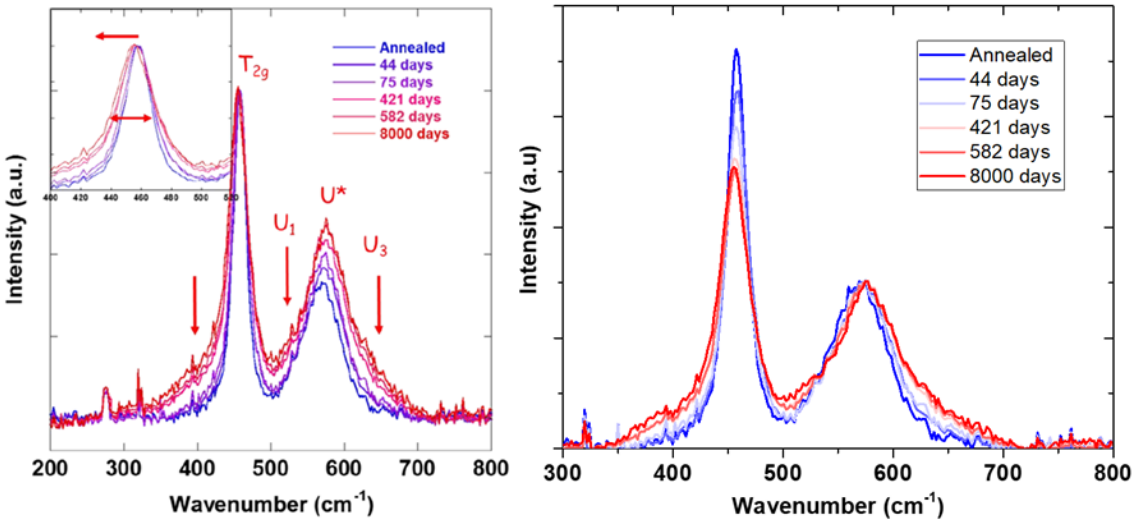

Figure 89 Average Raman spectra (the 200-800 cm^{-1} region) of the periodic acquisitions with the Capra4 samples having different levels of cumulated self-irradiation damage. The insert focuses on the T_{2g} band line profile. The arrows indicate some of the observed evolutions in the average spectra. Figure on the left, spectra normalized with respect to T_{2g} line intensity, on the right: spectra normalized with respect to U* intensity.

4.2.2.3 Methodology for the acquisition of characteristic features from the spectra

To further quantify the data, it is necessary to fit the spectra, to extract some characteristic parameters: the frequency and width of the T_{2g} mode, and the U*/T_{2g} intensity ratio (as was done in the previous chapter). Here, we still consider the U* line as a whole, for simplicity. This quantification can be achieved in two distinct ways:

- (i) a simple line fitting of the average spectra,
- (ii) the line fitting of all the individual spectra, with a further use of the corresponding histograms, or the arithmetic mean values, in a more statistical approach.

Without clearly understanding its physical interpretation at this point, we do not take into account the apparent asymmetry of the T_{2g} mode as it will be discussed later in this document.

Why should we need these different approaches? Here, as it will be discussed later, we are first looking for a frequency information. Still without anticipating the discussion, those frequency variations are necessarily small, less than a few reciprocal centimeters, at most. The reason behind this will be discussed in Chapter 5. The average spectrum cannot be easily corrected for small spectrometer drifts over time. It therefore contains an error on the absolute frequencies that is difficult to quantify. On the other hand, it is easy to correct the individual frequency profiles from these drifts. More, using the individual spectra, it is also straightforward to remove values that correspond to Pu-rich and U-rich clusters, in other words by masking/removing these values. To this end, we can use the spectrometer drifts-corrected frequency histograms. This last value is probably the most accurate. Three frequency values will be given:

- the maximum of the histograms,
- the arithmetic mean of the corrected frequencies of all spectra
- the arithmetic mean of the corrected frequencies after masking the data corresponding to Pu or U-rich clusters.

The evolution of the T_{2g} mode width is examined on the basis of the two last arithmetic averages.

Finally, the U*/T_{2g} intensity ratio was simply extracted from the average spectra, because of the high noise level of all individual acquisitions.

4.2.2.4 Evolution of the parameters extracted from the Raman spectra

The temporal evolution of these three parameters is shown in Figure 90 and Figure 91. One can see that they first evolve rapidly, before tending towards some saturation value. Once again, we can see that the variations of the parameters over time are relatively small, but they stand out clearly from their respective uncertainties. The trends are therefore clear.

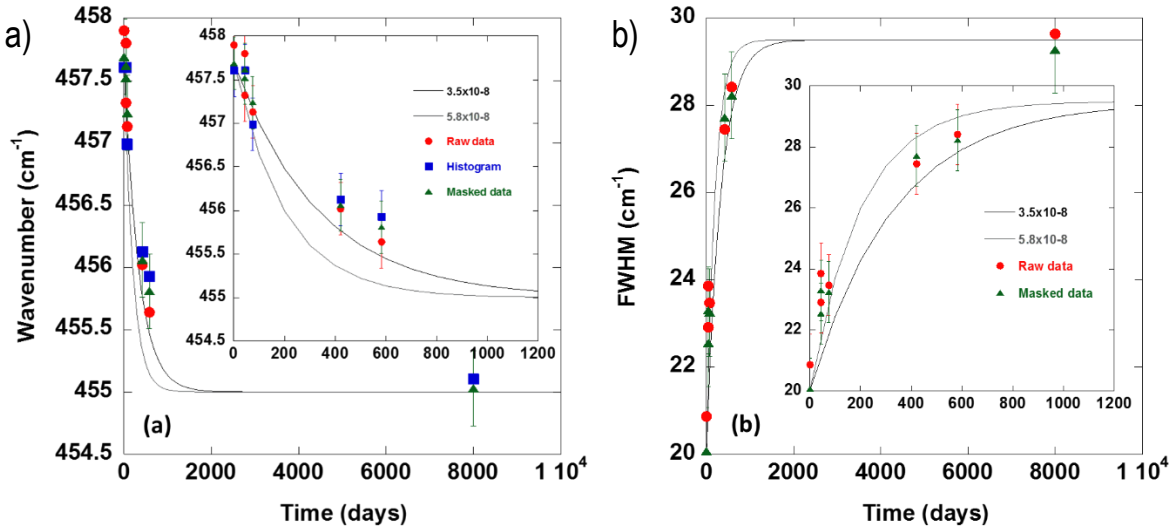

Figure 90 Evolution of the spectral parameters a) T_{2g} line frequency, b) T_{2g} line width with the self-irradiation effect. The experimental data is presented as dots and compared to fits (presented as lines) based on Eqn 10 with a $B\lambda'$ values extracted from Figure 86.

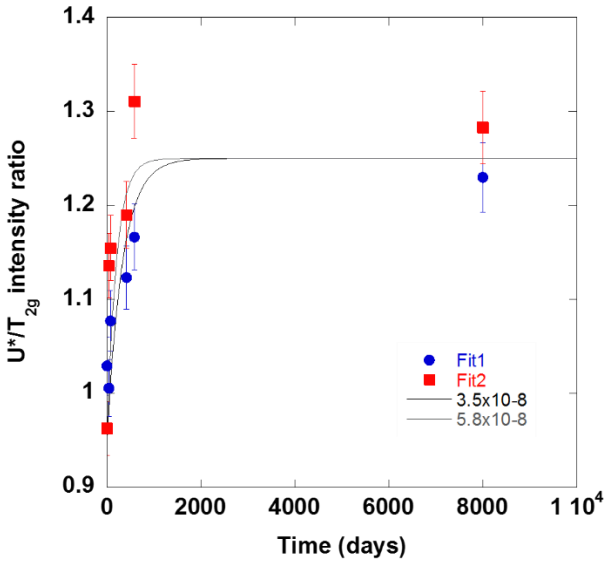

Figure 91 Evolution of the U* intensity normalized with the T_{2g} line intensity with the self-irradiation effect. The experimental data is presented as dots and compared to fits (presented as lines) based on Eqn 10 with a $B\lambda'$ values extracted from Figure 86.

In these figures, we also reproduce two evolutions based on the equation used to reproduce the lattice parameter swelling (or the opposite when the given characteristics decreases with time). Here, the "A" parameters, see Eqn 10 and Table 5 in Chapter 1, that correspond to the saturation of the experimental values, are simply taken from the corresponding figures. Parameters B.λ are those determined from the material swelling data, see Figure 86 and Figure 88. One can see that the time constants determined from the α-decay (3.5×10^{-8} s^{-1}) or the fit of the diffraction data (5.8×10^{-8} s^{-1}) can be used to follow the time evolutions of the main spectral features, accepting some uncertainty in the Raman data. To go further in this direction, more experimental points are obviously needed, notably after 600 days following sample annealing, which is beyond the timeline of this thesis.

The last information to be retrieved from all these measurements is the evolution of the line shift of the T_{2g} mode as a function of the average strain of the "average" lattice parameter, as determined with XRD. For small strains, line shifts can indeed be discussed according to different formalisms, namely phonon deformation potentials, or more simply the so-called Grüneisen parameter, see Section 2.2.3.4.4. For small strains, a linear behavior is expected between these parameters. Results are given in Figure 92, in which the lattice strain was recalculated from the fit of the diffraction data given in Figure 88. A linear dotted line is given, for visualization purposes. Here, we mainly trust the "masked" data, for which we try to give an error margin. Considering Figure 92, a purely linear behavior is obviously questionable, in particular for the highest strains.

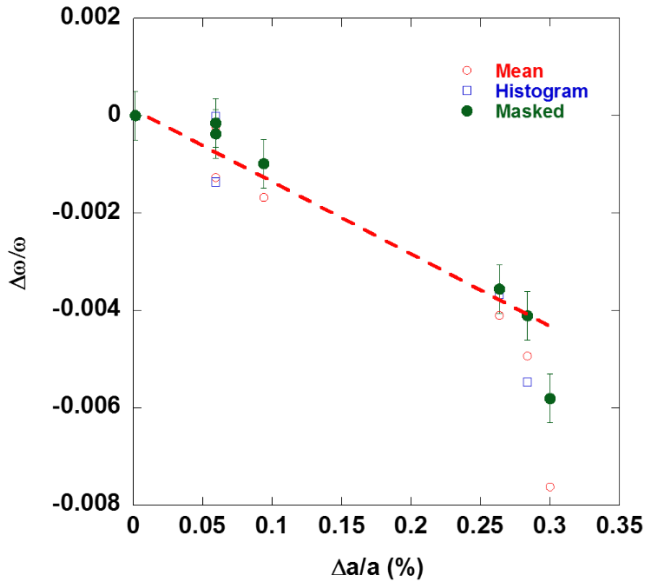

Figure 92 Evolution of $\Delta\omega/\omega$ vs the self-irradiation induced strain $\Delta a/a$. At this point, the linear dashed line is only a guide for the eyes.

4.2.2.5 The case of U- and Pu-rich spots

The evolution of the average spectra of the U-rich and the Pu-rich spots are shown in Figure 93 and Figure 94. For this comparison, only the two extremity cases, which are the freshly annealed and the 8000 days old samples are examined. The Raman images are available for both specimens, enabling to extract several spectra that are characteristic for these specific regions. In both figures, the characteristic spectra of the freshly annealed and the aged samples are shown in bluish and reddish colors, respectively. A few spectra are given for each sample and each type of spots, and the indicated figures show that they overlap almost perfectly in every cases. The characteristic T_{2g} frequencies of these clusters are close to 445 and 476 cm^{-1}, making them almost but not completely pure UO_2 and PuO_2 clusters, as already discussed in Chapter 3.

We first focus on the UO_2 clusters in Figure 93. Examination of the spectra immediately shows that the U* line gains some intensity, while the 2LO mode loses intensity. Once again, the U* line is not clearly resolved into its three expected components. The T_{2g} mode broadening is obvious. On the other hand, the T_{2g} mode does not seem to be shifting in frequency, contrarily to what was clearly observed in the matrix. Nevertheless, the line profile of the T_{2g} mode (asymmetry towards high wavenumbers) may suggest that the analyses are subject to a small error, more precisely that they might not be perfectly focused exclusively on clusters with the same sizes and uranium contents. Regarding this, looking at Figure 64 will help understand the reader about the size and variation of Pu content in the U-rich clusters, also for the Pu-rich clusters in the Capra4 sample surface.

Concerning the PuO_2 clusters in Figure 94, the second-order region does not give any clear information,

even if a decrease of the (already weak) 2LO mode is still observable. For the annealed sample, the U* signal is clearly resolved in three components, still to be assigned to the U_1, 1LO and U_3 signals. It is seen from the figure that the intensity of the U_1 mode may be predominant. These three modes tend to broaden upon self-irradiation. Finally, both a shift and a broadening of the T_{2g} mode are observed. In particular, the downshift is close to 2.5 cm^{-1}, a value that is similar to that observed for the average spectra, see Figure 89a.

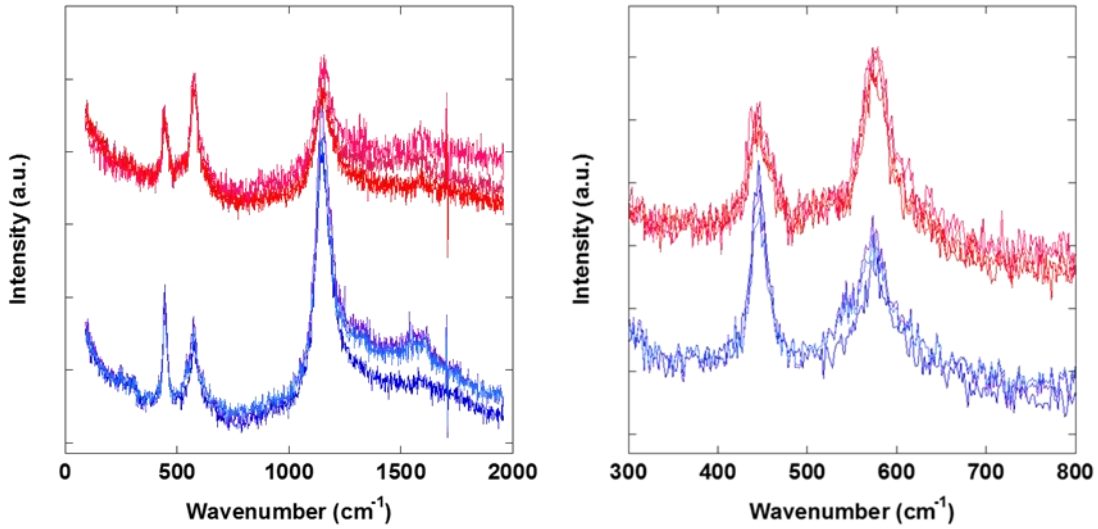

Figure 93 Some characteristic spectra of U-rich clusters, extracted from the Raman images of the annealed (blueish traces) and aged (reddish traces) samples. a) full spectrum. b) close-up of the first-order region.

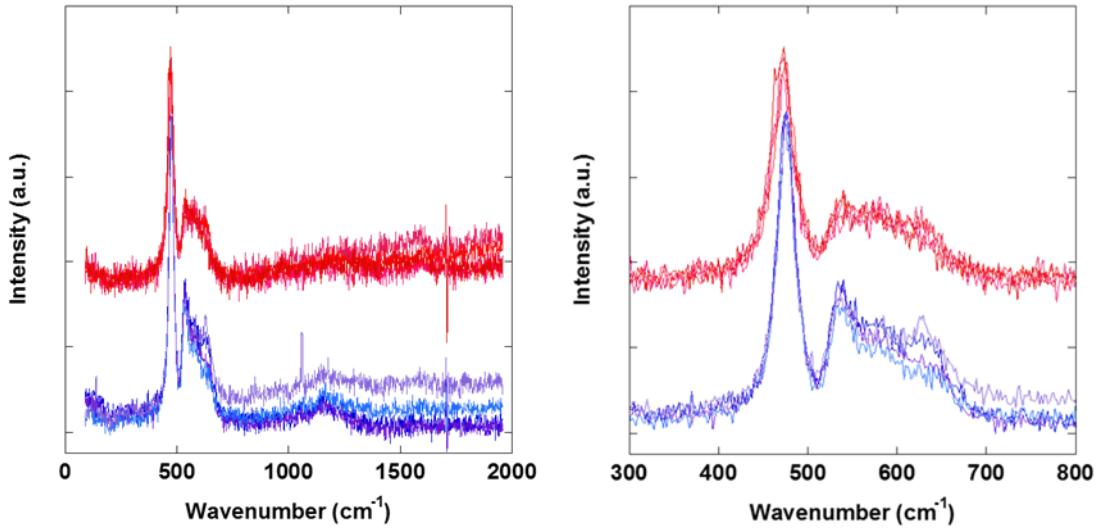

Figure 94 Some characteristic spectra of Pu-rich clusters, extracted from the Raman images of the annealed (blueish traces) and aged (reddish traces) samples. a) full spectrum. b) close-up of the first-order region

4.2.3 XANES

We first focus on the evolution of XAS signals from Capra4 samples. As a reminder, these measurements were carried out at the ROBL beamline at the ESRF, at 15K.

4.2.3.1 Capra4

The XANES results obtained on the annealed samples are given in the previous chapter. Here we simply discuss the evolution of the mean oxidation states with respect to self-irradiation effect. In what follows, we focus on the U-L_{III}, Pu-L_{III}, and Am-L_{III} edges for which the XANES spectra are given in Figure 95,

Figure 96 and Figure 97. A first examination of the spectra immediately shows that there is only little change in the line shape of the spectra at the three edges.

More information can be obtained fitting the spectra. Main results are given in Table 24, which gives the oxidation states of U, Pu and Am obtained by fitting through a linear combination of spectra of reference compounds (also given in Figure 95, Figure 96 and Figure 97). It appears that the U atoms are always slightly oxidized, the Pu atoms are slightly reduced whereas the Am cations are fully reduced to Am^{+3}. Regarding the analysis of the Am L_3 edge, due to the scarcity of this particular cation within the composition, the signal quality is low, which is visible especially in the region of the first EXAFS scattering. This fluctuation does not hinder the analysis in the XANES part and thus the linear combination analysis. Considering the evidences in the literature, it was expected that the reduction of plutonium atoms starts only once all the americium is reduced to the trivalent state [148]–[152]. Consequently, while the calculated value for this cation was also a close value to 3.00, no uncertainty was assigned to this calculation. We do not discuss any potential evolution in its oxidation state.

The global O/M ratio of the samples thus remains very close to the stoichiometry, even after long time exposure to the self-irradiation damage. This is mainly due to the charge compensation mechanism existing between U^{+5} which is present in a similar amount as the sum of Pu^{+3} and Am^{+3}. This result is thus in line with the most recent literature on the subject, which includes both experimental data and thermodynamics modeling.

We can therefore assume, as a preliminary assumption, that the average oxidation states of the various cations and thus the O/M ratio remain close to constant over time.

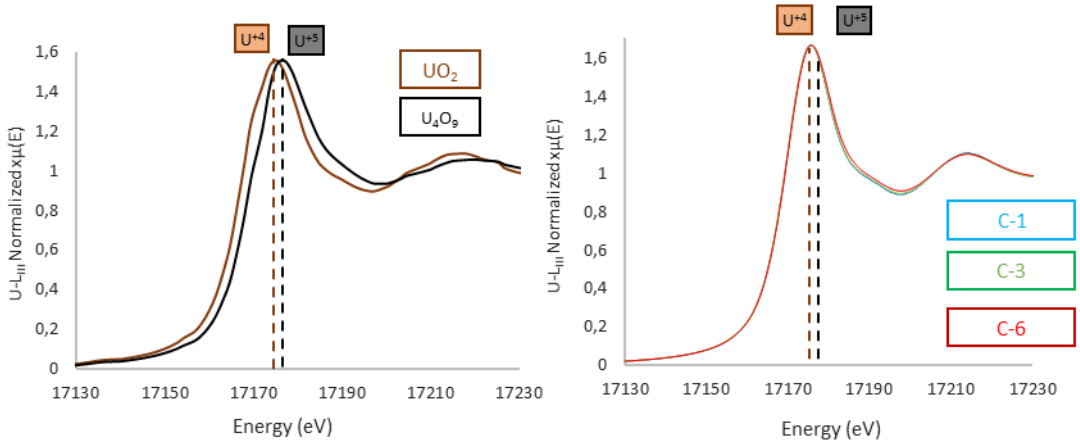

Figure 95 U-L_{III} XANES analysis of Capra4 samples. Left Side: reference spectra for comparison. Right Side: C-1 is 44 days old, C-3 is 134 days old, C-6 is 8000 days old Capra4 samples compared with the reference positions.

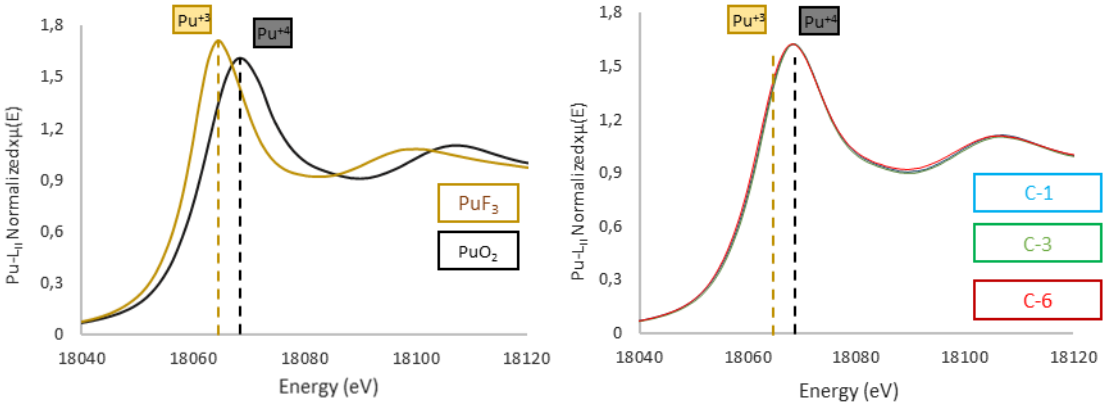

Figure 96 Pu-L_{III} XANES Analysis of Capra4 Samples. Left Side: reference spectra for comparison. Right Side: C-1 is 44 days old, C-3 is 134 days old, C-6 is 8000 days old Capra4 samples compared with the reference positions.

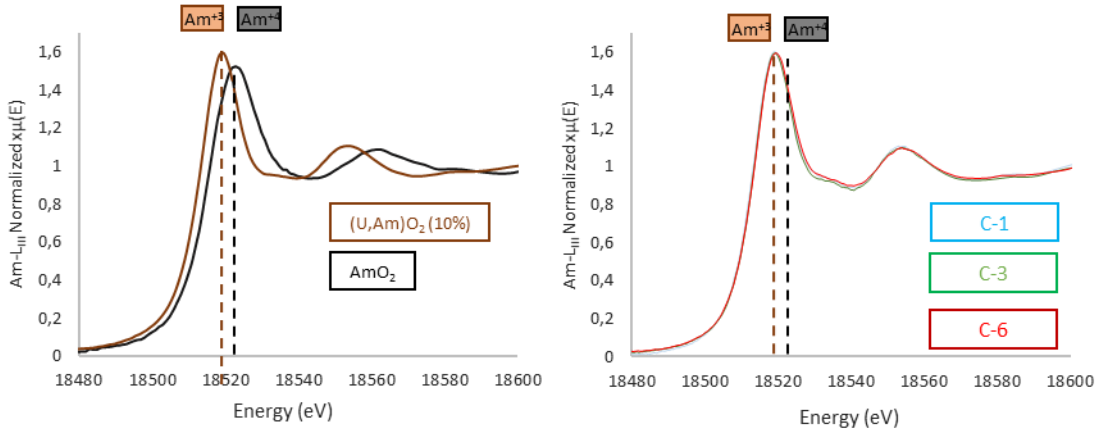

Figure 97 Am-L_{III} XANES Analysis of Capra4 Samples. Left Side: reference spectra for comparison. Right Side: C-1 is 44 days old, C-3 is 134 days old, C-6 is 8000 days old Capra4 samples compared with the reference positions.

Table 24 The changes in cation oxidation states and O/M ratios over time due to self-irradiation in the Capra4 samples. The red data is the O/M calculated using XRD using Duriez's equation (3)

Sample	C-1	C-2	C-3	C-4	C-5	C-6
Age (days)	44	75	134	356	518	9800
U^{+4} (%)	92.9	93.5	92.3	94.8	91.2	88.3
U^{+5} (%)	7.2	6.5	7.8	5.2	8.7	11.7
U^{+6} (%)	0	0	0	0	0	0
U	4.07(5)	4.07(5)	4.08(5)	4.05(5)	4.08(5)	4.12(5)
Pu^{+3} (%)	4.7	3.8	1.5	7.1	3.2	10.4
Pu^{+4} (%)	95.3	96.2	98.5	92.9	96.8	89.6
Pu	3.95(5)	3.96(5)	3.98(5)	3.93(5)	3.96(5)	3.90(5)
Am	3.0	3.0	3.0	3.0	3.0	3.0
O/M	2.00(1) 2.01(1)	2.01(1)	2.01(1)	2.01(1)	2.01(1)	2.01(1)

4.2.3.2 Trabant40

We do not give here the XANES spectra corresponding to the Trabant40 samples, as they are in all respects similar to those described above for the Capra4 samples. The average oxidation states obtained by fitting the spectra are given in Table 25. The extracted values are similar to those of the Capra4 samples. It still appears that the U atoms are slightly oxidized, whereas the Pu atoms are slightly reduced. The same charge compensation mechanism relating U^{5+}, Pu^{3+} and Am^{3+} states that is observed for the Capra4 also takes place for Trabant40 leading to a constant O/M ratio close to 2.00.

Table 25 The changes in cation oxidation states and O/M ratios over time due to self-irradiation in the Trabant40 samples. The red data is the O/M calculated with XRD using Duriez's equation (3)

Sample	T-1	T-2	T-3
Age (days)	44	356	9800
U^{+4} (%)	97.5	94.8	93.7
U^{+5} (%)	2.5	5.3	6.3
U^{+6} (%)	0	0	0
U	4.03(5)	4.05(5)	4.06(5)
Pu^{+3} (%)	5.1	0.6	3.5
Pu^{+4} (%)	95.9	99.4	97.3
Pu	3.99(5)	3.99(5)	3.99(5)
Am	3.0	3.0	3.0
O/M	2.00(1) 1.99(1)	2.01(1)	2.01(1)

4.2.4 EXAFS

4.2.4.1 Capra4

4.2.4.1.1 General aspect of the spectra and fit results

The UL_{III} and PuL_{II} EXAFS signals and the associated FT (Fourier transforms) for the six Capra4 samples are respectively shown in Figure 98 and Figure 99 . At the first glance, the comparison of the EXAFS and FT spectra intensity between the samples is consistent with the increase of disorder in the microstructure with the increased self-irradiation accumulated damage. This is evident with the progressive damping of the signals.

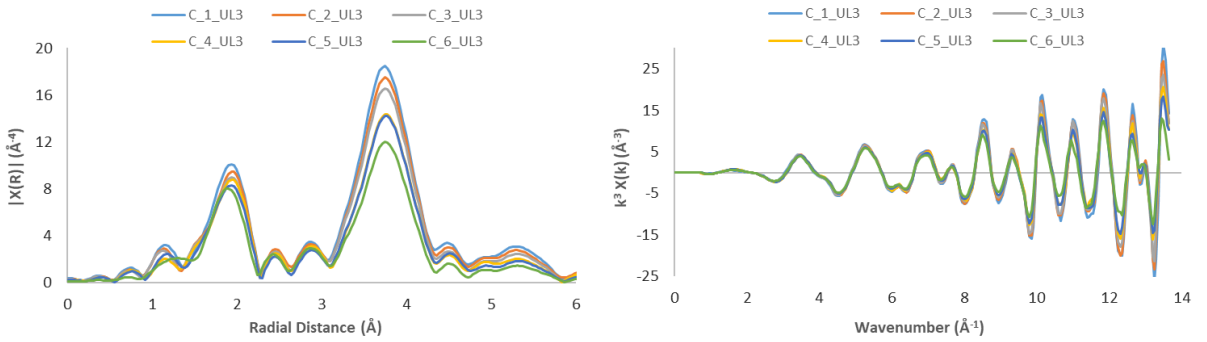

Figure 98 Comparison of the U L_{III} spectra of the Capra4 samples with the Fourier transform (extracted from a k range of 3.5-12.8 $Å^{-1}$) on the left and the EXAFS spectra on the right. C-1 is 44 days old, C-2 is the 75 days old, C-3 is 134 days old, C-4 is 421 days old, C-5 is 582 days old, C-6 is 8000 days old sample.

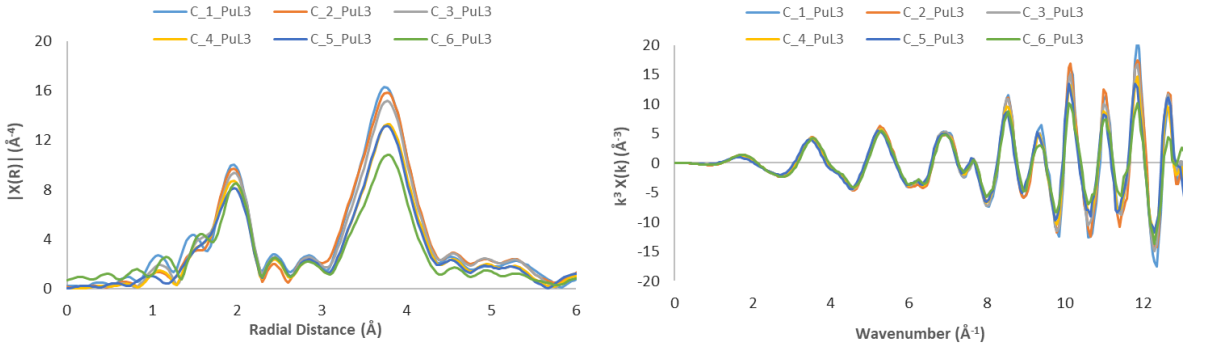

Figure 99 Comparison of the Pu L_{II} spectra of the Capra4 samples with the Fourier transform (extracted from a k range of 3.5-12.8 $Å^{-1}$) on the left and the EXAFS spectra on the right. C-1 is 44 days old, C-2 is the 75 days old, C-3 is 134 days old, C-4 is 421 days old, C-5 is 582 days old, C-6 is 8000 days old sample.

Despite the amplitude decrease with time, no significant modifications of the local structure around the cations are visible on the EXAFS spectra at both edges. The spectra of the six samples were thus fitted based on a defect-free fluorite-type structure model (as described C.4.5.2.1). The results of these fits (both as EXAFS spectra and FT) are shown in Figure 100 and Figure 101, respectively for the U-L_{III} and Pu-L_{II} edges.

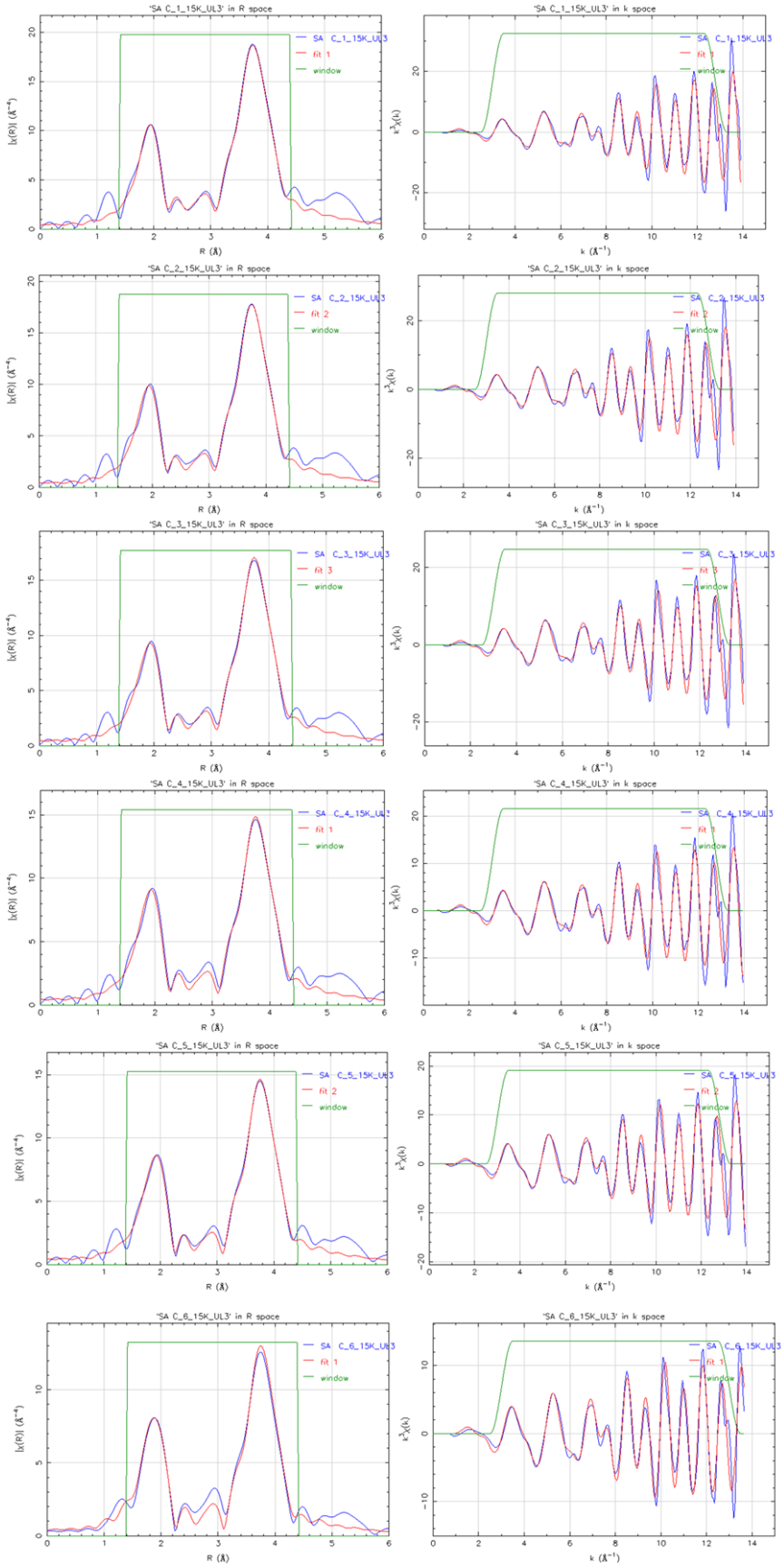

Figure 100 Experimental and fitted Fourier transform (on the left) and EXAFS spectra (on the right) of the Capra4 samples at U-L_{III} edge (fitted between 1.4 to 4.4 R (Å), k range from 3-12.8 A^{-1}). C-1 is 44 days old, C-2 75 days old, C-3 134 days old, C-4 421 days old, C-5 582 days old and C-6 8000 days old. The blue line corresponds to the experimental data, the red line to the fit and the green line to the range used for the fit (in the FT) or to calculate the FT (in the EXAFS spectra).

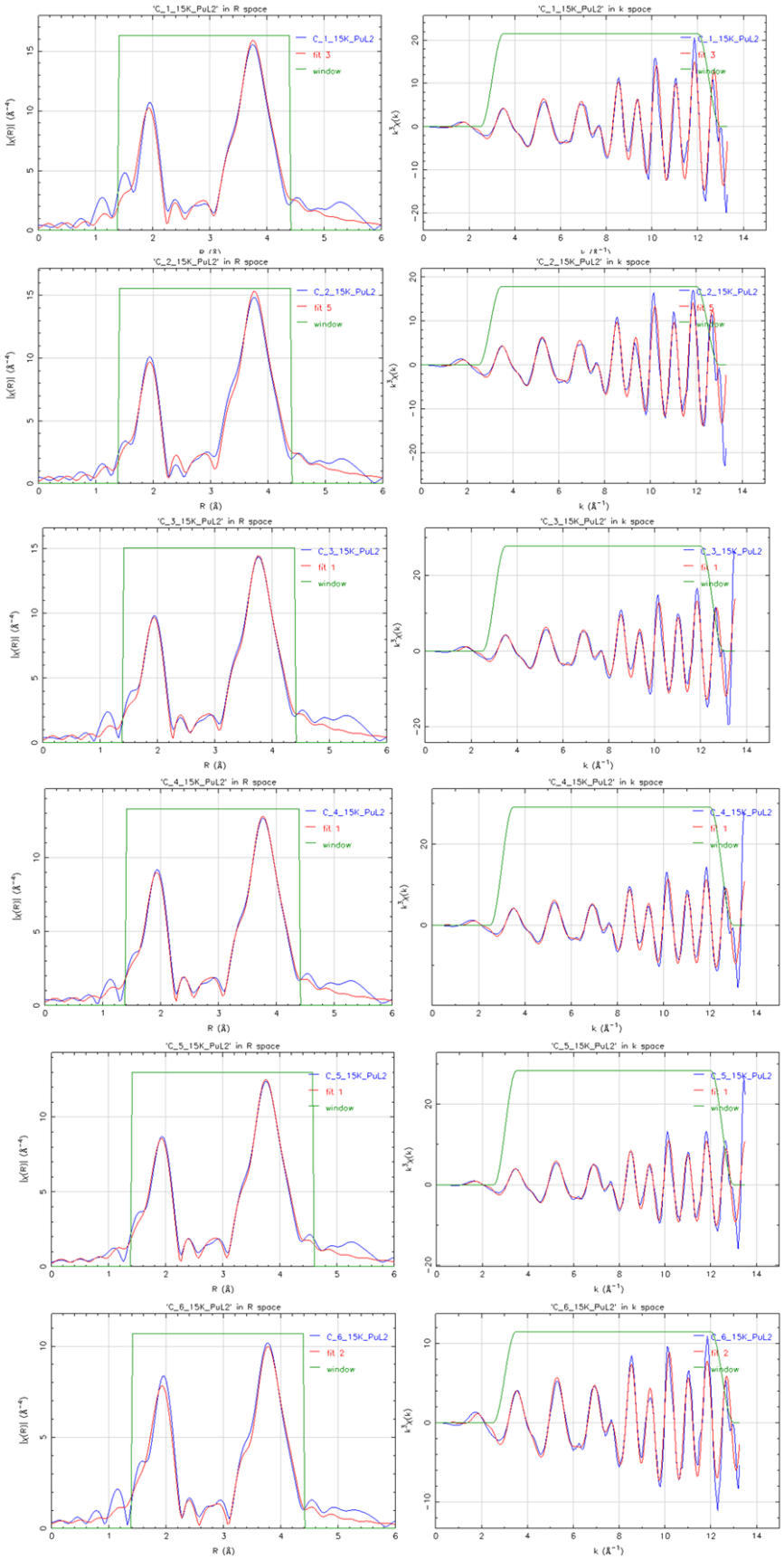

Figure 101 Experimental and fitted Fourier transforms (on the left), EXAFS spectra (on the right) of the Capra4 samples at Pu-L_{II} edge (fitted between 1.4 to 4.4 R (Å), k range from 3-12.5 A^{-1}). C-1 is 43 days old, C-2 75 days old, C-3 134 days old, C-4 421 days old, C-5 582 days old and C-6 8000 days old. The blue line corresponds to the experimental data, the red line to the fit and the green line to the range used for the fit (in the FT) or to calculate the FT (in the EXAFS spectra).

4.2.4.1.2 Evolution of distances and disorder in the first cation-oxygen and cation-cation shells

Regarding the results of the fit, we only focus here on cation-oxygen and cation-cation first shell distances. Considering that the EXAFS oscillations of the second cation-O coordination shell are almost superimposed with those of the first cation-cation coordination, except the distances obtained exhibited larger uncertainties than for the other shells. Therefore, we do not discuss the second shell distance. The values extracted from the fits are summarized in Table 26 and the associated main trends are given in Figure 102 and Figure 103.

Table 26 Capra4 samples structural parameters extracted from the fit of the EXAFS spectra at both U-L_{III} and Pu-L_{II} edges

Sample	Edge, (fit R value)	Coordination shell	R (Å)	σ^2 (Å^2)	E_0(eV)
C-1	U-L_{III}	U-O (1st)	2.345(5)	0.0034(2)	0.95(13)
43 days old	(0.0012)	U-M (1st)	3.848(5)	0.0012(2)	0.95(13)
	Pu-L_{II}	Pu-O (1st)	2.348(5)	0.0049(2)	2.22(23)
	(0.0040)	Pu-M (1st)	3.846(5)	0.0018(2)	2.22(23)
C-2	U-L_{III}	U-O (1st)	2.346(5)	0.0040(2)	1.69(15)
75 days old	(0.0016)	U-M (1st)	3.854(5)	0.0014(2)	1.69(15)
	Pu-L_{II}	Pu-O (1st)	2.348(5)	0.0054(2)	2.84(21)
	(0.0036)	Pu-M (1st)	3.851(5)	0.0020(2)	2.84(21)
C-3	U-L_{III}	U-O (1st)	2.345(5)	0.0044(2)	1.16(15)
134 days old	(0.0018)	U-M (1st)	3.855(5)	0.0016(2)	1.16(15)
	Pu-L_{II}	Pu-O (1st)	2.351(5)	0.0053(2)	2.50(18)
	(0.0033)	Pu-M (1st)	3.853(5)	0.0023(2)	2.50(18)
C-4	U-L_{III}	U-O (1st)	2.346(5)	0.0047(2)	1.88(16)
421 days old	(0.0020)	U-M (1st)	3.858(5)	0.0023(2)	1.88(16)
	Pu-L_{II}	Pu-O (1st)	2.346(5)	0.0059(2)	2.38(19)
	(0.0035)	Pu-M (1st)	3.853(5)	0.0029(2)	2.38(19)
C-5	U-L_{III}	U-O (1st)	2.344(5)	0.0051(2)	1.57(16)
582 days old	(0.0021)	U-M (1st)	3.857(5)	0.0024(2)	1.57(16)
	Pu-L_{II}	Pu-O (1st)	2.347(5)	0.0061(2)	0.97(18)
	(0.0030)	Pu-M (1st)	3.854(5)	0.0030(2)	0.97(18)
C-6	U-L_{III}	U-O (1st)	2.336(5)	0.0054(2)	0.33(24)
> 8000 days old	(0.0043)	U-M (1st)	3.856(5)	0.0031(2)	0.33(24)
	Pu-L_{II}	Pu-O (1st)	2.347(5)	0.0072(2)	2.89(22)
	(0.0046)	Pu-M (1st)	3.854(5)	0.0042(2)	2.89(22)

No evolutions of the first U-O and Pu-O distances (Figure 102a) with self-irradiation are observed. As observed in the annealed samples, the first oxygen distance always stays significantly below that estimated from the room temperature lattice parameter.

The evolution of the first cation-cation distance (shown in Figure 102b) follows an increasing trend rather similar to that of the lattice parameter. One can therefore assume that these evolutions can be described by the time constants $B\lambda$ extracted from the diffraction data (as will be discussed later in Figure 104).

As discussed, the lattice parameter should have been corrected for thermal expansion, which cannot be done precisely here because of the lack of available data. Nevertheless, accepting a thermal expansion coefficient close to $10^{-5}K^{-1}$, close to that accepted for UO_2 in this temperature range, the mismatch between the XRD and EXAFS distances is mostly explained for the first cation-cation distances, but the first cation-oxygen distances remain significantly too short.

Finally, the data obtained for the aged sample are perhaps more questionable, insofar they are seen to deviate significantly from the mean trends. In particular, the mean cation-cation distance can no longer predict the lattice parameter. However, their behavior is rather similar in terms of saturation after certain damage.

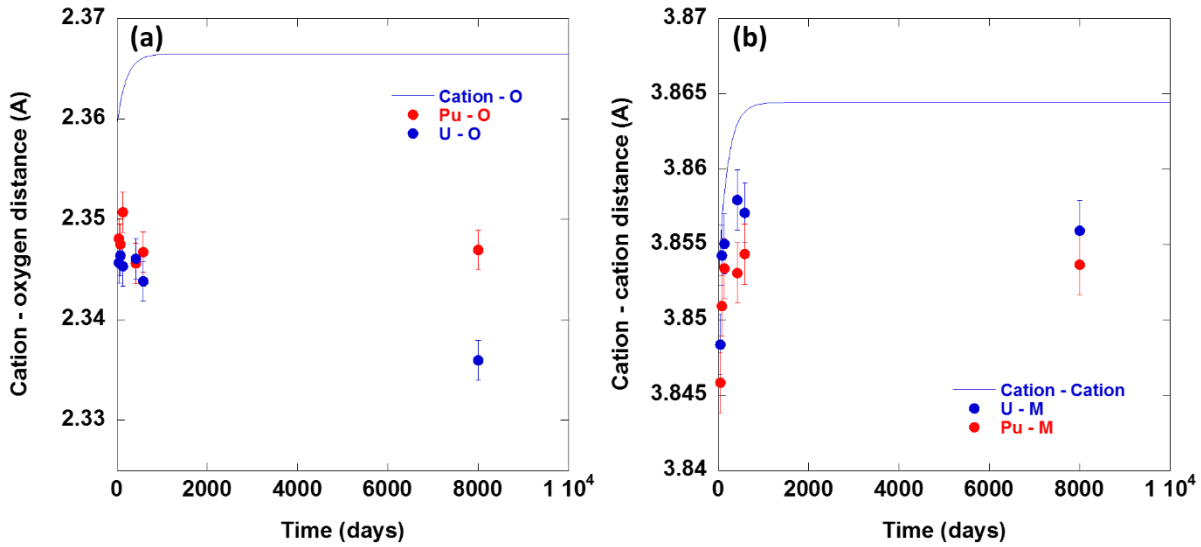

Figure 102 Evolution of the first cation-Oxygen (a) and cation-Cation distances. The dots represent the values obtained by fitting the EXAFS spectra (collected at 15 K) and the line the VCA distances calculated from the room temperature lattice parameter.

The corresponding DW factors are shown in a single plot in Figure 103. Keeping in mind that the acquisitions were made in 15K, the DW factor may be thought to be a good indicator of the level of positional disorder in the lattice. An increasing behavior is observed for the DW factor with the self-irradiation damage. This behavior looks similar to what was observed for the lattice parameter increase. In the same figure, we can see that this parameter is always higher for cation-oxygen distances than for cation-cation distances. This outcome still suggests some disorder in the oxygen sub-lattice.

Again, one can assume that these time evolutions can be described by the time constants extracted from the diffraction data, which we aimed to verify in Figure 104a and Figure 104b. In these two figures, the time constants determined both from Kato's correlation and the XRD data effectively describe the evolution of the Pu cation distance vs time. This is more questionable for the DW factors, for which the evolution seems slower.

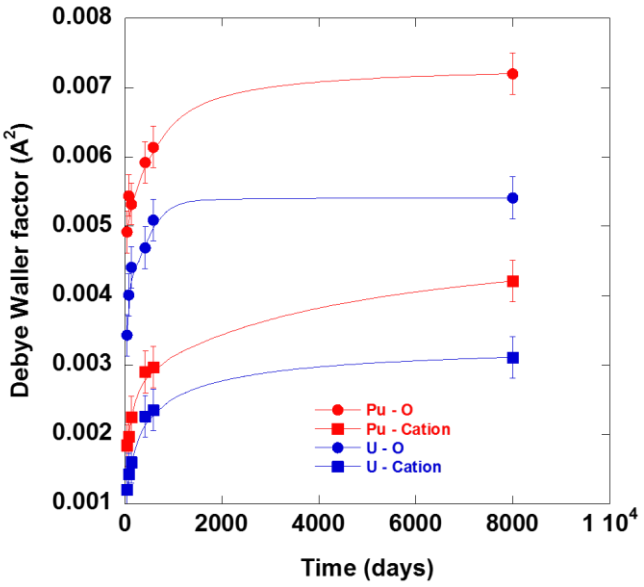

Figure 103 The calculated Debye Waller factors on the U-O, Pu-O, U-cation and Pu-cation bonds in the first coordination sphere. The full line are simple guides for the eyes.

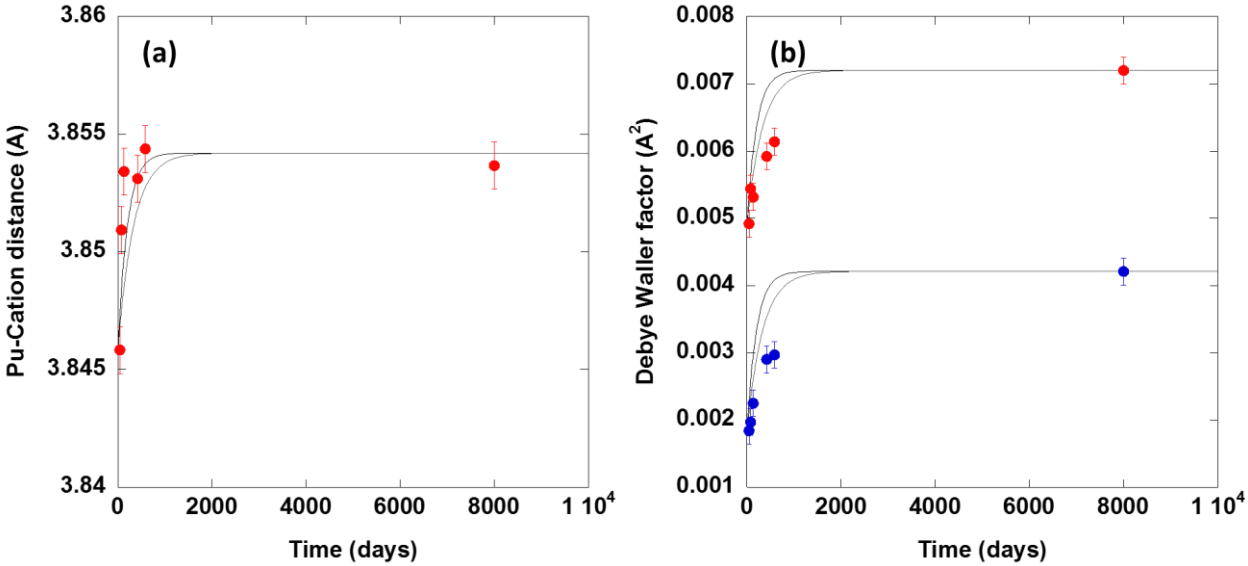

Figure 104 Comparison of some EXAFS data with the Kato's empirical correlation. For this comparison, the two time constants used are those extracted from Figure 86. (a) Evolution of the Pu-cation atomic distances in the first coordination sphere. (b) Evolution of the Debye Waller factors for Pu-O bonds (red full circles) and Pu – cation bonds (blue full circles).

4.2.4.2 Trabant40

The fitted EXAFS spectra of the Trabant40 samples are shown in Figure 105 and Figure 106 at the U-L_{III} and Pu-L_{II} edges respectively. The values extracted from the fits are summarized in Table 27 and the corresponding trends of the EXAFS data are plotted in the Figure 107a, b and Figure 108.

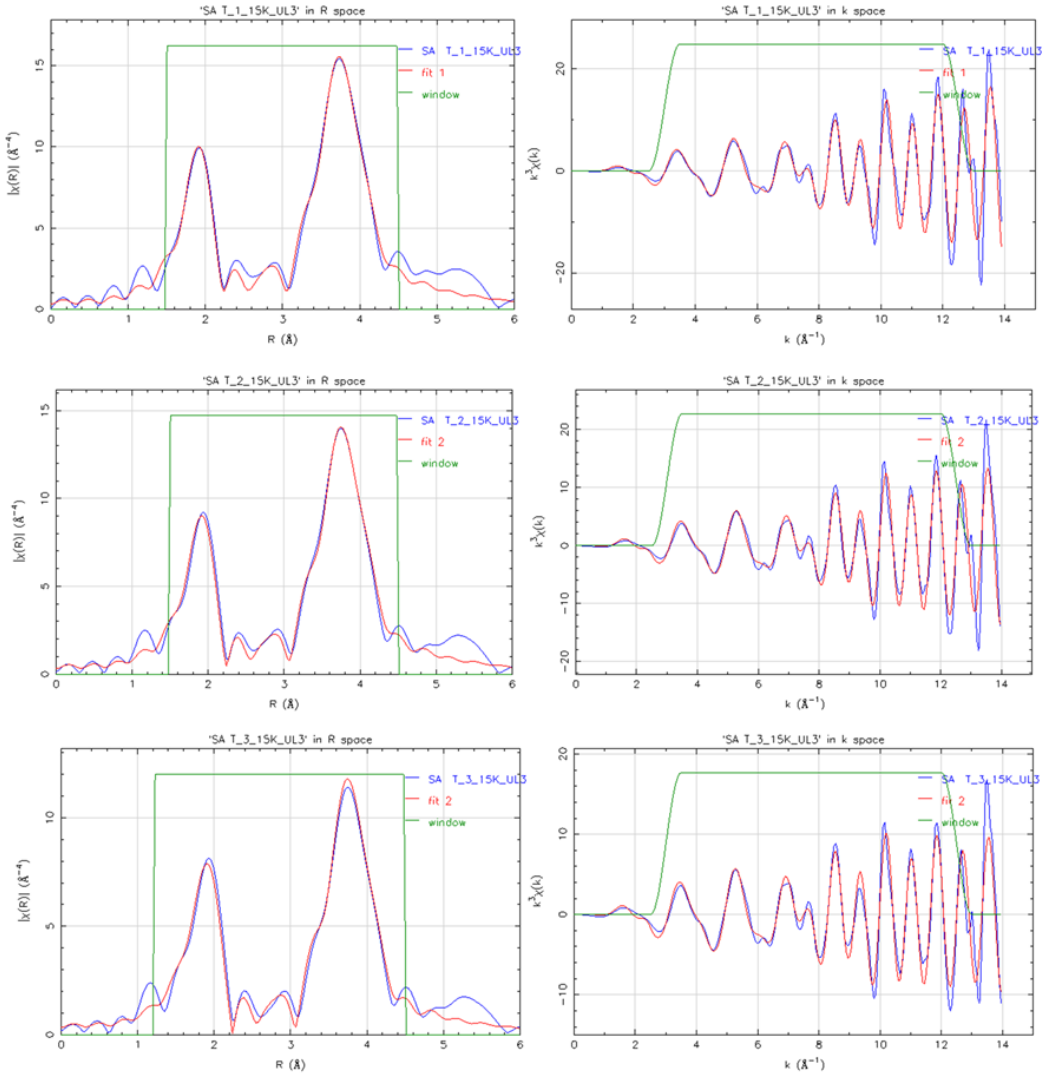

Figure 105 Experimental and fitted Fourier transform (on the left) and EXAFS spectra (on the right) of the Trabant40 samples at U-L_{III} edge (fitted between 1.5 to 4.5 R (Å), k ranges from 3-12.5 A^{-1}). T-1 is 43 days old, T-2 421 days old and T-3 8000 days old. The blue line corresponds to the experimental data, the red line to the fit and the green line to the range used for the fit (in the FT) or to calculate the FT (in the EXAFS spectra).

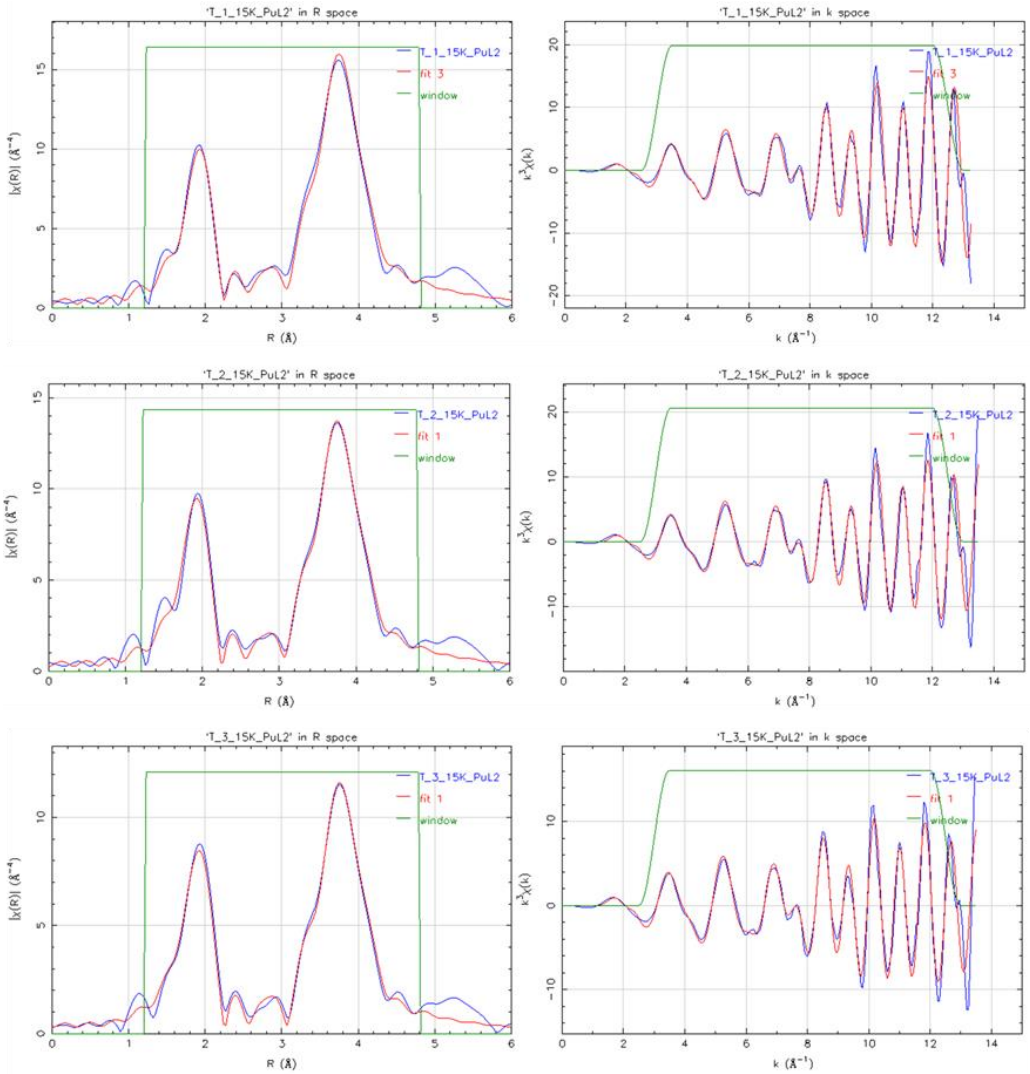

Figure 106 Experimental and fitted Fourier transform (on the left) and EXAFS spectra (on the right) of the Trabant40 samples at Pu-L_{II} edge (fitted between 1.2 to 4.8 R (Å), k ranges from 3 - 12.5 A^{-1}). T-1 is 43 days old, T-2 421 days old and T-3 8000 days old. The blue line corresponds to the experimental data, the red line to the fit and the green line to the range used for the fit (in the FT) or to calculate the FT (in the EXAFS spectra).

Table 27 Trabant40 samples structural parameters extracted from the EXAFS spectra measured at both U-L_{III} and Pu-L_{II} edges

Sample	Edge, (fit R value)	Coordination shell	R (Å)	σ^2 (Å^2)	E_0 (eV)
T-1	U-L_{III}	U-O (1st)	2.344(5)	0.0042(2)	0.17(24)
43 days old	(0.0050)	U-M (1st)	3.852(5)	0.0018(2)	0.17(24)
	Pu-L_{II}	Pu-O (1st)	2.343(5)	0.0052(2)	1.07(19)
	(0.0037)	Pu-M (1st)	3.845(5)	0.0020(2)	1.07(19)
T-2	U-L_{III}	U-O (1st)	2.344(5)	0.0052(2)	1.54(20)
421 days old	(0.0049)	U-M (1st)	3.855(5)	0.0023(2)	1.54(20)
	Pu-L_{II}	Pu-O (1st)	2.345(5)	0.0054(2)	1.74(23)
	(0.0050)	Pu-M (1st)	3.847(5)	0.0027(2)	1.74(23)
T-3	U-L_{III}	U-O (1st)	2.343(5)	0.0063(2)	1.23(23)
> 8000 days old	(0.0065)	U-M (1st)	3.855(5)	0.0032(2)	1.23(23)
	Pu-L_{II}	Pu-O (1st)	2.344(5)	0.0063(2)	1.02(22)
	(0.0052)	Pu-M (1st)	3.851(5)	0.0035(2)	1.02(22)

Figure 107 and Figure 108 present the data obtained from the fit, respectively the two first distances and their corresponding DW factors. Their time evolution is also compared to lattice parameter swelling

behavior, see the blue solid lines in the figures. For the distances (Figure 107), the lines were traced directly from the distances expected from the lattice parameter whereas only the time constant obtained by XRD were used in the case of the DW factors (Figure 108). The examination of these figures leads to the same conclusions as those drawn for the Capra4 samples:

- (i) the evolution of the cation-cation distances are in line with those expected from the lattice parameter obtained by XRD,
- (ii) the cation-oxygen distances, which are smaller than those expected from XRD, do not seem to show any evolution under self-irradiation,
- (iii) all DW factors increase following a trend that is not inconsistent with the lattice parameter trend obtained by XRD and suggested by the literature. In this case however, the EXAFS trend is obtained with only three points, which does not provide a good accuracy on the trend.

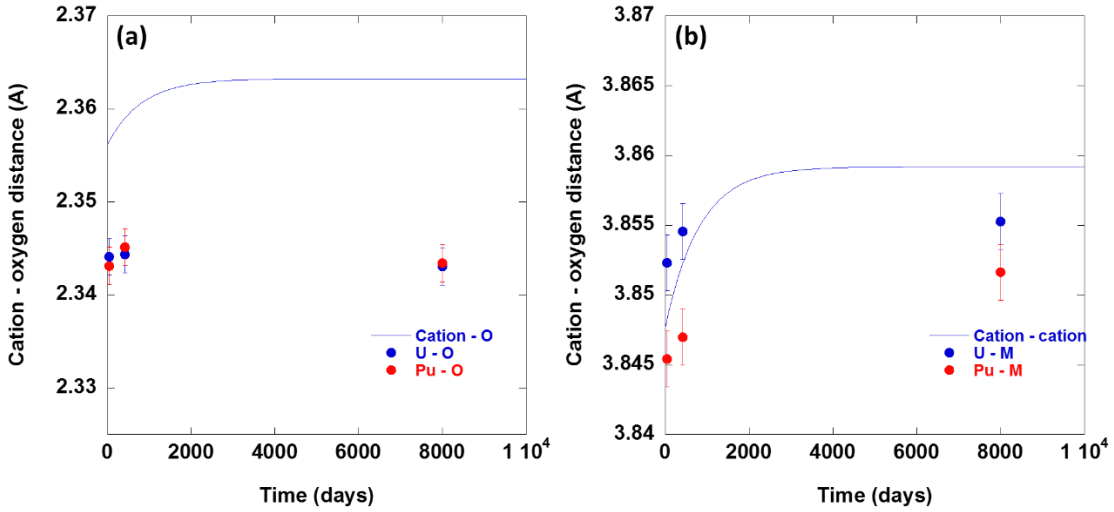

Figure 107 Evolution of the Metal-Oxygen atomic distances in the first coordination sphere, (b) Evolution of the Metal-Cation atomic distances in the first coordination sphere. The full lines were drawn using the time constants extracted from the XRD data, see Section 4.2.1.2.

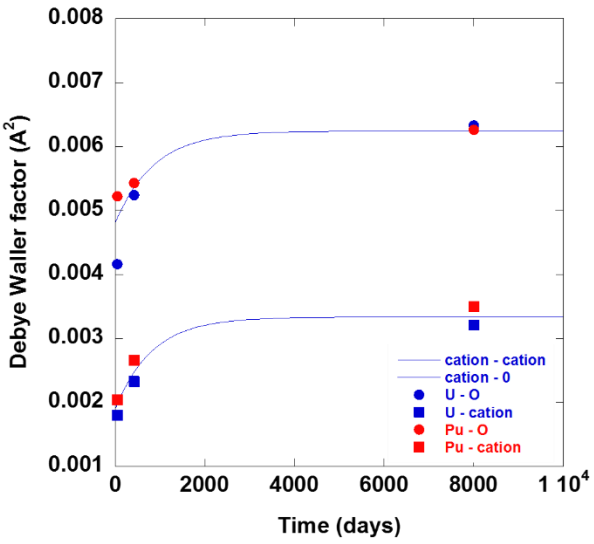

Figure 108 Debye Waller factors obtained by EXAFS for the first cation-O, and cation-cation shells. The dots are the experimental data and the full lines were drawn using the time constants extracted from the XRD data

4.2.5 First assessment of the results for the SFR-type samples

For both SFR-type samples, as expected, the time evolution of the lattice parameter obtained by XRD can be described according the expected behavior, with A and B values close to those reported by Kato.

This confirms that this lattice parameter change is mostly due to self-irradiation, and not to some oxidation or reduction process (as was sometimes observed in the literature [81]). This is consistent with the O/M ratio calculated from the oxidation states determined by XANES.

The first cation-oxygen and cation-cation distances obtained by EXAFS and their evolution with time are not as straightforward as the lattice parameter. The mean cation - cation distances and their evolution under self-irradiation correspond to those expected from the lattice parameter, bearing in mind that the EXAFS measurements were carried out at 15K. The cation-oxygen distances are however always much smaller than those expected in a perfect fluorite-type structure and do not seem to significantly change under self-irradiation. This will be discussed in Chapter 5.

Raman spectroscopy shows that the time evolution of the line shape of the spectra is rather weak. Nevertheless, our results reveal a downshift and a broadening of the Raman-allowed T_{2g} mode. The same finding also applies to the Pu-rich clusters that are present in the samples. Some asymmetry of the T_{2g} mode line progressively develops over time. The U* line as a whole seems to gain in intensity. In most cases, it cannot be clearly resolved into its three expected components. This is a clear indication of structural disorder building up in the samples under self-irradiation. Whether it can be directly related the Debye Waller factors obtained by EXAFS (which also increase under self-irradiation) or to the (although weak) oxidation of U cations and reduction of Pu cations observed by XANES will be discussed in Chapter 5.

4.3MIMAS Sample

Concomitantly to the analysis of the more homogeneous SFR samples, the MIMAS samples were also studied using the same methodology. In this part, we will use the results obtained on the “rather simpler” SFR samples as a basis for the analysis of the more complex MIMAS-type sample.

4.3.1 XRD

The evolution of the XRD pattern of the MIMAS sample since annealing is shown in Figure 109. Similar to the evolution in the Trabant40 sample, a progressive decrease in the intensity of the diffraction lines is observed overtime for this set of patterns, which will not be discussed here.

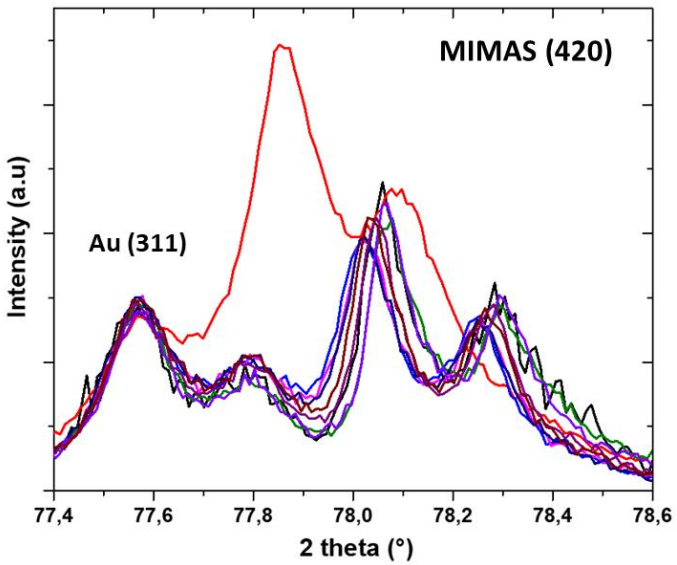

Figure 109 Evolution of MIMAS sample XRD patterns after annealing through the representative (420) diffraction peak of the fluorite-type structure (also showing the (311) Au diffraction peak used as a reference for both 2θ position and peak intensity af all data recorded after annealing). The **black** 3 days after annealing, **olive** 30 days after annealing, **violet** 131 days after annealing, **purple** 319 days after annealing, **wine** 535 days after annealing, **navy** 647 days after annealing, **magenta** 707 days after annealing, **blue** 796 days after annealing, **red**: sample before annealing (15 years)

From a first and purely visual point of view, only a relatively slow small overall shift towards the low 2θ angles. This slow shift can be explained with the fact that the diffraction line mostly reflects the U-rich agglomerates (see Figure 53). The evolution of the two other phases with the larger Pu contents is not directly visible on the pattern.

For this particular sample, the XRD pattern is fitted with three phases with three different mean Pu contents (as described in Section 3.2.1 of Chapter 3).

The calculated lattice strains of the three phases are shown in Figure 110. In this figure, the experimental trends are compared to those expected from Kato et al. [4] by assuming average Pu/(U+Pu) contents of 1, 10 and 29 %, as explained in Section 3.2.1. This assumption gives a satisfying trend to reproduce that lattice swelling of the Pu-rich agglomerates (black in Figure 110), but the comparison is not as straightforward for the two other phases. There is however undoubtedly a larger uncertainty on these strain values than on those obtained for the SFR-type samples. In particular, although the treatment of these XRD patterns seemed somehow acceptable in the early periods of the periodic data acquisition, it became rather more difficult as after a certain amount of time, the signals coming from the three phases overlapping due to the different swelling kinetics of the phases, as we will see.

These results were also fitted with the empirical formula describing the self-irradiation lattice swelling, as given in Figure 111. The results also compared with the expected trends calculated using the Kato's empirical correlation in Figure 110. The A and B values obtained after the fits are shown in Figure 111a, b and c for the corresponding phases. For the Pu-rich agglomerates, a saturation value close to 0.3% is obtained. Nevertheless, this same value can no longer describe the swelling of U-rich agglomerates and the same applies to the coating phase. The reason behind can be related to the overlapping of the signals due to different swelling kinetics of the phases as mentioned in the previous paragraph. The recorded A values for the U-rich agglomerates and the matrix phase is in the order of 0.25 %, but with a large uncertainty.

The λ' is always taken from the isotopy calculated for the MIMAS sample, while the B value can be found from the fitting and compared to what is given in Kato et al.[4]. The calculated Bλ' values after the fits are shown in Table 28. The difference in the calculated (fit) and estimated (Kato) Bλ' is quite different for the U-rich agglomerates and the intermediate phase. This is not unexpected as for the experimental data the

saturation lattice parameter increase does not even reach to 0.3%. For the Pu-rich agglomerates, however, a difference is observed by a factor of 1.4. This difference can be due to several factors but mainly can be associated to the overlapping of the signals.

From now on, we will we simply use the time constants computed from the Kato's correlation, which is ($3.39 \cdot 10^{-8}$ s^{-1}) for the Pu-rich agglomerates and ($2.9 \cdot 10^{-9}$ s^{-1}) for the U-rich agglomerates. These time constants will be more assuring for further discussion that we will later compare the EXAFS data with the XRD. For the U-rich agglomerates, it is hard to make a clear estimation in this region also due to the difference in the principal damage source for the defect creation (that is the α-particles for this particular region). Thus, we will keep this value for the following, as a simple guide for the eyes, even though it is very approximate.

Table 28 Comparison of the Bλ' values used for the estimated lattice parameter increase and the fitted data

Phase	B.λ' calculated with B from Kato et al.[4]	B.λ' calculated with B from fitting the experimental data
U-rich agglomerates	$2.92 \cdot 10^{-9}$ s^{-1}	$4.91 \cdot 10^{-9}$ s^{-1}
Intermediate phase	$1.17 \cdot 10^{-8}$ s^{-1}	$2.92 \cdot 10^{-9}$ s^{-1}
Pu-rich agglomerates	$3.39 \cdot 10^{-8}$ s^{-1}	$2.46 \cdot 10^{-8}$ s^{-1}

These data show, without much ambiguity, a non-uniform swelling of the different agglomerates. This difference has obviously to be related to the difference in Pu content of the different agglomerates. Concerning the Pu-rich phase, its behavior is in agreement with what was observed in Section 4.2.1, which was expected, as these agglomerates are very similar to the matrix phase of the SFR samples. Concerning the intermediate phase, a lot of discrepancy is observed in the strain, which makes it difficult to assess its behavior and compare it to the expected behavior. The latter would have been, in any case, approximate as this phase corresponds to everything that is not the U-rich or Pu-rich agglomerates, rather than a well-defined phase with a well-established Pu content. For the U-rich phase, its expected behavior is even more complicated to estimate. Its swelling with self-irradiation is obvious: a shrinkage of about 0.3% was observed after the annealing (interpreted as a signature of radiation-induced damage healing) and data in Figure 110 and Figure 111 clearly exhibits a slow but steady swelling. Two sources can however be contributing to this swelling. An (even low) amount of Pu can be present in the UO_2 agglomerates, generating an internal alpha dose. The alpha particles emitted from the plutonium surrounding these agglomerates also contribute to the defect injection. None of these effects are quantifiable at this point, and the description of the swelling in the U-rich phase remains hypothetical.

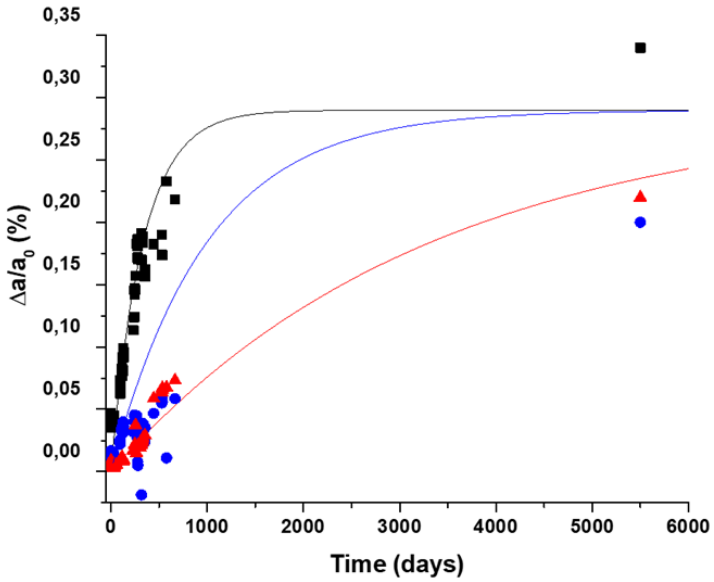

Figure 110 MIMAS sample lattice parameter increase. The full lines are calculated with the Kato's empirical formula, the scattered points are the experimental data. For the two cases, the **black** corresponds to Pu-rich agglomerates, the red corresponds to the intermediate phase, the blue corresponds to the U-rich agglomerates of the MIMAS sample.

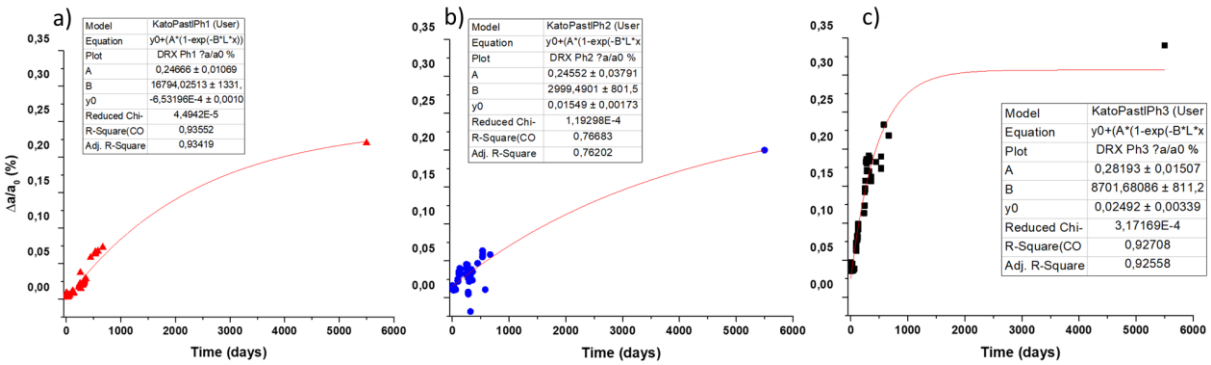

Figure 111 The result of the fitting the experimental data with the empirical formula, a) U-rich agglomerates, b) intermediate phase, c) Pu-rich agglomerates.

4.3.2 Raman spectroscopy and Raman imaging

As discussed in the previous chapter, the MIMAS material exhibits a heterogeneous microstructure. Raman imaging is thus employed to precisely locate its three distinct phases: U-rich agglomerates, the intermediate phase, and Pu-rich agglomerates. Then, from the Raman images, average spectra can be obtained for the different agglomerates. Thus, the current image analysis protocol is similar in all respects to that used in Section 3.3.3 of Chapter 3, except that the T_{2g} frequency images can no longer be directly translated into composition images as the T_{2g} frequency is now expected to be influenced by the self-irradiation effect.

Herein, we focus on the analysis of three particular samples: the freshly annealed sample (see the previous chapter), the aged sample (approximately 5500 days old), and a sample examined 400 days after annealing (400 days old). The Raman images of the 400 days and 5500 days old specimens are given in Figure 112 and Figure 113 (while the image of the freshly annealed sample is in Figure 59).

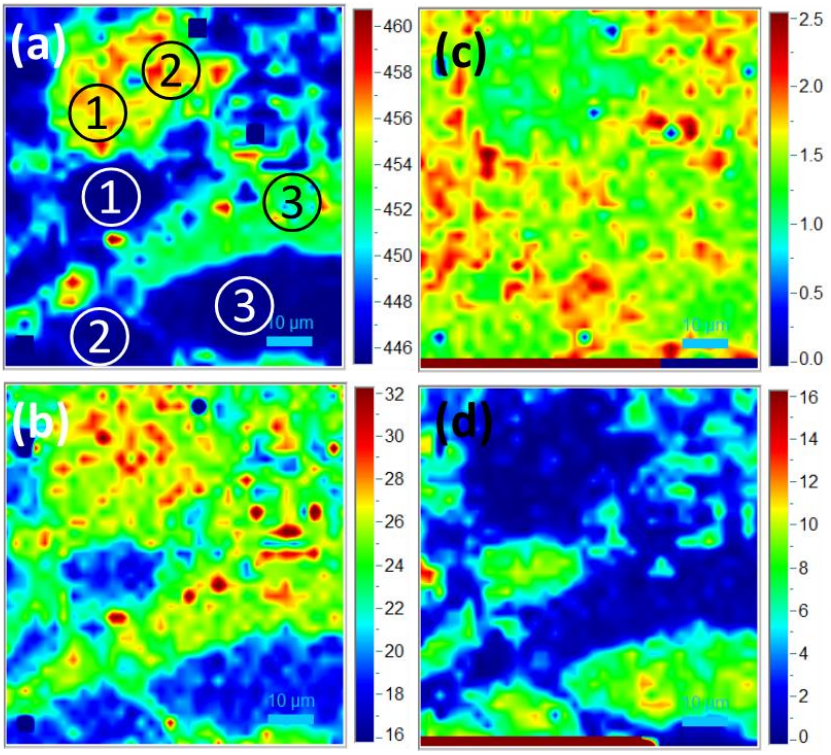

Figure 112 Images constructed from the Raman mapping of the 400 days old sample. The size of the images is 70 x 70 µm^2. (a): frequency of the T_{2g} mode (cm^{-1}). (b): line width of the T_{2g} mode (cm^{-1}). (c): U*/T_{2g} intensity ratio. (d): 2LO/T_{2g} intensity ratio. The circles indicate the agglomerates or regions for which spectra were averaged.

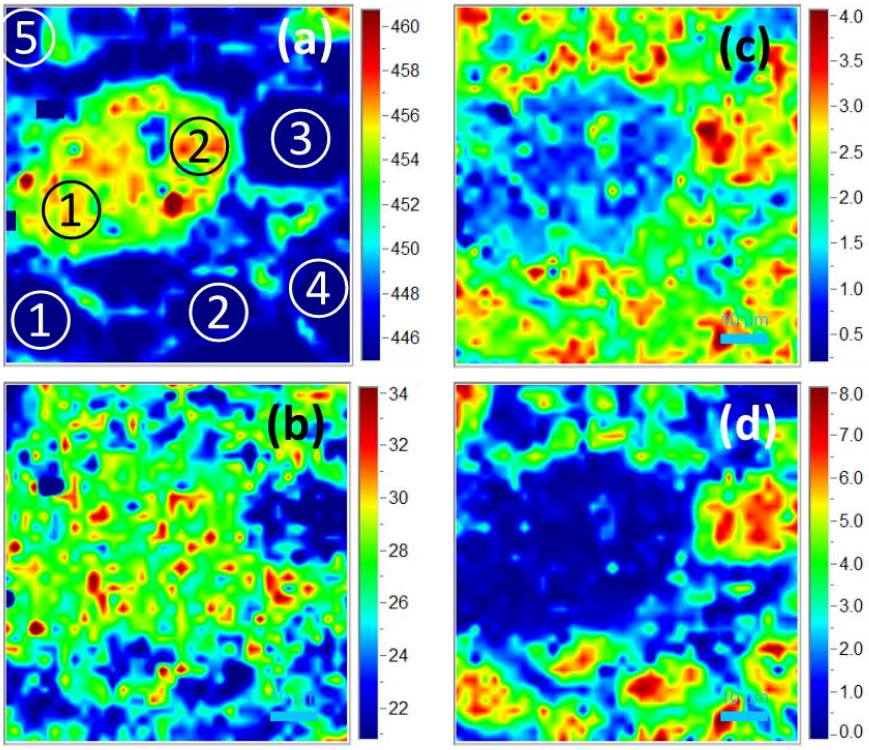

Figure 113 Images constructed from the Raman mapping of the 5500 days old sample. The size of the images is 70 x 70 µm^2. (a): frequency of the T_{2g} mode (cm^{-1}). (b): line width of the T_{2g} mode (cm^{-1}). (c): U*/T_{2g} intensity ratio. (d): 2LO/T_{2g} intensity ratio. The circles indicate the agglomerates or regions for which spectra were averaged.

On a first reading, the comparison of the T_{2g} width images of the two extremity cases which are the freshly annealed sample (shown in Figure 59b in the previous chapter) and the 5500 days old sample (Figure 113b) suggests that self-irradiation induces a rather strong broadening of the band (on an average of 5

and 8 cm^{-1} respectively for the U- Pu- rich agglomerates). This broadening is observed for all three phases of the material. In addition, there is also a strong evolution of the U^*/T_{2g} intensity ratio, at least by about a factor 2, on average (see Figure 59c and Figure 113c). The strongest intensity ratios are now rather observed for the UO_2 clusters. Finally, it is seen from Figure 59d and Figure 113d that the $2LO/T_{2g}$ ratio is lower for the aged sample than for the annealed one, by about a factor of about 2 for the U-rich agglomerates.

The U^*/T_{2g} and $2LO/T_{2g}$ intensity ratios of the different samples are compared (as function of the T_{2g} frequency) in Figure 114 (which is similar to what was plotted in Figure 61 in Chapter 3 for the annealed sample alone). In the figure, U^*/T_{2g} and $2LO/T_{2g}$ information is still drawn for each pixel of the images as a function of the T_{2g} mode frequency. A Pu content scale is also given, but is only applicable for the annealed sample for which the contribution of self-irradiation to the T_{2g} position is negligible). For the two other samples, this Pu content scale still gives a rough approximation of the Pu content.

First, a strong variation in the intensity of the 2LO mode as a function of Pu content is still observed for the aged samples (Figure 114a). The $2LO/T_{2g}$ intensity ratio is effectively seen to decrease for the lowest Pu contents, which confirms the reading of the images corresponding to this parameter. Additionally, self-irradiation induces a strong loss of intensity of this second-order mode for low Pu contents, of about a factor 2. Beyond a Pu/(U+Pu) content higher than about 15-20 at%, this intensity ratio no longer carries specific information.

The behavior of the U* (Figure 114b) line looks different, as self-irradiation induces a strong increase in its intensity for the lowest Pu contents, by a factor of about 3. The data from the annealed and 400 days old sample cannot be easily discriminated. Again, beyond a Pu content higher than about 15-20 at%, this intensity ratio no longer carries a clear information.

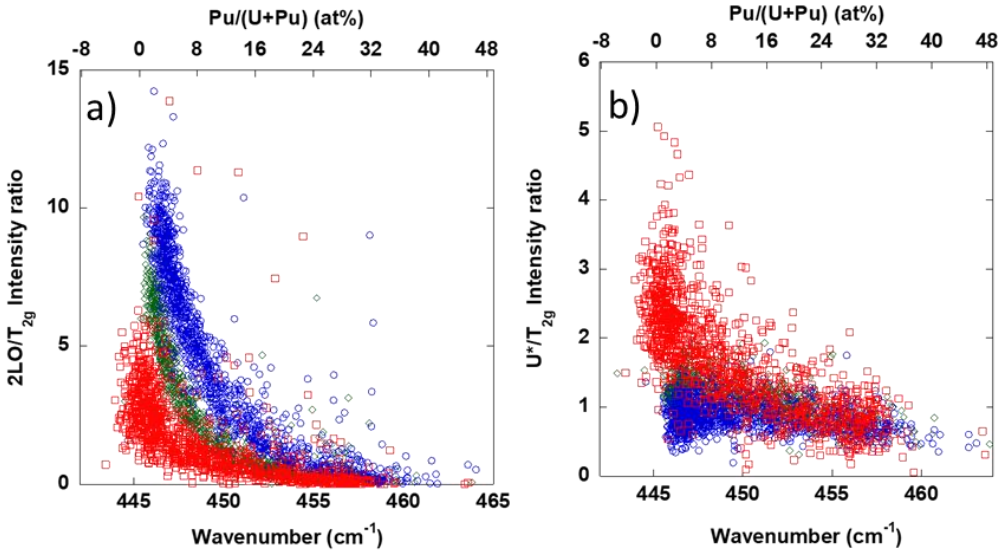

Figure 114 Evolution of the (a) $2LO/T_{2g}$ intensity ratio and (b) U^*/T_{2g} intensity ratio as a function of the T_{2g} wavenumber (also expressed as Pu/(U + Pu) content calculated with "Eqn(51)") for the, 40 days old sample (blue), the 5500 days old sample (red) and the 400 days old sample (green).

As already mentioned in the previous chapter, the individual spectra present a rather low signal to noise ratio. The analysis is thus rather performed on average data that are characteristic of U-rich and Pu-rich agglomerates. These average spectra, whose locations were already highlighted in Figure 59 in Chapter 3, Figure 112a and Figure 113a, are now compared, see Figure 115. Both the first- and second-order regions are considered.

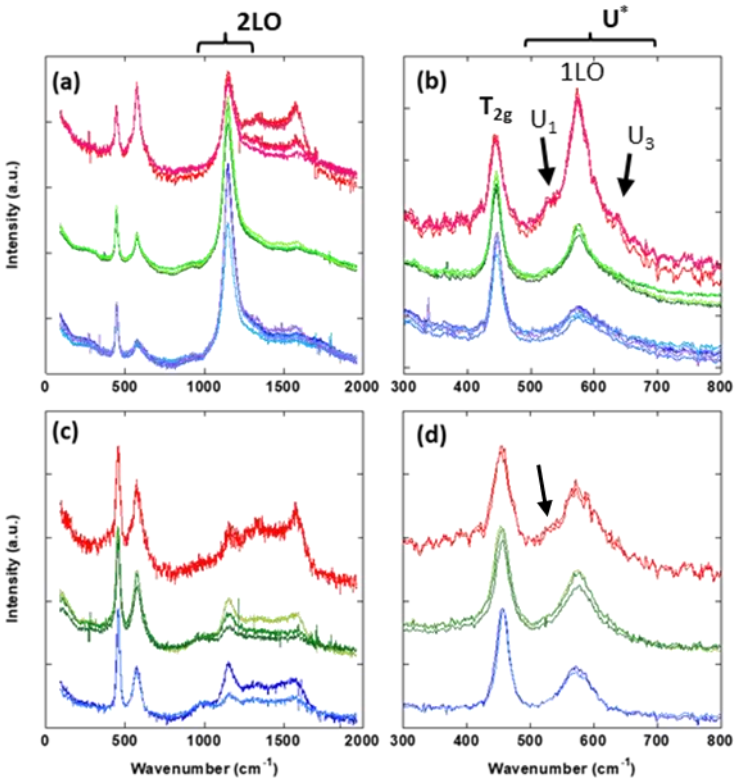

Figure 115 Examples of averaged Raman spectra for U - [(a) and (b)] and Pu-rich [(c) and (d)] agglomerates. Reddish lines correspond to the 5500 days old specimen; bluish lines correspond to the 40 days old specimen and the green lines correspond to 400 days old specimen (a) and (c) Complete spectra, between ≈100 and ≈ 2000 cm^{-1}. (b) and (d) Close-up of the first order region. The arrows highlight the U_1 signal, clearly detected for the aged sample.

Regarding the evolution of the T_{2g} mode, both for the Pu-rich and U-rich agglomerates, a strong line broadening as well as the downshift are evidenced upon self-irradiation, rather similar to the observation in the Capra4 sample. An asymmetry of this mode towards the low frequencies can also be discussed.
The evolution of the U* line as a whole is however more dependent on the Pu content of the agglomerates. When normalized to the T_{2g} mode intensity, it only increases slightly for Pu-rich agglomerates, an information buried in the noise of the measurement if we consider all the individual spectra, as was done in Figure 114b. On the contrary, a strong intensity increase is observed in U-rich agglomerates, similarly to what was observed in Figure 114b. Finally, in both cases, a shoulder at a lower frequency than the forbidden 1LO mode (the U_1 line) clearly stands out from the U* signal, see the arrows in Figure 115b and Figure 115d.

From Figure 115a, the decrease in intensity of the 2LO mode is obvious for the U-rich agglomerates, which can no longer be discussed with certainty for Pu-rich agglomerates, see Figure 115c.

Line fitting of those spectra, of the T_{2g} mode, in particular, gives the last trends. The time evolution of the T_{2g} mode frequency and width is given in Figure 116. They are given in the form of bar graphs, for simplicity. First, one can see that the agglomerates are not all rigorously equivalent, which is most probably due to the choice of the areas from which the spectra were averaged, and also to spectrometer drifts which cannot be easily corrected here. However, on average, one observes a progressive change both in the T_{2g} position and its width notably downshift of about 2.2 and 1.6 cm^{-1} for the Pu- and U-rich agglomerates, respectively, whereas broadenings of 11 and 8 cm^{-1} are observed for the same zones between the two extremity cases.

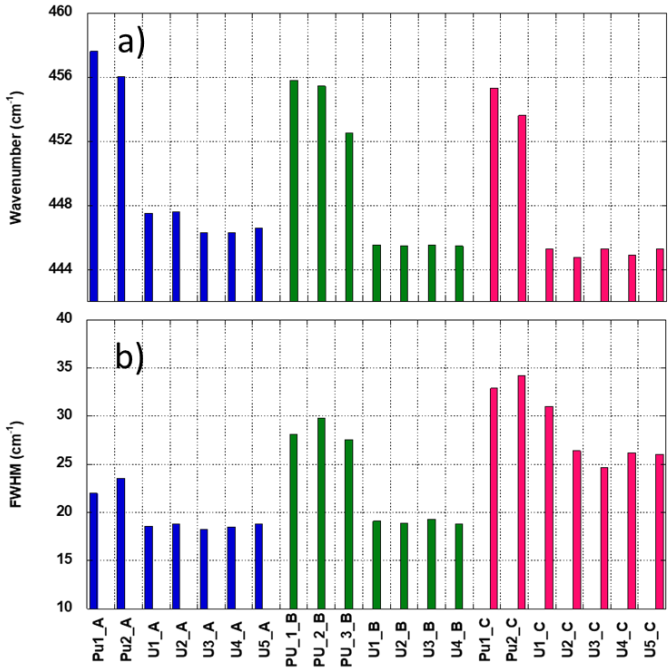

Figure 116 Evolution of the frequency and width of the T_{2g} mode for U- and Pu-rich agglomerates after line fitting. Corresponding spectra are plotted in Figure 115. The blue bars correspond to the 40 days old sample, the green bars correspond to the 400 days old sample and the red bars corresponds to the 5500 days old sample.

Figure 117 shows a summary of the four observable parameters in the Raman spectra (T_{2g} position and width, U^*/T_{2g} and $2LO/T_{2g}$ intensity ratios) and their evolution with the self-irradiation effects. The solid and dotted lines are only guides for the eyes, they attempt to take into account some of the main observations noted for the Capra4 sample. Clearly, we will not go any further in this discussion on the basis of the three samples analyzed.

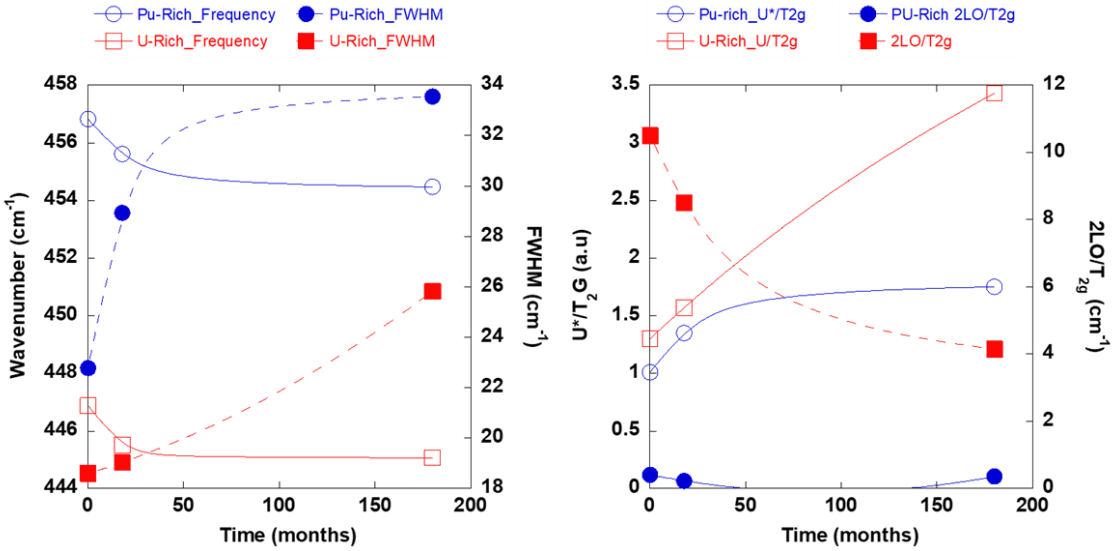

Figure 117 Evolution of the four observable parameters in the MIMAS sample drawn with the data obtained with 40 days, 400 days and 5500 days old MIMAS samples.

A first remark is that, similarly to the evolution in the Capra4 sample, the temporal evolution of the T_{2g} frequencies may be consistent with the trend of lattice swelling, even if the data from U-rich agglomerates may seem questionable.

Secondly, the temporal evolution of the somehow defect-sensitive spectral characteristics (T_{2g} line width and the U* line intensity) is different for U- and Pu-rich agglomerates. This could be due to two different main damage sources between the U- and Pu-rich agglomerates. As discussed, when analyzing the XRD

data (Section 4.3.1), the damage in the U-rich agglomerates results (probably mostly) from the alpha particles from the surrounding Pu and the recoil nucleus for the Pu agglomerates. This behavior might also be related to more fundamental origins, to be discussed in the next chapter.

Finally, concerning the U-rich agglomerates, the 2LO mode exhibit a strong, decreasing trend. This band thus, indirectly, tracks the self-irradiation effects. Nevertheless, beyond a Pu/(U+Pu) content of about 15%, the 2LO intensity is no longer sensitive to self-irradiation effects as long as the analysis is conducted at 532 nm due to the loss of resonance conditions.

4.3.3 XAS

As a reminder, these measurements were carried out at the MARS beamline at the SOLEIL synchrotron, using a micro beam (15×16 µm^2). The approach used to analyze the different areas of interest, as well as some of the limitations of the experimental protocol, were described in the previous chapter.

4.3.3.1 XANES

Figure 118 and Figure 119 show the U-L_3 (a) and Pu-L_3 (b) XANES spectra of the three MIMAS samples examined, as well as the corresponding reference signals collected on samples representative of the different possible oxidation states of both cations. Because of the measurement conditions, the annealed sample had to be used as a reference for the U^{+4} and Pu^{+4} oxidation states. This will add some uncertainties on the estimated oxidation states but is fairly reasonable considering the results presented in Section 4.2.3. Results of the linear combination fit can be found in Table 29.

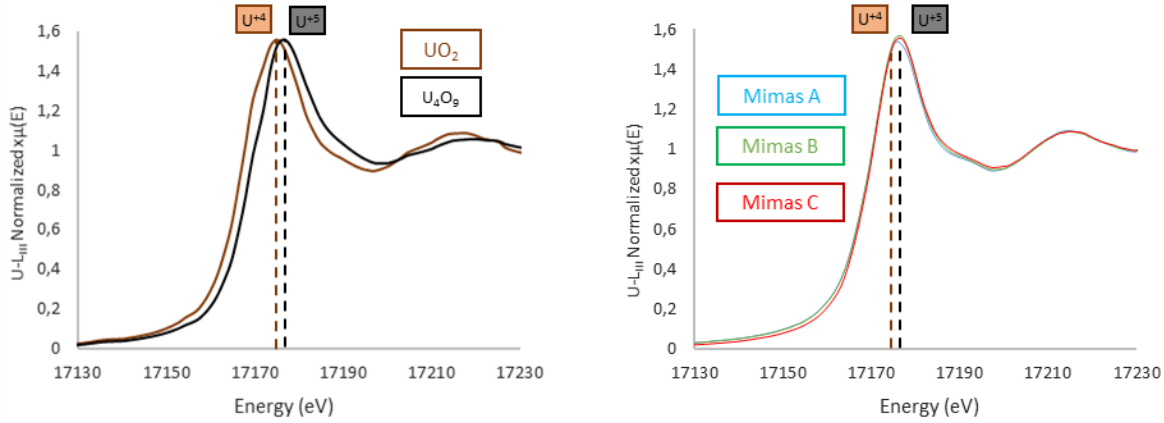

Figure 118 U-L_{III} XANES Analysis of MIMAS Samples. Left Side: Reference spectra for comparison. Right Side: MIMAS-A is 44 days old, MIMAS-B is 550 days old, MIMAS-C is 5500 days old Capra4 samples compared with the reference positions.

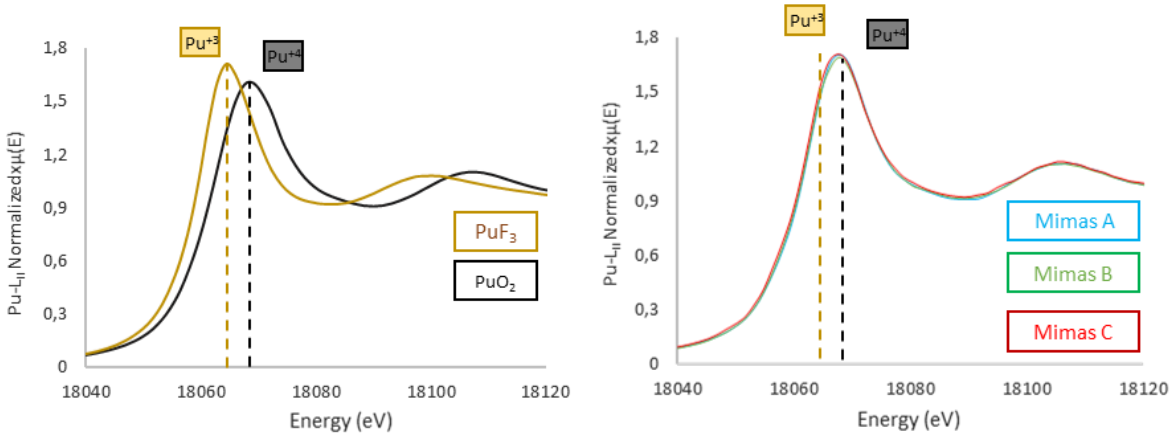

Figure 119 Pu-L_{III} XANES Analysis of MIMAS Samples. Left Side: Reference spectra for comparison. Right Side: MIMAS-A is 44 days old, MIMAS-B is 550 days old, MIMAS-C is 5500 days old Capra4 samples compared with the reference positions.

Table 29 The changes in cation oxidation states and O/M ratios over time due to self-irradiation in the MIMAS samples at U-rich and Pu-rich agglomerates

Age (days)	44	550	5500	44	550	5500
Zone	Pu-rich	Pu-rich	Pu-rich	U-rich	U-rich	U-rich
U	4.00 (5)	4.05 (5)	4.08 (5)	4*	4.00 (5)	4.06 (5)
Pu	4*	3.98 (5)	3.91 (5)	0	0	0
Am	3.0	3.0	3.0	0	0	0
O/M	2.00(1)	2.01(1)	2.01(1)	2.01(1)	2.00(1)	2.02(1)

* These values given for U in U-rich agglomerates and for Pu in Pu-rich could not be determined by linear combination as the corresponding spectra were used as calibration.

4.3.3.2 EXAFS

EXAFS spectra were also recorded on these agglomerates. We give here, simply for information, the average distances extracted from the EXAFS spectra, as well as the DW parameters. The corresponding data are plotted in Figure 120 and Figure 121 respectively. In the Figure 120, we also indicate the expected trend according to Kato's correlation [4]. In the context of EXAFS analysis, it is essential to consider the impact of varying X-ray energy levels on the penetration depth of the X-rays. Given the dispersion of the data, it is clear that the penetration depth of the X-rays was greater than the depth of the selected area and the increase with the energy meaning that the EXAFS results are a mixture of different Pu concentration areas and thus the ratio is not constant along the spectra. Besides, this change in the penetration depth also varies the mean free path of the fluorescence emission. Consequently, these results will not be further discussed.

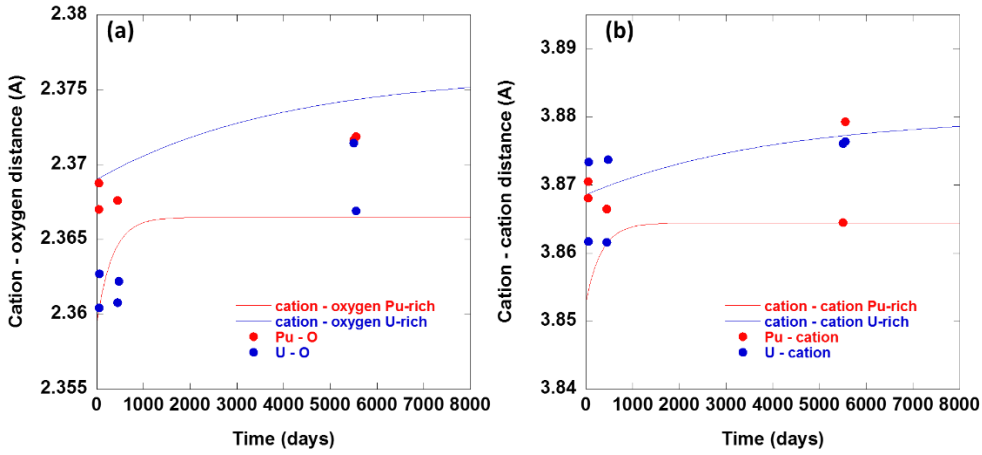

Figure 120 a) Evolution of the Cation-Oxygen atomic distances in the first coordination sphere, (b) Evolution of the Cation-Cation atomic distances in the first coordination sphere.

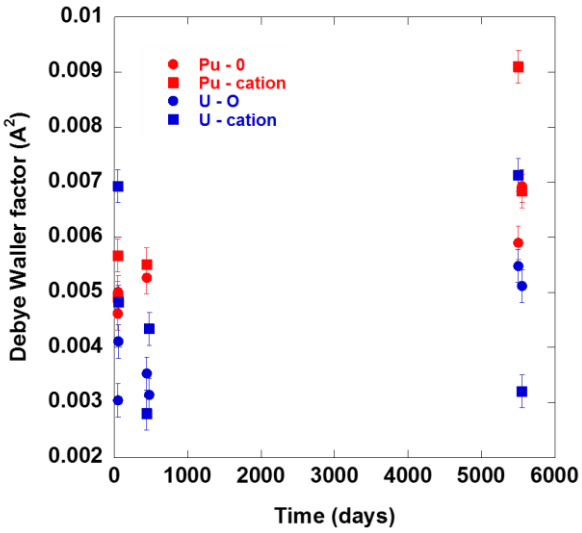

Figure 121 The calculated Debye Waller factors on the first cation-O cation-cation in the first coordination sphere.

4.3.4 First assessment of the results

MIMAS samples are by nature heterogeneous, *i.e.* made up of different agglomerates, with different Pu contents. As expected from the different Pu contents, XRD shows that the lattice parameter does not expand homogeneously in these agglomerates despite the measurement uncertainties. A more local probe, such as Raman spectroscopy, is therefore required. This is why we used Raman imaging for the analysis of this particular sample. From the analysis of the Raman images, the trends observed in the Pu-rich agglomerates are equivalent to those observed in the Capra4 samples, a sample that exhibits a similar mean Pu content. The data collected in the U-rich agglomerates look different, particularly those related to the intensity of the 1LO and 2LO modes, and the associated U_1 and U_3 signals. The XAS data do not seem immediately and confidently usable. While the XANES data does not exhibit significant shifts over time, it may suggest that the various agglomerates in the sample maintain a close-to-stoichiometric composition. The EXAFS data do not seem directly interpretable at this stage.

4.4Conclusion

The aim of this chapter was to describe and summarily analyze the self-irradiation effects on the three MOX samples studied in this thesis. For this purpose, and as suggested by the lattice swelling description from Kato analyses had to be carried out on a multi-year timescale. We therefore used samples at different "ages", *i.e.* time since their annealing. Those self-irradiation effects were investigated using three techniques: XRD, Raman spectroscopy and XAS.

Self-irradiation is at first known to cause lattice parameter expansion, up to a saturation at about 0.3%, this saturation being independent of the plutonium content. This is what was actually observed, on average. We will not discuss the second decimal of this strain at saturation here, as it undoubtedly lies beyond the uncertainty of all our measurements. This lattice expansion was clearly observed for SFR-type samples both from XRD and the EXAFS cation-cation distance. A similar lattice strain seems to be more or less clear for the MIMAS sample, at least for the Pu-rich agglomerates.

Within the time scale of this work, such a lattice expansion was not completely observed for the U-rich agglomerates, what the MIMAS-related data tend to highlight. In a first approximation, considering these agglomerates free of α-emitters (*i.e.* free of Pu), it seems clear that radiation damage only arises from the α particles emitted from the surrounding matrix phase and the Pu-rich agglomerates. Some scenarios related to the radiation damage and swelling in the U-rich agglomerates are explained in the last chapter. A third method was likely to provide some strain information, namely Raman spectroscopy, examining the frequency shift of the T_{2g} mode. A downshift of the T_{2g} mode of about 2.5 cm^{-1} was effectively observed in a Capra4 sample close to the saturation level of the lattice parameter. Similar results were obtained in the Pu-rich agglomerates of the MIMAS sample. This is perhaps some new data compared to previously published works, as will be discussed in Chapter 5.

These three methods also give us information on the structural disorder induced by self-irradiation, notably through Raman T_{2g} mode width and the EXAFS Debye Waller factors. An interesting point here is that all these data can be most probably and consistently understood with a rather similar time constant, to the current accuracy of the measurements. This time constant is always close to that reported by Kato. At this point, the data, in particular the EXAFS data, suggest an increasing positional disorder in the oxygen sub-lattice.

An everlasting question concerns the nature of the self-irradiation-induced defects and the origin of the Raman-forbidden signals in the spectra. Here, without questioning too much the literature at this point, we are faced with three issues:

- (i) in this work, it was not clearly possible to resolve this line into its three specific components,
- (ii) all the analyses carried out do not tell anything about any particular point or extended defects, or others,
- (iii) all the Raman analyses were carried out at 532 nm. More, from XANES results, deviations from stoichiometry are necessarily weak, to a certain extend.

Obviously, the rationale of the next chapter will be to discuss all the observations described in Chapters 3 and 4. In particular, the Raman results are to be discussed in terms of defect injection and resonant scattering.

Chapter 5. Discussion

In the last two chapters, we have examined three MOX samples with different Pu contents, using different characterization techniques. These samples enabled us, at least in part, to revisit the $(U,Pu)O_2$ Raman spectroscopy in the full Pu content range. We also used the same techniques to analyze the impact of self-irradiation, mainly remaining in the 0 – 40 at% Pu/(U+Pu) range. In both chapters, we remained as descriptive as possible and our results appear to be in line with the literature, to some extent.

Examining the results, we are aware that we used some rather strong assumptions: no strong deviation from the exact oxygen stoichiometry, no micro-strains. Moreover, some of the possible effects of the americium, accumulated in the sample since their fabrication, was not taken into account. This raises the question of the validity of these hypotheses.

Among the different methods used, it also appeared that most of them gave in a more or less straightforward way results in terms of lattice parameter, Pu content, bond lengths, and oxidation degrees. This is not the case using Raman spectroscopy, for which the results have to be interpreted, taking into account the lattice swelling, the continuous defect injection, their accumulation and the resonance effects. To this end, four different characteristic features were used, *i.e.* T_{2g} mode frequency and broadening, as well as the U^*/T_{2g} and $2LO/T_{2g}$ intensity ratios. This raises the question of the physical meaning of all those parameters, taking into account the experimental conditions used, the excitation wavelength in particular. We will also try to describe our results according to such a scenario.

Not discussed so far is a possible scenario that can help to understand our data. We know that the microstructure of samples will vary over time, with, to schematize, the initial creation of point defects, followed by the condensation of those defects to create extended defects, such as dislocations or even voids.

The purpose of this chapter is therefore to examine all these items.

5.1About the hypothesis used in this study: How acceptable are they?

In view of the heterogeneous nature of the samples analyzed here, mainly in the form of ceramics, the results were analyzed on the basis of certain assumptions that enabled this study to be pursued. In particular, the MOX materials were considered close to the exact stoichiometry and micro-strain-free. Furthermore, their americium content was not taken into account. In this first section, we simply examine the extent to which these assumptions can be considered as reasonable.

5.1.1 Stoichiometry and micro-strain in the ceramics

We simply start by rewriting the equation that relates the lattice parameter of $U_{1-y}Pu_yO_{2-x}$ to *y*, the Pu/(U+Pu) content and *x*, the hypo-stoichiometry. We will still use the equation (3) from Duriez *et al.*[66] without discussing the associated uncertainties, as we will see, there is probably no need to do so. This equation immediately tells us that a variation of about 8 at.% Pu/(U+Pu) has quite exactly the same impact on the lattice parameter as a deviation from stoichiometry of 0.02 in *x*. In terms of strain, both values lead to strain values close to ± 0.1%, which is the order of magnitude of values of the self-irradiation-induced strain, as described by many works [4], [81], [91].

A similar reasoning can be applied to the Raman data. Still using the Equation 51 derived by Medyk *et al.* [99], it is seen that an increase in the Pu/(U+Pu) content by about 8 at% leads to an upshift of the T_{2g} mode by about 3.5 cm^{-1}. Using Medyk *et al.*[99] Eqn (51), a deviation from stoichiometry of about a value of 0.02 leads to a downshift of the T_{2g} mode by about the same value. Again, in absolute values, this is the order of magnitude of the self-irradiation-induced shift of the T_{2g} mode.

Thus, in both cases, we are faced with an equation with two unknown parameters or even three if we consider the self-irradiation effects. At first, this is why the determination of the Pu content, whether on a global or more local scale, will be essential for all subsequent interpretations. This is obviously why three different methods were used to determine the Pu content, either on a local (µm) scale or on a more averaged scale, in a more or less direct way, depending on the method. In all cases, the Pu contents estimated from EPMA and Raman data are consistent, with a margin of error close to 1 at%. This error is equivalent to a lattice parameter change of about 0.01%. The comparison of the self-irradiation effects analyzed by means of XRD and Raman spectroscopy are well outside this error margin.

Oxygen stoichiometry is the main parameter to be perfectly controlled, as far as possible. All the annealing processes were carried out with this in mind, see A.1.1.2. One observes that hypo-stoichiometry and self-irradiation effects are clearly additive. At this point, XANES data were required, this was one of the main targets of these two measurement campaigns. The trends indicate that all samples were close to stoichiometry, to the measurement accuracy. Nevertheless, all ESRF data are given with a margin of error of around 0.01 for the calculated O/M ratio, *i.e.* more or less the above-discussed error margin. Again, self-irradiation effects analyzed using XRD or even Raman spectroscopy are still slightly outside this error margin. However, the SOLEIL/MIMAS data seem to us to be slightly less precise. For this sample, one must therefore accept that the annealing conditions have indeed brought the sample to a composition close to stoichiometry. This is indeed a feasible hypothesis considering that all the samples in this study were annealed with the same conditions (see A.1.1.2) and the results with the SFR samples (in ESRF campaign) has shown that the O/M of these samples yield 2.00(1), see Section 2.3.1 and Section 2.4. Thus, this last hypothesis is what is adapted in this study to be able to have further comments on the sample ageing (MIMAS samples) and its consequences.

Irrespective of the consequences of deviations from exact stoichiometry, strain effects are also to be discussed. It seems obvious that two types of strains are to be taken into account here: micro-strains, always present in this type of ceramics, for example along grain boundaries, as well as more "macroscopic" strains, for example induced by differential grain volume variations during the sintering process or even during the material swelling. In other words, it was assumed that the swelling and or the thermally-induced stresses were homogeneous in the material. Both origins cannot be completely excluded here. An order of magnitude of the micro-strain effects can be obtained by Raman imaging from a representative area of a stoichiometric UO_2 pellet, which was done in Ref. [145]. The contrast of the frequency images was found to be close to ± 1.5 cm^{-1}. Translated in terms of Pu concentration according to Eqn 51, one can immediately see that locally, the uncertainty on the local Pu content can be as large as ±3%. The consequences of the synthesis process cannot be simply evaluated and discussed here, but one can anticipate similar consequences in terms of uncertainty on the Pu content. Neglecting strain effects is therefore a rather strong assumption. This may explain, at least in part, the rather high scattering of the Raman data observed during the analysis of the annealed samples, see Chapter 3. However, most of the Raman data given in this document are averaged data, for which these micro-strain effects are mostly eliminated.

5.1.2 Americium content and enrichment

Another significant assumption was made regarding the influence of Am present in the sample on the results presented in the two previous chapters. We will not take into account the low Am enrichment of the samples during the time scale of this work. This cannot call into question what is discussed below.

5.1.2.1 Spatial distribution of americium in the samples

The sample isotopy of the different samples was discussed in Chapter 2. As shown in the corresponding tables and discussed in Section 2.1.1, a significant part of the americium in the samples results from ^{241}Pu decay since fabrication. The distribution of this americium strictly follows that of plutonium. The remaining part of the americium was present before fabrication, *i.e.* before sintering at 1700°C for 4 h. In this case, americium results from the decay of ^{241}Pu contained in the starting plutonium powder and it is thus found distributed similarly to plutonium in the green pellets. During sintering, it is generally expected that diffusion of plutonium and americium will be roughly similar, as their diffusion coefficients in UO_2 are fairly close [153]. The distribution of the americium present after sintering is thus also expected to follow that of plutonium, in agreement with experimental results[154]. The spatial distribution of Am in the samples can thus be assumed to follow that of Pu, which was indeed verified using the X-ray fluorescence mapping of the MIMAS sample, as well as the mappings and quantitative line scans collected with EPMA.

The consequence of the presence of americium should be considered mostly in the Capra4 and the MIMAS samples as they have Am/(Pu+Am) contents of 6.2 and 8.3 wt.%, respectively, at the time of this study. This isotopic analysis reveals that the average Am/(U+Pu+Am) ratio in the Pu-rich agglomerates of the MIMAS sample is slightly below ≈ 2 wt.%. The matrix phase of the Capra4 sample exhibits a ratio around 2.5 wt.%, while the Pu-rich spots within the same sample demonstrate a ratio that can extend up to 8.3 wt.%, considering pure PuO_2 clusters (or rather, pure $(Pu,Am)O_2$ clusters). These observations were further supported by the quantitative line scans presented in Figure 45 and Figure 48 in Chapter 3[2]. For the Trabant40 sample, on the other hand, the Am content is much lower, close to 1% in the matrix phase, and up to 2.5% in the Pu-rich clusters.

[2] It has to be noted that americium standards for microanalysis are rare. The best standards currently available to our laboratory are actually the uranium-free $(Pu,Am)O_2$ (micronic) spots present in the Capra4 sample. Americium measurements in the Capra4 sample are thus almost inherently consistent with its calculated composition, as the latter is used as input for the calibration. However, we can be confident that this americium quantitative calibration is not too erroneous as it was also used in numerous other samples with various Pu and Am/Pu contents and always delivered results that were close to the expected values.

5.1.2.2 Influence of americium on the lattice parameter

It is essential to note that americium is commonly found within the solid solution, where it substitutes for uranium and plutonium. For the $(U,Am)O_2$ solution, up to an Am/(U+Am) ratio of about 0.3, the oxygen stoichiometry is preserved thanks to charge compensation mechanism, implying the oxidation of uranium to U^{5+} up to a fraction equal to the proportion of Am^{3+}. Concerning the $(U,Pu,Am)O_2$ solid solution, a similar charge compensation mechanism is still observed, implying U^{4+}, U^{5+}, Pu^{3+}, Pu^{4+} and Am^{3+} cations.

At this stage, we do not want to go into too much detail, a few orders of magnitude are sufficient for our purposes. We simply use some of the few available results in the literature that concern the $U_{1-x}Am_xO_{2\pm\delta}$ solid solution. We will restrict ourselves in the 0 – 30 at% Am content range, which is sufficient for the analysis of the MIMAS samples and the matrix phase of the Capra4 samples.

For this analysis the XRD data have been extracted from Ref [155]. In the considered Am content range and for samples close to the exact oxygen stoichiometry, a decrease of the lattice parameter with Am enrichment is noted and can roughly be described according to:

$$a(U_{1-x}Am_xO_2) = 5.47 - 0.05\,x \qquad \text{Eqn (53)}$$

An Am enrichment of 2.5 at%, as is the case for the matrix phase of the Capra4 samples, leads to a lattice parameter shrinkage of about 0.001 Å and a corresponding strain value lower than -0.02%. This effect is very weak and can therefore be neglected.

5.1.2.3 Effect of americium doping on the $(U,Am)O_2$ Raman spectra

Only a few Raman spectra of $U_{1-x}Am_xO_{2\pm\delta}$ have been reported in the literature [101], [156]–[158]. We will not detail them here as the acquisition conditions of the spectra are not equivalent from one source to another. Nevertheless, the characteristics of the spectra are known to evolve with the Am content. Summarizing the main trends, (i) an upshift and a strong broadening of the T_{2g} mode; (ii) a progressive upshift of the U* region; (iii) a continuous change in the relative intensities of the different lines are observed with the increase in the Am content. In particular, the upshift of the T_{2g} mode most probably translates the decrease of the lattice parameter of the fluorite structure with the increase of the Am content. Using the data of Ref. [101], an enrichment close to 10% in Am is seen to lead to a line upshift close to 1 cm^{-1}. Considering everything, the Am content can be neglected for the MIMAS and the matrix phase of the Capra4 samples, remaining within the error margin of all our measurements.

The Am content can reach 8 wt.% in Pu-rich clusters, in particular for the Capra4 samples. We cannot go further in the analysis of the effects of this enrichment here, to our knowledge, there is no available data on the solid solution of $(Pu,Am)O_2$. Nevertheless, if we take into account what has been described above, it is likely that this effect can no longer be completely neglected in these Pu-rich agglomerates. This would make it possible, among other things, to understand the difference in the quality of the spectra (their intensity in particular) observed for the Capra4 and Trabant40 samples.

This brief discussion therefore tends to show that the effects of americium should not call into question the majority of our observations.

5.2Interpreting Raman data

During this work, different methods were used, giving in a relatively straightforward way the information sought, *i.e.* the Pu content, the lattice parameters, the distances between atom pairs, the oxidation degrees. This is no longer the case for data extracted from Raman analyses, which are to be interpreted. From the analysis of the Raman images, it appears that four different spectral features bring information,

namely the T_{2g} mode frequency and width (and even perhaps its asymmetry) the U* intensity and its corresponding line shape, and finally the 2LO intensity. This information depends on the Pu content and the exciting wavelength. This is what this section is about.

5.2.1 The methodology used

From a methodological point of view, imaging methods have been used. All the individual data, in other words the individual spectra, appeared very noisy, and difficult to use as such. The data appeared noisy at first sight, which is due to (i) the measurement environment, (ii) the need to analyze a representative area of the sample in a given time frame (Raman imaging is always a matter of compromises between acquisition time and signal quality), (iii) most importantly the compositional and the likely mechanical heterogeneity of the sample. This is why we tried to analyze our data in a rather more statistical way, through averaging spectra over some regions of interest of the different samples. This is what enabled the analysis of the MIMAS samples, in particular. The analysis of a large number of data is therefore not clearly a handicap here. This made it possible to extract data that we consider reliable.

5.2.2 The frequency and width of T_{2g} mode as a function of the Pu content

Throughout this work, we used the conclusions of Medyk *et al*. [99] in order to translate the T_{2g} mode frequency in terms of composition. This approach can only be used for annealed samples, as we saw earlier.

In Figure 122, we first redraw some of the main data, using Figure 58. We no longer discriminate between the origins of the different data. We simply recall here that some additional data have been introduced compared to the work of Medyk *et al*., in particular in the high Pu content region of the graph.

A quadratic function was also used to fit this dataset (red curve in Figure 122), which is subsequently compared to the conclusions of Medyk *et al.* (blue curve in Figure 122). One can see that these two curves are virtually indistinguishable in the composition range used in this work, once again, this does not call into question our conclusions, as the difference between the two fits remains well within the error margin of all the frequency determinations. As a simple reminder, Equation 54 gives the result of this last adjustment.

$$\omega(U_{1-y}Pu_yO_2) = -7.14\times y^2 + 42.2\times y + 445.0 \qquad \text{Eqn (54)}$$

Perhaps more interesting is the need to use a quadratic function to understand the data, see in particular the apparent bowing which is observed to be the highest (~ 2 cm^{-1}) for a Pu/(U+Pu) content close to 50 at%.

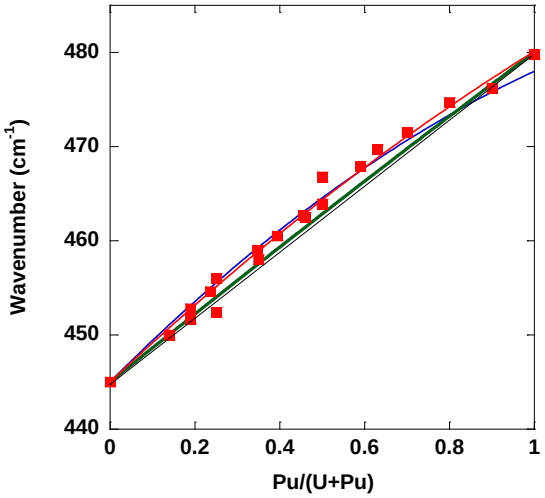

Figure 122 Evolution of the T_{2g} mode frequency with the Pu content. Red squares, experimental evidence. Blue and red traces, quadratic fits of the data according to Medyk et al. [99] (blue trace) and a quadratic fit that takes into account recent data in the high Pu content range. The Green line was drawn assuming a mean spring constant, see the text.

What could be the origin of such a deviation from a perfect linear behavior, still suggested by a Vegard's type law? First of all, there is no strict reason to observe a pure linear behavior. Coming back to Eqn 51 in Chapter 2, still within the harmonic approximation, we indeed expect a quadratic behavior, to some extent. Here, still within this approximation, the mass disorder does not have to be taken into account, as only oxygen is involved in this specific vibrational mode. Only a "spring constant disorder" or "bond disorder" has to be taken into account.

A first means to understand the data is obviously to consider an averaged, mean spring constant, more or less as we would have done in a virtual crystal approximation, with all the atoms in the unit cell at their expected Wyckoff positions. This has been described many times through the Random-Element-Iso-displacement Model, see for example Ref [116]. Conclusions from this model are plotted in Figure 122, see the green full line. To plot this line, we simply used two specific frequencies, those of UO_2 (445 cm^{-1}) and PuO_2 (480 cm^{-1}). Accepting this very crude and naïve model, deviations from purely linear behavior are effectively expected to be minor. Obviously, this first model does not explain the experimental evidence.

The spring constant is obviously sensitive to the overall bond distortion (bond length and bond angles), with a very simple rule that states "the closer the atoms, the larger the spring constant values", see Ref. [159], for example. In most cases, this rule applies.

To go further in the discussion, it becomes necessary to take into account some of the possible alloying affects. UO_2 and PuO_2 have quite different lattice parameters, meaning different U–O and Pu–O bond lengths. From this point, one can consider these bond lengths as completely rigid in the solid solution, or one can give them some possibility to progressive relaxation, depending on the Pu content. In the latter case, one can simply expect that the mean U–O (Pu–O) distances will be progressively shortened (extended) from that found for a UO_2 (PuO_2) composition. Such a behavior has indeed been observed for the $(Th,U)O_2$ and $(Th,Pu)O_2$ solutions from EXAFS measurements, with two clearly distinct bond lengths as a function of composition [160], see Figure 123. The effect is even stronger in $(U,Am)O_2$ oxides in which the differences between U-O and Am-O bonds measured through EXAFS is often larger than 0.060 Å, while both present only small variations with the Am content. One reason of this large difference in length is due to that all Am is in trivalent state in the solid solution for until Am/(Am+U) = 0.5 [101]. This is most probably not what was clearly observed in this work, see for example Figure 80 in Chapter 3, in which one finds that the U-O and Pu-O distances are not drastically different, as was previously observed by L. Medyk. [95] More, such a model that accept some bond relaxation does not clearly explain the apparent upshift in the Pu-rich region of the graph.

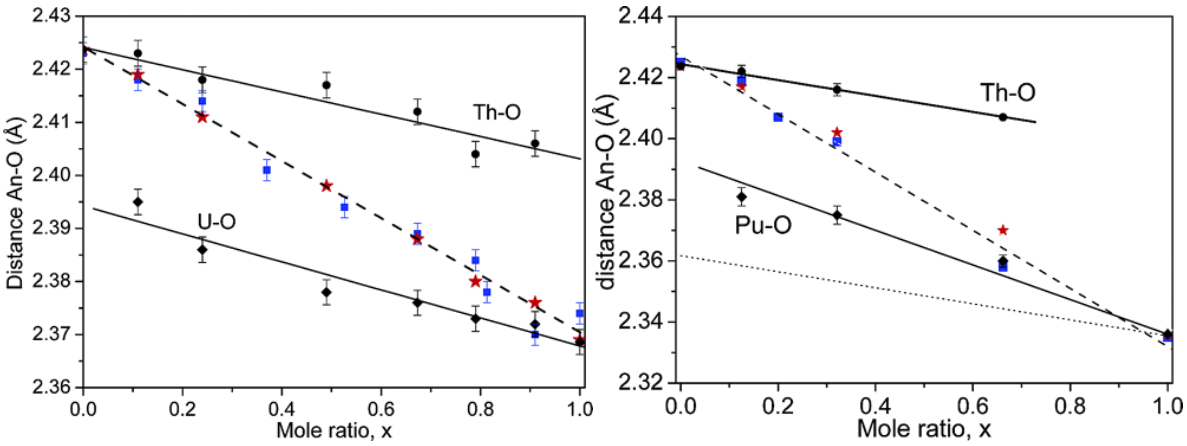

Figure 123 Evolution of cation-oxygen distances in $(Th_{1-x}U_x)O_2$ (left) and $(Th_{1-x}Pu_x)O_2$ (right) samples as functions of x as reported in [160]. The distances obtained through EXAFS are depicted as black marks for each cation and as red stars for their weighed average. The blue squares and dashed lines are the VCA cation-oxygen distances calculated respectively from XRD results and a Vegard law between the corresponding end members (i.e. ThO_2 and UO_2 or PuO_2).

On the other hand, what may seem more or less clear in this same Figure 80 is that the cation - O mean distance is always shorter than expected from their expected Wyckoff Positions. This result was also obtained by L. Medyk for other $(U,Pu)O_2$ compounds of similar Pu contents and thus differ significantly from $(Th,U)O_2$ and $(Th,Pu)O_2$ compounds. We assume that such modifications in the mean cation – oxygen distances are effectively required to accommodate the mismatch between the UO_2 and PuO_2 lattice parameters. As such, this last observation alone, still somewhat naïve, would explain the bowing of the of the T_{2g} mode vs the Pu content, at least in the 0 – 40 at% Pu/(U+Pu) composition range. It remains to be seen whether or not this observation, shorter cation – O bonds as compared to their expected positions in the VCA approximation, is still valid for the highest Pu contents.

For an "ideal perfect crystal", more or less a situation expected for the parent UO_2 and PuO_2 crystals, the line width reflects the lifetime of the vibrational mode at a given temperature. In spite of some dispersion of the data, some broadening of the T_{2g} mode was effectively observed, in particular in the 20-80 wt.% Pu/(U+Pu) content range, see Figure 62a in Chapter 3. Such a broadening is usually simply related to "disorder". Here, one can also make a correlation between this broadening and the high Debye-Waller values systematically observed for the cation - O distances, either from dynamic (bond anharmonicity) or more importantly from static contributions, taking into account that most of the measurements were done at 15K. It is likely that this broadening also reflects, in part, such a bond length distribution.

5.2.3 Resonant scattering, and some consequences on the line shape of the $(U,Pu)O_2$ Raman spectra

In this work, the intensity of the 2LO mode was used to localize U-rich agglomerates, and discriminate them from Pu-rich agglomerates. As such, this information is not completely new, see for example Refs. [91], [97], [99] As a matter of fact, we have mentioned many times in this manuscript that the line shape of UO_2 Raman spectra depends on the excitation wavelength. This is also relevant for PuO_2, and most probably for $(U,Pu)O_2$ solid solutions. The specification of the excitation wavelength is therefore an essential data for the reading of the spectra, in this work we exclusively used the 532 nm excitation wavelength.

The analysis of resonance phenomena thus requires the use of many wavelengths, which to our knowledge has rarely been done for UO_2 and PuO_2. Here, important data are the excitation profiles, *i.e.* the evolution of the effective scattering cross-section of each mode with the excitation wavelength. As such, these profiles are not known for actinide oxides. However, such data partially exist for UO_2 and

PuO_2. They concern the evolution of the intensity of the 1LO and more notably the 2LO modes, using the intensity of the T_{2g} mode as an intensity reference. This is the approach we have adopted throughout this work. These data should therefore only be considered qualitatively, as there is no reason why the intensity of the T_{2g} Raman-active mode should not be affected by the resonance phenomenon.

Concerning UO_2, such profiles have been published recently, in particular that of the 2LO mode, see Figure 124. In terms of wavelengths, this profile is plotted using data recorded between 785 and 354 nm. We recall that this is a second-order mode, and therefore *a priori* Raman active. The evolution of the $1LO/T_{2g}$ intensity ratio appears to be similar, though less dramatic. One can immediately see that this profile is quite sharp and narrow, 400 meV at most. It is centered on 2.3 eV approximately, that is very close to the energy of the excitation used in the present investigation (2.33 eV).

From a pure experimental viewpoint, 1LO and 2LO scatterings are polarized, mainly observed in a parallel analysis configuration. This can be rather important from a pure experimental point of view: not all spectrometers have the same response to polarized light. The spectrometer used here did not exhibited such a dependence, on the basis of signals recorded with a (001) silicon single crystal for which the intensity remained quite constant whatever the orientation of the crystal with respect to the orientation of the incident electric field, see Appendix C C.3.

Finally, we mentioned in Chapter 2 the relationship between the electronic susceptibility and its first-derivative with respect to atomic motion, with the optical constants, the absorption coefficient α in particular. In this respect, the available data are not always consistent [126], [161]–[163]. Accepting absorption coefficients of the order of 10^{-5} cm at 532 nm, it is clear that Raman analysis becomes a "surface" analysis, with a penetration depth of the order of 500 nm, assuming the penetration depth as $1/2\alpha$. Optical data (absorption coefficients in particular) are therefore essential for evaluating resonant Raman scattering. Figure 124 shows that the absorption threshold is close to 2 eV for UO_2.

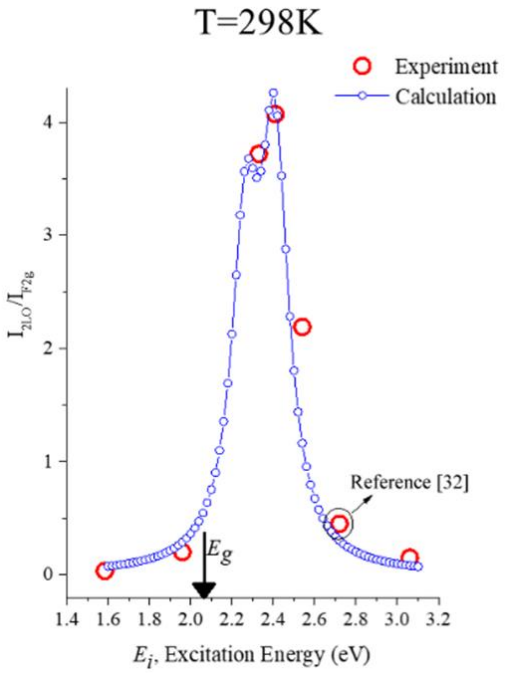

Figure 124 $2LO/T_{2g}$ intensity ration as a function of the excitation energy. Extracted from Ref. [141] Excitation wavelength used in our study is about 2.33 eV

The optical properties (absorption edge and optical constants) of PuO_2 were described in Refs. [164]–[166]. The absorption edge was determined at about 2.7 - 2.8 eV. Thus, PuO_2 is rather transparent up to about 440 nm. From those data, no strong resonance is expected with the wavelength used in this work, 532 nm. As it was observed for UO_2, the Raman spectra of PuO_2 also strongly depend on the excitation

wavelength. Main trends, extracted from Ref. [167], are given in Figure 125. Here, the spectra were acquired with the 785, 633, 561, 514, 488 and 457 nm laser lines. Again, the $2LO/T_{2g}$ intensity ratio is plotted in the figure. Again, it may be assumed that this intensity ratio closely reflects the evolution of the dielectric function as a function of excitation energy. From Figure 125, it is seen that the absorption edge is rather close to 2.6 eV.

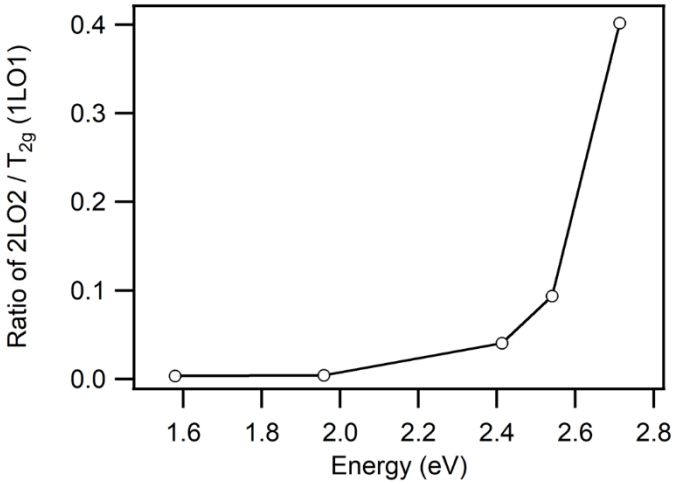

Figure 125 Evolution of the $2LO/T_{2g}$ intensity ratio vs the excitation energy [167]. Excitation wavelength used in our study is about 2.33 eV.

Both the resonance enhancement and the polarization dependence of the LO line series are in line with a mechanism based on the Fröhlich interaction, as observed and discussed previously for polar semiconductors such as CdS, ZnO, GaN, ... [100], [111], [114]. From this point it is clear that the absorption edge can be tuned with either temperature, strain, oxygen [141], [168], [169], and most probably heteroelements, meaning that the resonant threshold may be observed below or above the absorption edge determined for ambient pressure and temperature conditions. This is clearly what makes the analysis so complicated for these oxide materials.

In order to analyze what has been observed for the mixed oxide $(U,Pu)O_2$, see for example Figure 61b in Chapter 3, one can assume that the optical properties of $(U,Pu)O_2$ may be simply expressed as a linear combination of those of UO_2 and PuO_2, as in a simple "Vegard's law". The absorption edge of $(U,Pu)O_2$ in particular would thus be expressed as a linear combination of that of UO_2 and PuO_2 (absorption edges at about 2.0 and 2.8 eV, respectively). In the absence of any formal proof of this behavior, we regard it as "not too bad first approximation". Accepting that the width of the excitation profile depends only slightly on composition, and accepting such a linear dependence of the absorption edge, one can see that the resonance conditions are expected to be lost for a Pu/(U+Pu) content close to 30 wt.% while using the 532 nm excitation. This is indeed what is observed in Figure 61b in Chapter 3.

The $2LO/T_{2g}$ ratio therefore appears, at least in part, as a probe of the resonance conditions, and therefore indirectly as a probe of electronic properties of the actinide oxides. Using the 532 nm excitation wavelengths, it is seen is that not all agglomerates of a conventional MIMAS-type heterogeneous MOX fuel will be "seen" and analyzed in a same way, in particular in the 500-700 cm^{-1} range or close to the 2LO mode. One can also think, still without formal proof, that any excitation in the 2-2.8 eV range selectively probes a range of Pu content. It would be worth investigating. Once again, one can see the importance of the annealing conditions, which enable to work with samples close to the exact oxygen stoichiometry, whose optical properties are controlled.

5.2.4 The U* signal, and the 1LO mode.

Another characteristic feature of the $(U,Pu)O_2$ Raman spectrum is clearly the U* group of lines. It is evidently dominated by the "Raman-forbidden" but infrared-active 1LO mode. Most of the time, this group of lines is also referred as a "Raman defect-induced spectrum". Even if the 1LO mode implies a small amplitude movement of the cation, these lines fall in a frequency range for which vibrational modes are oxygen-dominated, see for example the O and U partial phonon density of states available in Ref. [143]. This characteristic signal is not a unique characteristic feature of actinide oxides, being observed in part for ceria [170], [171]. The 1LO mode, as well as the U_1 and U_3 lines, is also resonance enhanced, again, a scenario to be attributed to the Fröhlich electron - phonon interaction. In most cases, using resonant excitation conditions in particular, the intensity of the 1LO mode seems to overwhelm that of U_1 and U_3 modes, preventing their clear observation. Nevertheless, it is not clear whether the U_1 and U_3 modes have a similar resonance profile to the 1LO and 2LO modes. It seems not, based on Refs [172], [173]. A similar finding was clearly reported also for PuO_2 [167].

It is generally accepted that the 1LO mode finds its origin with the presence of structural defects. Perhaps more precisely, the observation of this mode in Raman spectra suggests some deviations from the perfect fluorite structure, the loss of the inversion symmetry in particular. Indeed, for centrosymmetric structures, the observation of infrared modes in Raman spectra is usually considered as evidence of the loss of the center of inversion. Therefore, it is understandable that the presence of any structural defect, punctual as well as extended, is sufficient to activate this mode. More, in the case of a solid solution such as the one presently considered, the EXAFS and XRD data we collected suggested a rather organized cationic sub-lattice, and a more disordered oxygen sub-lattice, in line with many previous works [61], [95], [101], [148]. One therefore intuitively expects an increase of the 1LO mode intensity when enriching the solid solution in Pu, while, at the same time, the resonance conditions are progressively lost. This is probably the reason why the intensity of this mode seems to remain almost constant during the Pu enrichment of the solid solution, see, for example, [129] and Figure 57 in Chapter 3. This may also explain the differences observed in the $1LO/T_{2g}$ intensity ratio images for the annealed samples, the maximum intensity of this ratio being rather observed in the MIMAS coating phase (Pu/U+Pu) content around 10 %). One also sees that a similar reasoning allows explaining why this signal is also observed for slightly hyper stoichiometric UO_{2+x} [174]. The lattice distortions arising from differences in the ionic radii between the different oxidation states of U cations allow charge balance and thus differences in U^{4+}-O and U^{5+}-O distances.

The U_3 shoulder was always observed, or at least suggested by the adjustment of the U* signal into three resolved components, for all the spectra. On the other hand, the U_1 shoulder seems to be mostly observed after self-irradiation. According to Ref. [129], neither of the two peaks seem to shift with the excitation energy, as expected for a first-order mode. Literature shows that the relaxation of the $k \approx 0$ selection rule due to defects or finite crystallite size not only broadens the Raman allowed modes, but can also cause new modes to appear, which may correspond *to* $k \neq 0$ phonons. A prototypical example is obviously graphene [175]. Nevertheless, the frequencies of U_1 and U_3 modes do not clearly correspond to the maxima observed in the computed or measured density of state curves, see Ref. [138], [143]. More, U_3 mode frequency seems to lie slightly above the cut-off frequency of the VDOS, whereas U_1 is rather observed in a forbidden frequency gap between the LO2 and TO2 branches. One can therefore assume that these two signals have different origins, and more importantly that they are not zone-edge modes of the perfect fluorite structure activated by some relaxation of the $k \approx 0$ selection rule. Nevertheless, it is known that point defects usually change the vibrational structure of a solid. Both U_1 and U_3 mode are therefore most probably induced by the presence of at least two specific structural defects, or at least two defects with different atomic environments around it. Most probably, they cannot be considered as completely "local" modes insofar as their frequencies rather overlap with the bulk phonon spectrum, and thus they are not strictly localized in space. Interestingly, similar signatures were reported for hypo-stoichiometric CeO_{2-x}. Bands in the 480−600 cm^{-1} region were observed and associated with the presence of oxygen vacancies accompanied by the formation of reduced Ce^{3+} sites. More in details,

Density Functional Theory (DFT) computations revealed that that the coordination cube around $Ce^{4+/3+}$ ions in hypo-stoichiometric CeO_{2-x} strongly influences the spectral properties [171]. In particular, it was shown that, in the Raman spectra of bulk CeO_{2-x}, a clear distinction could be made between Raman bands arising from Ce^{3+} in direct proximity to the oxygen defect, characterized by a computed band at 500 cm^{-1}, and those originating from Ce^{3+} located in the second coordination sphere of the oxygen vacancy, giving rise to a band at 480 cm^{-1}. Since the crystal structures are similar, with more or less the same vibrational spectra, it is not unreasonable to look for a similar explanation for actinide oxides, even if hypo-stoichiometry cannot be completely involved here.

Finally, it should be noted that some works associate the U_3 line with the presence of U_4O_9 on the surface of the samples, translating a slight surface oxidation. Even if it cannot be totally rejected, it seems difficult to accept this hypothesis since the U_3 signal, or at least a signal with a similar frequency, is observed for PuO_2. Such a phase is unknown in the Pu-O binary diagram. Furthermore, this signal was found to be resonantly enhanced using an excitation at 785 nm [32]. This is most probably not the case here.

It also seems completely unrealistic to assume that there are only two types of defect environments in such a self-irradiated ceramic material, including self-irradiation ones. The U_1, 1LO and U_3 signals have been found for different situations: annealed, polished, irradiated material, grain boundaries in a ceramic... In all cases, the intensity of these signals depends on the excitation wavelength, and on the thermal history of the material. It is therefore not unreasonable to assume that the Raman analysis probes only two specific defect environments, with their own specific electronic energy levels, that are tuned close to the excitation energy during Raman measurements. Here, it remains to determine what these defects environments are. Clearly, DFT-based computations seem necessary to propose some possible scenarios. However, at present, it is not clear whether this type of computation is sufficiently reliable for the actinide oxides.

Finally, resonant multi-phonon processes were also observed for other oxides, and in particular for a number of polar semiconducting materials [114]. A last but important question is to determine if this forbidden scattering actually requires the presence of defects (local loss of the translation invariance, or at least the inversion center), or not. From this reference, it seems not, even if we will see below that the introduction of some structural defects modifies the relative intensities of the 1LO and 2LO modes.

5.3 Self-irradiation effects probed with Raman spectroscopy

Why should we use Raman spectroscopy to study these effects? Throughout this work, we have seen that MOX fuels are inherently heterogeneous. MIMAS-type fuel is a perfect example. Most probably, Raman spectroscopy appears to be the only laboratory method for analyzing this type of material and its subsequent evolution under radiation. As we have seen, all spectral characteristics change to a greater or lesser extent under radiation, and this is what we will be examining in the following section.

5.3.1 The T_{2g} Frequency and width: lattice swelling, phonon confinement

Focusing on the T_{2g} mode, the only Raman-allowed mode from the first-order selection rules, it can be seen that self-irradiation first induces a strong broadening of this mode, which was already documented for UO_2, PuO_2 as well as for $(U,Pu)O_2$ [72], [97]. It also seems to induce a mode downshift, which has not been systematically reported. Finally, as already suggested in Refs. [72], [97], a small asymmetry of this mode towards the low frequencies seems to be detected. First, these characteristics may have experimental origins, overheating (due to laser exposition) and/or deviation from the oxygen stoichiometry

[99] of the old (before annealing) samples or over time after annealing. We are aware that both origins cannot be completely ruled out, even if, from an experimental point of view, many precautions have been taken, as described in Chapter 3.

If these experimental origins are disregarded, the downshift of this mode can *a priori* be explained in two different ways. The first approach is to consider that the mode softening directly translates the lattice expansion, in other words the strain of the material upon self-irradiation. Different approaches can be used to relate strain to Raman shifts. Within the scope of this study, the most intuitive one is most probably the use of the so-called Grüneisen parameter. The details with this parameter are already explained in 2.2.3.4.4. In its microscopic formulation, the Grüneisen parameter γ is a measure of how a specific phonon frequency is altered under a small change in the geometry (volume) of the crystallographic unit cell. In other words, it quantifies the phonon anharmonicity.

For isotropic materials, or materials with cubic lattice symmetry, the Grüneisen parameter γ is simply a scalar that refers to an isotropic change in the volume *V*, according to [117], [170]:

$$\frac{\Delta\omega}{\omega_0} = -\gamma\frac{\Delta V}{V_0} \approx -3\gamma\frac{\Delta \mathrm{a}}{a_0} \qquad \text{Eqn (55)}$$

Where ω_0, V_0 and a_0 are the vibrational frequency, unit cell volume and lattice parameter under ambient pressure and temperature conditions, and $\Delta\omega$, ΔV and $\Delta \mathrm{a}$ are the corresponding changes with pressure and/or temperature.

As a rule, the Grüneisen parameters are usually close to unity. This parameter is usually obtained examining samples *vs* temperature or isostatic pressure. In Chapter 2, we distinguished between isobaric and isothermal parameters. When the so-called "anharmonic effects" are low, the dimensionless Grüneisen γ_T and γ_P parameter should be similar for isothermal and isobaric lattice parameter changes. This was notably observed for CeO_2 [170].

The isothermal Grüneisen parameter has been was estimated at 1.28 from the pressure dependence of the T_{2g} mode [100]. We used two different data sets [176], that were found to be equivalent within the experimental accuracy, to extract the isobaric Grüneisen parameter, that leads to another, but much lower value, close to 0.5. For those estimations, we used commonly accepted values for the coefficient of linear expansion (9.802 10^{-6} K^{-1} [177]) and the Bulk modulus (207±2 GPa [100]).

Clearly, these two data sets do not match, which can be explained by the strong anharmonicity of this mode. Nevertheless, only an order of magnitude seems necessary here, since there is no strict reason why this value should be strictly the same for UO_2, PuO_2 and the mixed crystals $(U,Pu)O_2$. More, there is no reason why the elastic properties of virtually defect-free and irradiated materials should be strictly the same. Eqn 55 shows that this order of magnitude is close to a few cm^{-1} for a strain value of 0.3%. This order of magnitude effectively matches the observed T_{2g} mode downshift values, which was observed for the matrix phase of the Capra4 samples, the Pu-rich agglomerates of the MIMAS sample, and even the Pu-rich clusters of the Capra4 sample. Close to the lattice parameter swelling saturation, line downshifts of about 2.5 cm^{-1} were consistently observed. Figure 89 suggests a value close to 0.5 for this parameter. Examining Figure 89, it was seen that the data were not completely consistent with a linear behavior of the frequency change as a function of volume change. A first way of analyzing this deviation from linearity is obviously to consider the uncertainty of our data, and the small number of data used to draw this graph. A second way of explaining this deviation from linearity is to take into account the injection of defects into the materials.

The T_{2g} mode downshift might indeed also be a direct consequence of the introduction of point or extended defects in the crystal lattice, that may induce a partial or a complete relaxation of the $k \approx 0$ selection rule. This is consistent with the fact that both molecular dynamic simulations ref.[12], [13] and

TEM observations ref.[10], [91] show that point defects progressively arrange themselves into dislocations and voids, creating nano-domains. When the amount of defects is quite large, inducing small characteristic lengths or mean coherent sizes below ≈ 15 nm, these effects are usually discussed according to the phenomenological phonon confinement model [115], also known as the spatial-correlation model. Depending on the dispersion of the optical branches in the Brillouin zone, a shift and asymmetrical broadening of the Raman-allowed line is usually observed. The disorder transforms sharp Raman lines, resulting from wavevector (*k*) conservation in crystals, into phonon densities of states induced-features. The range of phonon wave vectors that contributes to the Raman line shape is determined by the mean crystallite size, or even the mean distance between defects, and is usually approximated by $\Delta k \approx 2\pi/l$, where *l* is a characteristic length. These confinement effects have been widely discussed for most semiconductor materials [178] and more interestingly here for CeO_2 [179]. In the latter case, it was clearly observed that the T_{2g} mode of the CeO_2 nanoparticles shifts progressively to lower energies while the line shape of this feature gets progressively broader and asymmetric on the low-energy side as the particle size gets smaller, below ca15 nm.

Examining Capra4 samples, The T_{2g} band was progressively developing some asymmetry on its low frequency side. Interestingly, this asymmetry was clearly detectable after 421days of self-irradiation, that is, after a certain irradiation dose (corresponding to an increase of the lattice parameter already larger than 0.2 %). As the examination of the phonon dispersion curves [142]–[144] shows a strong bending of the LO1 branch towards the low frequencies, this hypothesis cannot be completely ruled out. The T_{2g} mode downshift observed here would show that the characteristic length (a mean distance between defects) is effectively lower than 15 nm, what is not known here, and even perhaps unlikely as the diffraction patterns do not show strong specific line broadening. Without TEM images, it will be difficult to go any further in this discussion. However, some TEM images of equivalent samples are shown below. We will see that this assumption is not completely unrealistic.

One note that both origins, strain and confinement, cannot be easily discriminated here.

5.3.2 The intensity of 1LO and 2LO modes: loss or shift of the resonance conditions

A comparison of the results regarding the 1LO and 2LO bands obtained for the MIMAS and the Capra4 samples most probably do not allow understanding the results in a consistent way. The self-irradiation consequences on the line shape of the Raman spectra seem drastic for the U-rich agglomerates of the MIMAS sample, while they appear weak for the Pu-rich agglomerates, and the matrix of the Capra4 sample. This is obviously completely counterintuitive; this can be understood by taking into account the fact that the analysis is quite exactly resonant for U-rich agglomerates.

Schematically, for the specific wavelength used here, a clear distinction can be made between Pu/(U+Pu) contents above and below around 15%, in other words in resonant and off-resonance conditions. In off-resonance conditions, it is seen that the 2LO mode do not carry any specific information. Only a slight increase of the 1LO mode intensity was observed, which may be a consequence of the fact that the crystal lattice is already intrinsically distorted.

In the U-rich composition range, the situation is completely different, as a strong increase (decrease) of the 1LO (2LO) mode was readily observed.

The 2LO is a probe of the resonance conditions. Its intensity strongly decreases with the injection of defects in the fluorite lattice and the resulting swelling of the lattice parameter. This fact has been extensively reported in previous studies [72], [97], [99], [122], [180]. It is known that the absorption edge is strongly shifted with pressure, temperature and even hyper- or hypo-stoichiometry. First, one can first

think that the absorption threshold is red-shifted with the increase of the lattice parameter, in a way similar to what has already been observed with temperature [129]. Moreover, the introduction of structural defects most probably leads to an equivalent finding, even though we cannot provide formal proof. Another consequence of the introduction of structural defects is most probably to blur or smooth out the resonance conditions. The loss of intensity of this mode thus effectively tracks any deviation from the perfect $UO_{2.00}$ fluorite structure, in an indirect way however.

The 1LO probes deviations from the perfect fluorite lattice. One therefore intuitively expects an increase in the intensity of the 1LO mode with defect injection in the material, while, at the same time, the resonance conditions are progressively lost. The consequence of defect injection is therefore not simply and directly quantifiable. Such an analysis conducted at 532 nm can therefore lead to a biased view of the results.

5.4Swelling described by Kato's law: Possible scenarios associated with defects

During self-irradiation, the materials studied in this work remain crystalline, even for the highest doses. The main consequence of self-irradiation effects is the swelling of the lattice parameter of UO_2, PuO_2 and $(U,Pu)O_2$ solid solution. This swelling, as measured using XRD, is always close to 0.3%, in line with the literature consensus [4], [91]. Therefore, we will not discuss the second decimal of this value here, which remains well within the uncertainty of the measurements, see all the comments above. This swelling was also detected by other methods, in particular Raman spectroscopy and EXAFS. All the main causes of uncertainty have been discussed, the Am content in particular. We will not go into them again here. Nevertheless, with the light of the results obtained in this study, as well as the available information in the literature, we will try to analyze the related phenomena in the microscopic scale that influence the lattice parameter increase. This latter is the main purpose of this section.

To go further in this discussion, one needs a scenario, an approximate or even an oversimplified one, that takes into account that the materials remain crystalline in spite of the extent of the radiation damages. This was partially discussed in the first chapter, in Section 1.2.2.1. Such a scenario is necessarily at an atomic scale. At such an atomistic length scale, irradiation events mainly lead to electronic excitation but also to the creation of point defects such as vacancies or interstitials, as well as other extended defects. The presence of these defects, and their time evolution, can be visualized by means of TEM analysis, see for example Refs.[10], [91], see also the Figure 128 and Figure 132 given below. As a matter of fact, such TEM analysis could not be done within the framework of this work. We will refer to, instead, some of the images given in de Bona *et al.* [11]. In that particular work, the images were obtained after different self-irradiation times of $(U,^{238}Pu)O_2$ solid solutions, with Pu/U+Pu contents around 2.5 and 10 at %. The creation of these defects and their evolution over time can also be studied by MD simulations [12], [13]. Even if the doses and time scales used in these simulations do not necessarily correspond to those characteristic of self-irradiation effects, they will most probably allow us to propose a first scenario in which point defects (Frenkel pairs (U, O), but more generally vacancies and interstitials) first accumulate in the material and then progressively aggregate to form interstitials clusters, voids, Frank loops, and then dislocations. After a given cumulated dose, a steady state is reached and dislocations reorganize into dislocation networks creating misoriented nanodomains [12], [13]. Basically, the microstructure change induced by this scenario seems consistent with the main TEM observations [10], [91], as we shall see below. Thus, the evolution from point defects toward extended defects can be thought to contribute to minimize the overall elastic strain in the samples, explaining in part the saturation of the lattice parameter increase. Nevertheless, at such an atomistic scale, it is likely that all these different events (creation of Frenkel pairs, creation of extended defects, then saturation of the lattice parameter) cannot be completely separated in time.

At this point, a few orders of magnitude are also required. Here, we assume that extended defects do not contribute significantly to the expansion of the lattice parameter. It is understood that these defects necessarily lead to micro-strains, both compressive and tensile, in a more or less local scale, depending on the elastic constants of the material considered. Nevertheless, those strains have to compensate locally. One therefore mainly needs to discuss the effect of point defects, Frenkel-type defects in particular, even if this is undoubtedly very restrictive. It is accepted that the energy thresholds for the formation of these defects are close to 20 and 40 eV for O and (U, Pu) atoms respectively, simply considering the known data for pure UO_2. Thus, one intuitively expects more O-induced Frenkel pairs than U-induced ones. As a first and obviously very crude, approximation, we only consider the effect of Frenkel pairs due to oxygen. In other words, we don't have the necessary elements to go further beyond this simple direction. For such a purpose, we first consider the effects of hyper- and hypo-stoichiometry on the lattice parameter of UO_2, or even $(U,Pu)O_2$. Indeed, this can be discussed more or less directly.

The effects of the oxygen vacancies (hypo-stoichiometry) or even interstitials (hyper-stoichiometry) in the lattice parameter swelling or shrinkage were already described in the preceding chapters. As a reminder, hypo-stoichiometry is described by the Duriez's equation (Eqn 3), while for the hyper-stoichiometry is described with the following formula, extracted from Ref [181].

$$a = 5.470 - 0.13x \qquad \text{Eqn (56)}$$

In both cases, x refers to hypo- or hyper-stoichiometry considering the MO_{2-x} .

Here a simple defect balance is used to create a scenario based on oxygen Frenkel pairs. In the balance, the 'x' is taken as 0.01, signifying the creation of one Frenkel pair for every 200 oxygen atoms in the lattice. By combining both equations (3) and (56), this straightforward yet oversimplified calculation shows that to reach to the saturation state, about 4 % of the atoms must be in the form of Frenkel pairs.

We're aware that one makes a tremendous approximation here: (i) the two equations quoted above take into account that hypo- (hyper-) stoichiometry leads to the creation of U^{3+} (U^{5+}), for the charge balance, (ii) our samples are considered as stoichiometric, and although for the global charge compensation a scenario is proposed with a balance between U^{+5}, Pu^{+3} and Am^{+3} concentrations (see Section 4.2.3.1), nothing is known about local charge compensation mechanisms. This was the purpose of the XANES measurements campaigns, which did not give us any additional information, the oxidation states of the U and Pu cations remaining virtually constant, to the uncertainty of the measurements, (iii) this hypothesis certainly yields an overestimation for the number of oxygen Frenkel pairs, while the corresponding U pair are not taken into account, (iv) obviously, more complex defects geometries are to be expected, (v) the possible substitution or precipitation of the recoil nuclei was not considered.

This simple estimation, once again very primitive, tends to show that a relatively low content of so-called "point" defects, a few at % at most, may be sufficient to explain the lattice swelling. This defect content is most probably close to the detection threshold of the methods used in this work, XANES in particular. For the latter, HERFD-XANES would be a better option to have better insights, nevertheless a coupled use of HERFD-XANES and µ-beam could not be possible on our samples. In this context, the application of a simple rigid ion model (as detailed in reference [182]) will most probably unable to give us any further information neither; as it is by far too imprecise for such a purpose. Therefore, from our perspective, pursuing further discussion at this point would involve excessive speculation.

Other data available in the literature can also be used to support this discussion, namely the evolution of the thermal conductivity, the hardness, and some TEM images as function of self-irradiation. These data, obtained from different studies are presented in Figure 126, Figure 127 and Figure 128 respectively. In these figures, the self-irradiation effects on material properties were still investigated using UO_2 samples

doped with ^{238}Pu. It is beyond the scope of this work to discuss them in detail, nevertheless, they can be referred to provide a few elements of understanding.

The thermal conductivity of a material is briefly the measure of its ability to conduct heat. The thermal transport in materials is due to the coexistence of electron and phonon conduction and the strong interaction between them. In our case, phonons dominate thermal conduction, particularly the acoustic phonons. This means that one cannot make a strict link between our Raman measurements and the material's thermal conductivity. Nevertheless, the mechanisms of phonon scattering through point or extended defects (phonon-impurity scattering and phonon-boundary scattering) should remain rather similar. Hardness is a measure of the resistance of a given material to plastic deformation. It is generally assumed that material hardening takes place because of dislocation movements and dislocation generation within the crystal structure of the material. At this point, one can make the simplistic assumption that hardness is a measure of the presence of dislocations. The presence of these dislocations can be observed with the TEM images, see Figure 128.

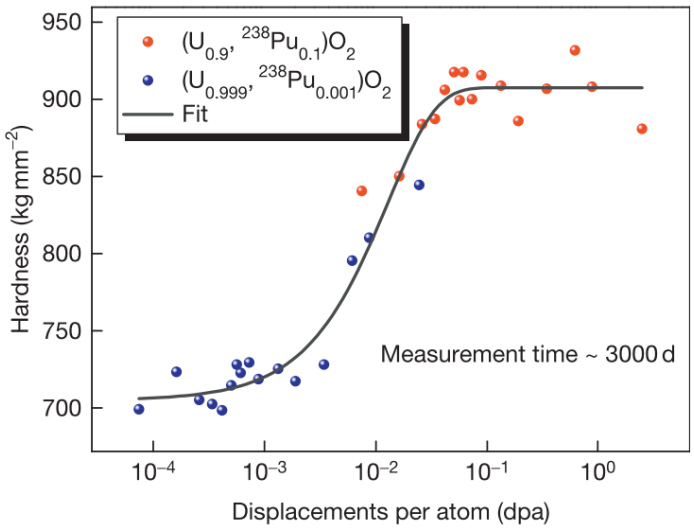

Figure 126 Change in hardness over time for two alpha-doped materials, represented as a function of dpa [183]

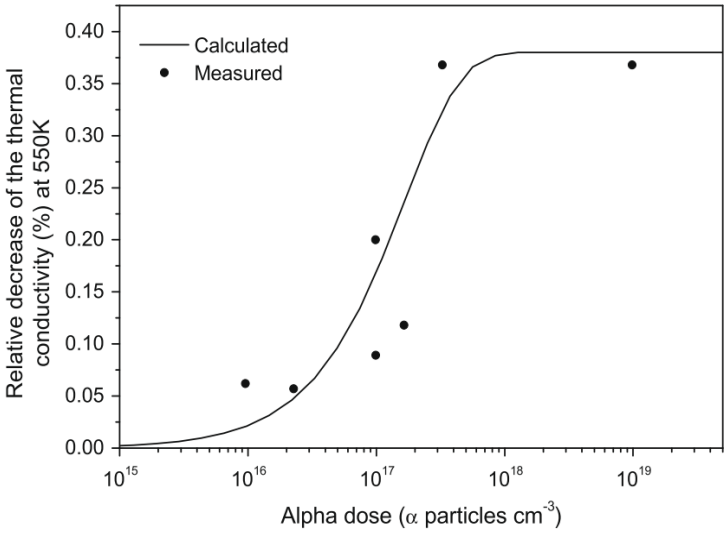

Figure 127 The thermal conductivity decrease with the cumulated α-dose for UO_2 and $(U,Pu)O_2$ samples. Measured and calculated data [184]

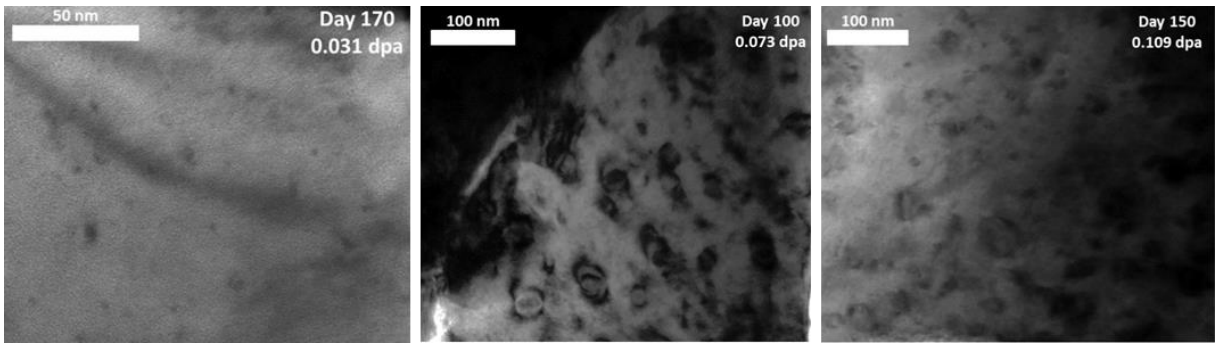

Figure 128 TEM picture of different $(U,Pu)O_2$ samples a) at 0.031 dpa damage, b) at 0.073 dpa damage, c) at 0.109 dpa [11]

It is seen in the figures that most of the data are generally given in the literature as a function of the displacement per atom (dpa). The correspondence between self-irradiation time or even dose and this value was described in Chapter 1. For such a purpose, we redraw some of our data as a function of this last variable, see Figure 129 and Figure 130. The data presented in these figures are derived from the Capra4 sample, mainly because this is the sample for which we had the most data over time, although based on only a relatively limited dataset consisting of only 5 to 6 data points.

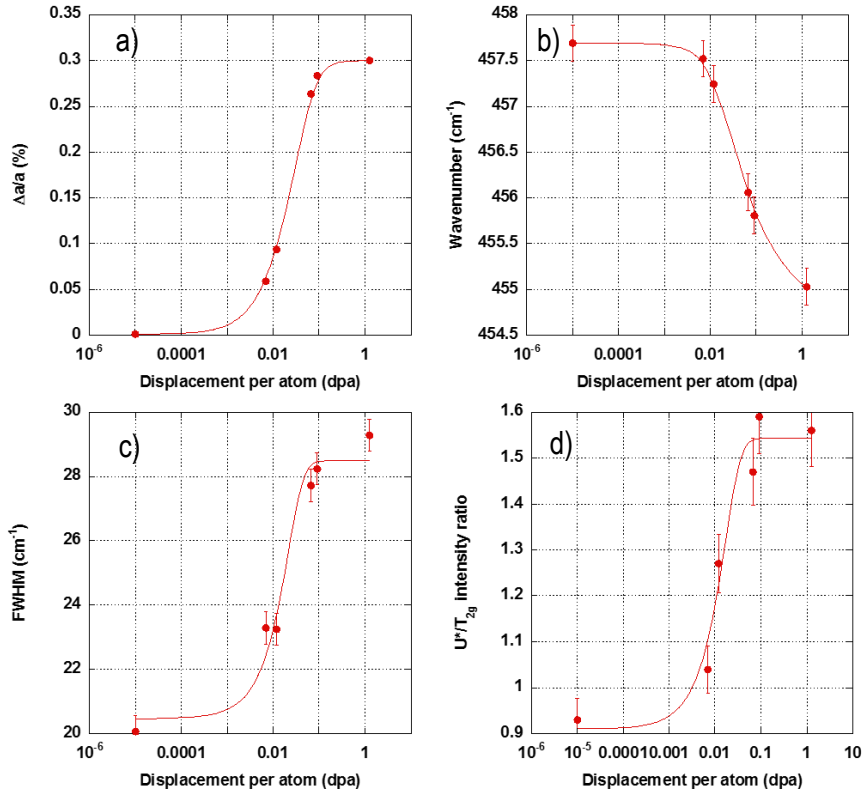

Figure 129 Observed parameters in the Capra4 sample, evolution with dpa on a logarithmic scale a) Strain evolution $\Delta a/a_0$, b) T_{2g} frequency evolution c) T_{2g} line width evolution d) U^*/T_{2g} intensity evolution

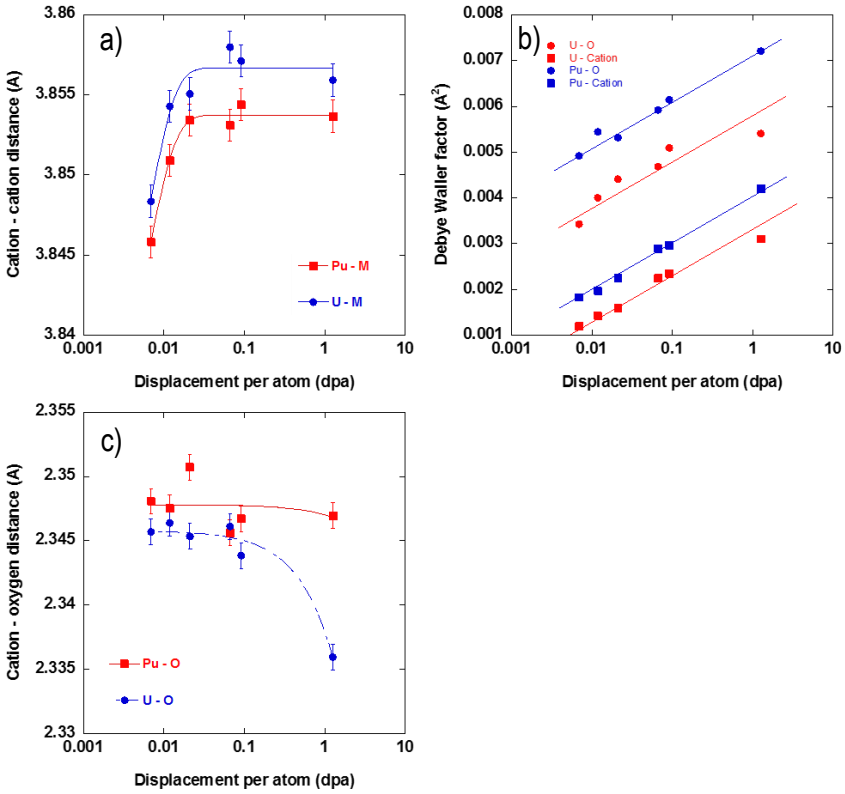

Figure 130 Observed EXAFS parameters in the Capra4 sample, evolution with dpa on a logarithmic scale a) Cation-cation distance b) Debye Waller factor c) Cation-Oxygen distance

At this point, one last piece of information is still probably missing: can all these results be described in the form of a single universal curve? Obviously, we have no proof of this. However, judging from Figure 131, it seems that this hypothesis is not completely unreasonable, at least as far as the swelling of matter is concerned. Once again, these data concern ^{238}Pu-doped UO_2 samples. The two data sets obtained for the ^{238}Pu-doped (2.5% and 10%) UO_2 samples are effectively found on a single universal curve.

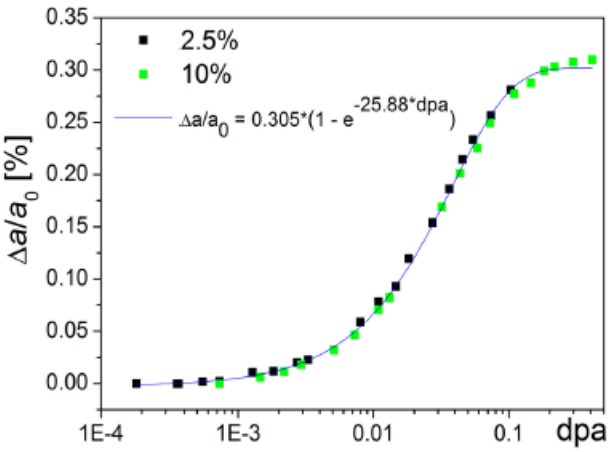

Figure 131 Observed material swelling with dpa plotted using a logarithmic scale. Green dots: UO_2 doped with 10 at% ^{238}Pu, black dots: UO_2 doped with 2.5 at% ^{238}Pu. Extracted from Ref [11]

Before attempting to comment in more detail on all these figures, we note that they all use the same dpa self-irradiation time conversion scale, see Chapter 1.

What do all these figures tell us? First of all, they are all drawn on a logarithmic scale, so the time (dpa) scale is expanded. They more or less exhibit a sigmoid-like evolution. We can't help but refer to the simplified scenario described above: (i) creation of point defects, (ii) progressive creation of dislocation

loops, (iii) all point defects condense into extended defects. Such a scenario, obviously oversimplified, can undoubtedly explain most of our results, but still without formal proof.

In the first of these regimes, we can therefore assume that only a few point defects are created. In this case, one has to accept a more or a less linear relationship between the rate of defects created and the expansion of the lattice parameter. We only have two data points to verify this assumption, meaning that we cannot be very precise in this discussion. In the second of these regimes, it is more or less obvious that all the parameters are evolving that includes the expansion of the lattice parameter, all of the off-resonance Raman data (U^*/T_{2g}, $2LO/T_{2g}$, T_{2g} frequency and width), the distances between first-cation shell… Besides the macroscopic data, thermal conductivity and hardness in particular, evolve in quite the same way. During this same regime, the T_{2g} mode begins to develop some asymmetry towards low wavenumbers, which we have tried to comment on in terms of confined optical modes. According to our data, this asymmetry becomes observable from 421 days, meaning approximately 0.06 dpa. Figure 128 also shows the development of dislocation loops, for a similar dpa value. One can therefore assume that, in this second regime, the quantity of point defects keeps on increasing, while some of them begin to condense into extended defects. The fact that Raman measurements suggest confined modes to take place at very small coherent domain sizes, below 15 nm. Figure 128b most probably tends to highlight some of these areas, still without being able to describe them completely. At this point, the Raman data, the slight increase of the relative intensity of the "defect band" in particular, can obviously tell us nothing more. In the third regime, all parameters tend to remain more or less constant. In this latter regime, self-irradiation continues to produce defects, especially point defects. However, in order to minimize the stored elastic energy, most of these defects have to be condensed into extended defaults, or even surfaces. In this context, the lattice parameter no longer has any reason to evolve any more.

This oversimplified model also shows that the initial size of the grains making up the initial material is likely to modify the thresholds observed in this work, as well as in the references used. Such a size effect is probably to be expected for grain sizes well below the µm scale, once again, without formal proof from our results. Here one needs to keep in mind that all interfaces and even extended defects serve as recombination sites for vacancies and interstitials beyond a given concentration, among other effects, meaning that they play an important role in reducing the concentrations of point defects produced by irradiation: vacancies and interstitials migrate to the interfaces, where they recombine.

In this simple model that we discussed, we obviously neglected the contribution of He bubbles. Still according to the study of E. De Bona [11], the observation of the He bubbles was possible after a certain damage accumulated in the lattice, which was in the order of $1.2x10^{18}$ He/g, corresponding to 0.328 dpa. The associated TEM images with this latter study are shown in Figure 132, where in the given images, the size of the He bubbles was homogeneous and in the order of 2nm. Such a dpa value obviously falls into the third regime, as described above.

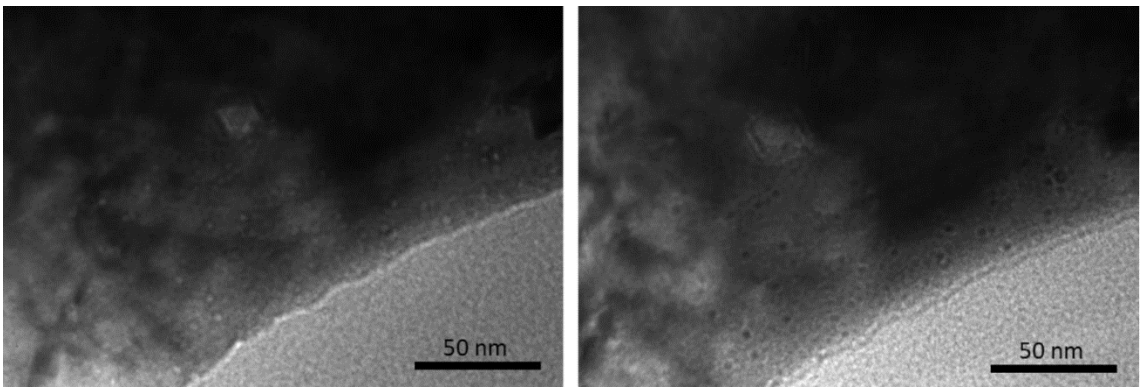

Figure 132 Observation of the Helium bubbles in the damaged MOX sample recorded after 0.328 dpa of damage. [11]

A final comment in this section concerns the MIMAS sample, for which our data show differential expansion of the U- and Pu-rich agglomerates as a function of self-irradiation time. It should be noted

here that our data could not be translated directly into terms of dpa, as U-rich agglomerates are *a priori* free of short half-life α-emitters (Pu and Am), still as a first approximation. The influence of the α-particles (mean free path of about 15 µm) and the recoil nuclei (mean free path around 15 nm) will obviously be very different. As a reminder, the size of all these agglomerates are in the order of 10 µm, which means that the core of the U-rich agglomerates will only be subjected to α particles. Still assuming a simplistic hypothesis that states that the radiation dose is similar for the different types of agglomerates, we can see that recoil nuclei (ballistic damage) will cause more damage than the light Helium nuclei (principally electronic stopping).

These effects are also widely discussed in the literature. It therefore becomes clear that our data need to be compared more closely with those in the literature, which we were unfortunately unable to do completely during the time available for this study.

5.5 Conclusion

In this chapter, we have attempted to discuss and interpret our main results. Throughout this work, we have reported and analyzed our results while relying on a few assumptions that can be considered as rather strong. In particular, we have neglected the contributions of the americium content, any deviations from stoichiometry and the micro-strains, which are inherent for the MOX materials studied. With the exception of the Pu-rich clusters detected in SFR-type fuels, it appears that these assumptions do not call into question the main trends observed throughout this work.

Then, we focused on the interpretation of the Raman spectroscopy data. This method is perhaps the simplest to implement on a laboratory scale for the analysis of PWR and SFR fuels. Our three samples have enabled us to revisit, in part, the data acquired for $(U,Pu)O_2$ solid solution. It emerged that the conclusions reached in a previous study should not be called into question in the concentration range selected for this study, *i.e.* between 0 and 40 at% Pu. We also sought to analyze resonance effects, on the basis of very recently published data. Indeed, analysis at a single wavelength (532 nm in this work, *i.e.* exactly under resonant conditions for UO_2) can obviously highlight U-rich agglomerates in a heterogeneous material. The 1LO infrared mode was systematically detected, interpreted simply by the loss of the inversion center in the fluorite-type crystal structure.

The effects of self-irradiation on the shape of Raman spectra were then discussed. In off-resonant conditions, *i.e.* above around 15 at% Pu, these effects were found to be weak: a shift and broadening of the active Raman mode with T_{2g} symmetry, and a slight increase in the $1LO/T_{2g}$ intensity ratio. For lower Pu contents, the 2LO mode becomes a probe of the material's electronic properties. Swelling of the crystal lattice and injection of defects are likely to lead to a red shift and blurring of the excitation profile.

In the last part of this chapter, we have aimed at proposing a scenario that takes into account our main observations, as well as some data available in the literature. Analyzed on a logarithmic scale, most of these data exhibit a sigmoidal evolution on a dpa scale, with a threshold systematically close to 0.01 dpa. It is tempting to attribute these three domains to the creation of "point" defects, such as Frenkel pairs or more complex defects environments, followed by the progressive formation of dislocations. In the saturation regime, all point defects are expected to condense into extended defects, surfaces or even porosity.

We are aware that this scenario remains hypothetical, as our data do not allow us to go any further in this interpretation.

Conclusion and Perspectives

This thesis focused on a comprehensive analysis of the self-irradiation effect on MOX fuels, *i.e*. uranium plutonium mixed oxides. The macroscopic level consequence of the self-irradiation, *i.e.* the progressive swelling of the material and its saturation at 0.3% increase of the initial lattice parameter was already known in the literature. However, the microscopic level explanation of this occurrence was missing. To fill this gap, we investigated one LWR type and two SFR type fuels, with the primary objective of understanding the microstructural changes due to self-irradiation effect.

The existing literature suggests that self-irradiation has different impacts on the cationic and oxygen sublattices of the fluorite symmetry. The study was thus based on a multiscale approach using four different characterization techniques each bringing specific microstructural data: XRD, EPMA, Raman microscopy and XAS.

Considering the availability of the samples, we were presented with two challenges. First, based on the literature, the effects expected from self-irradiation are somewhat weak, and relatively slow compared to the timeframe of this study. We thus chose to select samples that had been fabricated decades ago and had since accumulated a significant alpha dose. A simple annealing then allowed to obtain the fresh counterparts of these old samples, providing two possibilities for the study of self-irradiation. On one hand, these effects could be analyzed by direct comparison of old and annealed samples. On the other, the annealed samples were studied all along the thesis to describe the effects of accumulation of self-irradiation damage.

The other challenge resided on the sample inherent chemical heterogeneity at the micron scale. This meant that the samples could not be simply used as a whole. The samples were thus characterized with spatially resolved methods when available. This allowed for a thorough description of the plutonium heterogeneity at the micro scale. Additionally, taking into account this heterogeneity made it possible studying the $(U,Pu)O_2$ solid solution over a large range of Pu contents (Pu/(U+Pu) ratios between 0 and 40 wt%) with only three samples.

This study began with the analysis of the samples after annealing *i.e.* the samples free from self-irradiation. The objective here was to obtain a thorough description of the samples microstructure before any self-irradiation damage had been accumulated, to be used as a reference state for the subsequent study of the self-irradiation effects. Additionally, these characterizations were necessary to evaluate the efficiency of the annealing. The XRD data validated the extent of the annealing that can be considered as defect free. Besides, the XANES spectra and the XRD data confirmed that the O/M ratio was close to stoichiometry in these samples. Under these conditions, it was possible to use XRD and Raman spectroscopy to derive an average or local Pu/(U+Pu) content that could be compared to the EPMA (chemical) analysis. For all the samples, the Raman data closely resembled the EPMA data, with an estimated error margin of approximately +/- 1% in Pu/(U+Pu) ratios. Surprisingly, the diffraction data, while generally considered reliable, showed greater disparities when compared to the chemical data.

Upon analyzing the EXAFS data, deviations from a perfect fluorite-type structure were observed. The data, especially those collected at low temperatures (15K), indicated a relatively well-organized cationic sub-lattice (consistent with the XRD data, this technique being most exclusively sensible to that sublattice) and a more disordered oxygen sub-lattice aligning with the literature. Notably, the first U-O and Pu-O distances were both systematically shorter than expected based on the lattice parameter.

Regarding the observations in the U* and 2LO band intensities, it was observed that as the Pu content increased, the intensity of these bands progressively decreased. This was due to the progressive loss of

the resonant conditions. Once the Pu/(U+Pu) content reaches approximately 15 wt%, these bands become nearly impossible to exploit, due to their very low intensities. The behavior of the U* line intensity was particularly interesting. In ideal circumstances, this intensity should increase when probing regions with higher Pu contents because this band is, in fact, Infrared active, and its activity arises from the breakdown of perfect symmetry, the loss of the inversion center in particular. However, it is important to note that this band is also sensitive to resonant conditions, which means it loses its intensity in a progressive manner as the Pu content increases. As a result, the obtained results arise from a compensation mechanism between these two phenomena.

In our investigation of the self-irradiation effect on the Raman spectrum, we have made observations, some of which align with previously documented findings. One such observation involves the shift of the T_{2g} line towards lower wavenumbers. A progressive shift in the T_{2g} mode was observed with self-irradiation until a saturation at about 2.5 cm^{-1}. The magnitude of this shift is consistent with our expectations based on calculations using the Grüneisen parameter. The time evolution of this shift is consistent with that observed for the lattice parameter, even though the data do not allow for a description as precise as that available for the lattice parameter. The existing literature regarding this shift was up to now contradictory, but the systematic approach employed in this study provides a clear evidence of its existence.

Moreover, the evolution in the T_{2g} mode width and the Debye-Waller factors provided insights into the structural disorder induced by self-irradiation. The first parameter is associated with the phonon lifetime and the second reflects the variations in distances among neighbors, thus associated with the disorder within the corresponding atomic shell. Here, the evolution of both parameters exhibited similar time constants. Notably, these time constants (taking into account the current accuracy of the measurements) closely aligned with those determined from Kato's values used in the empirical correlation that shows the lattice parameter increase due to self-irradiation damage overtime (dose, damage).

Regarding the saturation of the lattice parameter increase, we have proposed a simple balance that is based only on the oxygen Frenkel pairs. According to this calculation, to reach the saturation state in lattice swelling, 4 % of the atoms must be in the form of Frenkel pairs. This level is unfortunately outside of the sensitivity range of the XAS technique. Thus, techniques that are more precise could be proposed to obtain more insights about this. For example, a possible experimental campaign in HERFD-XANES technique could be used.

The majority of the observable parameters studied underwent a sigmoidal type of evolution with the self-irradiation damage (when plotted with respect to dpa in the log scale). These parameters include the T_{2g} position and its width, the U^*/T_{2g} and $2LO/T_{2g}$ intensity (in the off-resonance conditions) and the distance in the first neighbor in the cation-oxygen shell. The sigmoidal curve can be separated into three domains and these domains are associated with three types of defects explained in a scenario in conjunction with the TEM and MD studies. According to this scenario, the Frenkel type defects accumulate in the system until a damage level of 0.01 dpa, where after this threshold value, these point defects form Frankel loops and upon further increase of the self-irradiation damage, which is in the order of 0.07 dpa, the third domain of the curve is reached where the Frank loops form dislocation networks creating misoriented nanodomains. This behavior was later associated with the evolutions in the thermo physical properties such as the hardness and the thermal conductivity of the MOX materials.

Finally, from an application perspective, our findings can be compared to the duration between the fabrication of the fuel and its storage prior its use in a reactor.

Considering the Capra4 sample as a representative MOX fuel to be used in a reactor. Our investigation, in accordance with the literature, shows that the point defects transform into Frank loops (according to the proposed scenario) starting from a damage level of 0.01 dpa, as shown in Figure 129. This level of damage is accumulated in 72 days (after annealing, here fabrication) for this particular sample. The

consequence of this phenomenon to the physico chemical properties is visible in Figure 126 and Figure 127 through the change in hardness and the thermal conductivity of the material. Subsequently, the third region of the sigmoid curve is reached after a damage level of 0.07 dpa, which corresponds to a 421 days of damage accumulation after annealing. Thus, according to the scenario proposed, the Frank loops will be the predominant defect type (due to self-irradiation) of the MOX fuels prior its use in reactor.

As a future perspective, the same samples could be investigated using different excitation wavelengths. By utilizing an excitation wavelength significantly lower than the UO_2 absorption threshold, such as 785 nm or 633 nm, that we can analyze the spectra outside of resonant conditions. Whereas, employing wavelengths like 488 nm and 457 nm will allow us to probe the samples under resonant conditions over the full Pu/(U+Pu) range. Such an investigative campaign will help validating the resonance conditions of the samples studied. Besides, this approach could help us better observe the evolutions in the U_1 and U_3 defect bands, in which, we could not have any outcomes in this study regarding their origins.

Concerning the oxygen sublattice in our samples, our EXAFS data has revealed a significant distortion that deviates from the expected configuration. To gain a more comprehensive understanding of this deformation, however, a complementary experiment using Electron Energy Loss Spectra (EELS) can be conducted on the same samples. This additional analysis will provide valuable insights into the extent of this distortion, particularly when compared with the EELS spectra of UO_2 as a reference.

Given the absence of a TEM in our laboratory, we relied on existing literature data to support our study with this characterization technique. However, it is worth noting that a potential TEM experimental campaign could have been conducted to capture images, such as those of the Capra4 sample 421 days after annealing, as well as the samples before and after annealing. This approach would have allowed us to gain a more in-depth understanding of the nanodomains and their correlation with the changes observed in the Raman spectra.

External irradiation experiments would also provide valuable insights that could be compared with our current results. Here for an external irradiation experiment, an α-source could be considered. In this case, the primary damage source would be only the He particles as the recoiling nucleus has a mean free path of only in the orders of few nanometers. From this essence, this experiment could serve as a useful benchmark for simulating the accumulation of He bubbles on the U-rich agglomerates within the MIMAS sample. To simulate the effect of recoiling nuclei, experimental systems such as the JANNUS facility could be employed. In this case, the energy and size of the incident particles should be carefully matched with the recoiling nucleus of a heavy atom like U or Pu for a more accurate and relevant comparison with the self-irradiation scenario.

Appendix A. Sample preparation in the ATALANTE facility

A.1 A short introduction to the L26 Laboratory in the Atalante facility

Except the techniques that are based on synchrotron radiation, all other sample preparation and characterization techniques were performed in the L26 laboratory of the Atalante facility in CEA Marcoule. The L26 laboratory was commissioned in 2018 with the purpose of characterizing nuclear materials mainly Pu-bearing compounds. These materials primarily emit α radiation, necessitating their storage and manipulation within glovebox systems maintained under an inert atmosphere at room temperature. The glovebox systems are meticulously designed to prevent any escape of α emitters, ensuring a secure environment for conducting nuclear material experiments and averting their spread beyond the protection barriers. Because of the ^{241}Am presence in most of Pu-base samples, the gloveboxes are also equipped with an additional lead-doped glass to attenuate ^{241}Am 60 keV gamma emission [185].

In this laboratory, some of the equipment are completely nuclearized (*i.e.* completely installed inside the glovebox system) such as the wire saw, the polishing machine or the optical microscope. Some of the instruments are partially nuclearized such as the Raman spectroscopy or the optical microscope, while some of them are installed completely out of the gloveboxes such as the EPMA and XRD.

For the non-nuclearized devices, however, the samples are either decontaminated before the measurements such as for the case in EPMA, or inserted in an isolated system that can be connected to the glove box such as the case for the XRD. A general view of the L26 laboratory is shown in Figure 133 below.

For the synchrotron radiation-based experiments on the other hand, a thorough sample preparation was carried out to prepare the sample for the measurements while complying with the rules of the beamline, notably including keeping the sample in a double containment sample holder.

Figure 133 The L26 laboratory of the Atalante facility in CEA Marcoule. Figure adapted from [95]

In the following sections, the materials as well as all the characterization methods that are used in this study will be detailed. When necessary, the sample preparation for each experiment are also detailed in the corresponding subsections.

A.1.1 Sample Preparation

The fabrication processes for the samples used in this study (PWR-type MIMAS and two SFR-type: Capra4 and Trabant40 fuel pellets) are initially outlined in this section. This is followed by the explanation of the thermal treatment technique applied to heal the defects. Furthermore, the preparation of these samples for their subsequent characterization is detailed. For simplicity, we will collectively refer to these samples as 'MOX' unless specific distinctions are required.

A.1.1.1 Fabrication of the samples

A.1.1.1.1 The MIMAS type MOX fuel

Briefly, this fuel is produced by a two-step process, where the first step consists of blending and milling of UO_2 and PuO_2 powders. This mixture is called the master mix and corresponds to a Pu/U+Pu ratio of around 30%. The mixture is then exposed to dilution with the depleted UO_2 to a targeted U/Pu ratio, which is between 5-10%Pu/U+Pu.

During the sintering (4h at 1700°C), the close contact between the micronized UO_2 and PuO_2 particles induces a partial interdiffusion, which therefore leads to formation of a $(U,Pu)O_2$ solid solution with varying Pu contents, depending on their location in the material [186]. Such a fabrication process leads to a sintered ceramic material consisting in three distinct "phases" which can be easily identified within pseudo quantified Pu EPMA image (see for example Figure 44 in Section 3.1.1 of Chapter 3). These three phases are designated as:

- U-rich agglomerates result from the UO_2 that is used for dilution,
- Pu-rich agglomerates result from the master mix and thus presenting a Pu/(U+Pu) content around 30 wt.%,
- a “matrix” with intermediate Pu contents located between the two others’ agglomerates. The “matrix” is also known as the so-called “coating phase” [97], [104], [187] in the literature.

A.1.1.1.2 Capra4 and Trabant40 samples

CAPRA4 (Consommation Accrue de Plutonium dans les RApides) was manufactured in CEA Cadarache at the LEFCA facility in 1996. The fabrication of this sample was performed with the industrial COCA (CObroyage CAdarache) process [188]. Unlike the MIMAS process, the COCA process is made of a single step process that is only based on blending and milling of UO_2 and PuO_2 powders and does not include the dilution step with the UO_2 [189]. This brings a rather more homogenous microstructure comparing to the MIMAS type MOX. The production scheme of the MIMAS and the COCA process is given in Figure 134. The sintering conditions for this sample is 1943 K for 4h under Ar/H_2 7% [59].

The TRABANT40 (TRAnsmutation and Burning of ActiNides in Triox) type MOX fuel was produced at the Joint Research Centre Karlsruhe in Germany in 1998, intended for irradiation at HFR-Petten in the Netherlands [190]. The sintering conditions for this particular sample involved heating it to 1923 K for 6 hours under an atmosphere of either pure argon or a 1% hydrogen mixture with argon. Similar to the Capra4 fabrication process, Trabant40 is manufactured using a sequence that includes co-grinding, sieving, pressing, and sintering of UO_2 and PuO_2 powders [59].

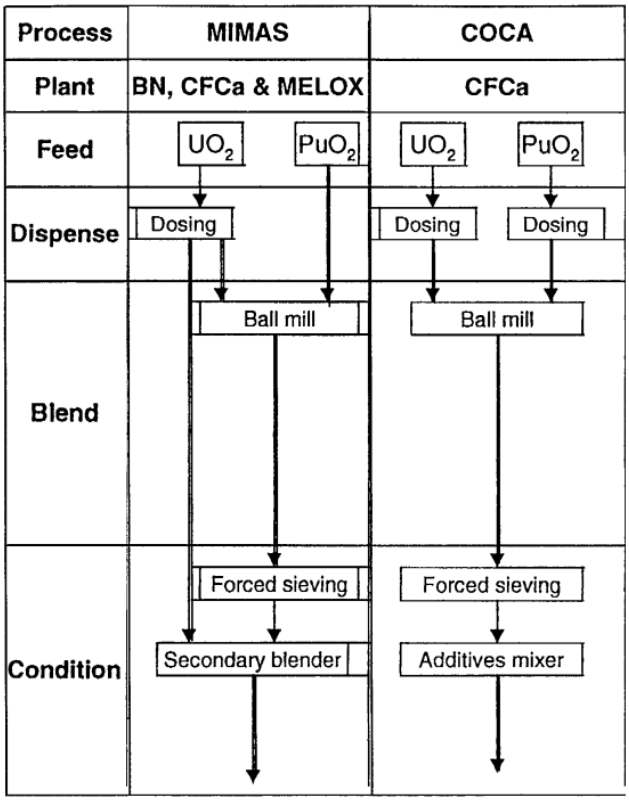

Figure 134 Schematic flowsheets of the MIMAS and COCA processes for MOX fuel production which is followed by pressing and sintering of the powders [189]

A.1.1.2 Thermal treatment of the samples

Prior sending the samples to treatment, small pieces of the initial MOX pellets were cut in the desired cross section (*i.e.* either in the circumferential or longitudinal orientation) with an average mass of 200-300 mg and a thickness of 2-3 mm. This was done under water using either the wire saw or the lab scale cutting machine equipped with a wheel dedicated to the cutting of the ceramic materials. The latter equipment is shown in the left side of Figure 135.

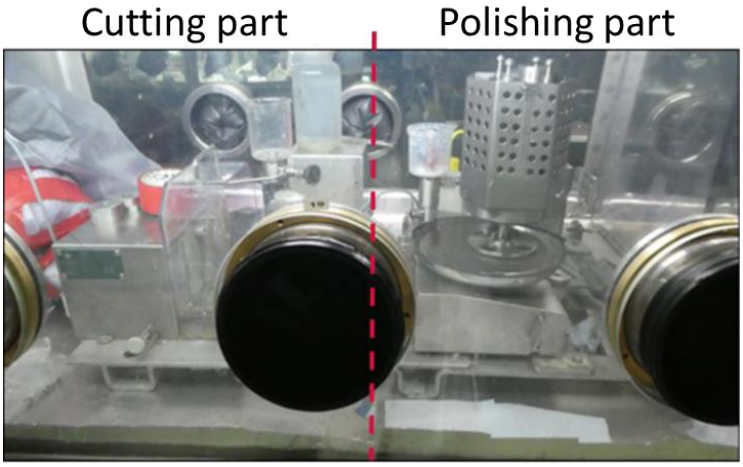

Figure 135 The photo of the glovebox #1 in L26 lab, where the cutting and polishing of the samples are taken place. The photo adapted from [191]

Since the annealing is performed in another laboratory of the same facility (LN0 laboratory in Atalante), certain safety measures are implemented for the transfer of the samples from one lab to another. To minimize exposure to air, samples are double-confined within a specialized hermetic bag (manche). For

the cases where sample activity exceeds the 500µSv/hr threshold, stainless steel is employed as a shielding material to attenuate radiation and to protect the carrier personnel. Prior the transfer, the sample is controlled by a radiation protection specialist within the facility to ensure that the preparation is adequately done for a safe transfer. The same procedure is also followed for accepting back the sample from LN0 after its annealing.

The LN0 laboratory of the Atalante facility in CEA Marcoule is equipped with a specially designed furnace provided by ECM Technologies shown in Figure 136. To regulate the oxygen partial pressure at the furnace's gas inlet and outlet, the system was connected to a boiler chamber at the gas entrance and a zirconia probe from Setnag company at the outlet.

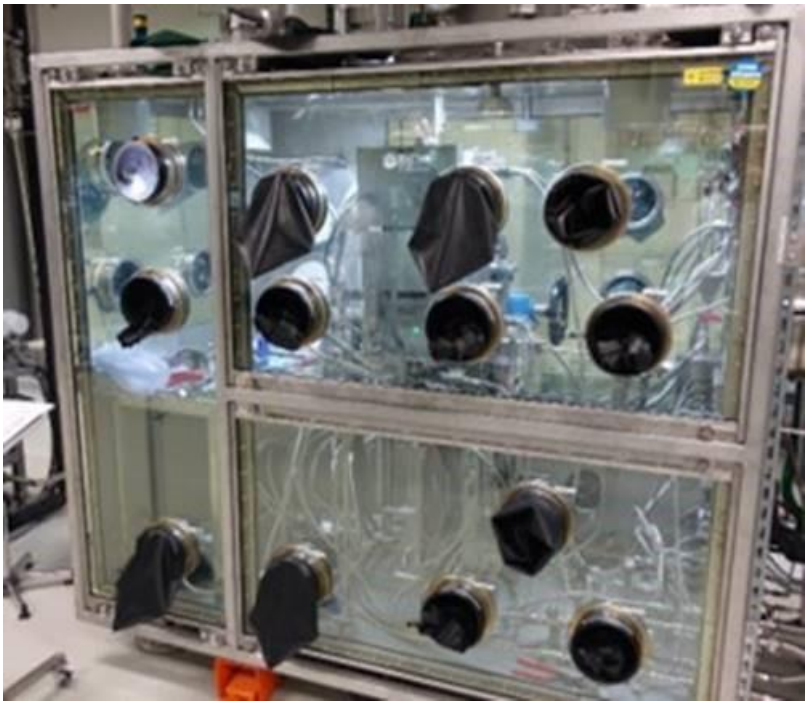

Figure 136 The furnace placed in the LN0 laboratories used for the thermal treatment of the samples

For all the samples the same annealing conditions were adapted, 8 h at 1473 K under an atmosphere made of Ar/4.3%H_2/1200 ppm H_2O, ($\Delta G_{O2} \approx -420$ kJ/mol at 1473 K). The conditions ensured to have a (virtually) defect-free state in the microstructure and keep the O/M as close as possible to 2.00. Cooling down to room temperature was performed at 6 °C/min, under the same atmosphere. For determining the annealing conditions, the information available in the literature is used, notably the thermal recovery studies mentioned in Section 1.2.3 of Chapter 1.

The annealing brings the lattice parameter to its original state *i.e.* free from the contribution of the self-irradiation damage increase. The annealed sample is not a fully representative of the as fabricated material, yet it can be considered a “defect-free” replica of the aged, self-irradiated sample. The annealing quality can be later verified with its corresponding XRD pattern.

A.1.1.3 Preparation of polished cross section of the sample

In order to have a better observation of the sample microstructure and to have a better signal quality during the characterization (especially for the case of EPMA and Raman spectroscopy), the samples were polished to the so-called “mirror like” state. For this, the samples are first coated in a polyester resin (SCANDIPLAST provided by Scandia) in order to keep the sample fixed in a certain position and mounted in a 25 mm cylinder compatible with the sample holders of the characterization tools. The samples were then polished using rotating discs containing silicon carbide abrasive grains (ESCIL) under about 1450 g.

Discs having different grain sizes were used at each stages with the following decreasing order: P400 (35 µm grains), P600 (26 µm grains), P800 (22 µm grains) and P1200 (10 µm grains). The final “mirror-like” surface (see Figure 137) is obtained with a diamond-based suspension with a granulometry of 0.7 µm (MM140 provided by Lamplan) used on a dedicated cloth (TOUCHLAM 2TS4 provided by Lamplan).

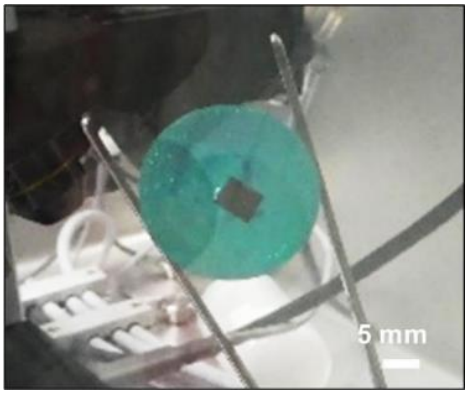

Figure 137 An example of a MOX sample surface polished to the "mirror-like" state. The green zone is the epoxy resin, while the dark piece (embedded in the resin) is the MOX sample. The photo adapted from [191]

A.2 Optical microscopy and alpha self-radiography

Once the samples are polished, the sample surface was observed using an optical microscope, whose design is shown in Figure 138. The microscope is installed in a glovebox, while the control system (x, y, z displacement stages) are available outside of the glovebox. The turret is equipped with an Olympus camera and five objectives with ×1.25, ×10, ×20, ×50 and ×100 magnifications.

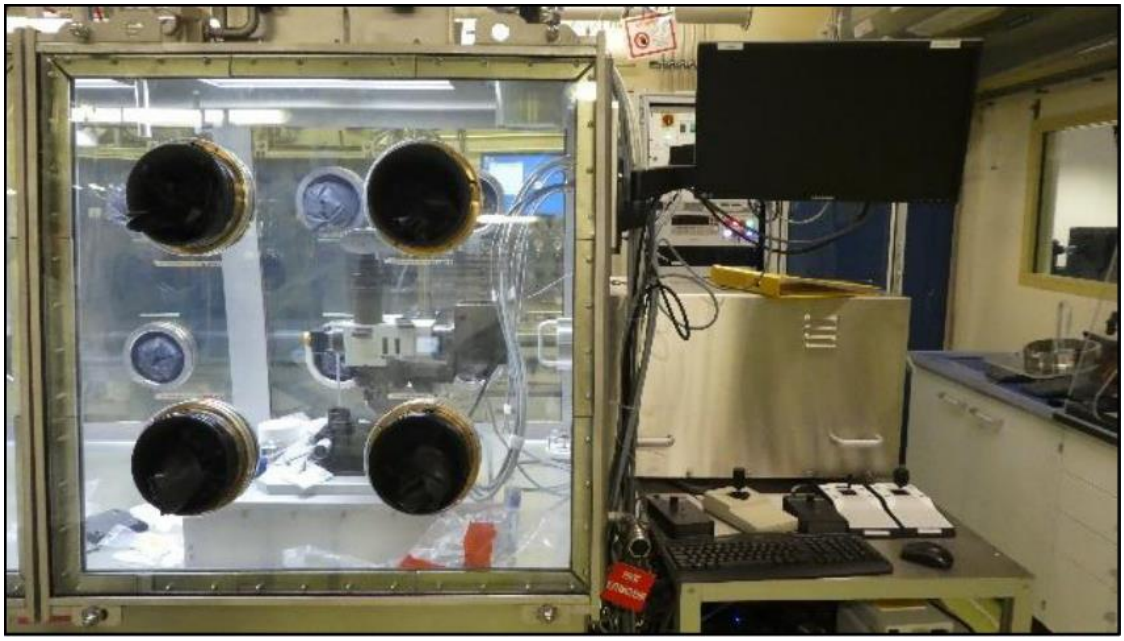

Figure 138 Optical microscope system in the L26 laboratory. Microscope is installed inside the glovebox and the control board is on the right side of the glovebox. Photo adapted from [191]

This glovebox is also equipped with an alpha autoradiography system, which is a method employed to generate visual representations of alpha emitter distribution. In the context of MOX samples, this technique primarily highlights regions enriched with plutonium. It is one of the oldest technique for detecting radioactivity, and was extensively used for application in the physical and life sciences since the 20th century [192]. For its application, the polished mirror sample is positioned against a CsI(Tl) scintillator. When alpha particles are emitted, they interact with the scintillator, causing it to emit photons.

These emitted photons are then detected by a camera positioned behind the scintillator. Since plutonium is a much more intense alpha emitter than depleted uranium, significant contrast can be measured between uranium-rich clusters and clusters containing plutonium. This technique is limited in spatial resolution and only allows for qualitative analysis of highly heterogeneous samples (such as MOX fuels produced using the MIMAS process). Furthermore, it is highly sensitive to the flatness of the sample surface and surface contaminants that absorb or emit alpha particles.

For this study, this method is primarily used to have a quick idea about the plutonium homogeneity and its distribution by keeping track of the Pu rich agglomerates for the case of the MIMAS type fuel. For the SFR type fuels, however, the technique does not produce relevant results, both because their Pu-rich spots are small and the matrix Pu content is relatively large. The alpha self-radiographies coming from these samples, thus, do not present any brightness contrast within the sample surface.

Appendix B. Optical and alpha self-radiography of the Samples

B.1MIMAS Sample

In the adapted experimental procedure, optical and alpha self-radiographies of the samples are taken before and after the annealing process. This imaging approach allows the observation of the microstructure of the samples at the micrometer scale. The primary objective behind this practice is to ensure that the microstructure is not altered by the annealing process.

For the MIMAS type MOX sample, the Figure 139 and Figure 140 corresponds to the optical images of the samples before and after annealing. The sample surface was exposed to the preparation route that is explained in Section A.1.1.3. Specifically, when examining the MIMAS sample, it becomes evident that the optical images reveal distinct regions of uranium-rich (lighter grey) and plutonium-rich (darker grey) zones on the sample's surface (visible in the larger magnifications). This differentiation becomes even more pronounced at higher magnifications.

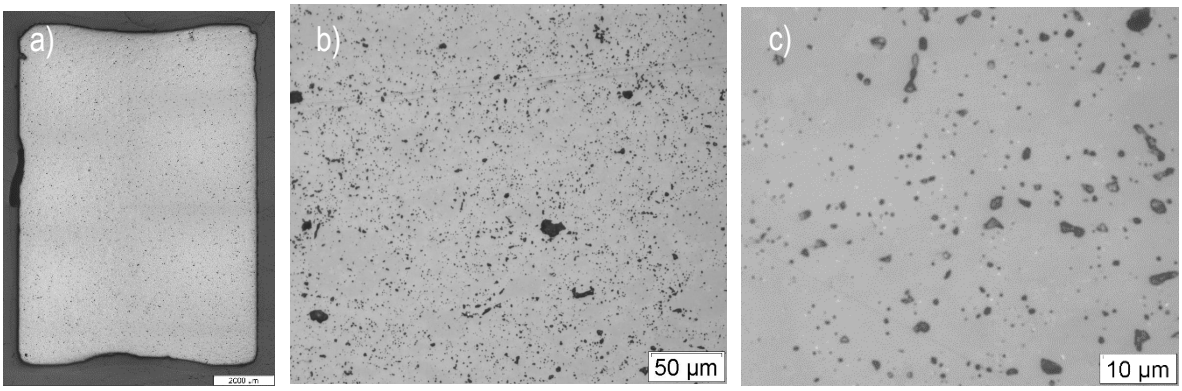

Figure 139 Optical image of the MIMAS sample surface before annealing a) image of the whole pellet (reconstructed from ×1.25 images), b) and c) at larger magnifications

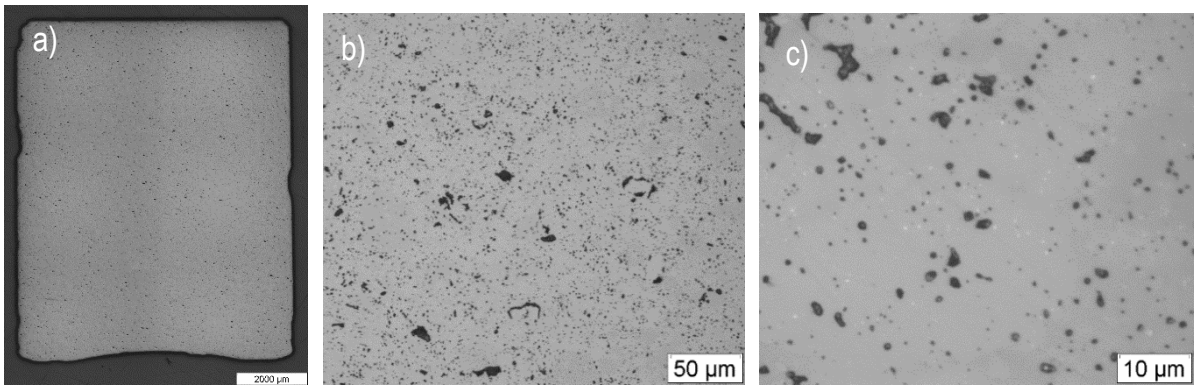

Figure 140 Optical image of the MIMAS sample surface after annealing a) image of the whole pellet (reconstructed from ×1.25 images), b) and c) at larger magnifications

The optical images of the samples before and after annealing reveal some insights into their microstructure. Notably, the size of the porosities in these samples predominantly falls within the range of < 5µm, with some instances reaching approximately 20 µm. These images serve as a reference points for assessing any alterations or transformations in the sample's microstructure. However, it is noteworthy

that no visible changes are observed after the annealing process, indicating the stability of the sample's characteristics throughout the thermal treatment.

Following that, the Figure 141a and Figure 141b shows the alpha self-radiography images of the MIMAS samples.

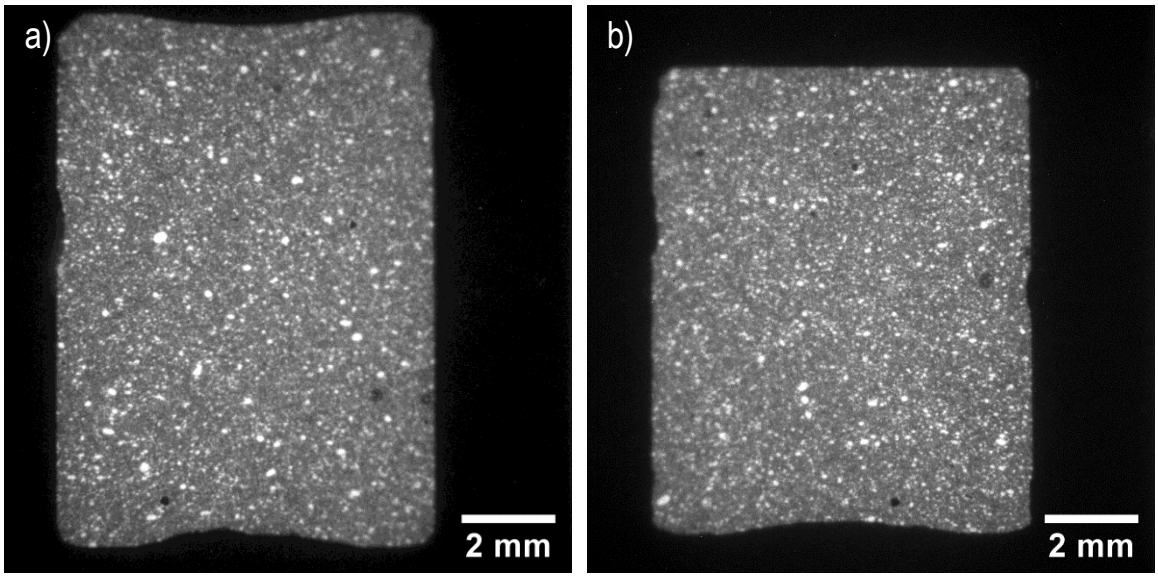

Figure 141 Alpha self-radiography images of the MIMAS samples a) before annealing and b) after annealing

From these images, it is possible to observe the Pu-rich clusters highlighted by the bright areas. Although there is no quantification of the results, a simple visual assessment shows no evidence of cation interdiffusion that alters the distribution of Pu as a result of the annealing of the sample.

B.2SFR Samples (Capra4 and Trabant40)

Concerning the Capra4 samples, the optical images of the samples before and after annealing are presented in Figure 142 and Figure 143. Notably, this particular sample exhibits larger surface porosities when compared to the MIMAS sample. The observed scratches, particularly noticeable in Figure 142a are Figure 143a result of the surface polishing process. Additionally, in are Figure 142b and Figure 143c, it is also possible to observe the U-rich spots located at the light grey zones.

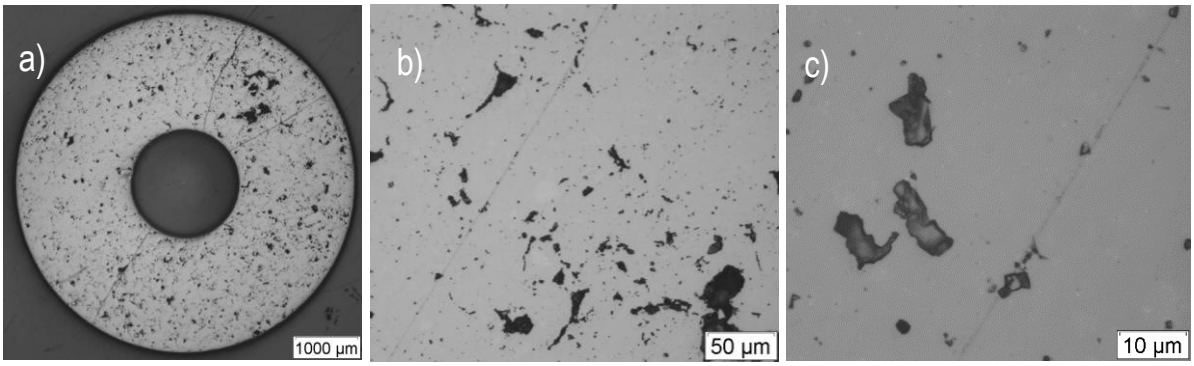

Figure 142 Optical image of the Capra4 sample surface before annealing a) image of the whole pellet (reconstructed from ×1.25 images), b) and c) at larger magnifications

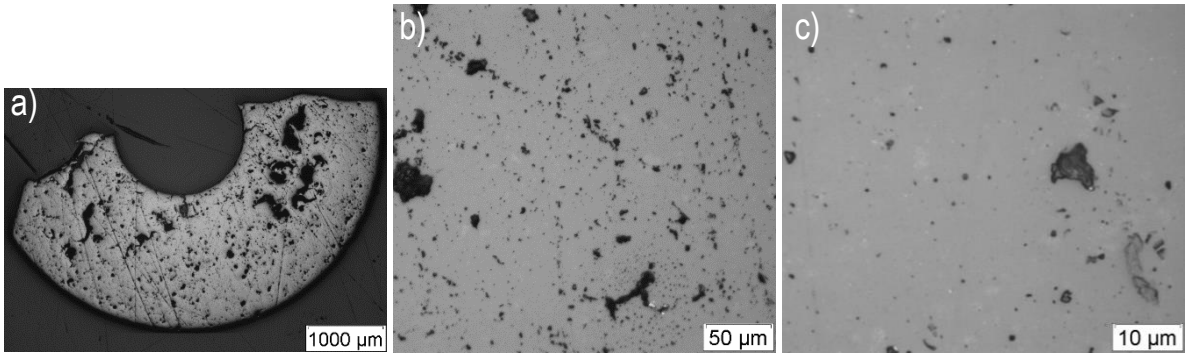

Figure 143 Optical image of the Capra4 sample surface after annealing a) image of the whole pellet (reconstructed from ×1.25 images), b) and c) at larger magnifications

Regarding the Trabant40 sample, on the other hand, our laboratory faced a shortage of this material to create a polished specimen from the existing material. Consequently, it was not possible to conduct analysis with this old specimen throughout the thesis, but only with the annealed specimen. Here, the Figure 144 shows to the optical images of the annealed specimen of this sample. The light grey zones can also be seen in Figure 144b, which corresponds to the location of the U-rich spots.

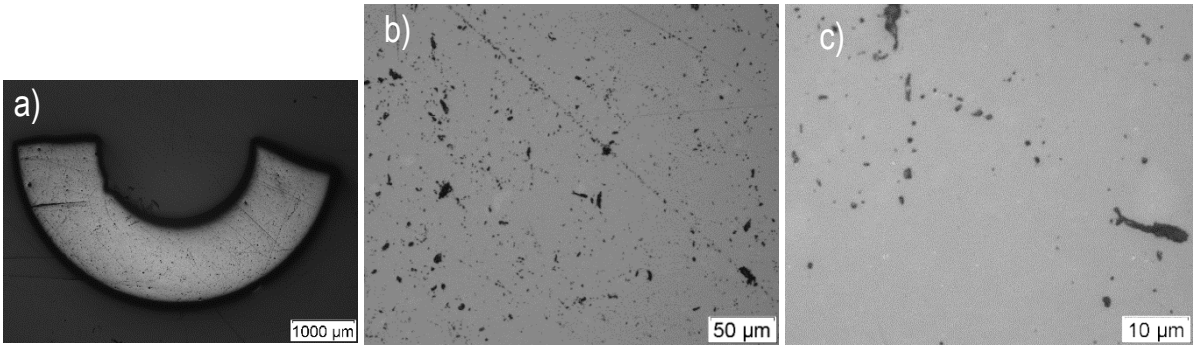

Figure 144 Optical image of the Trabant40 sample surface after annealing a) image of the whole pellet (reconstructed from ×1.25 images), b) and c) at larger magnifications

Appendix C. Characterization Techniques

C.1Electronprobe micro analyzer (EPMA)

C.1.1 Equipment and sample preparation

For this study, the CAMECA SX100 EPMA installed equipped with four WDS spectrometers in the L26 laboratory was used for the spatially resolved elemental analysis. As shown in the Figure 145, the EPMA is installed outside the glovebox. Thus, prior the acquisitions, the samples are decontaminated in order to keep the EPMA sample chamber free of contamination. For this reason, only samples mounted in resin and polished can be analyzed in this device.

Besides, the samples are coated with a carbon layer (of a few tens of nm) before being introduced into the sample chamber. This conductive coating is mostly necessary because of the very low conductivity of the embedding resin.

Figure 145 A photo of the CAMECA SX100 EPMA that is installed in the L26 laboratory in the Atalante facility

C.1.2 Measurement conditions

The electron beam (generated from a 100 µm tungsten filament) acceleration was set at 20 kV and the probe current was between 50 and 100 nA. Measurements were performed with four different WDS spectrometers at the U Mα, Pu Mβ, Am Mα (using PET or L-PET type analyzer crystals: $C_5H_{12}O_4$, 2d = 0.874 nm) and O Kα lines (using an L-PC1 type multilayer analyzer: W-Si, 2d = 6.1 nm).In such conditions, the probed volume for the actinide M line in $(U,Pu)O_2$ has a diameter and a depth of about 0.8 and 0.5 µm, respectively. These values were calculated based on Monte-Carlo simulation (considering U Mα in UO_2) with the Casino V2.5 software [193].

C.1.3 Elemental mapping

Two kinds of elemental mappings were recorded, referred to as large and detailed mappings. Large mappings are 1024 × 1024 pixels collected with horizontal and vertical steps of 1 µm obtained by sample stage displacement, with a counting time of 20 ms.stp^{-1}. Detailed mappings were collected on 100 × 100 µm^2 zones, with horizontal and vertical steps of 0.2 µm (hence 500 × 500 pixels), obtained by beam displacement, with a counting time of 100 ms.stp^{-1}. Large mappings are used to assess the global distribution of plutonium in the pellet and to identify zones of interest for more precise characterization, notably by Raman spectroscopy. Detailed mappings are used for direct comparison with Raman and µXAS results.

C.1.4 Line profiles of quantitative measurements

Quantitative measurements were also performed on the samples along horizontal profiles of 300 to 700 µm with a 1 µm step obtained by the sample stage displacement. The counting time was 15 s on the peak maximum and 5s for background measurements both before and after each peak. Mass fractions were measured using the X-PHI correction method [194] that is implemented in the CAMECA Peaksight V6.5 software and which is based on the Φ(ρz) quantitative correction method. Calibrations were performed on a UO_2 pellet for U Mα and O Kα and on a PuO_2 pellet for Pu Mβ. The interference of U Mγ line on the Pu Mβ line was taken into account through calibration on the same UO_2 pellet. For Am, as no standards were available, the calibration was performed on a Pu(Am)-rich of a Capra4 sample. It was considered that the Am/(Pu+Am) ratio in this spot is equal to that calculated for the overall sample (seeTable 10 Initial (1996) and the present (2023) isotopic composition (Isotope/(Pu + Am) or isotope/U) of the Capra4 MOX fuel used in this study.Table 10, in Chapter 2). The absence of uranium in the spot that is selected for calibration was checked before recording the Am Mα intensity.

C.1.5 Pseudo-quantification of plutonium mappings

Pseudo-quantification of the plutonium EPMA mappings was performed by using assuming a simplified linear relation between the Pu Mβ intensity (count number) and the Pu mass fraction [187]. The parameters of this relation is determined for each Pu Mβ mapping by comparing the distribution of count numbers in the mapping and that of plutonium mass fractions extracted from the quantitative profile measurements. Porosity were identified as spots with low intensity of both U and Pu. A false color scale was used to create the plutonium pseudo-quantified images presented in this document.

C.1.6 Plutonium content distribution

To evaluate the Pu contents distribution and their homogeneity in the samples, histograms can be extracted from the pseudo-quantified plutonium EPMA mappings. These histograms will be presented as a function of the plutonium content (or rather the Pu/(U+Pu+Am) wt% ratio). It is however important to take into account that they effectively are histograms of the counts numbers of the mapping. For this reason, these histograms are not exactly representative of the physical plutonium content distribution in the samples. This is mostly due to the Poisson noise of the measurements as described in the next paragraph.

Because the counting time is short (generally 20 ms per point), the theoretical measured count number is about a few hundred per pixel. The measured count number is a random variable that follows a Poisson law with a λ parameter equal to the theoretical count number. The apparent plutonium content distribution

is thus a convolution of the physical distribution and a Poisson law and is by consequence wider than the physical distribution[3].

For a very large count number (N > 10 000), this would be of small consequence as the relative standard deviation would be lower than 1%. For the EPMA mappings used for this study however, the distribution is generally centered on a count number between 100 and 200, which respectively lead to relative standard deviations of 10% and 7%. As an example, this means that even a perfectly homogeneous sample with a Pu/(U+Pu+Am) ratio of 25 wt% corresponding to a theoretical count number of 150 would result in an EPMA plutonium content histogram consisting of a normal distribution centered on 25 wt% with a FWHM (full width at half maximum) of about 4.8 wt%.

The determination of the implicit ("physical") distribution is not trivial and was not the purpose of this work. Instead, an approximation can be used by assuming that this distribution P is composed of a single or a sum of Gaussian components $P_i(\mu_i, \sigma_i^2)$ each centered on μ_i(mean) and having a variance σ_i^2 [195]

$$P = \sum_i P_i(\mu_i, \sigma_i^2) \qquad \text{Eqn (57)}$$

By assuming that the theoretical count number is large enough (typically $\mathrm{N} > 20$, which generally corresponds to a Pu/(U+Pu+Am) ratio larger than 2 %), the count number of each pixel can be approximated as a random variable following a normal distribution centered on N and with a variance also equal to N. The apparent distribution D can thus be described as the sum of the convolutions of each "physical" Gaussian component $P_i(\mu_i, \sigma_i^2)$ by a Gaussian distribution $G_i(0, N)$, representing the instrumental contribution (*i.e.*, centered on 0 and with a variance equal to the number of counts). This result is still not simple enough, as the variance of the instrumental contribution is not constant and will change in the count number range on which the convolution is calculated. However, it can be simplified if the relative variance of the assumed physical distribution is large enough and/or if that distribution is centered on a large enough count number[4]. In such conditions, this instrumental contribution can be approximated by a Gaussian $G_i(0, \mu_i)$ also centered on 0 but with a variance equal to μ_i, which is thus a constant for each physical distribution. Consequently, the product of each convolution is also a Gaussian distribution, noted $C_i(\mu_i, \sigma_i^2 + \mu_i)$, that is centered on μ_i and with a variance V_i equal to $\sigma_i^2 + \mu_i$.

$$\begin{aligned} D = \sum_i P_i(\mu_i, \sigma_i^2) * G_i(0, N) \;&\approx \sum_i P_i(\mu_i, \sigma_i^2) * G_i(0, \mu_i) \\ &= \sum_i C_i(\mu_i, \sigma_i^2 + \mu_i) = \sum_i C_i(\mu_i, V_i) \end{aligned} \qquad \text{Eqn (58)}$$

[3] The so-called "physical distribution" is not even exactly the plutonium content distribution. The count number of each pixel is only a measurement of the average of the plutonium content in the probed volume during the measurement. Heterogeneities smaller than this volume are thus averaged in the measurements and are thus diluted in the EPMA histograms. This effect was notably evidence by Simeon et al. [191] on rather homogeneous (U,Pu)O_2. Moreover, the mappings are recorded line after line and, in each line, by lateral displacement of the sample holder. For vertical displacements, the sample is thus moved of 1 µm along the y-axis between every lines and that position does not change during the measurements. For the horizontal displacement though, the counting time of 20 ms per point is achieved by continued displacement of the sample holder. The probed volume thus "moves" even during the measurements for each pixel.

[4] If these conditions are not met, the apparent distribution obtained by the convolution becomes dissymmetric and can even be off-centered compared to the physical distribution. This is because the standard deviation increases as the count number increases, thus adding a larger noise to the data for larger count numbers. For the conditions used in this study, the worst conditions were obtained for a distribution centered on 115 counts with a relative standard deviation of 7.5%, which already showed a little (but not significant) off-centering (corresponding to a shift lower than 0.25 wt% in Pu/(U+Pu+Am) ratio).

This is quite useful as μ_i and V_i values can be easily obtained by fitting the apparent distribution D (*i.e.*, the distribution extracted from the EPMA mapping) with a sum of Gaussian distributions. The standard deviation (or $FWHM_i$) corresponding to each of the underlying physical Gaussian components can thus be simply calculated.

$$\sigma_i = \sqrt{V_i^2 - N_i^2} \qquad \text{Eqn (59)}$$

$$FWHM_i = 2 \times \sigma_i \times \sqrt{2 \ln 2} \qquad \text{Eqn (60)}$$

This methodology is not intended to give an exact representation of the distribution of Pu contents in the samples. It is rather a simple way to extract some characteristics from the matrix phase of the homogeneous samples thus allowing for some comparisons:

- between before and after annealing for a given sample,
- between the similar Capra4 and Trabant40 samples,
- between EPMA and Raman microspectroscopy mappings.

This methodology was applied for the two SFR-type samples, but not for the MIMAS one. The latter has a very specific microstructure due to the process used for its manufacture (as described in Chapter 2 section 2.1) for which the dedicated methodology that has been used since several decades was applied [187], [196].

From a practical point of view, the count number distributions extracted from EPMA mappings were fitted with a sum of Gaussian components using the Fityk software [197]. The pixels corresponding to porosities (detected by thresholding on a sum-image of the uranium and plutonium mapping) were excluded from these distributions. For both Capra4 and Trabant40 samples, the apparent distributions is principally composed of a single mode, but no satisfying fits could be obtained with a single Gaussian component. To avoid multiplying the fit parameters, the fits were performed with two Gaussian components both centered on the distribution mode.

C.2X-ray diffraction (XRD)

C.2.1 Equipment

The sample stage of the XRD in the L26 laboratory is a custom design to handle the radioactive materials. It is a fully removable closed system with a 200 µm-thick beryllium window, which requires a careful handling. It can be easily plugged onto a glovebox, where the sample can be introduced. The system can then be then unplugged and positioned on the center of the goniometer. Figure 146 is a good demonstration of the sample stage connected on the glovebox and to the goniometer. The details of the sample stage and the experimentation with some of the actinide oxide materials are available in Vauchy et al [198].

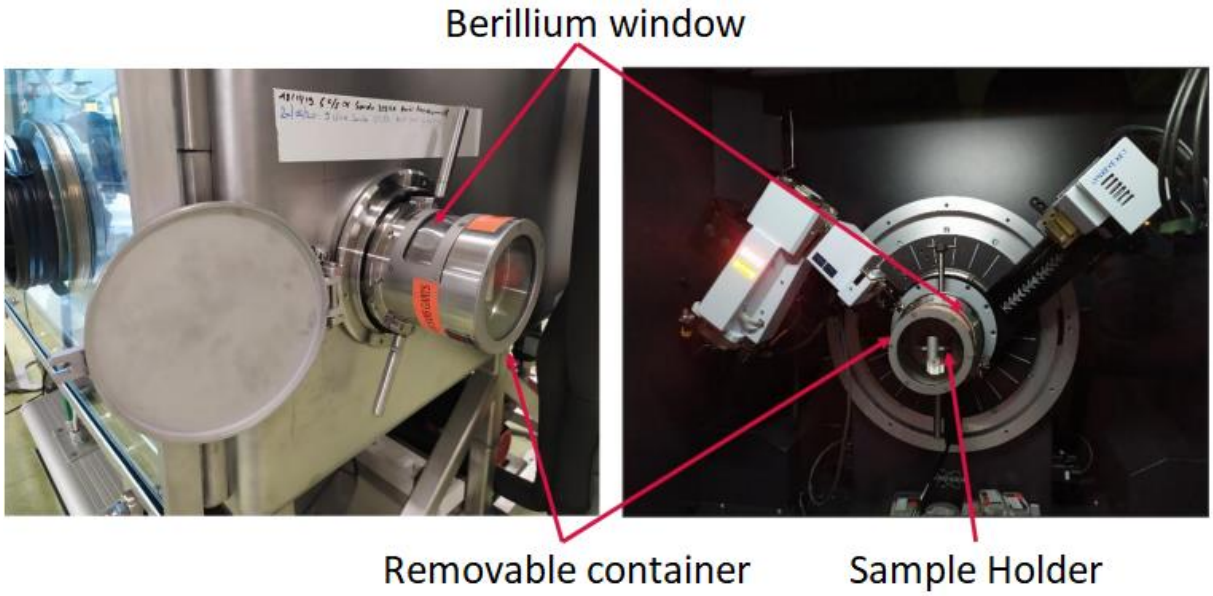

Figure 146 The sample holder designed for the X-ray diffractometer in the L26 laboratory, a) plugged on the glovebox, b) plugged on the middle of the goniometer. The figure is adapted from [191]

C.2.2 Sample Preparation

XRD samples were prepared by crushing and mixing 150-200 milligrams of MOX with ~20 mg of Au (Sigma-Aldrich, purity > 99.9%) in an agate mortar. Au was used as an internal reference for 2θ position. An organic grease is used to glue the MOX and the Au powder on a Bruker Si low background plate that is used as the sample holder.

C.2.3 Data acquisition and analysis

XRD was performed at room temperature using a Bruker D8 Advance diffractometer in θ−θ Bragg−Brentano geometry. It was equipped with a copper source [$\lambda(K_{\alpha1}/_{\alpha2})$ = 1.540598/1.54443 Å] and a Bruker LYNXEYE linear detector with a 3° opening angle. Diffraction patterns were recorded in a range of 2θ from 20 to 125°, with a 0.01° step and a counting time of 5 s per step.

Analysis and refinement of the X-ray patterns were performed using the TOPAS Bruker software [199] using the Le Bail method [200] and the Thompson−Cox−Hastings function for peak profile description [201]. The background was simulated using the default function suggested by the TOPAS software. For all samples, only *Fm*-3*m* phases were used for the refinement of the MOX materials. The 2θ zero-point deviation was corrected in the refinement by keeping the lattice parameter of the gold reference as a fixed variable (*Fm*-3*m* space group, lattice parameter of 4.0786 Å). For this particular diffractometer, the lattice parameters extracted from the MOX samples will be given with a minimum error of 0.001 Å (even though the error can be larger for phases present in a low amount or several phases too close to each other).

C.3Raman Microscopy

C.3.1 Equipment

Considering the fact that the $(U,Pu)O_2$ samples are rather radioactive, their Raman analysis must be performed in systems that are designed for radioactive materials. In the world, not more than a couple of laboratories possess Raman microscopes able to probe Pu-bearing solid samples. Within our knowledge so far, one of them is available in the USA in the [72], [167], [202] Savannah River National Laboratory, another one is in UK in the Sellafield National Laboratory [120], one is in JRC Karlsruhe [99] and the remaining two are at CEA Marcoule [97], [146].

One of the latter is installed in the L26 laboratory. The system (developed by Optique Peter [203]) is composed of a Horiba Jobin-Yvon iHR320 Raman spectrometer (outside the glovebox) coupled to a confocal microscope (inside the glovebox) as shown in Figure 147. The connection between the microscope and the spectrometer is done with optical fibers. The arrangement is equipped with two excitation wavelengths: 660 nm and 532 nm respectively corresponding to red and green lasers. Three different gratings (1200, 1800 and 2400 groove/mm^{-1}) can be used in the single stage spectrometer and the microscope is equipped with 4 objectives with ×5, ×20, ×50 and ×100 magnifications. The maximum power measured at the sample was 11mW and 50mW for the green and red lasers respectively. The power of the laser can be adjusted with filters to lower down the energy to a certain level such as to 100%, 25%, 10% and 1% of the maximum power.

Figure 147 The Raman microscope installed in the L26 laboratories in the Atalante facility (the spectrometer on the right, the microscope inside the glovebox system)

For Raman analyses, a custom sample holder (shown in Figure 148) was designed specifically by Optique Peter [203] for coated samples. This holder ensures a flat surface through an adjusting screw that compresses a spring, pressing the coating against the inner edge of the sample holder. If necessary, powders can also be examined by placing them on a support, such as glass slides or carbon adhesives.

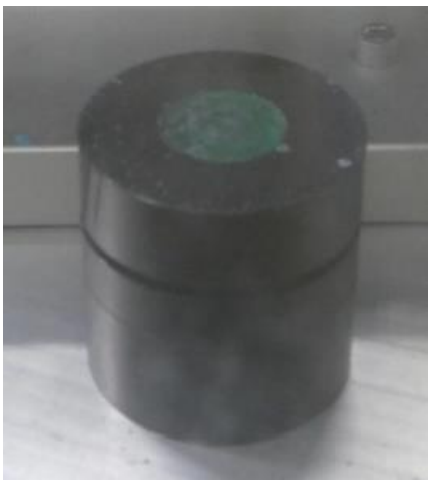

Figure 148 The sample holder designed Raman microscopy analysis of coated pellets

The sample holder is positioned on a motorized platform that can move in the x, y, and z directions and rotate. The z-axis motor, in conjunction with the Horiba-developed acquisition software Labspec 6.4.4 [204], can optimize the laser beam reflectivity at each analysis point using autofocusing. This detailed setup is perfectly suited for generating maps during data acquisition.

C.3.2 Spectra acquisition

All spectra were recorded using the ×100 objective under the 532 nm excitation wavelength and using a 1200 groove/mm grating. Such a configuration *a priori* ensured an accuracy on the frequency determination much better than 1 cm^{-1}. The spectrometer was calibrated using a silicon standard whose Raman line frequency has been fixed at 520.5 cm^{-1}. This accuracy is further enhanced with the light from a neon lamp that was injected in the path of the scattered light to get a permanent frequency calibration of the spectrometer. In general, the intensity of the signals used to reconstruct the images was relatively low, which is in the order of 200 counts for the T_{2g} position. As a result, a first data survey has shown that the accuracy on the frequency determinations could not be better than about ± 0.3 cm^{-1}. This uncertainty is a parameter to take into account as long as small line shifts are to be evidenced.

Spectra were recorded over the 90 to 1950 cm^{-1} wavenumber range. The incident power at the sample was adjusted to nearly 1 $mW/\mu m^2$ (using the 10% filter) to avoid overheating and/or modification of the sample upon laser illumination. In particular, no clear evolutions of the spectra were observed after several acquisitions that were run on the same spot.

The polarization of the scattered light was not completely analyzed. Nevertheless, it was verified that the setup had no strong polarization dependence, after analyzing the response of the silicon standard for various angles between the polarization of the incident beam and the crystal axis. For these different orientations, the response of the silicon standard remained almost constant after several tests.

C.3.3 Mapping

The idea of the technique is simply the acquisition of multiple Raman spectra on a selected zone in order to create the so-called Raman mappings. To break it down in a simple way, the technique starts with selecting an area on the sample surface for analysis. An operator defines a measurement step size, and a Raman spectrum is recorded at each point by moving the sample under a laser beam using a motorized stage (x, y). With motorization in the z-axis and the integrated option in the acquisition software, as mentioned in Section C.3.1, an autofocus system in the z-axis can be performed at each point to maximize the Raman signal. To achieve this, two methods are implemented in the Labspec software version 6 and

higher. The first is the "reflection" mode, which determines, using a photodiode in the microscope column, at which z-value the light reflected by the sample is the most significant. Considering the signal intensity, the adjustment takes between 1 or 2 seconds, and the z-value corresponds to the optical focus point, generally at the sample's surface. The second method is the "spectral" mode. In this case, the software measures a Raman spectrum at multiple z-values and determines at which position the Raman signal is the most significant. The signal can be either the entire spectrum or a range of wavenumbers defined by the operator. The first method is faster but does not necessarily provide the best signal as, depending on the material's refractive index, there may be a mismatch between the sample's surface and the focal point. However, depending on the intensity of the Raman signal from the material being studied, spectral autofocus can take several minutes and thus not suitable for acquiring mappings. Therefore, the approach that is employed in this study is to determine the difference in z between the two modes before performing 2D acquisitions and use it as an initial offset value. Subsequently, the mapping will be carried out using the "reflection" mode by imposing an "offset" of the previously obtained difference. The z-value is thus the one that would have been determined by the "spectral" mode but obtained in a shorter timeframe. This acquisition method is based on the assumption that the refractive index of the material does not vary within the analyzed surface, an assumption applied to the samples analyzed in this work.

The process of acquiring a Raman map proceeds as follows:

- Movement in the x and y directions of the stage to reach the next point in the grid.
- Movement in the z direction of the stage guided by the autofocus mode.
- Measurement of the spectrum for a duration specified by the operator and with a predefined number of acquisitions.

These steps are repeated for each point, resulting in a "hyperspectral data cube" where each point has a spectral dimension and two spatial dimensions, x and y. Nevertheless, it is necessary to remove non-chemical data from the maps before obtaining structural or compositional information from the sample. Thus, the following manipulations are made on the mappings before exploiting the data.

- Removal of cosmic rays (or spikes), which are electromagnetic waves originating from space. They manifest as very intense and narrow peaks in the spectra. Raman data processing software typically includes a correction tool that identifies and removes these artifacts by setting the intensity of these points to the average of the intensities of the two points surrounding the spike. Alternatively, two consecutive spectrum acquisitions are usually sufficient to eliminate cosmic rays, which is the method applied in this study.
- Baseline correction. This is typically modeled as a succession of straight lines or polynomials whose degree can be defined by the operator. The modeled baseline should follow the spectrum's background without minimizing the intensities of the bands. Software allows for subtracting the modeled baseline from the spectrum to obtain a flat background, but this step is optional. However, modeling is essential for refining the spectra later.
- Removal of luminescence spectra that can appear in impurities or pores, which result in a high baseline intensity that masks the Raman signal. The Labspec 6.4.4 software has an option that allows removing all spectra with intensities greater than the threshold defined by the operator in a selected wavenumber range. The threshold intensity value is adjusted based on the sample and the spectral quality of the map.

After these steps, the spectra can be refined. The operator determines the number of bands, and the software reflects their spectral characteristics such as are width, position or intensity, so that the resulting bands form a spectrum that closely matches the experimental spectrum. From the refined data, spectral variations corresponding to chemical or structural changes in the sample can be visualized. This step also helps identify any remaining "outlier" spectra that were not removed during the processing method. These may include spectra with only noise and no Raman signal, which could be due to pores or poor beam focusing. These outlier spectra can be identified by the values of band characteristics such as the band position. Once these spectra are identified and removed, the refinement process can be repeated.

Once the processing is completed, the analysis yields a 2D matrix for each spectral characteristic of the selected bands. To visualize variations in these characteristics related to the chemical and structural properties of the sample, data processing software (which is Labspec 6.4.4 in this work) assigns a color to each value according to the chosen scale. A summary diagram of the Raman map acquisition and processing method is shown in Figure 149.

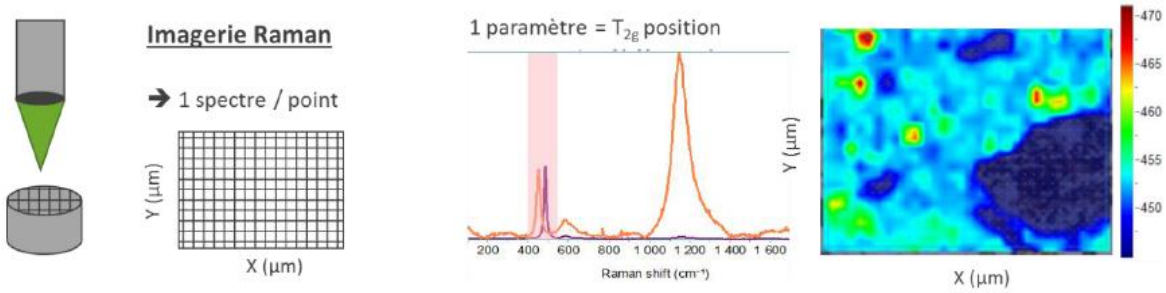

Figure 149 Diagram illustrating the process of acquiring and visualizing a Raman mapping [95]

For the samples concerned in this study, the Raman images were systematically constructed with a measurement step of 1 µm for the SFR and 2 µm for the MIMAS type MOX fuel, which is close to the actual spatial resolution of the method. The autofocus system of the instrument was used at every each acquisition points. The size of the examined areas (30 × 50 µm for the SFR) and (70 × 70 µm for the MIMAS) were chosen to get, as far as possible, representative maps for each sample. Typical acquisition times of individual spectra were in the 60 to 100 s range, to get an “acceptable” signal to noise (S/N) ratio for each measurement point. Minimal spectra preprocessing was preferred as it could introduce some artifacts. For some of the acquisitions (that are performed in the earlier period of the thesis), the light environment of the microscope was such that it was necessary to subtract its contribution in all the individual spectra. It was verified that this subtraction did not add additional uncertainty to the measurements, in particular for the frequencies extracted from the individual spectra. During the thesis, however, the CCD detector had to be replaced such correction was no longer necessary afterwards.

Besides the short-time-per-step acquisitions, some specific areas were identified in the images, and a few spectra were collected using much longer acquisition times, 300 s or more, to ensure capturing all the details of the spectra.

C.3.4 Data treament

Data processing (reconstruction of images from the information present in all spectra, histograms, line fitting, and acquisition of average spectra in some regions of the specimen) was achieved in part using the factory-supplied HORIBA Labspec 6.4.4 software. In particular, data averaging in specific regions (*i.e.* the constitutive agglomerates of the material) allowed significantly improving the S/N ratio of the spectra.

The same protocol was used to analyze the spectra of all samples, in particular for the determination of the frequencies. First, the integral intensity of the signal in a selected spectral range were graphically computed for each sample. This is a very fast on-screen method, which allows an immediate examination of the results. Band intensity ratios were in part obtained in such a way. From one sample to another, the selected spectral ranges were strictly the same, which allowed the direct comparison of the corresponding images. Then, line fitting was also used to extract spectral features. This allowed, among other things, a better determination of the different intensity ratios. In such a case, all the individual spectra were first truncated in different regions of interest. Then, a linear background was subtracted. The signals were subsequently fitted with mixed functions (Gaussian + Lorentzian) of same frequencies and widths. Line fitting with such a function does not really make physical sense, but it allows extracting comparable quantities from one sample to another.

C.4X-ray absorption spectroscopy (XAS)

In this study, synchrotron radiation was employed for both MIMAS and SFR type samples. For MIMAS-type samples, a micro-beam was utilized at the MARS beamline of the Soleil synchrotron [205] to independently probe the three phases, which include the U-rich and Pu-rich agglomerates, as well as the coating phase (as detailed in Chapter 4). The SFR type MOX samples, on the other hand, were analyzed on the ROBL beamline of the ESRF synchrotron [206]. The details of these experiments are given in the following sub-sections.

C.4.1 µ-XAS on the MARS beamline at Soleil Synchrotron

Three MIMAS type MOX samples having different levels of accumulated self-irradiation damage have been prepared and brought to the MARS beamline of the Soleil synchrotron. The description and the corresponding damage level of the samples are already detailed in Chapter 2 and Chapter 4 respectively.

C.4.2 Experimental set-up and sample preparation

In this synchrotron campaign, a micro beam was used, with a size of 15×16 μm^2 (FWHM) in the energy range used. Considering the size of the agglomerates of U-rich and Pu-rich (and the biggest zones of coating phase) phases in the MIMAS sample, it was possible to collect spectra of from each phase allocated in the sample.

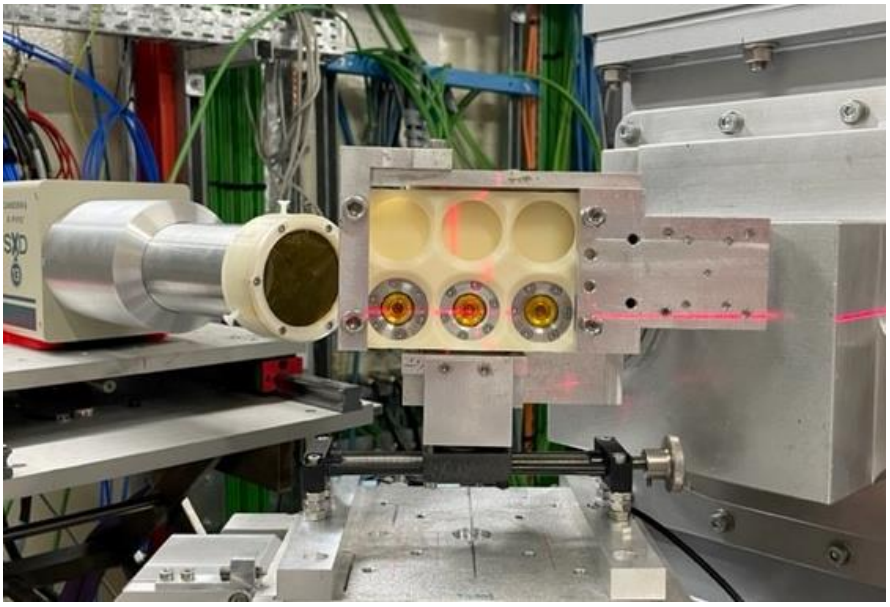

Figure 150 The fluorescence detector (on the left), the sample holder platform (in the middle). A red laser is used to locate the beam position, which is aimed to be on the sample surface

All samples brought were small pieces cut from the mirror-like polished pellet cross sections. The samples were cut in a rectangle form of 2x3 mm in size and 1 mm thickness to meet the activity limits indicated by the Soleil synchrotron, which was 18.5 GBq. The optical observation of the surface of the three sample are given in Figure 151. Each sample is placed in a sample holder consisting of two independent cells forming two confinement barriers. Both are equipped with Kapton windows, which is an organic material that has high mechanical and thermal stability as well as a high transmittance of X-rays. The three sample holders are visible (mounted on the beamline stage) in Figure 150.

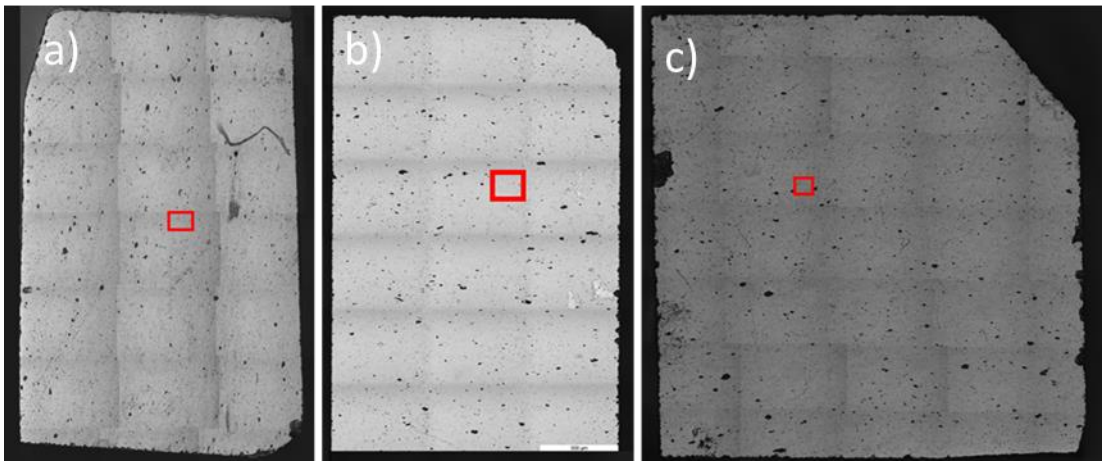

Figure 151 The optical images of the MIMAS samples brought to the MARS beamline. The samples are placed with the order of increased self-irradiation damage a) 44 days after annealing, b) 550 days after annealing, c) 5500 days after annealing. The red rectangle corresponds to the approximate zone that was already characterized with EPMA and Raman microscopy

Due to the confinement of the samples that is made of stainless steel as shown in *Figure 150*, only the fluorescence geometry was used to record the absorption information. Since the transmission geometry was not applicable in the beamline, the reference spectra used for energy calibration could not be collected continuously during each acquisition. Instead, the reference spectra were collected only once at the beginning of the experimental run. For the U L_{III} edge, the position of the Y K edge of a metallic Y foil (17038 eV) is used, while and the Zr K edge (17998 eV) of a metallic Zr foil was used both Pu L_{III} and Am L_{III} edges.

C.4.3 Measurements

For each sample, at first, X-ray fluorescence maps were recorded with the µ-beam at an energy of 18 keV, *i.e.*, above U, Pu and Am L_{III} edges. This allowed obtaining elementary maps for these three elements (U, Pu and Am). First, maps of several mm^2 were collected to help locating the zones that were already analyzed with EPMA and µ-Raman prior the campaign. In these zones, smaller mappings with a better spatial resolution were collected to locate precisely the zones having different Pu contents.

For all samples, at least two different zones of each phase (U-rich, Pu rich and coating) were identified in the X-ray fluorescence maps for measurements. On the determined positions, U L_{III} (17166 eV), Pu L_{III} (18057 eV) XANES/EXAFS and Am L_{III} XANES (18510 eV) spectra were then collected for the three samples (with the exception in the U-rich zones, where the collection of Pu and Am edges were skipped). All acquisitions were made at room temperature. A 13-element type Silicon drift detector (MIRION) is used for the measurements [207].

C.4.4 XAS in ESRF

C.4.4.1 Sample preparation and experimental setup

In total 9 SFR samples (6 Capra4 and 3 Trabant40 type) were prepared and brought to the ROBL beamline of the ESRF. For simplicity, the Capra4 are labeled as “C” and the Trabant40 are “Tr”. The brought samples simply have different levels of accumulated self-irradiation damage in their microstructure. With the order of the increased accumulated self-irradiation damage, they are labeled from C-1 to C-6 and from Tr-1 to Tr-3. The corresponding age of the samples are indicated in Table 24 and Table 25 in Chapter 4.

To meet the activity requirements indicated by the ROBL beamline of ESRF (maximum 185 MBq), all samples were crushed and ground into a fine powder in an agate mortar. The ground powder mixtures were pressed into 20 mg pellets (containing 0.8 mg of the MOX material) in a glovebox at the L26 laboratory. The pelletized samples were then confined in doubly confined polyethylene/teflon sample holders and transported to the beamline for the analysis. Spectra were collected using both transmission and fluorescence modes. Ionization chambers filled with N_2/Ar and an electrically cooled (Cryo-Pulse 5 Plus) 18-element germanium solid-state detector ere employed. The beam size and the distance between the sample and detector were adjusted to ensure compatibility with the fluorescence detector's linear range. The X-ray energy tuning was carried out using a double Si(111) crystal monochromator. Energy calibration of the spectra was performed using reference spectra, where the Y K edge (17038 eV) of a metallic Y foil is used for the U L_{III} edge, Zr K edge (17998 eV) was used for both Pu L_{III} and Am L_{III} edges, whereas. To serve as references, measurements of these metallic foils were taken concurrently with the samples in transmission mode, employing a second ionization chamber placed behind the foil. All acquisitions were made using a closed-cycle helium cryostat at 15K to reduce thermal disorder for the EXAFS spectra.
Measurements

XANES spectra were collected at the U, Pu and Am L_{III} edges (17166 eV, 18057 eV and 18510 eV respectively). For EXAFS, the L_{III} edge was also used for uranium, but the L_{II} edge (22266 eV) was used for plutonium, as the Am L_{III} would limit the energy range available at the Pu L_{III} edge. All spectra were collected both in fluorescence and transmission modes.

C.4.5 XAS Data analysis

C.4.5.1 XANES

Athena software was used to normalize the XANES spectra using a first order polynomial function for pre- and post-edge lines [208]. Regarding the fluorescence spectra, the self-absorption correction is performed using the same software, which was primarily essential for the U L_{III} edge spectra, given that uranium constitutes the majority of the cations within the matrix. The position of the absorption edge was picked as the first zero crossing of the second derivative. For the acquisitions made in ESRF the position of the absorption edge was later aligned with the corrected reference spectra obtained from the Yttrium K edge and Zirconium K edges. Nevertheless, this latter correction was not available in the Soleil Synchrotron campaign at least not for all acquisitions. Finally, to determine the average oxidation state of the cations, a reference spectrum of the compounds was used, and they were fitted together using the linear combination method within the Athena software. The references used for the linear combination method were UO_2 for U^{+IV}, U_4O_9 for U^{+V} (mixture of 50% of U^{+IV} and 50% of U^{+V}), PuF_3 for Pu^{+III}, PuO_2 for Pu^{+IV}, AmO_2 for Am^{+4} and $(U,Am)O_2$ for Am^{+3} [209]

C.4.5.2 EXAFS

C.4.5.2.1 The ESRF Campaign

In this campaign that concerns the SFR samples, the EXAFS spectra were collected up to 14 $Å^{-1}$ in the U L_{III} and Pu L_{II} edges. The Athena software was used to extract the EXAFS oscillations from the initial absorption spectra. The experimental EXAFS spectra were subjected to Fourier transformation across the k-range from 3 to 12.5 $Å^{-1}$ at the respective edges. Subsequently, curve fitting was done using the Artemis software version 0.8.012, with the fitting being carried out within the k_3 range spanning from 1.2 to 4.5 Å in terms of R values. To compute both the interatomic scattering paths and their associated

amplitudes, the FEFF 8.40 ab initio code was employed. Spherical clusters of atoms with an 8 Å radius were constructed for the UO_2 and PuO_2 crystal structures with a fluorite type arrangement (space group n°225, $Fm\bar{3}m$). Specifically, each cation position within the cluster comprised an equal distribution of 50% Pu and 50% U. The S_0^2 value was set at 0.92 for U and 1.0 for Pu shells, respectively. Furthermore, a global parameter was employed to vary the threshold energy shift (ΔE0).

C.4.5.2.2 The Soleil Campaign

The data quality obtained from the MIMAS samples was more complex than that from the SFR samples, largely attributable to the experimental setup and ambient conditions employed at the MARS beamline. For these samples, the EXAFS spectra were collected up to 12 $Å^{-1}$ in the U L_{III} and Pu L_{III} edges. However, when performing the Fourier transform, the k range was limited from 3.5 $Å^{-1}$ to only up to 9 $Å^{-1}$ due to a signal glitch occurring around 10.5 $Å^{-1}$.

For the U L_{III} edge, fitting was possible only at the k weights k_1 and k_2, while all k weights were applicable for the Pu L_{III} edge to perform the fit. An R range spanning from 1.3 to 4.5 Å was used for the fitting. The same crystal symmetry as indicated for the ESRF data treatment was employed. The S_0^2 value was set at 0.92 for the U shell and 0.9 for the Pu shell, respectively, while ΔE0 varied throughout the fits.

References

[1] World Nuclear Association, “Nuclear power in the world today,” 2022. [Online]. Available: https://world-nuclear.org/information-library/current-and-future-generation/nuclear-power-in-the-world-today.aspx.

[2] IRSN, “Cycle du combustible nucléaire en France. Technical note N°2018-00007,” 2018.

[3] S. Grandjean *et al.*, “CEA’s R&D on advanced fuel treatment with multi-recycling of plutonium and uranium,” *Glob. - 21st Int. Conf. Exhib.*, p. 5313, 2015.

[4] M. Kato *et al.*, “Self-radiation damage in plutonium and uranium mixed dioxide,” *J. Nucl. Mater.*, vol. 393, no. 1, pp. 134–140, 2009, doi: 10.1016/j.jnucmat.2009.05.020.

[5] T. D. Chikalla and R. P. Turcotte, “Self Radiation Damage Ingrowth in 238PuO2,” *Radiat. Eff.*, vol. 19, pp. 93–98, 1973.

[6] W. J. Nellis, “The Effect of Self-Radiation on Crystal Volume,” *Inorg. Nucl. Chem. Lett.*, vol. 13, pp. 393–398, 1977.

[7] M. Noe and J. Fuger, “Self-radiation effects on the lattice parameter of 238PuO2,” *Inorg. Nucl. Chem. Lett.*, vol. 10, no. 1, pp. 7–19, 1974, doi: 10.1016/0020-1650(74)80211-4.

[8] W. C. Mosley, “Self-Radiation Damage in Curium-244 Oxide and Aluminate,” *J. Am. Ceram. Soc.*, vol. 54, no. 10, pp. 475–479, 1971.

[9] C. Hurtgen and J. Fuger, “Self Irradiation Effects in Americium Oxides,” *Inorg. Nucl. Chem. Lett.*, vol. 13, pp. 179–188, 1977.

[10] T. Wiss *et al.*, “TEM study of alpha-damaged plutonium and americium dioxides,” *J. Mater. Res.*, vol. 30, no. 9, pp. 1544–1554, 2015, doi: 10.1557/jmr.2015.37.

[11] E. De Bona, “Grain size effects on radiogenic Helium gas in the nuclear fuel UO2. PhD thesis, Génie civil nucléaire. Université Paris-Saclay,” 2019.

[12] H. Balboa, L. Van Brutzel, A. Chartier, and Y. Le Bouar, “Damage characterization of (U,Pu)O2 under irradiation by molecular dynamics simulations,” *J. Nucl. Mater.*, vol. 512, pp. 440–449, 2018, doi: 10.1016/j.jnucmat.2018.07.056.

[13] L. Van Brutzel, J. M. Delaye, D. Ghaleb, and M. Rarivomanantsoa, “Molecular dynamics studies of displacement cascades in the uranium dioxide matrix,” *Philos. Mag.*, vol. 83, no. 36, pp. 4083–4101, 2003, doi: 10.1080/14786430310001616081.

[14] C. Guéneau, M. Baichi, D. Labroche, C. Chatillon, and B. Sundman, “Thermodynamic assessment of the uranium-oxygen system,” *J. Nucl. Mater.*, vol. 304, no. 2–3, pp. 161–175, 2002, doi: 10.1016/S0022-3115(02)00878-4.

[15] C. Guéneau *et al.*, “Thermodynamic modelling of advanced oxide and carbide nuclear fuels: Description of the U-Pu-O-C systems,” *J. Nucl. Mater.*, vol. 419, no. 1–3, pp. 145–167, 2011, doi: 10.1016/j.jnucmat.2011.07.033.

[16] M. Baichi, C. Chatillon, G. Ducros, and K. Froment, “Thermodynamics of the O-U system. IV - Critical assessment of chemical potentials in the U-UO2.01 composition range,” *J. Nucl. Mater.*, vol. 349, no. 1–2, pp. 17–56, 2006, doi: 10.1016/j.jnucmat.2005.09.001.

[17] C. Guéneau, A. Chartier, P. Fossati, L. van Brutzel, and P. Martin, *Thermodynamic and Thermophysical Properties of the Actinide Oxides*, vol. 7. 2020.

[18] B. E. Schaner, “Metallographic Determination of the UO2-U4O9 Phase Diagram,” *J. Nucl. Mater.*, vol. 2, no. 2, pp. 110–120, 1960.

[19] J. D. Higgs, B. J. Lewis, W. T. Thompson, and Z. He, “A conceptual model for the fuel oxidation of defective fuel,” *J. Nucl. Mater.*, vol. 366, no. 1–2, pp. 99–128, 2007, doi: 10.1016/j.jnucmat.2006.12.050.

[20] G. Leinders, T. Cardinaels, K. Binnemans, and M. Verwerft, “Accurate lattice parameter measurements of stoichiometric uranium dioxide,” *J. Nucl. Mater.*, vol. 459, pp. 135–142, 2015,

doi: 10.1016/j.jnucmat.2015.01.029.
[21] P. A. Tempest, P. M. Tucker, and J. W. Tyler, “Oxidation of UO2 fuel pellets in air at 503 and 543 K studied using X-ray photoelectron spectroscopy and X-ray diffraction,” *J. Nucl. Mater.*, vol. 151, no. 3, pp. 269–274, 1988, doi: 10.1016/0022-3115(88)90019-0.
[22] Y. Ma, “A study of point defects in UO2+x and their impact upon fuel properties. PhD thesis, Université d’Aix-Marseille Ecole,” Université d’Aix-Marseille, 2017.
[23] L. Lynds, W. A. Young, J. S. Mohl, and G. G. Libowitz, “X-Ray and Density Study of Nonstoichiometry in Uranium Oxides,” *Adv. Chem.*, vol. 39, pp. 58–65, 1963.
[24] B. T. M. Willis, “Structures of UO2, UO2+x and U4O9 by Neutron Diffraction,” *J. Phys.*, vol. 25, no. December, p. 431, 1964.
[25] B. T. M. Willis, “The Defect Structure of Hyper-stoichiometric Uranium Dioxide,” *Acta Crystallogr. Sect. A Found. Crystallogr.*, vol. A34, pp. 88–90, 1978, doi: 10.1021/ic400118p.
[26] Y. Li, “A fundamental understanding of the structures of oxygen defect clusters in UO2+x, U4O9 and U3O7: from the perspective of Tetris cubes,” *Acta Mater.*, vol. 194, pp. 482–495, 2020, doi: 10.1016/j.actamat.2020.05.032.
[27] W. Van Lierde, J. Pelsmaekers, and A. Lecocq-Robert, “On the phase limits of U4O9,” *J. Nucl. Mater.*, vol. 37, no. 3, pp. 276–285, 1970, doi: 10.1016/0022-3115(70)90157-1.
[28] B. Belbeoch, J. C. Boivineau, and P. Perio, “Changements de structure de l’oxyde U4O9,” *J. Phys. Chem. Solids*, vol. 28, no. 7, pp. 1267–1275, 1967, doi: 10.1016/0022-3697(67)90070-4.
[29] L. Desgranges, G. Baldinozzi, D. Simeone, and H. E. Fischer, “Structural Changes in the Local Environment of Uranium Atoms in the Three Phases of U4O9,” *Inorg. Chem.*, vol. 55, no. 15, pp. 7485–7491, 2016, doi: 10.1021/acs.inorgchem.6b00654.
[30] R. I. Cooper and B. T. M. Willis, “Refinement of the structure of β-U4O9,” *Acta Crystallogr. Sect. A Found. Crystallogr.*, vol. 60, no. 4, pp. 322–325, 2004, doi: 10.1107/S010876730401219X.
[31] L. Desgranges, G. Baldinozzi, D. Siméone, and H. E. Fischer, “Refinement of the α-U4O9 crystalline structure: New insight into the U4O9 → U3O 8 transformation,” *Inorg. Chem.*, vol. 50, no. 13, pp. 6146–6151, 2011, doi: 10.1021/ic200316b.
[32] L. Desgranges, G. Baldinozzi, P. Simon, G. Guimbretière, and A. Canizares, “Raman spectrum of U4O9: A new interpretation of damage lines in UO2,” *J. Raman Spectrosc.*, vol. 43, no. 3, pp. 455–458, 2012, doi: 10.1002/jrs.3054.
[33] L. Nowicki, F. Garrido, A. Turos, and L. Thomé, “Polytypic arrangements of cuboctahedral oxygen clusters in U3O7,” *J. Phys. Chem. Solids*, vol. 61, no. 11, pp. 1789–1804, 2000, doi: 10.1016/S0022-3697(00)00057-3.
[34] D. J. M. Bevan, I. E. Grey, and B. T. M. Willis, “The crystal structure of β-U4O9-y,” *J. Solid State Chem.*, vol. 61, no. 1, pp. 1–7, 1986, doi: 10.1016/0022-4596(86)90002-2.
[35] K. O. Kvashnina, S. M. Butorin, P. Martin, and P. Glatzel, “Chemical state of complex uranium oxides,” *Phys. Rev. Lett.*, vol. 111, no. 25, pp. 1–5, 2013, doi: 10.1103/PhysRevLett.111.253002.
[36] G. Leinders, R. Bes, J. Pakarinen, K. Kvashnina, and M. Verwerft, “Evolution of the Uranium Chemical State in Mixed-Valence Oxides,” *Inorg. Chem.*, vol. 56, no. 12, pp. 6784–6787, 2017, doi: 10.1021/acs.inorgchem.7b01001.
[37] K. B. Alberman and J. S. Anderson, “The Oxides of Uranium,” *J. Chem. Soc*, vol. 303, 1949.
[38] B. . Loopstra, “Neutron diffraction investigation of U3O8*,” *Acta Cryst*, vol. 17, pp. 651–654, 1964, doi: 10.1016/0025-5408(80)90096-3.
[39] B. O. Loopstra, “The Structure of Beta-U3O8,” *Acta Cryst.*, vol. B26, pp. 656–657, 1970, doi: 10.1107/S0567740870002935.
[40] H. R. Hoekstra, S. Siegel, and F. X. Gallagher, “The Uranium Oxygen System at High Pressure,” *J. Inorg. Nucl. Chem.*, vol. 32, pp. 3237–3248, 1970.
[41] H. R. Hoekstra, A. Santorot, and S. Siegel, “The Low Temperature Oxidation of UO2 and U4O9 *,” *J. Inorg. Nucl. Chem.*, vol. 18, pp. 166–178, 1961.
[42] L. Desgranges, G. Baldinozzi, G. Rousseau, J. C. Nièpce, and G. Calvarin, “Neutron diffraction study of the in situ oxidation of UO2,” *Inorg. Chem.*, vol. 48, no. 16, pp. 7585–7592, 2009, doi:

10.1021/ic9000889.
[43] E. F. Westrum and F. Grønvold, “Triuranium heptaoxides: Heat capacities and thermodynamic properties of α- and β-U3O7 from 5 to 350°K,” *J. Phys. Chem. Solids*, vol. 23, pp. 39–53, 1962, doi: 10.1016/0022-3697(62)90055-0.
[44] G. Leinders, J. Pakarinen, R. Delville, T. Cardinaels, K. Binnemans, and M. Verwerft, “Low-Temperature Oxidation of Fine UO2 Powders : A Process of Nanosized Domain Development,” *Inorg. Chem.*, vol. 55, no. 8, pp. 3915–3927, 2016, doi: 10.1021/acs.inorgchem.6b00127.
[45] G. Leinders, R. Delville, J. Pakarinen, T. Cardinaels, K. Binnemans, and M. Verwerft, “Assessment of the U3O7 Crystal Structure by X-ray and Electron Diffraction,” *Inorg. Chem.*, vol. 55, no. 19, pp. 9923–9936, 2016, doi: 10.1021/acs.inorgchem.6b01941.
[46] D. A. Andersson, G. Baldinozzi, L. Desgranges, D. R. Conradson, and S. D. Conradson, “Density Functional Theory Calculations of UO2 Oxidation: Evolution of UO2+x, U4O9−y, U3O7, and U3O8,” *Inorg. Chem.*, vol. 44, no. 22, pp. 2769–2778, 2013, doi: 10.1002/chin.201322001.
[47] B. . Loopstra, “The Phase Transition in alpha-U308 at 210°C,” *J. Appl. Cryst.*, vol. 3, pp. 94–96, 1970.
[48] G. C. Allen and N. R. Holmes, “A mechanism for the UO2 to α-U3O8 phase transformation,” *J. Nucl. Mater.*, vol. 223, no. 3, pp. 231–237, 1995, doi: 10.1016/0022-3115(95)00025-9.
[49] T. D. Chikalla, C. E. McNeilly, and R. E. Skavdahl, “The plutonium-oxygen system,” *J. Nucl. Mater.*, vol. 12, no. 2, pp. 131–141, 1964, doi: 10.1016/0022-3115(64)90132-1.
[50] E. R. Gardner, T. L. Markin, and R. S. Street, “The plutonium-oxygen phase diagram,” *J. Inorg. Nucl. Chem.*, vol. 27, no. 3, pp. 541–551, 1965, doi: 10.1016/0022-1902(65)80259-7.
[51] H. Kinoshita, M. Uno, and S. Yamanaka, “Phase relation assessment of the O-Pu-Zr system by thermodynamic modelling,” *J. Alloys Compd.*, vol. 354, no. 1–2, pp. 129–137, 2003, doi: 10.1016/S0925-8388(02)01340-3.
[52] C. Guéneau, C. Chatillon, and B. Sundman, “Thermodynamic modelling of the plutonium-oxygen system,” *J. Nucl. Mater.*, vol. 378, no. 3, pp. 257–272, 2008, doi: 10.1016/j.jnucmat.2008.06.013.
[53] D. Horlait, “Caractérisation structurale d’oxydes mixtes MIV1-xLnIIIxO2-x/2 (M = Ce , Th) préparés par voie oxalique. Etude multiparamétrique de la dissolution et évolution microstructurale. PhD Thesis. Chimie inorganique. Université Montpellier II - Sciences et Techn,” 2013.
[54] F. H. Ellinger, W. N. Miner, D. R. O’Boyle, and F. W. Schonfeld, “Constitution of Plutonium alloys - Los Alamos Scientific Laboratory Report,” 1968.
[55] L. Pauling, “XXIV. The Crystal Structure of the A-Modification of the Rare Earth Sesquioxides,” *Zeitschrift für Krist. - Cryst. Mater.*, vol. 69, no. 1–6, pp. 415–421, 1929, doi: 10.1524/zkri.1929.69.1.415.
[56] T. L. Markin and R. S. Street, “The Uranium-Plutonium-Oxygen Ternary Phase Diagram,” *J. Inorgranic Nucl. Chem.*, vol. 29, pp. 2265–2280, 1967.
[57] C. Sari, U. Benedict, and H. Blank, “A Study of the Ternary System of UO2-PuO2-Pu2O3,” *J. Nucl. Mater.*, vol. 35, pp. 267–277, 1970.
[58] T. Truphémus *et al.*, “Structural studies of the phase separation in the UO2-PuO2-Pu2O3 ternary system,” *J. Nucl. Mater.*, vol. 432, no. 1–3, pp. 378–387, 2013, doi: 10.1016/j.jnucmat.2012.07.034.
[59] P. Fouquet-métivier, “Study of the influence of americium on thermodynamic and structural properties of (U,Pu)O2±x mixed oxides. PhD thesis, Material chemistry,” Université Paris-Saclay, 2022.
[60] P. Chakraborty, C. Guéneau, and A. Chartier, “Modelling of plutonium diffusion in (U,Pu)O2±x mixed oxide,” *Solid State Ionics*, vol. 357, no. November, 2020, doi: 10.1016/j.ssi.2020.115503.
[61] J.-F. Vigier, P. M. Martin, L. Martel, D. Prieur, A. C. Scheinost, and J. Somers, “Structural Investigation of (U0.7Pu0.3)O2-x Mixed Oxides,” *Inorg. Chem.*, vol. 54, pp. 5358–5365, 2015, doi: 10.1021/acs.inorgchem.5b00392.
[62] T. Truphemus, “Study of Phase Equilibria as Function of Temperature in UO2-PuO2-Pu2O3 System for Nuclear Ceramics With High Plutonium Contents. PhD thesis, Matière condensée,

Nanosciences. Aix-Marseille Université," 2013.
[63] R. Vauchy, A. C. Robisson, F. Audubert, and F. Hodaj, "Ceramic processing of uranium-plutonium mixed oxide fuels (U1-yPuy)O2 with high plutonium content," *Ceram. Int.*, vol. 40, no. 7 PART B, pp. 10991–10999, 2014, doi: 10.1016/j.ceramint.2014.03.104.
[64] T. Ohmichi, S. Fukushima, A. Maeda, and H. Watanabe, "On the relation between lattice parameter and O/M ratio for uranium dioxide-trivalent rare earth oxide solid solution," *J. Nucl. Mater.*, vol. 102, pp. 40–46, 1981.
[65] R. D. Shannon, "Revised Effective Ionic Radii and Systematic Studies of Interatomie Distances in Halides and Chaleogenides," *Acta Cryst.*, vol. A 32, pp. 751–767, 1976.
[66] C. Duriez, J. P. Alessandri, T. Gervais, and Y. Philipponneau, "Thermal conductivity of hypostoichiometric low Pu content (U,Pu)O2-x mixed oxide," *J. Nucl. Mater.*, vol. 277, no. 2–3, pp. 143–158, 2000, doi: 10.1016/S0022-3115(99)00205-6.
[67] R. Vauchy, A. Robisson, R. C. Belin, P. M. Martin, A. C. Scheinost, and F. Hodaj, "Room-temperature oxidation of hypostoichiometric uranium-plutonium mixed oxides U1-y PuyO2 - A depth-selective approach," *J. Nucl. Mater.*, vol. 465, pp. 349–357, 2015, doi: 10.1016/j.jnucmat.2015.05.033.
[68] H. Föll, "Defects in Crystals Lecture Notes," *https://www.tf.uni-kiel.de/matwis/amat/def_en/*, 2004. .
[69] W. G. Wolfer, "Radiation Effects in Plutonium What is known ? Where should we go from here ?," *Los Alamos Sci 26*, no. 26, pp. 274–285, 2000.
[70] B. D. Wirth, A. J. Schwartz, M. J. Fluss, M. J. Caturla, M. A. Wall, and W. G. Wolfer, "Fundamental studies of plutonium aging," *MRS Bull.*, vol. 26, no. 9, pp. 679–683, 2001, doi: 10.1557/mrs2001.177.
[71] J. Soullard and A. Alamo, "Etude du ralentissement des ions dans une cible diatomique," *Radiat. Eff.*, vol. 38, pp. 133–139, 1978, doi: 10.1080/00337577808233221.
[72] E. Villa-Aleman, A. L. Houk, T. C. Shehee, and N. J. Bridges, "Raman signatures from age-dating PuO2 since last calcination," *J. Nucl. Mater.*, vol. 551, p. 152969, 2021, doi: 10.1016/j.jnucmat.2021.152969.
[73] L. Cognini *et al.*, "Helium solubility in oxide nuclear fuel: Derivation of new correlations for Henry's constant," *Nucl. Eng. Des.*, vol. 340, no. April, pp. 240–244, 2018, doi: 10.1016/j.nucengdes.2018.09.024.
[74] D. Prieur *et al.*, "Structural investigation of self-irradiation damaged AmO2," *J. Solid State Chem.*, vol. 212, pp. 7–12, 2014, doi: 10.1016/j.jssc.2013.12.016.
[75] H. Bateman, "The solution of a system of differential equations occurring in the theory of radioactive transformations," *Proc. Cambridge Philos. Soc*, vol. 15, no. 2, pp. 423–427, 1910, doi: 10.1016/0041-5553(73)90150-X.
[76] L. Morss, N. Edelstein, and J. Fuger, *The Chemistry of the Actinide and Transactinide Elements; Chapter 7 Plutonium*. Springer US, 2006.
[77] J. F. Ziegler, M. D. Ziegler, and J. P. Biersack, "SRIM - The stopping and range of ions in matter (2010)," *Nucl. Instruments Methods Phys. Res. Sect. B Beam Interact. with Mater. Atoms*, vol. 268, no. 11–12, pp. 1818–1823, 2010, doi: 10.1016/j.nimb.2010.02.091.
[78] W. J. Weber, "Ingrowth of lattice defects in alpha irradiated UO2 single crystals," *J. Nucl. Mater.*, vol. 98, pp. 206–215, 1981.
[79] W. J. Weber, "Thermal Recovery of Lattice Defects In Alpha Irradiated UO2 Crystals," *J. Nucl. Mater.*, vol. 114, pp. 213–221, 1983.
[80] W. J. Weber, "Alpha-irradiation damage in CeO2 ,UO2 and PuO2," *Radiat. Eff.*, vol. 83, no. 1–2, pp. 145–156, 1984, doi: 10.1080/00337578408215798.
[81] D. Horlait, F. Lebreton, P. Roussel, and T. Delahaye, "XRD monitoring of α self-irradiation in uranium-americium mixed oxides," *Inorg. Chem.*, vol. 52, pp. 14196–14204, 2013, doi: 10.1021/ic402124s.
[82] T. Wiss *et al.*, "Evolution of spent nuclear fuel in dry storage conditions for millennia and beyond,"

J. Nucl. Mater., vol. 451, no. 1–3, pp. 198–206, 2014, doi: 10.1016/j.jnucmat.2014.03.055.

[83] M. H. Rand, A. C. Fox, and R. S. Street, "Radiation Self-Damage In Plutonium Compounds," *Nature*, no. 4841, pp. 567–568, 1962.

[84] J. Soullard, "Contribution a L'Etude Des Defauts De Structure Dans Le Bioxyde D'Uranium Rapport CEA-R-4882," 1978.

[85] W. Breitung, "Oxygen self and chemical diffusion coefficients in UO2±x," *J. Nucl. Mater.*, vol. 74, no. 1, pp. 10–18, 1978, doi: 10.1016/0022-3115(78)90527-5.

[86] F. D'annucci and C. Sari, "Oxygen diffusion in uranium-plutonium oxide fuels at low temperatures," *J. Nucl. Mater.*, vol. 68, no. 3, pp. 357–359, 1977, doi: 10.1016/0022-3115(77)90265-3.

[87] A. S. Bayoğlu and R. Lorenzelli, "Oxygen diffusion in fcc fluorite type nonstoichiometric nuclear oxides MO2±x," *Solid State Ionics*, vol. 12, no. C, pp. 53–66, 1984, doi: 10.1016/0167-2738(84)90130-9.

[88] R. Evron, G. Kimmel, and Y. Eyal, "Thermal recovery of self-radiation damage in uraninite and thorianite," *J. Nucl. Mater.*, vol. 217, no. 1–2, pp. 54–66, 1994, doi: 10.1016/0022-3115(94)90304-2.

[89] D. Prieur, G. Pagliosa, J. Spino, R. Caciuffo, J. Somers, and R. Eloirdi, "Thermal recovery and lattice expansion of self-irradiated U 0.80Am0.20O2-x, an in situ high temperature x-ray diffraction study," *J. Solid State Chem.*, vol. 199, pp. 334–337, 2013, doi: 10.1016/j.jssc.2012.12.022.

[90] E. De Bona, A. Benedetti, O. Dieste, D. Staicu, T. Wiss, and R. J. M. Konings, "Radiation effects in alpha-doped UO2," *Nucl. Inst. Methods Phys. Res. B*, vol. 468, pp. 54–59, 2020, doi: 10.1016/j.nimb.2020.01.024.

[91] E. De Bona *et al.*, "Self-irradiation-induced disorder in (U,238Pu)O2," *MRS Adv.*, vol. 6, pp. 213–219, 2021.

[92] G. K. Williamson and W. H. Hall, "X-ray Line Broadening From Filed Aluminium and Wolfram," *Acta Metall.*, vol. 1, no. 1, pp. 22–31, 1953, doi: 10.1016/0001-6160(53)90006-6.

[93] D. Horlait, F. Lebreton, P. Roussel, and T. Delahaye, "XRD Monitoring of α Self-Irradiation in Uranium − Americium Mixed Oxides," *Inorg. Chem.*, no. 52, pp. 14196–14204, 2013.

[94] R. Mohun *et al.*, "Charged defects during alpha-irradiation of actinide oxides as revealed by Raman and luminescence spectroscopy," *Nucl. Instruments Methods Phys. Res. Sect. B Beam Interact. with Mater. Atoms*, vol. 374, pp. 67–70, 2016, doi: 10.1016/j.nimb.2015.08.003.

[95] L. Medyk, "L'enjeu de la maîtrise des propriétés locales (stœchiométrie, répartition cationique…) lors de la fabrication des combustibles (U,Pu)O2-x: potentialités de la microscopie Raman. PhD thesis. Physique Nucléaire Expérimentale [nucl-ex]. Université d'Orléans," 2021.

[96] M. Naji *et al.*, "Raman spectrum of plutonium dioxide: Vibrational and crystal field modes," *Phys. Rev. B*, vol. 95, no. 10, pp. 1–7, 2017, doi: 10.1103/PhysRevB.95.104307.

[97] Z. Talip *et al.*, "Characterization of un-irradiated MIMAS MOX fuel by Raman spectroscopy and EPMA," *J. Nucl. Mater.*, vol. 499, pp. 88–97, 2018, doi: 10.1016/j.jnucmat.2017.11.014.

[98] H. Li, P. Zhang, G. Li, J. Lu, Q. Wu, and Y. Gu, "Stress measurement for nonstoichiometric ceria films based on Raman spectroscopy," *J. Alloys Compd.*, vol. 682, pp. 132–137, 2016, doi: 10.1016/j.jallcom.2016.04.272.

[99] L. Medyk *et al.*, "Determination of the plutonium content and O/M ratio of (U,Pu)O2-x using Raman spectroscopy," *J. Nucl. Mater.*, vol. 541, p. 152439, 2020, doi: 10.1016/j.jnucmat.2020.152439.

[100] T. Livneh and E. Sterer, "Effect of pressure on the resonant multiphonon Raman scattering in UO2," *Phys. Rev. B - Condens. Matter Mater. Phys.*, vol. 73, no. 8, pp. 1–9, 2006, doi: 10.1103/PhysRevB.73.085118.

[101] E. Epifano *et al.*, "Extreme multi-valence states in mixed actinide oxides," *Commun. Chem.*, no. 59, pp. 1–11, 2019, doi: 10.1038/s42004-019-0161-0.

[102] R. M. Harker and C. Puxley, "Development of point defect Raman signatures in PuO2 through self irradiation, Plutonium Futures - the Science 2016, Baden-Baden, Germany," 2016, pp. 62–65, doi: 10.2789/069707.

[103] G. Guimbretière *et al.*, "Characterization of nuclear materials in extreme conditions: Raman

spectroscopy approach," *IEEE Trans. Nucl. Sci.*, vol. 61, no. 4, pp. 2045–2051, 2014, doi: 10.1109/TNS.2014.2311166.
[104] Z. Talip *et al.*, "Raman microspectroscopic studies of unirradiated homogeneous (U0.76Pu0.24)O2+x: the effects of Pu content, non-stoichiometry, self-radiation damage and secondary phases," *J. Raman Spectrosc.*, vol. 48, no. 5, pp. 765–772, 2017, doi: 10.1002/jrs.5092.
[105] M. J. Norgett, M. T. Robinson, and I. M. Torrens, "A proposed method of calculating displacement dose rates," *Nucl. Eng. Des.*, vol. 33, no. 1, pp. 50–54, 1975, doi: 10.1016/0029-5493(75)90035-7.
[106] R. Vauchy, "Etude du rapport O/M dans des nouveaux combustibles oxydes à base d ' U et Pu : élaboration et caractérisation de matériaux modèles U1-y PuyO2-x. PhD Thesis. Université de Grenoble.," 2014.
[107] P. Pourghahramani and E. Forssberg, "Microstructure characterization of mechanically activated hematite using XRD line broadening," *Int. J. Miner. Process.*, vol. 79, no. 2, pp. 106–119, 2006, doi: 10.1016/j.minpro.2006.02.001.
[108] C. Raman and K. Krishnan, "A New Type of Secondary Radiation," *Nature*, vol. 121, no. 3048, pp. 501–502, 1928.
[109] D. R. Neuville, D. De Ligny, and G. S. Henderson, "Advances in Raman Spectroscopy Applied to Earth and Material Sciences," *Rev. Mineral. Geochemistry*, vol. 78, pp. 509–541, 2014.
[110] R. Baddour-Hadjean and J. P. Pereira-Ramos, "Raman microspectrometry applied to the study of electrode materials for lithium batteries," *AIP Conf. Proc.*, vol. 1267, pp. 1137–1138, 2010, doi: 10.1063/1.3482342.
[111] P. Yu and M. Cardona, *Fundamentals of Semiconductors: Physics and Materials*. 2010.
[112] J. B. Renucci, R. N. Tyte, and M. Cardona, "Resonant Raman scattering in silicon," *Phys. Rev. B*, vol. 11, no. 10, pp. 3885–3895, 1975, doi: 10.1103/PhysRevB.11.3885.
[113] W. Hayes, R. Loudon, and J. L. Birman, "Scattering of Light by Crystals," *Phys. Today*, vol. 33, no. 4, p. 55, 1980, doi: 10.1063/1.2914020.
[114] M. Cardona, "Light Scattering in Solids II, Chapter 2 Resonance Phenomena," in *Light Scattering in Solids II*, Springer, 1982, pp. 19–178.
[115] H. Richter, Z. P. Wang, and L. Ley, "The one phonon Raman spectrum in microcrystalline silicon," *Solid State Commun.*, vol. 39, no. 5, pp. 625–629, 1981, doi: 10.1016/0038-1098(81)90337-9.
[116] I. F. Chang and S. S. Mitra, "Application of a modified random-element-isodisplacement model to long-wavelength optic phonons of mixed crystals*," *Phys. Rev.*, vol. 172, no. 3, pp. 924–933, 1968, doi: 10.1103/PhysRev.172.924.
[117] G. Lucazeau, "Effect of pressure and temperature on Raman spectra of solids: Anharmonicity," *J. Raman Spectrosc.*, vol. 34, no. 7–8, pp. 478–496, 2003, doi: 10.1002/jrs.1027.
[118] Z. V. Popović *et al.*, "Far-infrared spectroscopic study of CeO2 nanocrystals," *J. Nanoparticle Res.*, vol. 17, no. 23, pp. 1–7, 2015, doi: 10.1007/s11051-015-2859-y.
[119] I. Introduction, "Long-Wavelength Optical Lattice Vibrations in BaySr1−yF2 and SryCa1−yF2," *Phys. Rev.*, vol. 164, no. 3, pp. 1169–1184, 1967.
[120] M. J. Sarsfield, R. J. Taylor, C. Puxley, and H. M. Steele, "Raman spectroscopy of plutonium dioxide and related materials," *J. Nucl. Mater.*, vol. 427, no. 1–3, pp. 333–342, 2012, doi: 10.1016/j.jnucmat.2012.04.034.
[121] G. M. Begun, R. G. Haire, W. R. Wilmarth, and J. R. Peterson, "Raman spectra of some actinide dioxides and of EuF2," *J. Less-Common Met.*, vol. 162, no. 1, pp. 129–133, 1990, doi: 10.1016/0022-5088(90)90465-V.
[122] C. Jégou, R. Caraballo, S. Peuget, D. Roudil, L. Desgranges, and M. Magnin, "Raman spectroscopy characterization of actinide oxides U1-yPuyO2 : Resistance to oxidation by the laser beam and examination of defects," *J. Nucl. Mater.*, vol. 405, pp. 235–243, 2010, doi: 10.1016/j.jnucmat.2010.08.005.
[123] J. R. Schoonover, F. Weesner, G. J. Havrilla, M. Sparrow, and P. Treado, "Integration of elemental and molecular imaging to characterize heterogeneous inorganic materials," *Appl. Spectrosc.*, vol.

52, no. 12, pp. 1505–1514, 1998, doi: 10.1366/0003702981943202.
[124] V. G. Keramidas and W. B. White, “Raman spectra of oxides with the fluorite structure,” *J. Chem. Phys*, vol. 59, no. 3, pp. 1561–1562, 1973, doi: 10.1063/1.1680227.
[125] R. Downs, “The RRUFF Project: an integrated study of the chemistry, crystallography, Raman and infrared spectroscopy of minerals,” *Progr. Abstr. 19th Gen. Meet. Int. Mineral. Assoc. Kobe, Japan*, 2006.
[126] J. Schoenes, “Electronic transitions, crystal field effects and phonons in UO2,” *Phys. Rep.*, vol. 63, no. 6, pp. 301–336, 1980, doi: 10.1016/0370-1573(80)90158-1.
[127] H. He and D. Shoesmith, “Raman spectroscopic studies of defect structures and phase transition in hyper-stoichiometric UO2+x,” *Phys. Chem. Chem. Phys.*, vol. 12, no. 28, pp. 8108–8117, 2010, doi: 10.1039/b925495a.
[128] E. A. Stefaniak *et al.*, “Recognition of uranium oxides in soil particulate matter by means of μ-Raman spectrometry,” *J. Nucl. Mater.*, vol. 381, no. 3, pp. 278–283, 2008, doi: 10.1016/j.jnucmat.2008.08.036.
[129] J. M. Elorrieta *et al.*, “Raman study of the oxidation in (U, Pu)O2 as a function of Pu content,” *J. Nucl. Mater.*, vol. 495, pp. 484–491, 2017, doi: 10.1016/j.jnucmat.2017.08.043.
[130] J. Müller, W. Ibach, K. Weishaupt, and O. Hollricher, *Confocal Raman Microscopy*, vol. 66. 2018.
[131] E. E. Alp, S. M. Mini, and M. Ramanathan, “X-ray absorption spectroscopy: EXAFS and XANES - A versatile tool to study the atomic and electronic structure of materials,” *Synchrotron x-ray sources new Oppor. soil Environ. Sci. Work. Rep. Chapter 3*, pp. 25–36, 1990.
[132] “X-ray Spectra. Continuous and Characteristic Spectra,” *Ramdayalu Singh College Lecture Notes*. https://www.rdscollege.ac.in/studymaterial/1597736327.pdf?uid=.
[133] A. Kodre, I. Arčon, and J. P. Gomilšek, “X-ray absorption spectroscopy and related techniques,” *Acta Chim. Slov.*, vol. 51, pp. 1–10, 2004.
[134] M. Newville, “Fundamentals of XAFS,” *Rev. Mineral. Geochemistry*, vol. 78, pp. 33–74, 2014.
[135] J. J. Rehr, A. Ankudinov, and S. I. Zabinsky, “New developments in NEXAFS / EXAFS theory,” *Catal. Today*, vol. 39, pp. 263–269, 1998.
[136] L. Baumgarten, M. Angst, T. Bruckel, D. Richter, and R. Zorn, “F 4 X-ray Absorption Spectroscopy,” in *Scattering Methods for Condensed Matter Research: Towards Novel Applications at Future Sources*, vol. 33, 2012.
[137] Conradson S. D., “XAFS A Technique to Probe Local Structure,” *Los Alamos Sci. Reports*, vol. 26, pp. 422–435, 2000.
[138] R. Böhler *et al.*, “Recent advances in the study of the UO2 – PuO2 phase diagram at high temperatures,” vol. 448, pp. 330–339, 2014, doi: 10.1016/j.jnucmat.2014.02.029.
[139] M. M. Desagulier, J. Martinez, P. M. Martin, F. Lebreton, C. Guéneau, and N. Clavier, “Multi-scale structural investigation of uranium-plutonium mixed oxides (U1-yPuy)O2-x with high plutonium content,” *J. Nucl. Mater.*, vol. 585, no. March, 2023, doi: 10.1016/j.jnucmat.2023.154645.
[140] R. Vauchy, A. Joly, and C. Valot, “Lattice thermal expansion of Pu1-yAmyO2-x plutonium – americium mixed oxides,” *J. Appl. Crystallogr.*, vol. 50, pp. 1782–1790, 2017, doi: 10.1107/S1600576717014832.
[141] T. Livneh, “Resonant Raman scattering in UO2 revisited,” *Phys. Rev. B*, vol. 105, no. 4, pp. 1–10, 2022, doi: 10.1103/PhysRevB.105.045115.
[142] Y. Yun, D. Legut, and P. M. Oppeneer, “Phonon spectrum, thermal expansion and heat capacity of UO2 from first-principles,” *J. Nucl. Mater.*, vol. 426, no. 1–3, pp. 109–114, 2012, doi: 10.1016/j.jnucmat.2012.03.017.
[143] J. W. L. Pang *et al.*, “Phonon density of states and anharmonicity of UO2,” *Phys. Rev. B - Condens. Matter Mater. Phys.*, vol. 89, no. 11, pp. 1–11, 2014, doi: 10.1103/PhysRevB.89.115132.
[144] G. Dolling, R. A. Cowley, and A. D. B. Woods, “The Crystal Dynamics of Uranium Dioxide,” *Can. J. Phys.*, vol. 43, no. 2311, 1965.
[145] O. A. Maslova *et al.*, “Raman imaging and principal component analysis-based data processing on uranium oxide ceramics,” *Mater. Charact.*, vol. 129, pp. 260–269, 2017, doi:

10.1016/j.matchar.2017.05.015.
[146] O. Kahraman, F. Lebreton, P. Martin, and M. Mermoux, “Observable consequences of self-irradiation damage in a MIMAS-type MOX nuclear fuel as analyzed by x-ray diffraction, electron microprobe analysis, and Raman imaging. A possible methodological approach,” *J. Appl. Phys.*, vol. 132, no. 11, p. 115106, 2022, doi: 10.1063/5.0103348.
[147] P. Martin *et al.*, “XAS study of (U1−yPuy)O2 solid solutions,” *J. Alloys Compd.*, vol. 444–445, pp. 410–414, 2007, doi: 10.1016/j.jallcom.2007.01.032.
[148] R. Vauchy *et al.*, “Actinide Oxidation State and O/M Ratio in Hypostoichiometric Uranium-Plutonium-Americium U0.750Pu0.246Am0.004O2-x Mixed Oxides,” *Inorg. Chem.*, vol. 55, no. 5, pp. 2123–2132, 2016, doi: 10.1021/acs.inorgchem.5b02533.
[149] M. Osaka, T. Namekawa, K. Kurosaki, and S. Yamanaka, “Chemical thermodynamic representation of (U, Pu, Am)O2-x,” *J. Nucl. Mater.*, vol. 344, no. 1–3, pp. 230–234, 2005, doi: 10.1016/j.jnucmat.2005.04.047.
[150] M. Osaka, K. Kurosaki, and S. Yamanaka, “Oxygen potential of (Pu0.91Am0.09)O2-x,” *J. Nucl. Mater.*, vol. 357, no. 1–3, pp. 69–76, 2006, doi: 10.1016/j.jnucmat.2006.05.044.
[151] R. C. Belin, P. M. Martin, J. Lechelle, M. Reynaud, and A. C. Scheinost, “Role of cation interactions in the reduction process in plutonium-americium mixed oxides,” *Inorg. Chem.*, vol. 52, no. 6, pp. 2966–2972, 2013, doi: 10.1021/ic3023776.
[152] D. Prieur, U. Carvajal-Nunez, T. Vitova, and J. Somers, “Local and electronic structure of americium-bearing PuO2,” *Eur. J. Inorg. Chem.*, no. 9, pp. 1518–1524, 2013, doi: 10.1002/ejic.201201294.
[153] I. Sato, K. Tanaka, and T. Arima, “Diffusion behaviors of plutonium and americium in polycrystalline urania,” *IOP Conf. Ser. Mater. Sci. Eng.*, vol. 9, no. 012005, 2010, doi: 10.1088/1757-899x/9/1/012005.
[154] J. Simeon *et al.*, “Characterization by electron probe microanalysis, Raman spectroscopy and transmission electron microscopy of a MOX fuel sintered from a freeze-granulated powder,” *J. Eur. Ceram. Soc.*, vol. 42, no. 15, pp. 7237–7246, 2022, doi: 10.1016/j.jeurceramsoc.2022.08.056.
[155] J. F. Vigier *et al.*, “Synthesis and characterization of homogeneous (U,Am)O2 and (U,Pu,Am)O2 nanopowders,” *CrystEngComm*, vol. 24, no. 36, pp. 6338–6348, 2022, doi: 10.1039/d2ce00527a.
[156] M. Naji *et al.*, “An original approach for Raman spectroscopy analysis of radioactive materials and its application to americium-containing samples,” *J. Raman Spectrosc.*, vol. 46, pp. 750–756, 2015, doi: 10.1002/jrs.4716.
[157] F. Lebreton *et al.*, “Peculiar Behavior of (U,Am)O2-δ Compounds for High Americium Contents Evidenced by XRD, XAS, and Raman Spectroscopy,” *Inorg. Chem.*, vol. 54, no. 20, pp. 9749–9760, 2015, doi: 10.1021/acs.inorgchem.5b01357.
[158] D. Horlait, R. Caraballo, F. Lebreton, C. Jégou, P. Roussel, and T. Delahaye, “Self-irradiation and oxidation effects on americium sesquioxide and Raman spectroscopy studies of americium oxides,” *J. Solid State Chem.*, vol. 217, pp. 159–168, 2014, doi: 10.1016/j.jssc.2014.05.025.
[159] O. Pagès, A. V. Postnikov, M. Kassem, A. Chafi, A. Nassour, and S. Doyen, “Unification of the phonon mode behavior in semiconductor alloys: Theory and ab initio calculations,” *Phys. Rev. B - Condens. Matter Mater. Phys.*, vol. 77, no. 12, 2008, doi: 10.1103/PhysRevB.77.125208.
[160] S. Hubert, J. Purans, G. Heisbourg, P. Moisy, and N. Dacheux, “Local structure of actinide dioxide solid solutions Th1-xU xO2 and Th1-xPuxO2,” *Inorg. Chem.*, vol. 45, no. 10, pp. 3887–3894, 2006, doi: 10.1021/ic050888y.
[161] T. R. Griffiths, H. V. S. A. Hubbard, and M. J. Davies, “Electron transfer reactions in non-stoichiometric ceria and urania,” *Inorganica Chim. Acta*, vol. 225, no. 1–2, pp. 305–317, 1994, doi: 10.1016/0020-1693(94)04062-1.
[162] T. R. Griffiths and H. V. S. A. Hubbard, “Absorption spectrum of single-crystal UO2: Identification of and effect of temperature on the peak positions of essentially all optical transitions in the visible to near infrared regions using derivative spectroscopy,” *J. Nucl. Mater.*, vol. 185, no. 3, pp. 243–259, 1991, doi: 10.1016/0022-3115(91)90510-E.

[163] P. Ruello, K. D. Becker, K. Ullrich, L. Desgranges, C. Petot, and G. Petot-Ervas, “Thermal variation of the optical absorption of UO2: Determination of the small polaron self-energy,” *J. Nucl. Mater.*, vol. 328, no. 1, pp. 46–54, 2004, doi: 10.1016/j.jnucmat.2004.03.002.

[164] T. Mark McCleskey *et al.*, “Optical band gap of NpO2 and PuO2 from optical absorbance of epitaxial films,” *J. Appl. Phys.*, vol. 113, no. 1, pp. 1–7, 2013, doi: 10.1063/1.4772595.

[165] B. L. Scott *et al.*, “High quality epitaxial thin films of actinide oxides, carbides, and nitrides: Advancing understanding of electronic structure of f-element materials,” *Coord. Chem. Rev.*, vol. 266–267, no. 1, pp. 137–154, 2014, doi: 10.1016/j.ccr.2013.09.019.

[166] I. D. Prodan, G. E. Scuseria, and R. L. Martin, “Covalency in the actinide dioxides: Systematic study of the electronic properties using screened hybrid density functional theory,” *Phys. Rev. B - Condens. Matter Mater. Phys.*, vol. 76, no. 3, pp. 2–5, 2007, doi: 10.1103/PhysRevB.76.033101.

[167] E. Villa-Aleman, N. J. Bridges, T. C. Shehee, and A. L. Houk, “Raman microspectroscopy of PuO2 particulate aggregates,” *J. Nucl. Mater.*, vol. 515, pp. 140–149, 2019, doi: 10.1016/j.jnucmat.2018.12.022.

[168] J. C. Crowhurst *et al.*, “A combined theoretical and experimental investigation of uranium dioxide under high static pressure,” *J. Phys. Condens. Matter*, vol. 27, no. 26, 2015, doi: 10.1088/0953-8984/27/26/265401.

[169] T. R. Griffiths, H. V. S. A. Hubbard, G. C. Allen, and P. A. Tempest, “A new method for the determination of x in UO2+x: Optical absorption spectroscopy measurements,” *J. Nucl. Mater.*, vol. 151, no. 3, pp. 313–317, 1988, doi: 10.1016/0022-3115(88)90025-6.

[170] R. Schmitt *et al.*, “A review of defect structure and chemistry in ceria and its solid solutions,” *Chem. Soc. Rev.*, no. 49, pp. 554–592, 2020, doi: 10.1039/c9cs00588a.

[171] C. Schilling, A. Hofmann, C. Hess, and M. V. Ganduglia-Pirovano, “Raman Spectra of Polycrystalline CeO2: A Density Functional Theory Study,” *J. Phys. Chem. C*, vol. 121, no. 38, pp. 20834–20849, 2017, doi: 10.1021/acs.jpcc.7b06643.

[172] L. Desgranges, A. Canizares, and P. Simon, “Annealing of the Raman defect peaks in He-implanted UO2,” *J. Nucl. Mater.*, vol. 559, p. 153405, 2022, doi: 10.1016/j.jnucmat.2021.153405.

[173] P. Simon, A. Canizares, N. Raimboux, and L. Desgranges, “How can Raman spectroscopy be used to study nuclear fuel ?,” *MRS Bull.*, vol. 48, no. 2, pp. 118–123, 2023, doi: 10.1557/s43577-022-00371-w.

[174] J. M. Elorrieta, L. J. Bonales, N. Rodríguez-Villagra, V. G. Baonza, and J. Cobos, “A detailed Raman and X-ray study of UO2+x oxides and related structure transitions,” *Phys. Chem. Chem. Phys.*, vol. 18, no. 40, pp. 28209–28216, 2016, doi: 10.1039/c6cp03800j.

[175] L. M. Malard, M. A. Pimenta, G. Dresselhaus, and M. S. Dresselhaus, “Raman spectroscopy in graphene,” *Phys. Rep.*, vol. 473, pp. 51–87, 2009, doi: 10.1016/j.physrep.2009.02.003.

[176] G. Guimbretière *et al.*, “High temperature Raman study of UO2: A possible tool for in situ estimation of irradiation-induced heating,” *J. Raman Spectrosc.*, vol. 46, no. 4, pp. 418–420, 2015, doi: 10.1002/jrs.4661.

[177] D. G. Martin, “The thermal expansion of solid UO2 and (U, Pu) mixed oxides - a review and recommendations,” *J. Nucl. Mater.*, vol. 152, no. 2–3, pp. 94–101, 1988, doi: 10.1016/0022-3115(88)90315-7.

[178] I. H. Campbell and P. . Fauchet, “The Effects of Microcrystal Size and Shape on the One Phonon Raman Spectra of Crystalline Semiconductors,” *Solid State Commun.*, vol. 58, no. 10, pp. 739–741, 1986.

[179] J. E. Spanier, R. D. Robinson, F. Zhang, S. W. Chan, and I. P. Herman, “Size-dependent properties of CeO2-y nanoparticles as studied by Raman scattering,” *Phys. Rev. B - Condens. Matter Mater. Phys.*, vol. 64, no. 245407, pp. 1–8, 2001, doi: 10.1103/PhysRevB.64.245407.

[180] K. Rickert, T. A. Prusnick, M. M. Kimani, E. A. Moore, C. A. Merriman, and J. M. Mann, “Assessing UO2 sample quality with μ-Raman spectroscopy,” *J. Nucl. Mater.*, vol. 514, pp. 1–11, 2019, doi: 10.1016/j.jnucmat.2018.11.009.

[181] K. Teske, H. Ullmann, and D. Rettig, “Investigation of the oxygen activity of oxide fuels and fuel-

fission product systems by solid electrolyte techniques. Part I: Qualification and limitations of the method," *J. Nucl. Mater.*, vol. 116, no. 2–3, pp. 260–266, 1983, doi: 10.1016/0022-3115(83)90110-1.
[182] R. Vauchy, S. Hirooka, M. Watanabe, and M. Kato, "Breaking the hard-sphere model with fluorite and antifluorite solid solutions," *Sci. Rep.*, vol. 13, no. 1, pp. 1–7, 2023, doi: 10.1038/s41598-023-29326-0.
[183] T. Wiss, "Radiation Effects in UO2," in *Comprehensive Nuclear Materials: Volume 2.18*, Elsevier Inc., 2012, pp. 465–480.
[184] D. Staicu, T. Wiss, V. V. Rondinella, J. P. Hiernaut, R. J. M. Konings, and C. Ronchi, "Impact of auto-irradiation on the thermophysical properties of oxide nuclear reactor fuels," *J. Nucl. Mater.*, vol. 397, no. 1–3, pp. 8–18, 2010, doi: 10.1016/j.jnucmat.2009.11.024.
[185] D. F. Swinehart, "The Beer-Lambert law," *J. Chem. Educ.*, vol. 39, no. 7, pp. 333–335, 1962, doi: 10.1021/ed039p333.
[186] A. Massih, "Models for MOX fuel behaviour, SKI Report 2006:10."
[187] G. Oudinet *et al.*, "Characterization of plutonium distribution in MIMAS MOX by image analysis," *J. Nucl. Mater.*, vol. 375, no. 1, pp. 86–94, 2008, doi: 10.1016/j.jnucmat.2007.10.013.
[188] E. Picard, J. Noirot, R. L. Moss, H. Plitz, K. Richter, and J. Rouault, "First In-Pile Experimental Results of High- Plutonium-Content Oxide Fuel for Plutonium Burning in Fast Reactors," *Nucl. Technol.*, vol. 129:1, pp. 1–12, 2000.
[189] H. Bairiot, J. Van Vliet, G. Chiarelli, J. Edwards, S. H. Nagai, and F. Reshetnikov, "Overview Of MOX Fuel Fabrication Achievements," *MOX Fuel Cycle Technol. Mediu. Long Term Deploy.*, pp. 80–101, 1999.
[190] C. Fuchs *et al.*, "Project CAPRA Fabrication of 3 fuel pins TRABANT2 for irradiation in HFR-Petten," 1998.
[191] J. Simeon, "Frittage et développement de la microstructure du combustible nucléaire MOX RNR. PhD thesis, Physique Nucléaire Expérimentale. Université Grenoble Alpes," 2022.
[192] A. . Rogers, *Techniques of autoradiography*. Elsevier/North-Holland Biomedical Press, 1979.
[193] D. Drouin, A. R. Couture, D. Joly, X. Tastet, V. Aimez, and R. Gauvin, "CASINO V2.42 - A fast and easy-to-use modeling tool for scanning electron microscopy and microanalysis users," *Scanning*, vol. 29, no. 3, pp. 92–101, 2007, doi: 10.1002/sca.20000.
[194] C. Merlet, "Quantitative Electron Probe Microanalysis: New Accurate Φ (ρz) Description," *Mikrochim. Acta*, vol. 12, pp. 107–115, 1992, doi: 10.1007/978-3-7091-6679-6_8.
[195] A. El Abdi, "Génération 3D aléatoire de microstructures de combustibles nucléaires MOX et homogénéisation mécanique," 2021.
[196] G. Oudinet, "Analyse d'images et modélisation 2D/3D de la microstructure du combustible MOX. PhD Thesis. Université de Saint-Étienne," 2003.
[197] M. Wojdyr, "Fityk: A general-purpose peak fitting program," *J. Appl. Crystallogr.*, vol. 43, pp. 1126–1128, 2010, doi: 10.1107/S0021889810030499.
[198] R. Vauchy *et al.*, "New sample stage for characterizing radioactive materials by X-ray powder diffraction: Application on five actinide dioxides ThO2, UO2, NpO2, PuO2 and AmO2," *J. Appl. Crystallogr.*, vol. 54, pp. 636–643, 2021, doi: 10.1107/S1600576721002235.
[199] "Topas 4.2 - User Manual," 2009.
[200] A. Le Bail, "Whole powder pattern decomposition methods and applications: A retrospection," *Powder Diffr.*, vol. 20, no. 4, pp. 316–326, 2005, doi: 10.1154/1.2135315.
[201] P. Thompson, D. E. Cox, and J. B. Hastings, "Rietveld refinement of Debye–Scherrer synchrotron X-ray data from Al2O3," *J. Appl. Crystallogr.*, vol. 20, no. 2, pp. 79–83, 1987, doi: 10.1107/S0021889887087090.
[202] E. Villa-aleman, D. D. Dick, J. H. Christian, and B. J. Foley, "Laser-induced annealing of aged PuO2," *J. Raman Spectrosc.*, no. 52, pp. 1486–1489, 2021, doi: 10.1002/jrs.6185.
[203] "Hot lab equipments." www.optiquepeter.com.
[204] Horiba Scientific, "LabSpec 6 Spectroscopy Suite: Reference Manual," 2015.

[205] P. L. Solari, S. Schlutig, H. Hermange, and B. Sitaud, “MARS, a new beamline for radioactive matter studies at SOLEIL,” *J. Phys. Conf. Ser.*, vol. 190, 2009, doi: 10.1088/1742-6596/190/1/012042.
[206] W. Matz *et al.*, “ROBL - A CRG beamline for radiochemistry and materials research at the ESRF,” *J. Synchrotron Radiat.*, vol. 6, no. 6, pp. 1076–1085, 1999, doi: 10.1107/S0909049599010663.
[207] MirionTechnologies, “X-PIPS | Réseau SDD à 13 Éléments.”
[208] B. Ravel and M. Newville, “ATHENA, ARTEMIS, HEPHAESTUS: Data analysis for X-ray absorption spectroscopy using IFEFFIT,” *J. Synchrotron Radiat.*, vol. 12, no. 4, pp. 537–541, 2005, doi: 10.1107/S0909049505012719.
[209] D. Prieur *et al.*, “Local structure and charge distribution in mixed uranium-Americium oxides: Effects of oxygen potential and am content,” *Inorg. Chem.*, vol. 50, no. 24, pp. 12437–12445, 2011, doi: 10.1021/ic200910f.

Table of Contents

RÉSUMÉ

La France met en œuvre industriellement le retraitement des combustibles nucléaires usés pour extraire l'uranium et le plutonium des combustibles à base d'UO_2 usés. Le dioxyde de plutonium ainsi obtenu, et contenant principalement l'isotope fissile ^{239}Pu, est ensuite mélangé à du dioxyde d'uranium appauvri pour produire du $(U,Pu)O_2$ ou MOX (mélange d'oxydes). Le combustible MOX n'est actuellement pas recyclé après irradiation. Afin de se rapprocher d'un cycle du combustible nucléaire entièrement fermé, un multi-recyclage du plutonium, basé sur l'extraction du plutonium du combustible MOX usé, est nécessaire. Cette technologie est en cours d'étude dans le programme nucléaire français. Après irradiation, les combustibles MOX présentent une composition isotopique du plutonium enrichie en ^{238}Pu, ^{240}Pu et ^{241}Pu au détriment de l'isotope ^{239}Pu. Étant donné les activités α (alpha) significativement plus élevées des isotopes ^{238}Pu (633,4 GBq/g), ^{240}Pu (8,4 GBq/g) et ^{241}Am (127 GBq/g), créé par désintégration béta du ^{241}Pu, par rapport à celle du ^{239}Pu (2,3 GBq/g), les combustibles MOX fabriqués avec cette nouvelle composition isotopique seront soumis à des conditions d'auto-irradiation α beaucoup plus sévères que les combustibles actuels. Ceci constitue l'un des défis associés au multi-recyclage du plutonium. En effet, au niveau macroscopique, l'auto-irradiation α entraîne un gonflement du réseau cristallin en raison notamment des défauts ponctuels créés par les cascades de collisions générées par l'émission des noyaux de recul lors des désintégrations α. Cette augmentation du paramètre de maille de $(U,Pu)O_2$ en fonction du temps est plutôt bien documentée dans la littérature et une loi empirique a été établie. Cependant, une compréhension complète des mécanismes sous-jacents à l'échelle microscopique demeure incomplète. Dans ce contexte, ce travail de thèse se concentre sur la caractérisation et la compréhension des défauts générés par l'auto-irradiation α dans les MOX et leur impact sur les propriétés microstructurales du combustible. À cette fin, des échantillons de MOX présentant différentes microstructures et homogénéités en U/Pu et ayant accumulé différents niveaux de dommages d'auto-irradiation ont été étudiés sur toute la période de la thèse. L'originalité de ces travaux de thèse réside dans l'utilisation combinée de techniques expérimentales pour des caractérisations allant de l'échelle macroscopique jusqu'à l'échelle atomique. Ainsi, la répartition locale U/Pu a été caractérisée par EPMA (microsonde électronique) afin d'évaluer, avec une résolution de l'ordre du micromètre, le niveau d'homogénéité cationique des échantillons étudiés et d'y sélectionner des zones d'intérêt pour des analyses plus poussées. L'évolution du paramètre de maille a été suivi par DRX (diffraction des rayons X) qui a également renseigné sur le niveau d'endommagement structural à l'échelle des cristallites en fonction de la dose α accumulée. Cependant, les informations obtenues avec ces techniques se limitent aux cations. Des informations sur le sous-réseau d'oxygène ont été obtenues en utilisant la spectroscopie Raman qui a permis également d'étudier les évolutions de la symétrie locale de la maille cristalline. Enfin, l'analyse des spectres de XAS (spectroscopie d'absorption des rayons X) collectés au sein des synchrotrons SOLEIL et ESRF a permis d'étudier les évolutions de l'ordre à courte distance, avec l'évolution des sphères de coordination O et cation autour des atomes d'U et de Pu. Par ailleurs, les spectres XAS ont également permis de déterminer les états d'oxydation des différents cations suivant les dommages d'auto-irradiation. En résumé, cette recherche combine des études par DRX, spectroscopie Raman, XAS et EPMA pour identifier les défauts structuraux causés par les effets de l'auto-irradiation α dans les MOX

Mot clef : Combustibles nucléaires, MOX, Caractérisation des matériaux, Microscopie Raman, Spectrométrie d'absorption des rayons X

ABSTRACT

In France, spent nuclear fuel reprocessing is used industrially to extract uranium and plutonium from spent UO_2-based fuels. The obtained plutonium dioxide, containing mainly the fissile ^{239}Pu isotope, is then mixed with depleted uranium dioxide to produce $(U,Pu)O_2$ or MOX (mixed oxides) fuels. MOX fuel is not currently recycled after irradiation. In order to move closer to a fully closed nuclear fuel cycle, multi-recycling of plutonium, based on the extraction of plutonium from spent MOX fuels, is required. This technology is currently being studied in the French nuclear program. After irradiation, MOX fuels have a plutonium isotopic composition enriched in ^{238}Pu, ^{240}Pu and ^{241}Pu at the expense of the ^{239}Pu isotope. Given the significantly higher α (alpha) activities of ^{238}Pu (633.4 GBq/g), ^{240}Pu (8.4 GBq/g) and ^{241}Am (127 GBq/g) isotopes, created by beta decay of ^{241}Pu, compared with that of ^{239}Pu (2.3 GBq/g), MOX fuels manufactured with this new isotopic composition will be subject to much more severe α self-irradiation conditions than current MOX fuels. This is one of the challenges associated with plutonium multi-recycling. Indeed, at the macroscopic level, α self-irradiation leads to a swelling of the crystalline lattice due in particular to the point defects created by the collision cascades generated by the recoil nuclei resulting from α decays. This increase in the lattice parameter of $(U,Pu)O_2$ as a function of time is fairly well documented and an empirical law has been reported in the literature. However, a comprehensive understanding of the underlying mechanisms at the microscopic scale remains incomplete. In this context, this thesis work focuses on the characterization and understanding of defects generated by α self-irradiation in MOX and their impact on the microstructural properties of the MOX fuel. To this end, MOX samples with different microstructures and U/Pu homogeneities and having accumulated different levels of self-irradiation damage were studied throughout the thesis period. The originality of this thesis work lies in the combined use of complementary experimental techniques for characterizations ranging from the macroscopic to the atomic scale. The local U/Pu distribution was characterized by EPMA (electron microprobe) in order to assess, with a micrometer resolution, the samples' cationic homogeneity and to select areas of interest for further analysis. The evolution of the lattice parameter was monitored by X-ray diffraction (XRD), which also provided information on the level of structural damage at the crystallite level as a function of the accumulated α dose. However, the information obtained with these techniques is limited to the cations. Information on the oxygen sublattice was obtained using Raman spectroscopy, which also made it possible to study changes in the local symmetry of the crystal lattice. Finally, analysis of the XAS (X-ray absorption spectroscopy) spectra collected at the SOLEIL and ESRF synchrotrons enabled to study changes in the short-range order, with the evolution of the O and cation coordination spheres around the U and Pu cations. XAS spectra were also used to determine the oxidation states of the cations depending on the self-irradiation damage. As a summary, this research combines XRD, Raman spectroscopy, XAS and EPMA studies to identify the structural defects caused by α self-irradiation effect in MOX fuels.

Keywords: Nuclear fuel, MOX, Material characterization, Raman microscopy, X-ray absorption spectroscopy